UNIVERSITY OF AMSTERDAM

UvA-DARE (Digital Academic Repository)

Exploring the link between neutron stars and fast radio bursts

Pastor-Marazuela, I.

Publication date
2022
Document Version
Final published version

Link to publication

Citation for published version (APA):
Pastor-Marazuela, I. (2022). *Exploring the link between neutron stars and fast radio bursts*.

General rights
It is not permitted to download or to forward/distribute the text or part of it without the consent of the author(s) and/or copyright holder(s), other than for strictly personal, individual use, unless the work is under an open content license (like Creative Commons).

Disclaimer/Complaints regulations
If you believe that digital publication of certain material infringes any of your rights or (privacy) interests, please let the Library know, stating your reasons. In case of a legitimate complaint, the Library will make the material inaccessible and/or remove it from the website. Please Ask the Library: https://uba.uva.nl/en/contact, or a letter to: Library of the University of Amsterdam, Secretariat, Singel 425, 1012 WP Amsterdam, The Netherlands. You will be contacted as soon as possible.

UvA-DARE is a service provided by the library of the University of Amsterdam (https://dare.uva.nl)

Download date:11 Nov 2022


Exploring the link between Neutron Stars and Fast Radio Bursts
Inés Pastor-Marazuela
Exploring the link
between Neutron Stars
and Fast Radio Bursts
Inés Pastor-Marazuela

Exploring the link between Neutron Stars and Fast Radio Bursts

Inés Pastor-Marazuela

© 2022, Inés Pastor-Marazuela
contact: ines.pastor.marazuela@gmail.com

Exploring the link between Neutron Stars and Fast Radio Bursts
Thesis, Anton Pannekoek Institute, Universiteit van Amsterdam

Cover by Gabriel and Jimena Pastor Marazuela
Printed by Gildeprint

UNIVERSITY OF AMSTERDAM

ANTON PANNEKOEK INSTITUTE

ALERT

The research included in this thesis was carried out at the Anton Pannekoek Institute for Astronomy (API) of the University of Amsterdam. It was supported by the Netherlands Research School for Astronomy (NOVA) and ASTRON.

Exploring the link between Neutron Stars and Fast Radio Bursts

ACADEMISCH PROEFSCHRIFT

ter verkrijging van de graad van doctor
aan de Universiteit van Amsterdam
op gezag van de Rector Magnificus
prof. dr. ir. P.P.C.C. Verbeek
ten overstaan van een door het College voor Promoties ingestelde commissie,
in het openbaar te verdedigen in de Agnietenkapel
op dinsdag 1 november 2022, te 12.00 uur

door

Inés Pastor-Marazuela

geboren te Segovia

Promotiecommissie:

Promotor(es):	prof. dr. R.A.M.J. Wijers	Universiteit van Amsterdam
Copromotor(es):	dr. A.G.J. van Leeuwen	ASTRON
Overige leden:	prof. dr. B.W. Stappers	The University of Manchester
	dr. S. Bhandari	Joint Institute for VLBI ERIC
	dr. B.A. Rowlinson	ASTRON & Universiteit van Amsterdam
	prof. dr. R.A.D. Wijnands	Universiteit van Amsterdam
	prof. dr. L. Kaper	Universiteit van Amsterdam

Faculteit der Natuurwetenschappen, Wiskunde en Informatica

A mi familia

L'Astronomie est utile, parce qu'elle nous élève au-dessus de nous-mêmes; elle est utile, parce qu'elle est grande; elle est utile, parce qu'elle est belle... C'est elle qui nous montre combien l'homme est petit par le corps et combien il est grand par l'esprit, puisque cette immensité éclatante où son corps n'est qu'un point obscur, son intelligence peut l'embrasser tout entière et en goûter la silencieuse harmonie.

Henri Poincaré

Contents

1

Introduction

Looking up at the night sky far away from the city lights is perhaps one of the most humbling experiences I can think of. To realise how small, insignificant we are when compared to the stars we are able to discern, which are just a tiny fraction of the whole Universe we live in. And yet as humans we are capable of wondering how we got here, how the Universe formed and evolved, and what kind of intriguing objects and phenomena are still unknown to us. With our human limitations, we perceive the sky as something eternal and unchanging. However, not only does the range of light extend much further than the optical wavelengths we are able to see, from radio to gamma-rays; there are also variable sources that are rarely observed with the naked eye during the lifespan of a single person. Within our Solar System, we can see comets and asteroids when they approach the Sun. Further in the Galaxy there are, for example, variable stars, as well as neutron stars that emit periodic signals as they rotate, known as pulsars.

Other variable sources of light are ‘‘transients’’ that can rapidly appear and vanish in the sky. They can be, for instance, the explosions of stars known as supernovae, the merger of two dead stars, or the disintegration of a star when it gets too close to a supermassive black hole. These transients are some of the most energetic phenomena in the Universe. The combination of this energetic nature and the difficulty of catching them given their short duration makes them fascinating to me. Fast Radio Bursts (FRBs) are a particular type of transient only visible at radio wavelengths, and they were first discovered only fifteen years ago. Their duration is shorter than the blink of an eye, but they reach Earth after travelling through Space for billions of years after they are produced in distant galaxies. The existence of these bright radio flashes was not predicted by any major theory, and their exact nature is still strongly debated. However, since I first heard about FRBs shortly before I started my PhD until the present day, the field has been revolutionised by an extraordinary amount of new discoveries. My thesis reflects this transformation, which I have had the amazing chance of witnessing in real time and even participate in.

In this chapter I will introduce the discovery history of FRBs, and the main properties of the population as we know it today. This includes the different classes we distinguish at present, the observed properties of the bursts, and the host galaxies in which they have been localised. I will next expound the different theories that have been put forward about what could produce them and how they could be generated, while contrasting these to the current observations. Next I will detail the propagation effects that alter the detected signals, and enumerate some of the main equations that can be used to infer the properties of the media the bursts have travelled through. Later I will mention the main radio telescopes that have made important contributions to the FRB field, mainly focusing on those I have used during my thesis, as well as some of the main multi-wavelength FRB searches that have been carried out. Finally, I will outline this thesis.

1.1 Fast Radio Bursts

1.1.1 Discovery

In 2007, an unforeseen radio burst with a duration of just a few milliseconds was discovered. Lorimer et al. (2007) found the burst in archival pulsar observations, taken with the Parkes radio telescope back in 2001, and it was so bright it saturated some of the receivers. But the most striking property about this source was its large dispersion delay; it far exceeded the Galactic contribution to the dispersion, quantified with the Dispersion Measure (DM), expected from Milky Way (MW). This unambiguously placed the source at extragalactic distances, which implied an extremely high burst luminosity.

This discovery suggested the existence of a whole population of short, bright extragalactic radio bursts, since the derived all-sky rate upper limit was comparable to that of other cosmological transients. It was not until several years later, however, that the detection of four additional bursts with similar properties was confirmed (Thornton et al. 2013), and the appellation ‘‘Fast Radio Bursts’’ was coined. Because of the large energies inherent to bright bursts at such distances, these findings generated enthusiasm in the scientific community, and single burst searches started to be carried out. An example of an FRB signal (dynamic spectrum) is shown in Fig. 1.1.

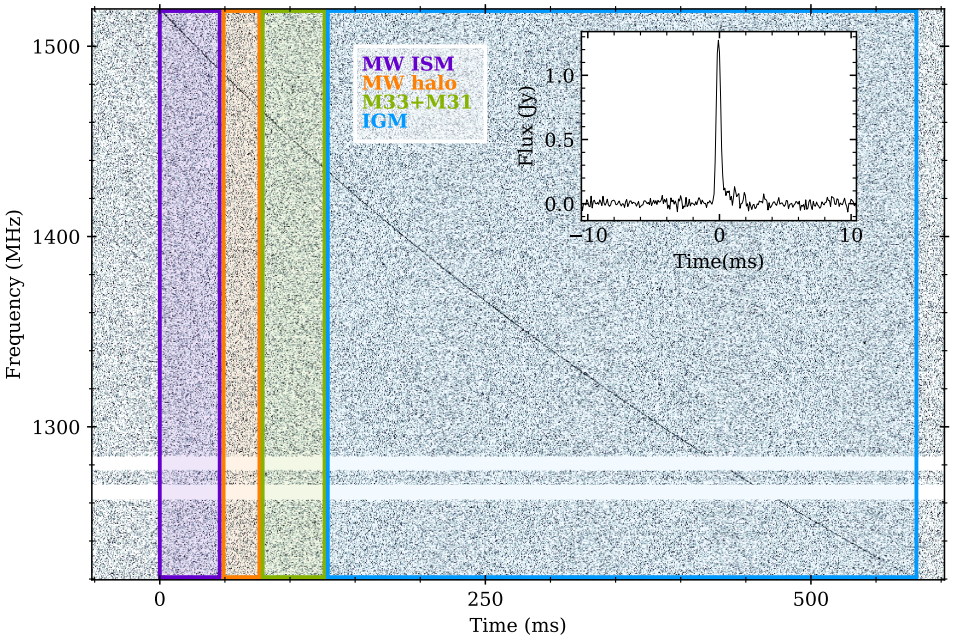

Figure 1.1: Dynamic spectrum of FRB 20191108A that travelled through the circumgalactic environment of the Local Group galaxies M33 and M31 (adapted from Connor et al. 2020). The signal (dark grey) arrives later at lower frequencies. The delay contributions from the Milky Way, its halo, the galaxies M33 and M31 are dwarfed by the effect of the intergalactic medium. The white horizontal lines are frequency channels affected by radio frequency interference. The inset plot shows the dedispersed pulse profile of the burst.

The FRB discovery rate remained quite low during almost a whole decade. Their astrophysical origin was even put into question for a while due to the lack of detections by instruments other than Parkes, as well as to the existence of ‘‘perytons’’; terrestrial transients that imitated the dispersion of real astrophysical FRBs, but that turned out to be generated when a microwave door was opened before it stopped at the Parkes site (Petroff et al. 2015b). Some radio telescopes soon started dedicated FRB follow-up observations of specific sources, while others have initiated all-sky FRB surveys in order to find new bursts. Since the original discovery fifteen years ago, hundreds of new FRBs have been detected with numerous instruments. From these hundreds of detections, intriguing properties have started to appear.

1.1.2 One-offs versus repeaters

One of the most noticeable properties of an FRB is how often it repeats. This has led to the classification of FRBs into two main groups.

The one-off or non-repeating FRBs, as their name indicates, are those that have only been seen once. The majority of known FRBs, including the ‘‘Lorimer’’ burst, appear to belong to this class. The current number of published one-off FRBs is around 600, with a large majority of those detected with a single instrument within its first year of survey (CHIME/FRB Collaboration et al. 2021a). The properties of all published FRBs are accessible through the Transient Name Server (TNS) database[1].

The other type of FRBs are the repeaters, which are those that have been seen multiple times. The first known repeater, FRB 20121102A, was originally detected in 2012 as a single burst (Spitler et al. 2014), but several bursts from the same location and with the same DM were seen in later observations (Spitler et al. 2016). While FRB 20121102A remained the only known repeater for several years, at present there are 24 repeaters. The majority of those were detected with CHIME/FRB (CHIME/FRB Collaboration et al. 2019a,c; Fonseca et al. 2020; Bhardwaj et al. 2021; CHIME/FRB Collabortion 2021), and three more were found to repeat with other instruments (Kumar et al. 2019; Price et al. 2019; Luo et al. 2020; Niu et al. 2022).

Unlike pulsars, the time between consecutive bursts from repeating FRBs is not periodic. However, the bursts of the most active repeaters appear clustered in time; we often refer to periods of elevated burst rates as *activity cycles*. Two FRBs have been found to show periodic activity cycles, which means they emit bursts at irregular times during an active window of time, and then become quiescent before turning active again. The first FRB that was found to show such behaviour, FRB 20180916B (CHIME/FRB Collaboration et al. 2020), has a period of $\sim$ 16.3 days. The original repeater, FRB 20121102A, was later also found to show an activity cycle of $\sim$ 160 days (Cruces et al. 2020; Rajwade et al. 2020). These sources are two of the most active and earliest detected repeaters, and the detection of a periodicity was possible because of the short cycle of FRB 20180916B and the long time monitoring of FRB 20121102A. Although no periodic activity cycles have been detected in other repeaters, one might expect to find such behaviour there too, if all repeaters have the same underlying physical origin. Besides periodicity, the activity of repeaters can be very different from one another. Some FRBs have only been seen twice in

[1] TNS database: https://www.wis-tns.org/

a space of time of hours to weeks[1]. Others, like FRB 20201124A (Lanman et al. 2022; Kumar et al. 2022; Xu et al. 2021), can show sporadic bursts before going through sudden periods of high activity, and then go back to quiescence.

One of the greatest enigmas currently surrounding FRBs is whether one-offs and repeaters arise from a common origin. One-offs could well repeat at a much lower rate, making it difficult to detect multiple bursts from the same source. This interpretation is supported by some observational properties, which appear to be similar for repeaters and one-offs: their sky distribution, DM, scattering timescales, fluences and host galaxy types (CHIME/FRB Collaboration et al. 2021a; Bhandari et al. 2022). However, the burst morphologies seem to come in different types (Pleunis et al. 2021a). One-offs can show single broadband components (Fig. 1.2a), single narrowband components (Fig. 1.2b), or multiple components peaking at the same frequency (Fig. 1.2c, see Chapter 6). On the other hand, bursts from all repeating FRBs present a characteristic morphology of multiple components drifting downwards in frequency, the so-called ‘‘sad trombone’’ effect (See Fig. 1.2d, Chapter 4 and Hessels et al. 2019). Repeater bursts are on average wider in time and narrower in frequency than one-off bursts. Whether these morphological differences are explained by different progenitor types and/or emission mechanisms is currently under debate.

1.2 Observed Fast Radio Burst properties

Fast radio burst searches are typically carried out in radio observations with high time and frequency resolution and a few hundred MHz bandwidth. The searches consist in finding highly dispersed, narrow single pulses. This is unlike pulsars (See Section 1.3.1), where searches for periodic emission are carried out instead. The observational setup enables us to characterise the properties of newly discovered FRBs. From the currently available FRB population, several properties can be inferred, and some general attributes are starting to emerge. This allows for some initial comparisons between FRBs with other astrophysical transients and model predictions. The main FRB attributes are detailed in the following section.

The DM of a radio signal is proportional to the amount of ionised plasma encountered by the radio waves throughout their propagation path (See Section 1.5.1). FRBs usually have large DMs, in excess of the expected MW contribution from the existing Galactic electron density models, NE2001 (Cordes & Lazio 2003) and YMW16 (Yao et al. 2017). This implies they are emitted at extragalactic distances. Typical FRBs have an average DM of ~ 500 pc cm^{-3}, in the unit used to measure DMs. The lowest DM FRB source found to date is the repeater FRB 20200120E, with DM=88 pc cm^{-3}, and it was localised to a globular cluster in the nearby galaxy M81 (Bhardwaj et al. 2021; Kirsten et al. 2022). The highest DM FRB is a hitherto one-off burst found by CHIME/FRB, FRB 20180906B with DM=3038 pc cm^{-3} (CHIME/FRB Collaboration et al. 2021a), while the FRB with the second largest DM is presented in Chapter 6.

1.2.1 Spectro-temporal properties

The temporal width of FRBs is usually of the order of a millisecond. Some bursts, including one-offs and repeaters, display multiple components (Figs. 1.2c and 1.2d, Hessels et al. 2019;

[1] See https://www.chime-frb.ca/repeaters for a list of the number and date of CHIME/FRB repeater detections.

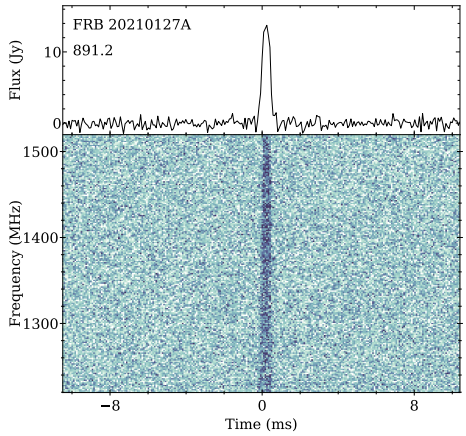

(a) FRB 20210127A (Chapter 6). Example of a broadband, single component FRB with no detectable scattering and scintillation.

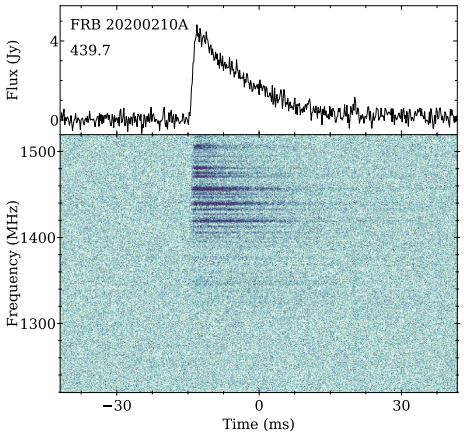

(b) FRB 20200210A (Chapter 6). Example of a scattered (exponential decay of the intensity in the pulse profile) and scintillating (variations of the intensity with frequency) narrowband FRB.

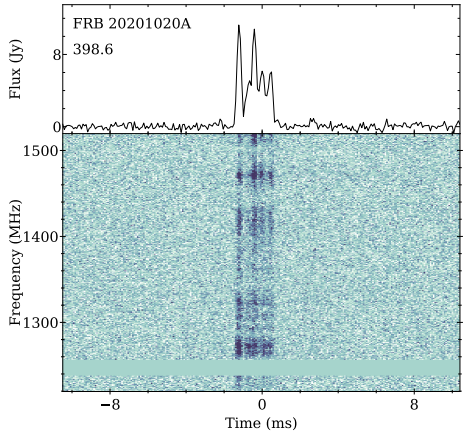

(c) FRB 20201020A (Chapter 5). Example of an FRB with five regularly spaced components showing scintillation.

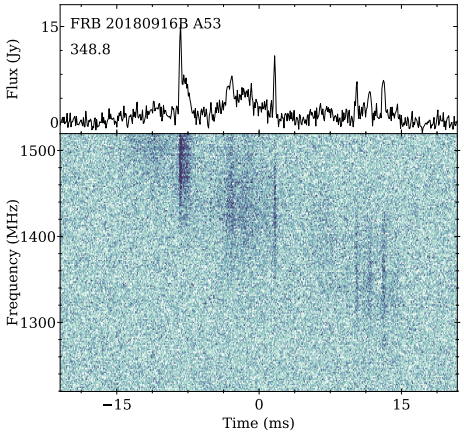

(d) Burst A53 from the periodic repeater FRB 20180916B (Chapter 4). Example of a multi-component burst drifting downwards in frequency (“sad trombone” effect).

Figure 1.2: Dynamic spectra of four FRBs presented in this thesis. In each subfigure, the bottom panel shows the dedispersed dynamic spectrum, and the top panel shows the pulse profile, the FRB identifier, and the DM ($\mathrm{pc\,cm^{-3}}$).

Pleunis et al. 2021a). In these cases, the width of each subcomponent is similar to the average single-component FRB width, while the total duration can be of tens of milliseconds, and even as high as two seconds (CHIME/FRB Collaboration et al. 2021b). The observed width can be affected by instrumental broadening. Blind FRB searches are typically carried out in incoherent dedispersion mode, which means the data is recorded with zero dispersion, then divided into a large number of frequency channels, and finally a time delay corresponding to the desired DM is applied to each frequency channel (Equation 1.3). This means that some dispersion is still contained within each frequency channel, which effectively broadens the observed width. The intrinsic burst widths are thus usually narrower than observed (Petroff et al. 2019). Scattering is a propagation effect that also widens the observed width, although this effect can be easily corrected for when fitting the pulse profile. Coherent dedispersion can be implemented when the DM is known, which is the case for repeating FRBs. Coherent dedispersion directly records the data at the desired DM. Repeater follow-up observations have thus revealed burst microstructure as narrow as a few tens of nanoseconds (Nimmo et al. 2022a, 2021; Majid et al. 2021).

The frequency range in which FRBs have been detected goes from 8 GHz (FRB 20121102A, Gajjar et al. 2018) to 110 MHz (FRB 20180916B, Pastor-Marazuela et al. 2021; Pleunis et al. 2021b, see Chapter 4). However, only repeaters have been seen at such extreme frequencies. The lowest frequency detections of one-off FRBs go down to 400 MHz (CHIME/FRB Collaboration et al. 2019b), while the highest frequency one-off detections do not exceed 1600 MHz. The intrinsic FRB frequency extent is often hard to determine, since the observing bandwidths of all instruments are limited, and a large fraction of the bursts extend from the bottom to the top of the observing band. Repeater bursts are however known to be narrowband, with lower average bandwidths than one-offs (Pleunis et al. 2021a; Pastor-Marazuela et al. 2021, see Chapter 4).

1.2.2 Energetics

Fast radio bursts have typical peak flux densities S_{peak} between 0.1 and 100 Jy. The fluence, obtained by integrating the flux density over the duration of the burst, typically extends from one to a few hundred Jy ms. The first known FRB, the ‘‘Lorimer burst’’, remains one of the brightest FRBs detected to date, with a fluence estimated to be ~ 800 Jy ms (Ravi 2019). Given the similarity in the peak flux densities between FRBs and pulsar pulses, but the $\sim 10^6$ larger distance of FRBs compared to pulsars, FRB luminosities are $\sim 10^{12}$ times greater (Nimmo et al. 2022a). Their spectral energies usually range from 10^{30} to 10^{34} erg Hz^{-1}. Some works have reported evidence for an increased excess DM for lower fluence sources, which is to be expected from a population originating at different distances. There is however a large spread in the implied luminosities, which indicates FRBs cannot be used as standard candles (Shannon et al. 2018; Petroff et al. 2019), and hence cannot accurately measure distances.

1.2.3 FRB rates

Back in September 2018, when I started this thesis, only about 30 FRB detections had been reported. That number has dramatically increased to the more than 600 known at the time of writing. The rate at which FRBs occur is often reported as an all-sky rate above a certain fluence threshold, measured in FRBs per sky per day. Most instruments that have carried out FRB

searches report a similar all-sky rate of $\sim 10^{3-4}$ sky^{-1} day^{-1} for a fluence threshold of 1 Jy ms (Champion et al. 2016; Bhandari et al. 2018; Shannon et al. 2018; Farah et al. 2019; CHIME/FRB Collaboration et al. 2021a, see Chapter 6). Although early works found small evidence for an anisotropic FRB sky distribution, larger FRB samples reveal an isotropic population of FRBs. Although localisations to host galaxies have now confirmed it, this was further evidence that FRBs have an extragalactic origin.

1.2.4 Scattering and scintillation

The different media through which the radio waves travel leave an imprint on the observed burst properties. These are referred to as propagation effects, and the main ones are the dispersion measure, scattering, scintillation and Faraday rotation. The study of these effects can give us essential information about the circumburst environment, but also about the properties of the Inter Galactic Medium (IGM) that is otherwise harder to characterise, and about the electron distribution in the MW Inter Stellar Medium (ISM). These propagation effects have been well known and studied in Galactic pulsars for decades, and they have been established to equally affect FRBs since the first handful of detections.

Scattering, which is described at length in Section 1.5.2, can be distinguished as a frequency-dependent exponential decay of the pulse profile intensity due to multi-path propagation. An example of a scattered FRB is shown in Fig. 1.2b. The timescale at which the intensity decays is proportional to the strength of the electron density fluctuations the FRB has experienced along its propagation path. Scattering also produces an angular broadening of the source size. The ‘‘Lorimer burst’’ was already found to show a scattering tail (Lorimer et al. 2007; Ravi 2019), as did various of the next few FRBs to be discovered (Thornton et al. 2013; Ravi et al. 2015; Petroff et al. 2015a; Masui et al. 2015). The typical scattering timescales that can be measured in the L-band (i.e., around 1.4 GHz) given the time resolution of most FRB instruments (0.01-1 ms) are too large to be explained by the MW contribution at high Galactic latitudes. Their origin is thus in most cases extragalactic. The initial CHIME/FRB Catalog (CHIME/FRB Collaboration et al. 2021a) presents the first sample of bursts large enough to start constraining the intrinsic FRB properties, including scattering. By simulating the propagation effects for diverse FRB population models, Chawla et al. (2022) conclude the observed scattering distribution is most likely to be produced in the circumburst environment (the environment surrounding the FRB sources) and/or the circumgalactic medium of galaxies in the foreground of the FRB host. Meanwhile, Ocker et al. (2021) determine the halos of foreground galaxies usually make very small contributions to the scattering of FRBs, thus making the circumburst environment the main contributor to scattering.

Scintillation is a propagation effect too, produced by refraction in the turbulent media through which FRBs propagate, which imprints frequency fluctuations on the FRB spectra. Two examples of scintillating FRBs can be found in Figs. 1.2b and 1.2c. A thorough description of this phenomenon is presented in Section 1.5.3. The spectral width of these fluctuations, referred to as the scintillation bandwidth, is frequency dependent and it decreases the more turbulent the propagation medium is. At L-band, with the typical instrumental frequency bandwidth and spectral resolution, any observable scintillation at high Galactic latitudes is likely to be produced in the MW. This can be confirmed with the NE2001 (Cordes & Lazio 2003) and YMW16 (Yao

et al. 2017) MW electron density models. Although scintillation by itself is unlikely to provide insightful information about the FRB sources, its study can be of special interest if a burst presents simultaneous scintillation *and* scattering. The presence of scintillation in a scattered burst indicates the source angular size is spatially unresolved, and this can allow one to set constraints on the distance between the FRB source and the scattering screen. Masui et al. (2015) applied this principle to the one-off FRB 20110523A, and determined the scattering screen must lie within 44 kpc from the source, and thus within its host galaxy. Ocker et al. (2022b) were able to conclude the scattering screen of the repeater FRB 20190520B is located less than 100 pc away from the source. In Chapter 6, we present an FRB where this principle highly constrains the distance to its scattering screen too.

1.2.5 Polarisation

Polarisation, which describes the way the electric field of the radio waves is oriented, is another key feature that can shed light on the nature and the geometry of FRBs, as well as on the environment surrounding them. A table with the polarisation properties of FRBs with available polarisation data can be found in Caleb & Keane (2021, Table 2). To date, only about half of the repeaters and $\sim$ 4% of the one-offs have available polarisation information. Although the observed bursts with available polarimetric data present diverse properties, some prevailing features are staring to appear. The large majority of repeaters are 100% linearly polarised, including the first repeater FRB 20121102A (Michilli et al. 2018), the periodic repeater FRB 20180916B (CHIME/FRB Collaboration et al. 2019c), FRB 20190303A, FRB 20190520B, FRB 20190604A (Fonseca et al. 2020; Niu et al. 2022; Feng et al. 2022), FRB 20190711A (Day et al. 2020; Kumar et al. 2020), and FRB 20200120B (Bhardwaj et al. 2021). Although the average linear polarisation degree of one-off FRBs is lower than that of repeaters, several examples of high linear polarisation (>90%) have been found there too, including FRB 20171209A, FRB 20180714A (Osłowski et al. 2019), FRB 20180924B, FRB 20190608B (Day et al. 2020), FRB 20181112A (Cho et al. 2020), and FRB 20210206A (CHIME/FRB Collaboration et al. 2021b). Circular polarisation appears to be far more uncommon amongst repeaters; only the repeating FRB 20201124A exhibits varying degrees of circular polarisation unlikely to be explained by Faraday conversion alone (Xu et al. 2021). Although the majority of one-offs show a negligible degree of circular polarisation, a few are >20% circularly polarised: FRB 20110523A (Masui et al. 2015), FRB 20140514A (Petroff et al. 2015a), FRB 20160102A (Caleb et al. 2018), and FRB 20190611B (Day et al. 2020). Only one repeater (FRB 20171019A, Kumar et al. 2019) and one one-off (FRB 20210213A CHIME/FRB Collaboration et al. 2021b) appear to be unpolarised, although based on a multi-frequency polarisation study of repeating FRBs (Feng et al. 2022), depolarisation might be occurring at frequencies above their observing bandwidths.

The Polarisation Position Angle (PPA), which measures the orientation of the linear polarisation, appears to be flat within each burst on most repeating and one-off FRBs (i.e. Michilli et al. 2018; CHIME/FRB Collaboration et al. 2019c). The repeater FRB 20180301A, however, has been seen to show diverse PPA swings within individual bursts, and PPA changes from one burst to the next (Luo et al. 2020). The one-off FRB 20110523A displayed a rotating PPA (Masui et al. 2015), and the multi-component FRB 20181112A presented PPA swings within each component (Cho et al.

2020). The bicomponent bursts FRB 20190102C and FRB 20190611B showed a PPA difference between each of their components, while FRB 20190608B displayed a downward evolution of its PPA (Day et al. 2020). The PPA of the periodic repeater FRB 20180916B, although it appears constant during and between bursts, shows slight PPA variations of just a few degrees on very short timescales ($\lesssim 100$ μs Nimmo et al. 2021). Similar small intra-burst PPA variations are seen in FRB 20200120E with < 10 μs timescales (Nimmo et al. 2022a).

Although this heterogeneous picture might appear difficult to reconcile with a single FRB origin, Galactic pulsars are known to display disparate polarisation properties as well. These generally show high degrees of linear polarisation, and PPA variations following an ''S shape'' interpreted as a change in the magnetic field orientation as the Neutron Star (NS) rotates, known as the Rotating Vector Model (RVM, Radhakrishnan & Cooke 1969). But many pulsars are known to show high fractions of circular polarisation, to be fully unpolarised, or to have PPAs that do not follow the RVM predictions (e.g. Radhakrishnan & Rankin 1990).

The polarisation angle can evolve with frequency as a result of Faraday rotation (See Section 1.5.4). That propagation effect, imprinted on the radio wave as it travels through a magnetised medium, can be quantified through the Rotation Measure (RM). Here too the observed FRB RM properties are very diverse. Two repeating FRBs associated to compact persistent radio sources present extreme RMs $\gtrsim 10^5$ rad m^{-2}; the RM of FRB 20121102A shows an erratic decrease in absolute RM value by $\sim 15\%$ per year (Michilli et al. 2018; Hilmarsson et al. 2021), while FRB 20190520B goes through irregular changes in the magnitude and the sign of its RM (Niu et al. 2022; Anna-Thomas et al. 2022). These properties must be explained by complex magneto-ionic environments surrounding the FRB locations; the vicinity of supermassive black holes, highly magnetised wind nebulae or dense supernova remnants have been suggested as potential explanations. FRB 20180916B was originally found to have a moderate RM of ~ -115 rad m^{-2} that remained constant for about two years, but it is currently experiencing a secular decrease in its absolute value (CHIME/FRB Collaboration et al. 2019c; Mckinven et al. 2022). Other repeaters have RMs from hundreds to thousands of rad m^{-2} (FRB 20180301A, FRB 190303A, FRB 20190417A, and FRB 20201124A, Luo et al. 2020; Fonseca et al. 2020; Feng et al. 2022; Xu et al. 2021), while the RM of others is compatible with what we expect from the MW. The RM of some one-off FRBs has also been reported to range in the hundreds or thousands of rad m^{-2} (FRB 20160102A, FRB 20190608B, FRB 20191108A, FRB 20200917A, Caleb et al. 2018; Day et al. 2020; Connor et al. 2020; Mckinven et al. 2021), but to date none of them are as extreme as FRB 20121102A and FRB 20190520B. In general, the observed RMs reflect that FRBs can originate in environments with diverse magnetic properties.

1.2.6 Localisation

Although the excess dispersion with respect to the expected Milky Way contribution observed in FRBs pointed towards an extragalactic origin, this was not definitely confirmed until the localisation of FRBs to their host galaxies. The first FRB to be localised in this manner was the first repeater, FRB 20121102A (Chatterjee et al. 2017); by having access to several bursts from the same source, the exact origin of the emission could be determined with a much higher precision. The host galaxy of FRB 20121102A was identified as a dwarf, star-forming galaxy at a redshift of

$z \sim 0.2$ (Tendulkar et al. 2017, see Fig 1.3a). This is the same galaxy type where Superluminous Supernovae (SLSNe) and Long Gamma-ray Bursts (LGRBs), the explosions of the most massive stars, usually occur. Furthermore, a Persistent Radio Source (PRS) was found to be co-located with the origin of the bursts (Marcote et al. 2017).

In contrast, the second FRB to be localised was a one-off event, FRB 20190523A (Ravi et al. 2019), and its host was determined to be a massive galaxy with a low Star Formation Rate (SFR) at a redshift $z \sim 0.66$. The difference in host galaxy types between FRB 20121102A and FRB 20190523A originally suggested that the progenitors of the two FRBs could have been formed through different evolutionary channels.

At present, nineteen FRBs have been localised to their host galaxies; six repeaters and thirteen one-offs[1]. Fast radio burst host galaxies display a broad range of masses, colours, and star formation rates, but a significant fraction of host galaxies show spiral arms (Mannings et al. 2021) and are similar to the Milky Way in mass and SFR. A sample of FRB host galaxies, including repeaters and one-offs, with different morphologies, masses and star formation rates is displayed in Fig. 1.3.

Some FRBs have been localised with a precision that enables the characterisation of the circum-burst environment. The third repeater, FRB 20180916B, was pinpointed to be ~ 250 pc away from a nearby star-forming region within its host galaxy, a face-on spiral (Marcote et al. 2020; Tendulkar et al. 2021, see Fig. 1.3b). Similarly, the one-off FRB 20190608B is co-located with a bright star-forming region in one of the spiral arms of its host galaxy (Chittidi et al. 2021, see Fig. 1.3c). These FRBs are very likely associated with the nearby star-forming regions, and this points towards a rapid progenitor formation channel. The closest repeating FRB to have been localised so far, FRB 20200120E, is however located in a Globular Cluster (GC) (Bhardwaj et al. 2021; Kirsten et al. 2022, see Fig. 1.3f). Since GCs harbour old stellar populations, this association suggests a delayed formation channel, thus challenging some FRB progenitor models.

Identifying the galaxies that can harbour FRBs, as well as the precise location within the galaxy and the conditions of the local environment where FRBs originate, permits to compare them to the environment where other types of transients occur. This is an essential step in identifying what the FRB progenitors are. From the still limited sample of localised FRBs, Bhandari et al. (2022) find that the FRB host properties match that of Core-collapse Supernovae (CCSNe) and Short Gamma-ray Bursts (SGRBs), but they do not follow stellar mass and formation, and differ from the Long Gamma-ray Bursts (LGRBs) and Superluminous Supernovae (SLSNe) hosts. As it will be later discussed in Section 1.3.3, CCSNe mark the transition of a massive star into a neutron star or a black hole, which are some of the suggested FRB progenitors. Meanwhile, SGRBs are produced at the merger of two NSs, which could indicate a different type of FRB origin.

1.3 Progenitor models

The nature of the objects that produce FRBs is one of the most debated topics in the field. The term progenitor refers to *what* kind of astrophysical objects can emit FRBs. Given their large amounts of energy and their short duration, compact objects are often invoked in these models. Originally, the lack of observed repetitions from the first known FRBs led to the proposition of "cataclysmic"

[1] An up-to-date list of localised FRBs and references can be found here: https://frbhosts.org/

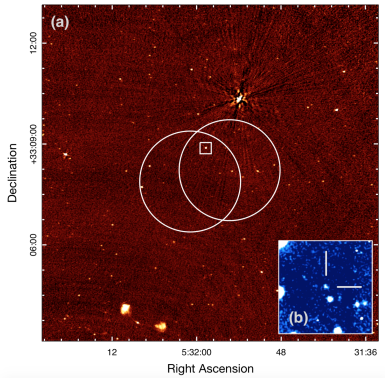

(a) FRB 20121102A host (Chatterjee et al. 2017).

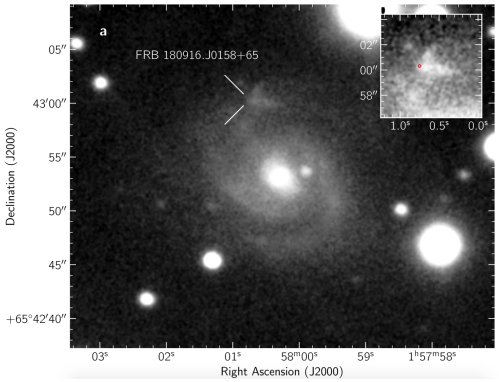

(b) FRB 20180916B host (Marcote et al. 2020).

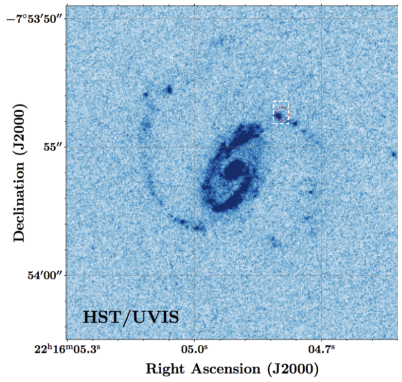

(c) FRB 20190608B host (Chittidi et al. 2021).

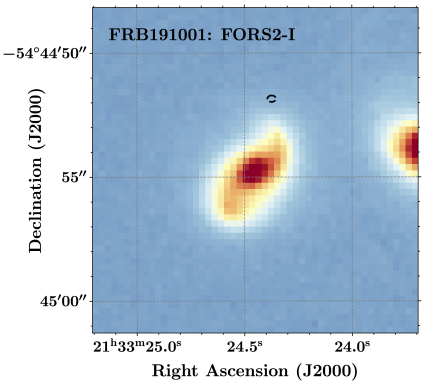

(d) FRB 20191001A host (Heintz et al. 2020).

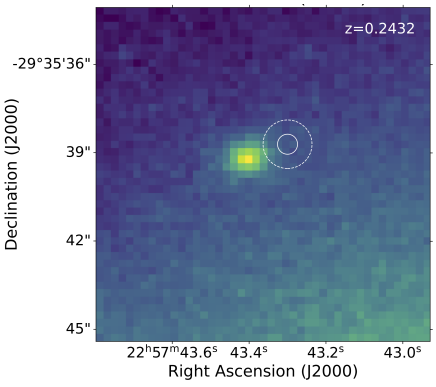

(e) FRB 20191228A host (Bhandari et al. 2022)

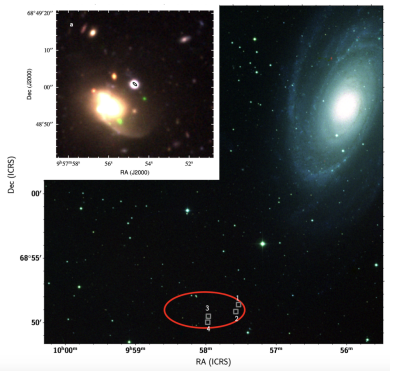

(f) FRB 20200120E host (Bhardwaj et al. 2021; Kirsten et al. 2022).

Figure 1.3: Sample of six FRB host galaxies displaying different morphologies, star-formation rates and masses.

events as the origin of FRBs. The discovery of a repeating FRB changed the perspective; at least some FRB progenitors are not destroyed after the emission of a radio burst. The current progenitor models can be classified by the type of source involved in the process; by whether they produce one-offs or repeaters; as periodic versus aperiodic repeaters; or by whether they are persisting or cataclysmic processes. Below we describe some of the leading FRB progenitor models, where we distinguish those that involve an isolated NS, those produced by compact object interactions and can be long-lived, cataclysmic models, and a last class of models invoking exotic sources or processes.

1.3.1 Isolated neutron stars

Neutron stars (NSs) are the compact objects that form when the nuclear fusion in the core of stars with masses between $\sim 8\,M_\odot$ and $25\,M_\odot$ stops after reaching the iron ($^{56}_{26}$Fe). Once fusion stops, the core of the star collapses under its own gravity while the outer layers are suddenly kicked out in what is known as a supernova (SN) explosion. The core of the stellar progenitor has masses roughly between 1.4 and $3\,M_\odot$, and after collapsing, this mass is compacted into a sphere with a radius of just ~ 10 km. Neutron stars are thus some of the densest objects in the universe, with densities reaching $\sim 10^{10}\,\mathrm{g\,cm^3}$. Neutron stars have two additional unique properties: first, they rotate at an extremely high speed, with a spin period typically ranging from milliseconds to a few seconds. Second, they possess exceptionally powerful magnetic fields, from 10^8 G to 10^{15} G, making them the strongest magnets in the Universe (See Chapter 2).

The term ‘‘neutron star’’ was coined in 1934 by Baade & Zwicky (1934), which predicted these to be produced after a regular star goes trough a Supernova (SN) stage. However, the existence of NSs remained elusive until 1968, when Jocelyn Bell discovered a new type of astrophysical radio source in the sky showing extremely regular pulsations with a period of about ~ 1 s that could not be explained by a terrestrial or artificial origin (Hewish et al. 1968). These sources were named *pulsars* (*pulsa*ting *r*adio stars). Such short duration and high brightness could only be explained by a compact, energetic source like a rotating NS. In the following decades, pulsar discoveries continued at a fast pace. Nowadays, roughly 3000 neutron stars have been found in the MW, and they display a broad range of properties and have been seen to shine in the whole electromagnetic spectrum.

To understand the NS periodic modulation observed in pulsar emission, we can compare it to the way a lighthouse works. The magnetic poles of the NS are misaligned with respect to its rotation axis. Regular radio emission is produced in the open magnetic field lines, close to the NS surface, while the high energy thermal emission comes from a hot spot on the surface of the star. Plasma around the neutron star must rotate with it, because the amazingly strong magnetic field locks it in place. However, at a large enough radius $r_L = c\Omega$, the plasma cannot rotate with the star, because this would force it to go faster than the speed of light. Since this is not possible, the plasma co-rotation is discontinued at the light cylinder radius r_L (see Fig. 1.4), and the magnetic field lines are open beyond it. Close to the light cylinder, the giant pulses as those seen in the Crab pulsar are thought to be generated, and synchrotron radiation produces high-energy (X/γ-rays) non-thermal emission. As the NS rotates, we see the emission when the radio beams from the

dipoles cross the Earth's line of sight, and in this way we observe a periodic modulation of the flux. A pulsar toy model is depicted in Fig. 1.4.

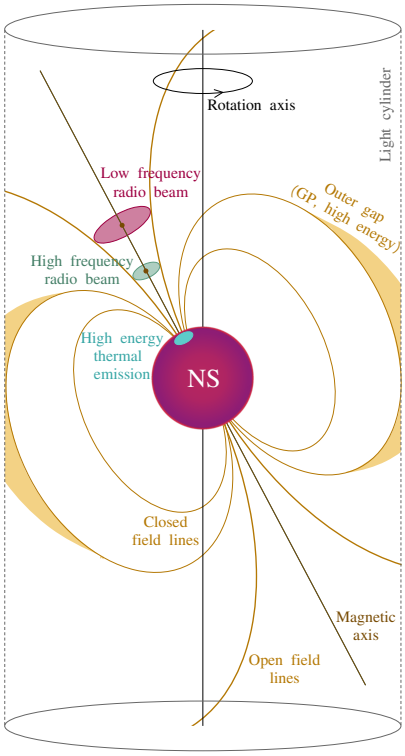

Figure 1.4: Pulsar toy model with the Neutron Star (NS) at the center, showing the rotation axis in black, the light cylinder in gray, the open and closed magnetic field lines in golden. The low frequency radio beam (crimson) is produced higher in the magnetosphere, and the high frequency radio beam (green) lower. The high energy radiation (X-rays, cyan) is produced close to the NS surface.

Neutron stars can be subdivided into different types depending on their age, spin period (P), period derivative ($\dot{P}$), or magnetic field strength, as shown in Fig. 2.2 of Chapter 2. Further categorising is based on the presence of a companion or a Supernova Remnant (SNR), and on the wavelength at which the NS is visible (Kaspi & Kramer 2016). The bulk of the NS population consists of rotation-powered pulsars, seen mainly at radio wavelengths, with periods between 0.1 and 10 s and magnetic fields between 10^{10} and 10^{13} G. Millisecond pulsars are NSs that have been spun up, reaching periods as short as just a few milliseconds, through the accretion of matter from a companion star in a binary system (Lorimer 2008). While high energy emission (X-rays and γ-rays) is common in millisecond and young pulsars (Abdo et al. 2010), some old pulsars are exclusively seen at high energies, like the X-ray Dim Isolated Neutron Stars (XDINSs,

see Chapter 2 and van Kerkwijk & Kaplan 2007; Mereghetti 2011). While searches for pulsars through periodic emission in the data have proved fruitful for most NS classes, the radio-emitting NSs known as Rotating RAdio Transients (RRATs) are characterized by erratic emission that can only be revealed through single pulse radio searches (Keane & McLaughlin 2011). Some young NSs present extreme magnetic fields ranging from 10^{13} to 10^{15} G and demonstrate a wide variety of high-energy outburst behaviour. Originally classified as Soft Gamma Repeaters (SGRs) and Anomalous X-ray Pulsars (AXPs), these are now referred to by the general term of *magnetars* (*magnet*ic st*ars*). Only a small fraction are known to have a (periodic) radio emission, and their rotation periods range from 1 to 10s of seconds (Kaspi & Beloborodov 2017). Such strong magnetic fields have complex configurations, and give rise to twists and reconnection of the magnetosphere, bursting activity, and high-energy emission.

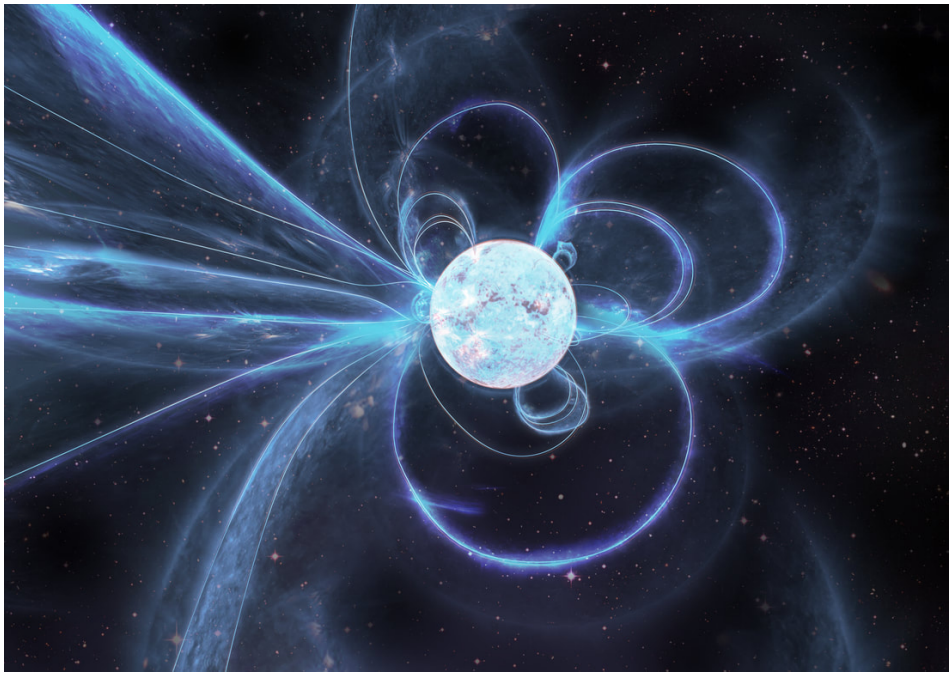

Figure 1.5: Artistic interpretation of a magnetar in outburst. The central sphere shows the NS, while the contorted lines represent its complex magnetic field morphology. The open magnetic field lines on the left are the product of a magnetic reconnection and are though to cause the high-energy flare. Credit: Carl Knox (OzGrav)

Among astrophysical phenomena, NSs are the closest to FRBs, observationally. They share similar emission frequencies, dispersion delay and other propagation properties, and a number of intrinsic spectro-temporal features. Some energetic young pulsars, such as the Crab, emit Giant Pulses (GPs), and an extreme version of those has been proposed as a potential explanation for FRBs (Cordes & Wasserman 2016; Lyutikov et al. 2016). Although most radio pulsars display periodic emission that is not observed in FRBs, RRATs have an irregular bursting behaviour

akin to repeating FRBs; the distinction between these two classes was uncertain when only a handful of FRBs were known (Keane & McLaughlin 2011); although it has since become clear the energetics are vastly different.

The luminosities of singular pulsar radio pulses are many orders of magnitude lower than that of FRBs, but recent magnetar discoveries are slowly starting to reduce the gap. In 2020, the previously known Galactic magnetar SGR 1935+2154 went into an X-ray outburst. It also emitted an extremely bright radio burst detected by two independent instruments (Bochenek et al. 2020; CHIME/FRB Collaboration 2020). Additionally, the magnetar XTE J1810–197 entered a state of radio and high energy outburst in 2018, and radio observations revealed the presence of giant pulses exhibiting complex spectro-temporal structure reminiscent of repeating FRB bursts and multi-component one-off FRBs (Maan et al. 2019; Caleb et al. 2021). Ultra-Long Period Magnetars (ULPMs) were proposed to explain the periodic bursting emission of FRB 20180916B and FRB 20121102A when the evidence for the existence of such ULPMs was scarce (Beniamini et al. 2020), but the recent discoveries of an 18 min magnetar (Hurley-Walker et al. 2022) and a 76 s magnetar (Caleb et al. 2022) with complex spectro-temporal properties analogous to some FRBs are providing decisive support for this interpretation. The collection of these discoveries indicate that at least some FRBs could be caused by magnetar bursts.

1.3.2 Compact object interactions

Although Black Holes (BHs) and White Dwarfs (WDs) are also energetic compact objects, these sources lack the magnetic field strength that NSs have. That field strength is the key ingredient in most FRB emission mechanism models. However, the interaction of BHs, WDs, and NSs with their surrounding media, orbiting objects or binary companions, has been proposed on multiple occasions to explain the production of radio bursts through magnetospheric interactions of the objects in the system. These systems or configurations are often long-lived, and could thus account for repeating FRBs.

Black holes are space-time singularities where the gravity is so strong, that no particles, including photons, can escape it. According to the ‘‘no-hair’’ theorem, BHs in equilibrium can be simply described by their mass and their spin — no magnetic fields (Mazur 2000). Stellar mass BHs are the remnants of stars with original masses above $\sim 25\,M_\odot$. Like NSs, they are produced by the gravitational collapse of the stellar core once fusion stops. But unlike NSs, the core is so massive ($\gtrsim 3\,M_\odot$ Oppenheimer & Volkoff 1939; Tolman 1939) that the neutron degeneracy pressure cannot counterbalance gravity. Stellar mass black holes can increase their mass through accretion or through mergers with other compact objects. SuperMassive Black Holes (SMBHs), on the other hand, are enormous black holes with masses in the $10^{6-9}\,M_\odot$ range known to reside in the center of most massive galaxies. They are responsible for the Active Galactic Nuclei (AGN) and quasar emission, that can outshine all other stars in the galaxy combined. How such massive objects have formed and evolved, especially when the Universe was still very young (Mortlock et al. 2011; Bañados et al. 2018), is not yet fully understood. Since BHs do not emit any kind of electromagnetic radiation, they have to be detected indirectly. This can be done, for instance, by studying the motion of stars around an invisible center of mass, as it was done to accurately estimate the mass of the SMBH in the center of our galaxy, Sgr A* (Ghez et al.

2000). In X-ray binaries, the presence of a compact object is determined through the strong X-ray emission produced by the heated material the compact object accretes from a stellar companion. To determine whether the compact object is a NS or a BH, one can study the spectral variability of the X-ray binary, or determine the mass of the accretor through a dynamical mass measurement (Belloni & Motta 2016). Gravitational Wave (GW) detectors can now be used to detect the GWs emitted right before the merger of a binary BH system (LIGO Scientific Collaboration and Virgo Collaboration et al. 2016). Even more recent are the first images of the shadow produced by the gravitational light bending at the event horizon of M87*, the SMBH at the center of the M87 galaxy, and of Sgr A* (EHT Collaboration 2019, 2022).

White dwarfs are the stellar remnant of stars with initial masses <8 $M_\odot$. Unlike NSs and BHs, they are not formed by a sudden SN explosion. Instead, when the star is not able to commence the fusion of the next element, the core becomes a sphere of electron-degenerate matter composed of carbon and oxygen in most cases (CO WD), or oxygen, neon, and magnesium in the case of the most massive WDs (ONe or ONeMg WD). When the core becomes electron-degenerate, the outer layers of the star are slowly expelled, leaving behind a planetary nebula with a bare core – the white dwarf – at the center (Hansen & Liebert 2003). These WDs are roughly the size of the Earth, and have masses below the Chandrasekhar limit of $\sim 1.4\,M_\odot$ (Chandrasekhar 1983). Since WDs no longer have an internal source of energy, they slowly start cooling down from the very hot temperatures with which they were formed. The conditions of WDs are extreme, with magnetic fields in the 10^{4-9} G range, rotation periods of $\sim 1-100$ h, and typical densities of $10^{4-7}\,\mathrm{g\,cm^{-3}}$, but they are not quite as extreme as NSs. For this reason, they are less often regarded as potential FRB progenitors.

Binary NSs have been proposed to produce repeat bursts through magnetospheric interactions that can occur in close NS encounters in dense stellar clusters (Dokuchaev & Eroshenko 2017), or alternatively in binary NS systems that would additionally be the source of GW emission (Zhang 2020a). The repeating FRBs FRB 20121102A and FRB 20190520B are associated to two Persistent Radio Sources (PRSs), which have been suggested to be low-luminosity Active Galactic Nuclei (AGN; Chatterjee et al. 2017; Niu et al. 2022). This has inspired models invoking SMBHs or AGN. The plasma surrounding SMBHs is known to harbour strong magnetic fields, and Zhang (2017, 2018b) suggest NSs traveling through those magnetized regions could produce radio bursts via magnetospheric reconnections. This scenario predicts periodic activity modulations matching the NS orbital period, and it could explain the large Rotation Measure (RM) and the PRSs observed in the repeaters FRB 20121102A and FRB 20190520B. Alternatively, Vieyro et al. (2017) propose FRB emission from the interaction of an AGN jet with a cloud of material surrounding it. Meanwhile, Yi et al. (2019) argue stellar mass BHs in binary systems with stellar companions could produce radio bursts at the collision between the clumpy accreted material and the BH jets. Ultra-Luminous X-ray sources (ULXs, Gúrpide et al. 2021), which are X-ray binaries with extreme luminosities surpassing the Eddington limit for stellar mass BHs, have also been suggested to produce FRBs through relativistic shocks of their outflows (Sridhar et al. 2021). This could also justify the periodic activity observed in some repeaters. Gu et al. (2016) contemplate FRB emission in a close WD-NS system where the NS accretes magnetised material from the WD. Asteroids or comets colliding with a NS surface have further been conjectured to produce

radio bursts with periodic activity cycles (Geng & Huang 2015; Dai & Zhong 2020; Mottez et al. 2020).

1.3.3 Cataclysmic models

If not all FRBs are produced by a single progenitor class, the alternative would be that repeaters are produced by long-lived systems while one-offs are the result of cataclysmic events. The cataclysmic event category comprises different types of compact object mergers. Binary Neutron Star (BNS) mergers have been suggested to produce short radio bursts through pre-merger electromagnetic interactions between the two NSs in the last stages of the inspiral (e.g. Hansen & Lyutikov 2001; Piro 2012; Lyutikov 2013; Totani 2013; Wang et al. 2016), or right after the merger before the ejecta becomes optically thick for radio emission (Yamasaki et al. 2018). The WD formed right after a binary WD merger has also been hypothesised to emit a bright radio burst (Kashiyama et al. 2013). In Black Hole-Neutron Star (BHNS) systems, the interaction of the BH with the magnetic field of the NS might release radio emission at the moment of coalescence (McWilliams & Levin 2011; Mingarelli et al. 2015; D'Orazio et al. 2016). BH-WD and NS-WD collisions have also been suggested to produce radio bursts (Li et al. 2018; Liu 2018). Compact object mergers are however not the only cataclysmic events suggested to produce FRBs. The collapse of supramassive NSs into black holes as their rotation slows down has also been proposed to generate bright radio bursts (the ''blitzar'' model, Falcke & Rezzolla 2014; Zhang 2013), and primordial black holes exploding into white holes have been suggested to give rise to coherent radio pulses (Barrau et al. 2014; Rees 1977).

Although Supernovae (SNe) are explosions that mark a sudden transition in the evolutionary stage of a star, there are currently no models that predict FRB emission as part of the supernova engine, although Egorov & Postnov (2009) suggest FRBs could be produced by the shock of a SN explosion with the magnetosphere of a NS companion. Type Ia SNe are thermonuclear explosions that occur when an accreting WD reaches the Chandrasekhar mass, and the WD is disrupted (Mazzali et al. 2007). Since no compact object is left after the explosion, it cannot give rise to future electromagnetic activity. Core-collapse Supernovae (CCSNe), on the other hand, mark the transition of a massive star into a NS or a BH (Burrows & Vartanyan 2021). Superluminous Supernovae (SLSNe) are extremely bright SN explosions which are believed to be produced by different mechanisms, with one of them involving the birth of a magnetar (Kasen & Bildsten 2010; Woosley 2010). If FRBs are produced by young magnetars, one could expect to see radio bursts a few years after a CCSN or a SLSN explosion, once the ejecta become optically thin enough for the radio emission to escape, which could take from decades to centuries (Piro 2016; Kashiyama & Murase 2017; Metzger et al. 2017; Margalit et al. 2018).

1.3.4 Exotic models

A few models exist that do not belong into the previous categories, including some that do not involve compact objects or that can be considered as more speculative due to the lack of observational support. Some models hypothesise FRBs are produced by superconducting cosmic strings (e.g. Vachaspati 2008; Cai et al. 2012) or by giant magnetic dipoles of dark matter (Thompson 2017). The collapse of strange star crusts – neutron stars containing strange quarks (Zhang et al.

2018), novae marking the birth of quark stars (Shand et al. 2016), and the collapse of a neutron star due to dark matter accretion (Fuller & Ott 2015) have also been speculated to produce FRBs. Even the remote scenario of FRBs being the signature of spacecraft from extragalactic civilisations has been proposed (Lingam & Loeb 2017).

1.4 Emission mechanism

The emission mechanism refers to *how* FRBs are produced. The extreme FRB properties described above, mainly their short durations, energetics, and exceptional brightness temperatures, require a coherent emission process to explain the observed bursts. Additional properties like the burst spectro-temporal morphologies and polarisation must also be explained by the emission process. Unlike the diversity of progenitor models that exist, only a limited number of emission mechanisms can account for the observed FRB properties. But in the same way the FRB progenitors might not be unique, different emission mechanisms might be required to explain the entire FRB population. The leading proposed mechanisms can be grouped in models invoking compact object magnetospheres (neutron stars, magnetars or occasionally black holes), and a synchrotron maser mechanism (Zhang 2020b).

Neutron stars alone exhibit a variety of radio emission presenting several analogies to FRBs, although the mechanism of these different processes is still not fully understood. The main neutron star radio emission types include rotation-powered emission, giant pulses, and magnetar radio emission. The rotation-powered emission observed in pulsars is thought to arise tens to hundreds of km above the NS polar caps, and it is a coherent process likely to involve electron-positron pairs (Harding 2017). Several pulsar-like models have been proposed to explain FRB emission, but they are challenging to reconcile with the main observed properties. For instance, collective plasma emission, referred to as plasma maser models (Melrose 2017), cannot explain the high FRB luminosities (Lu & Kumar 2018). Coherent curvature radiation from electron-positron pair creation in ‘‘sparks’’ moving along the magnetic field lines have been long proposed to explain pulsar radio emission (Ruderman & Sutherland 1975); the main critique of this model is that coherence cannot be maintained for long enough (Melrose 1978). To overcome this, the formation of particle bunches or ‘‘solitons’’ has been proposed; they are formed through a two-stream instability that results in much longer timescales than the individual electron-positron sparks lifetime (Melikidze et al. 2000). It has been suggested that the explosive FRB events could satisfy the required highly non-stationary environments for the soliton formation (e.g. Katz 2014; Lu & Kumar 2018; Yang & Zhang 2018). Such an emission mechanism could explain the subcomponent downward drift observed in repeating FRBs (Wang et al. 2019). However, a strong electric field $E_{\parallel}$ parallel to the magnetic field of the NS is required in order to sustain the emission for the observed FRB timescales (Kumar et al. 2017). Alfvén waves could develop such $E_{\parallel}$ (Kumar & Bosnjak 2020), but whether this is feasible remains an open question.

Some young pulsars, the Crab being the canonical example, show ‘‘giant pulses’’, which are shorter in duration, brighter, and are not necessarily aligned with the main pulse profile (e.g. Hankins et al. 2016). An extreme version of those, often referred to as ‘‘super-giant pulses’’, has been proposed to explain FRBs (Cordes & Wasserman 2016; Lyutikov et al. 2016; Connor et al. 2016). The timescales and luminosities of ‘‘nano-shots’’ from the Crab pulsar have been

recently seen to be comparable to some bursts from a nearby repeating FRB (Nimmo et al. 2022a), suggesting a similar emission mechanism might be at play. It is however uncertain whether the same emission mechanism can explain the luminosity of the most distant one-off FRBs.

Magnetars, unlike pulsars, are powered by the dissipation of their strong magnetic fields. Magnetars have been long known to produce bright radio pulses during periods of high activity (Camilo et al. 2006). Flaring magnetars were thus some of the earliest proposed models to explain FRB emission (Popov & Postnov 2010, 2013; Katz 2016; Lyubarsky 2020). Such flares are thought to be produced during the reconnection of the twisted magnetosphere of an active magnetar, suddenly releasing large amounts of energy (Lyutikov 2002). The discovery of a bright radio burst from SGR 1935+2154, bridging the luminosity gap between pulsars and FRBs, currently favors the magnetar emission mechanism (Bochenek et al. 2020; CHIME/FRB Collaboration 2020).

The synchrotron maser models propose coherent radio emission arising from relativistic shocks. A compact object central engine is required to produce relativistic outflows that shock the material surrounding it, for instance a supernova remnant. Low frequency radio bursts were already proposed to arise from Gamma-ray Burst (GRB) events before FRBs were first detected (Usov & Katz 2000; Sagiv & Waxman 2002). Since the discovery of FRBs, several synchrotron maser models involving different physical conditions have been discussed. The simplest case scenario is a vacuum synchrotron model neglecting the plasma effects (Ghisellini 2017), but the required conditions are challenging to satisfy by established astrophysical systems, and it has difficulties explaining the luminosity of cosmological FRBs. Of the models including plasma effects, some consider a weakly magnetised plasma. The conditions required to produce coherent radio emission could be satisfied by NSs formed by WD accretion-induced collapse or WD mergers (Waxman 2017), or by weakly magnetised NSs undergoing accretion-induced explosions (Long & Pe'er 2018). However, radio emission is predicted to happen only in a very narrow frequency range. Models considering highly magnetised plasma have been more widely discussed; a strongly magnetised burst propagates through the magnetised medium until it reaches the plasma within the nebula, producing the radio burst. In most cases, the proposed central engine is a flaring magnetar (Lyubarsky 2014; Beloborodov 2017; Metzger et al. 2019), but as stated in Section 1.3.2, super-Eddington accreting binaries, such as Ultra-Luminous X-ray sources (ULXs), have also been suggested to power the bursts (Sridhar et al. 2021; Sridhar & Metzger 2022). These models could explain the PRSs observed around FRB 20121102A and FRB 20190520B, the 100% linear polarisation of certain FRBs, and the subcomponent downward frequency drift (Metzger et al. 2019). Additionally, they predict high-energy radiation accompanying the radio bursts. However, Particle In Cell (PIC) simulations suggest the mechanism is highly inefficient (Plotnikov & Sironi 2019), and the expected time delay between major flares is much larger than observed. Finally, the model cannot explain the small PPA variations observed in $\sim \mu$s timescales in certain repeating FRBs (Nimmo et al. 2021, 2022a).

1.5 Propagation effects

Along their travel path, the FRB radio waves encounter different media: in the vicinity of the source, in the host galaxy where the bursts were produced, the Inter Galactic Medium (IGM), any intervening galaxies, and finally the Inter Stellar Medium (ISM) of the MW before reaching

Earth. These different media affect the propagation of the radio waves, modifying their speed and direction. The propagation effects leave an imprint on the morphology of the observed burst, and provide valuable information about the matter they have traversed. They can also hinder the detection of certain bursts by lowering their Signal-to-Noise ratio (S/N). In the next sections, I describe the main propagation properties observed in FRBs, and in particular in Apertif FRBs, and give some of the most useful equations for FRB analysis.

1.5.1 Dispersion

The dominant propagation effect observed in FRBs, and the first one to be perceived upon their discovery, is dispersion. Empirically, dispersion is a delay in the arrival time of lower frequencies with respect to higher frequencies of the radio waves. This dispersion is produced when the radio waves propagate through a homogeneous ionised plasma along their travel path. The plasma has a frequency-dependent refractive index that modifies the light velocity:

$$v_g = c\sqrt{1 - \left(\frac{\nu_p}{\nu}\right)^2}, \quad \text{with} \quad \nu_p = \sqrt{\frac{e^2 n_e}{\pi m_e}}, \tag{1.1}$$

where v_g is the frequency-dependent light velocity, and ν_p is the plasma frequency. The arrival time delay is thus proportional to the amount of ionised material the radio waves encounter, and it increases quadratically with decreasing frequencies. It is quantified with the Dispersion Measure (DM) in $\mathrm{pc\,cm^{-3}}$, defined as:

$$\mathrm{DM} \equiv \int_0^D n_e(l)\, dl, \tag{1.2}$$

where D is the distance the burst has travelled in pc, and n_e the electron density in electrons $\mathrm{cm^{-3}}$ along the travel path dl.

Following Chapter 4 of Lorimer & Kramer (2004), the DM of an FRB can be computed from the arrival time delay $t_2 - t_1 = \Delta t$ in ms between two frequencies ν_1 and ν_2 in GHz, and it can be expressed as:

$$\mathrm{DM(pc\ cm^{-3})} = \frac{\Delta t}{\mathscr{D}(\nu_1^{-2} - \nu_2^{-2})} \tag{1.3}$$

where $\mathscr{D}$ is the dispersion constant defined as:

$$\mathscr{D} \equiv \frac{e^2}{2\pi m_e c} = 4.1488064239(11)\,\mathrm{GHz^2\,cm^3\,pc^{-1}\,ms}, \tag{1.4}$$

which is often approximated to $\mathscr{D} \sim 4.15\,\mathrm{GHz^2\,cm^3\,pc^{-1}\,ms}$.

Since the DM is proportional to the amount of electrons in the line of sight, it is often used as a proxy for distance. However, distance determination from the DM alone can be quite tricky,

since the observed DM of an FRB is the sum of the contributions from the different components in the line of sight:

$$\mathrm{DM_{FRB}} = \mathrm{DM_{MW\ ISM}} + \mathrm{DM_{MW\ halo}} + \mathrm{DM_{IGM}} + \frac{\mathrm{DM_{host}} + \mathrm{DM_{local}}}{1+z} \tag{1.5}$$

Other contributions, like the Earth's ionosphere, and the interplanetary medium of the Solar System, are often negligible. Galaxies within the line of sight of the observed FRB can also contribute to the dispersion. The MW ISM contribution can be estimated from the NE2001 (Cordes & Lazio 2003) and YMW16 (Yao et al. 2017) models of the free electron distribution in the MW. The MW halo contribution is estimated to be 30-200 pc cm^{-3} independently of the ISM contribution (Prochaska & Zheng 2019; Yamasaki & Totani 2020). The IGM contribution is well approximated by a redshift-dependent linear function for $z \lesssim 3$, $\mathrm{DM_{IGM}} \simeq 1000z$ pc cm^{-3} (Ioka 2003; Inoue 2004; Zhang 2018a); the value of the slope is being improved through the localisation and redshift determination of distant FRBs (Macquart et al. 2020) and cosmological simulations (Batten et al. 2021). The most difficult contributions to determine are the FRB host galaxy and local environment DMs. The host contribution is highly dependent on the type of galaxy (mass, morphology, age), its orientation with respect to the MW, and the distance between the galaxy centre and the burst location; it can thus vary from tens to thousands of pc cm^{-3} (Chawla et al. 2022). The FRB local environment contribution to the DM is also highly uncertain; some FRBs appear to be produced in clean environments, while the properties of others suggest they occupy dense, complex environments. This translates as a broad range of potential local DM contributions. Nevertheless, FRBs are invaluable tools to probe the distribution of matter in the IGM and other galaxies, as early works from the still limited FRB population have proved (Macquart et al. 2020; Connor & Ravi 2021).

In order to estimate the propagation effects described hereafter, the bursts are often dedispersed, i.e. corrected for the dispersion measure in order to obtain their observed pulse profile, $I_{\mathrm{obs}}(t)$.

1.5.2 Scattering

When the radio waves propagate through an inhomogeneous or turbulent plasma, they are scattered in different directions depending on their frequency. As a result, the radio waves reaching Earth that were emitted together may have travelled different path lengths, and waves with a longer path will arrive later. This translates empirically as an exponential decay of the burst intensity, as can be seen in Fig. 1.2b. The observed dedispersed pulse shape $I_{\mathrm{obs}}(t)$ will be a convolution of the intrinsic pulse shape $I_{\mathrm{int}}(t)$ with a one-sided decaying exponential with a constant known as the scattering timescale (τ_{sc}):

$$I_{\mathrm{obs}}(t) = I_{\mathrm{int}}(t) \circledast (e^{-t/\tau_{\mathrm{sc}}} u(t)), \tag{1.6}$$

where $u(t)$ is the step function; $u(t < 0) = 0$ and $u(t \geq 0) = 1$. The intrinsic pulse profile can generally be described by one or multiple gaussians. The scattering timescale increases with the strength of electron density fluctuations along the line of sight, and it depends strongly on frequency, with lower frequencies being much more scattered:

$$\tau_{sc} \propto \nu^{-\alpha}. \tag{1.7}$$

The frequency scaling index α depends on the variations of the electron density along the travel path. In the simplest case scenario where all the scattering is produced by a single thin screen midway along the propagation path, the theoretical frequency scaling index is $\alpha = 4$. In the case of a turbulent medium along the whole travel path, $\alpha = 4.4$. In pulsars, the observed frequency-dependent scattering timescale often differs from the thin screen and turbulent medium theoretical values, with an average $\alpha \sim 3.86$ (Löhmer et al. 2002; Bhat et al. 2004; Lewandowski et al. 2015). This difference is often interpreted as the presence of anisotropic scattering mechanisms (Geyer & Karastergiou 2016). In FRBs, the amount of frequency scaling index measurements is still scarce, but it seems to be compatible with the $\alpha \sim 4 - 4.4$ theoretical predictions.

Since the IGM is mostly homogeneous, the main contributions to the scattering of an FRB occur either in the circumburst environment, the FRB host galaxy, the Milky Way, and occasionally in intervening galaxies within the travel path. The NE2001 (Cordes & Lazio 2003) and YMW16 (Yao et al. 2017) models for the distribution of free electrons in the MW also provide with estimated Galactic contributions to the scattering timescale. If the observed scattering timescale greatly differs from the expected MW contribution, the scattering was plausibly produced close to the burst source.

1.5.3 Scintillation

The propagation through an inhomogeneous or turbulent medium produces a supplementary effect: scintillation. As the radio waves that have traveled through different paths arrive on Earth, they interfere constructively and destructively depending on frequency. As a result, the burst shows ‘‘patchy’’ intensity fluctuations in frequency, as can be seen in Figs. 1.2b and 1.2c. The typical bandwidth of the fluctuations is known as the scintillation bandwidth ($\Delta\nu_{sc}$), and it is proportional to the inverse of the frequency-dependent scattering timescale:

$$\Delta\nu_{sc} \propto \tau_{sc}^{-1} \propto \nu^{\alpha}. \tag{1.8}$$

The scintillation bandwidth is often interpreted as the Full Width at Half-Maximum (FWHM) of the Auto-Correlation Function (ACF) of the burst spectrum fitted to a lorentzian function. For a burst spectrum $S(\nu)$ with n frequency samples, the ACF for each possible frequency lag $\Delta\nu \in [0, \nu_n - \nu_0]$ is defined as follows:

$$\mathrm{ACF}(\Delta\nu) = \frac{\sum_{i=0}^{n}(S(\nu_i))(S(\nu_i + \Delta\nu))}{\sqrt{\sum_{i=0}^{n}(S(\nu_i))^2 \sum_{i=0}^{n}(S(\nu_i + \Delta\nu))^2}}. \tag{1.9}$$

The expected MW contribution to scintillation can also be estimated from the Galactic electron density models NE2001 and YMW16.

1.5.4 Faraday Rotation

The propagation effects discussed above can be determined from the total intensity of the burst. However, radio waves are electromagnetic radiation, and can thus be decomposed into Stokes parameters I, Q, U, and V, which describe the polarisation of the waves. I is the total intensity, $L = \sqrt{Q^2 + U^2}$ is the linear polarisation intensity, and V is the circular polarisation intensity (see Lorimer & Kramer 2004, for further detail).

When the medium the radio waves travel through is magnetised, the propagation frequency will be higher for the right-hand than for the left-hand circularly polarised emission. Although these effects are negligible for the average burst velocity, a polarised signal will present variations of the Polarisation Position Angle (PPA) with wavelength λ:

$$\mathrm{PPA} = \mathrm{RM}\,\lambda^2 \tag{1.10}$$

These variations are quantified with the Faraday Rotation Measure (RM), which is proportional the integral of the free electron density times the magnetic field strength parallel to the line of sight $B_\parallel$:

$$\mathrm{RM\,(rad\ m^{-2})} = \mathscr{R} \int_0^D n_e(l)\, B_\parallel(l)\, dl, \tag{1.11}$$

with $\mathscr{R} = \dfrac{e^3}{2\pi m_e^2 c^4} \sim -0.81$. The resulting RM is a sum of all the magnetic field contributions throughout the line of sight. The sign depends on the magnetic field orientation, with a positive RM for a magnetic field towards the observer. Models of the MW RM exist, which allows to better estimate the extragalactic RM contribution. A redshift correction must be applied for magnetic fields located at cosmological distances, with $\mathrm{RM_{host}} = \mathrm{RM_{obs}}(1+z)^2$.

Two main techniques for measuring the RM of a radio pulse exist. The most straightforward technique, often referred to as QU-fitting, consists in fitting the oscillations of the Stokes Q and U parameters to

$$Q = L\cos\alpha \quad \text{and} \quad U = L\sin\alpha, \tag{1.12}$$

where L is the linear polarisation amplitude and $\alpha = 2(\mathrm{RM}\lambda^2 + \psi_0)$ gives the frequency (or wavelength) dependent phase produced by the Faraday rotation. A large number of Q/U oscillations in the observing bandwidth is the signature of a large RM. The second method, named RM-synthesis, essentially consists in computing the Fourier transform of the linearly polarised signal, and then finding its maximum. The Fourier transform of the linearly polarised signal $L(\lambda^2) = Q(\lambda^2) + iU(\lambda^2)$ is given by (Burn 1966; Brentjens & Bruyn 2005):

$$F(\phi) = \int_{-\infty}^{+\infty} L(\lambda^2) e^{-2i\phi\lambda^2} d\lambda^2, \tag{1.13}$$

Where $\phi\,(\mathrm{rad\,m^{-2}})$ is termed the Faraday depth, and the RM is given by the ϕ that maximises $|F(\phi)|$.

1.6 Fast Radio Burst searches

So far, FRBs have been uniquely detected at radio wavelengths, with radio telescopes from all over the world participating in these FRB searches. While extensive searches have been carried out in the entire electromagnetic spectrum (Section 1.6.6), the detection of multi-wavelength counterparts remains elusive and one of the main challenges in discriminating between current progenitor models and emission mechanisms (Sections 1.3 and 1.4).

1.6.1 Radio observations

Fast Radio Burst observations are carried out from Earth using radio telescopes. The wavelength of radio emission is much longer than that of optical light, and this has several consequences for the design of the instruments and the observations. The angular resolution of a telescope can be approximated with the Rayleigh criterion (Rayleigh 1879), $\theta \approx 1.22 \times \lambda/D$, where θ is the angular resolution, λ is the wavelength and D is the diameter of the (circular) telescope. This implies that to achieve a similar angular resolution, the diameter of a radio telescope needs to be much larger than an optical telescope. On the other hand, optical telescopes require the use of mirrors with an extremely well polished surface, since even the smallest irregularities can be harmful for the image quality. Given the longer radio wavelengths, radio telescopes do not need to use mirrors, since surfaces or even mesh-like structures can reflect the light. These surfaces can be more uneven, and thus easier to manufacture than optical telescope mirrors. The terrestrial atmosphere absorbs a large range of wavelengths in the electromagnetic spectrum, and only optical, near infrared and radio light can reach the surface of Earth. Radio waves of astronomical origin have the additional advantage that they can be seen even during daytime and with cloudy weather. Current radio telescopes are mainly classified into single-dish telescopes and interferometers, and some of the main ones that have contributed to make significant FRB discoveries are described below, and shown in Fig. 1.6 in their approximate position on the globe.

1.6.2 Single-dish telescopes

Single-dish telescopes, as their name indicates, are radio telescopes with a single antenna, usually with a spherical or parabolic surface that reflects the light to its focal point. Single-dish telescopes are often built on a platform that allows the telescope to point in different directions. Some radio telescopes, however, are so large that the dish is fixed to the ground while a steerable or movable receiver suspended above the dish is in charge of pointing in different directions. This is the case for the late Arecibo and the Five-hundred-meter Aperture Spherical Telescope (FAST) radio telescopes.

Some of the main single-dish telescopes that have allowed to make breakthrough discoveries in the FRB field are the following: The Parkes 64 m radio telescope in Australia was used to make the first FRB detections, and it remained the only instrument to do so for several years (Lorimer et al. 2007; Keane et al. 2012; Thornton et al. 2013). The 305 m Arecibo radio telescope in Puerto Rico was the second instrument to detect an FRB, with the discovery of the first repeater FRB 20121102A and subsequent repeat bursts, thus proving the astrophysical nature of these signals (Spitler et al. 2014, 2016). It was subsequently used to make very sensitive repeater follow

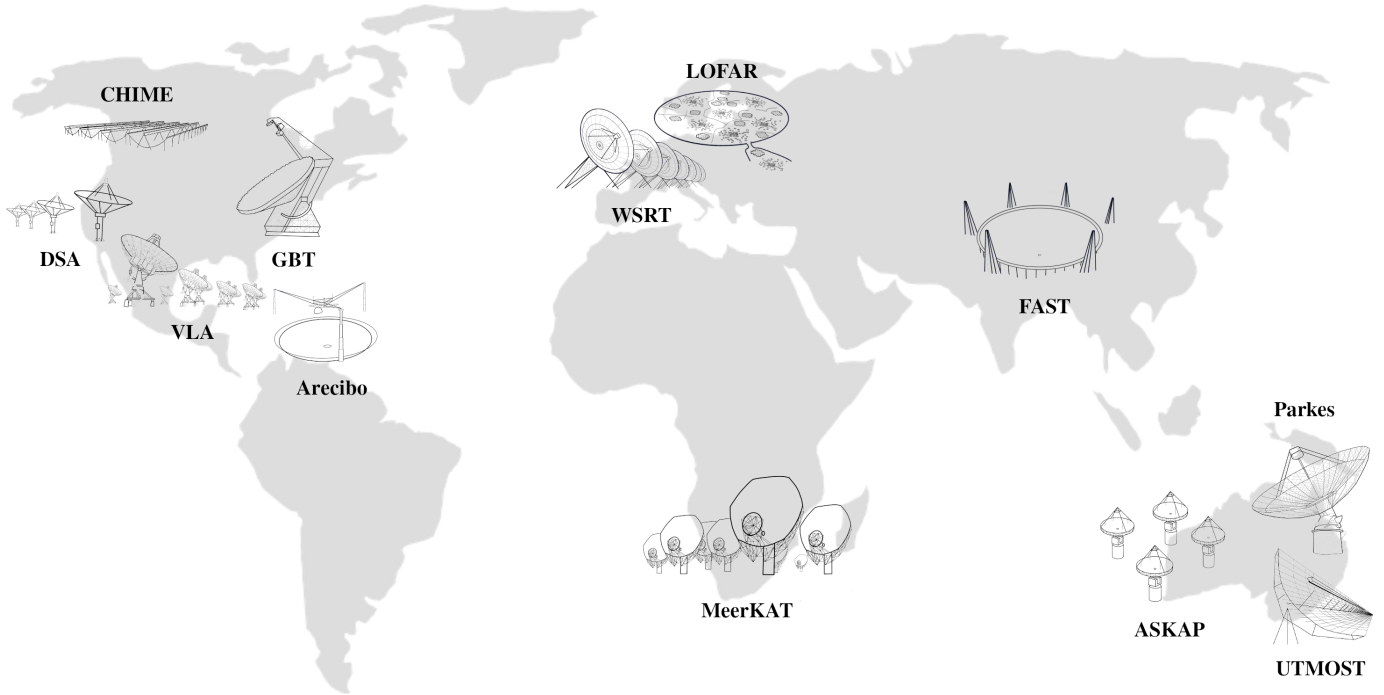

Figure 1.6: The world looking at the radio sky. Schematic representations of some of the radio telescopes with major contributions to the FRB field in their approximate location on the globe.

up observations (i.e. Hewitt et al. 2021, and references therein) before it was sadly destroyed. The Green Bank Telescope (GBT, 110 m) in West Virginia, US, was used to make the first detection of a linearly polarised FRB with a large RM (Masui et al. 2015), and it has carried out sensitive repeater follow-up observations allowing for the highest frequency detection of an FRB up to 8 GHz (Gajjar et al. 2018). Regular follow-up observations with the 76 m Lovell telescope, in the UK, allowed for the discovery of a ~ 160 day periodicity in the repeating FRB 20121102A (Rajwade et al. 2020). The 500 m FAST in China is currently the largest telescope in the world. Its gigantic diameter is currently being exploited to detect large samples of repeat bursts (Luo et al. 2020; Li et al. 2021; Niu et al. 2022; Xu et al. 2021; Feng et al. 2022), and to find very faint, highly dispersed one-off FRBs (Niu et al. 2021).

1.6.3 Interferometers

Radio interferometers consist of arrays of various antennas observing all together. Although the sensitivity of an interferometer is given by the total area of the dishes that compose it, the maximal distance between the dishes can be much larger than the diameter of a single dish, thus significantly increasing the angular resolution it can achieve. Building an array of several small dishes is generally cheaper than building a large single dish. Summing the signals from different telescopes, in the process known as beamforming, is however complicated and computationally expensive.

Several interferometers throughout the world have been used to make some of the most important FRB discoveries. The first one was the localisation of the first repeater, FRB 20121102A, with observations taken with the Karl G. Jansky Very Large Array (VLA, Chatterjee et al. 2017). The VLA is an interferometer consisting of twenty-eight 25 m dishes located in New Mexico, US. The upgraded Molonglo Observatory Synthesis Telescope (UTMOST), in Australia, consists of two cylindrical antennas, each one 778 m times 12 m in size, aligned in the east-west direction with a 15 m separation. It was used to make the first interferometric detections of a sample of one-off FRBs (Caleb et al. 2017), and later detections have allowed to build a collection of FRBs at 843 MHz, including an FRB with intriguing spectro-temporal microstructure (Farah et al. 2018, 2019). The Deep Synoptic Array (DSA), an array of ten 4.5 m dishes in California, US, made one of the first one-off FRB localisations, to a massive galaxy (Ravi et al. 2019). The Australian Square Kilometre Array Pathfinder (ASKAP) consists of 36 antennas of 12 m in diameter each, and it reported its first detections very close in time to UTMOST. ASKAP has gathered a sample of bright, low DM FRBs detected in incoherent mode, allowing for initial FRB population studies (Bannister et al. 2017; Shannon et al. 2018). By applying interferometry, it has now collected the largest single-instrument sample of localised one-off FRBs (Bannister et al. 2019; Bhandari et al. 2020b,a; Heintz et al. 2020; Bhandari et al. 2022). The European Very-long-baseline-interferometry Network (EVN) uses a multitude of radio telescopes with different designs located throughout Europe, to observe as a single interferometer. Its extensive baseline has allowed to localise several repeating FRBs with milliarcsecond precision (Marcote et al. 2020; Kirsten et al. 2022; Nimmo et al. 2022b). Additionally, some of the individual single dishes that form the EVN, mainly the 100-m Effelsberg Telescope in Germany, can obtain polarised data with high spectro-temporal resolution. MeerKAT, a precursor to the Square Kilometre Array (SKA)

in South-Africa, consists of 64 antennas of 13.5 m in diameter each with a maximum baseline of 8 km, and it has recently started producing the first FRB results within the MeerTRAP project, including repeater follow up and one-off detections (Platts et al. 2021; Caleb et al. 2020; Rajwade et al. 2022). The interferometer that has made some of the most noteworthy FRB discoveries is the Canadian Hydrogen Intensity Mapping Experiment (CHIME), consisting of four cylindrical reflectors, each 100 m $\times$ 20 m in size, located side by side. It has produced the largest single-instrument FRB sample to date, containing more than 500 FRBs (CHIME/FRB Collaboration et al. 2021a) including almost 20 repeaters (CHIME/FRB Collaboration et al. 2019a,c; Fonseca et al. 2020; CHIME/FRB Collabortion 2021; Bhardwaj et al. 2021).

1.6.4 Westerbork Synthesis Radio Telescope

The Westerbork Synthesis Radio Telescope (WSRT) is an array of fourteen 25 m dishes aligned in the East-West direction, reaching a maximal baseline of 2.7 km, located in the Netherlands. Some of the dishes are shown in Fig. 1.7. The interferometer was originally inaugurated in 1970. It was recently upgraded by setting up a new instrument named Apertif (APERture Tile In Focus), a set of Phased Array Feeds (PAFs) installed at the focal point of each dish producing 40 Compound Beams (CBs), which effectively increased the original Field of View (FoV) by a factor of 30, reaching $\sim 8.2\,\mathrm{deg}^2$ (Adams & van Leeuwen 2019; van Cappellen et al. 2022).

In July 2019, the Apertif observations started, lasting until February 2022. The operations included an imaging survey and a time-domain survey. The time-domain survey was carried out by the Apertif Radio Transient System (ARTS; van Leeuwen et al. 2022), using the eight equidistant dishes of the array to efficiently combine them at full sensitivity. ARTS operates at a central frequency of 1370 MHz with a bandwidth of 300 MHz, which corresponds to the observing frequencies where FRBs were originally found (Lorimer et al. 2007). It reaches a spectro-temporal resolution of 195 kHz/82 μs, which allows for fine morphological characterisation of the detected bursts. Since FRB data acquisition and searching is very computer intensive, a 41-node GPU cluster was installed at the Westerbork site, with one node serving as master, and the remaining 40 nodes processing the data from one CB each. FRB searches are carried out in consecutive steps. First, FRB candidates are identified in real time with the Apertif Monitor for Bursts Encountered in Real Time (AMBER)[1], that finds single pulses within the data applying different trial DMs and optional Radio Frequency Interference (RFI) mitigation (Sclocco et al. 2016). Next, the Data Analysis of Real-time Candidates (DARC)[2] pipeline determines whether to store the Stokes-IQUV data of the candidate FRB, and whether to trigger a LOFAR observation. DARC is also in charge of conducting the offline processing of the burst candidates. Due to the presence of RFI and noise fluctuations, real-time radio burst searches produce an excessive amount of FRB candidates that would take an unreasonable time to classify by human eye. For this reason, the following step of the pipeline is a machine learning classifier of the candidate bursts applying a deep learning algorithm, called `single_pulse_ml`[3] (Connor & van Leeuwen 2018). Finally, the candidates that the machine learning classifier ranks highest are sent in an email to the observers for human

[1] `AMBER`: https://github.com/TRASAL/AMBER
[2] `DARC`: https://github.com/loostrum/darc
[3] `single_pulse_ml`: https://github.com/liamconnor/single_pulse_ml

Figure 1.7: Six of the Westerbork Synthesis Radio Telescope dishes with an FRB hunter for scale. The white boxes at the focal point of each dish are the Apertif PAFs.

inspection and action. Given the distribution of the dishes, Apertif can localise the detected bursts to ellipses that are very narrow in the East-West direction, but are longer in the North-South direction.

1.6.5 LOFAR

The LOw Frequency ARray (LOFAR) is currently the radio telescope observing at the lowest frequencies in the world. Originally comprised by various antennas distributed throughout the Netherlands, the project soon became international, and additional antennas were installed in other Europeans countries. These vast distances allow for a very high angular resolution. The main, central stations can be seen in Fig. 1.8; they are located near Exloo (Netherlands) and known as the ‘‘Superterp’’.

Unlike other radio telescope dishes observing at higher frequencies that can point in the direction of the target field, LOFAR consists of omnidirectional ground-level antennas, and the pointing is made by beamforming in the desired direction. The High-Band Antennas (HBA) observe in a frequency range between 110 and 240 MHz, while the Low-Band Antennas (LBA) observe in the 30-80 MHz range (van Haarlem et al. 2013). LOFAR has a multitude of key science objectives,

Figure 1.8: Drone image of the LOFAR core, known as ‘‘Superterp’’. The HBA are the compact black tiles, and the LBA the scattered dipoles. Image credit: LOFAR / ASTRON.

from deep extragalactic surveys to solar physics and space weather. One of the primary objectives is studying pulsars and other astrophysical transients (Stappers et al. 2011). Some major pulsar discoveries have been possible thanks to LOFAR; therefore, since the discovery of FRBs, several attempts of finding FRBs with LOFAR have been carried out. As it will be further discussed in Chapter 4, all efforts of finding FRBs at such low frequencies were unsuccessful until very recently, including blind one-off searches (Coenen et al. 2014; Karastergiou et al. 2015; Sanidas et al. 2019) and targeted repeater searches (Houben et al. 2019; Chawla et al. 2020).

1.6.6 Multi-wavelength and multi-messenger observations

Multi-wavelength and multi-messenger observations of FRBs could provide decisive information to determine the exact nature of some, if not all, FRBs. Several progenitor models and emission mechanisms predict FRB counterparts at different wavelengths, neutrinos, cosmic rays or gravitational waves, occurring before, simultaneous or after the radio burst. Any counterpart detection would thus significantly narrow down which models are valid. The detection of a bicomponent bright radio burst (Bochenek et al. 2020; CHIME/FRB Collaboration 2020) coincident in time with two high-energy flares from SGR 1935+2154 (Mereghetti et al. 2020a) further motivates

multi-wavelength FRB searches to unequivocally establish the connection between FRBs and magnetars.

Several efforts of trying to detect multi-wavelength or multi-messenger FRB counterparts have been implemented. One of the first attempts consisted in triggering follow-up observations of the one-off FRB 20140514A several hours to days after the detection in different radio frequencies, optical, and high-energy (Petroff et al. 2015a). Other research has focused on archival data searches for transient or persistent emission in the optical (Tingay & Yang 2019; Xin et al. 2021; Li et al. 2022), hard and soft X-rays, and γ-rays (Zhang & Zhang 2017; Xi et al. 2017; Cunningham et al. 2019; Anumarlapudi et al. 2020; Martone et al. 2019; Verrecchia et al. 2021). Active repeaters offer a unique opportunity for simultaneous follow up in radio and other wavelengths, or targeted follow-up searches during the predicted active phases. This has been possible for the first repeater FRB 20121102A (Scholz et al. 2017; Hardy et al. 2017; MAGIC Collaboration et al. 2018), the periodic repeater FRB 20180916B (Panessa et al. 2020; Casentini et al. 2020; Tavani et al. 2020b; Scholz et al. 2017; Guidorzi et al. 2020; Laha et al. 2022), the FAST analogue to the first repeater, FRB 20190520B (Niino et al. 2022), and a source with an extremely active epoch of activity, FRB 20201124A (Piro et al. 2021).

The aforementioned works have mostly resulted in non-detections, with limited exceptions. (De-Launay et al. 2016) discovered a transient γ-ray source coincident in space and time with the one-off FRB 20131104A, but Shannon & Ravi (2017) argue that the transient was most likely an AGN flare. Li et al. (2022) reported the detection of the optical transient AT2020hur coincident in space and during an active phase of the periodic repeater FRB 20180916B, although the association between the two sources remains subject to debate. If the association is found to be real and further simultaneous optical detections are found, this could be the signature expected from synchrotron maser models (Metzger et al. 2019; Beloborodov 2020). As discussed in Section 1.3, FRBs could be emitted during a compact object merger, or by young magnetars born after BNS mergers; in such case, gravitational waves should be associated to FRBs. However, Callister et al. (2016) demonstrated the binary black hole rate to be roughly 5% of the FRB rate, and the predictions from BNS and BHNS mergers to be similar. Furthermore, Zhang et al. (2020a) established that only 6% of repeating FRBs could be formed through BNS mergers. Hence, if compact object mergers can engender FRBs, it would only be a very small fraction of both the repeaters and one-offs. Several high-energy observations have put tight constraints on the X-ray and γ-ray luminosity simultaneous to repeater bursts. However, the FRB cosmological distances have not yet allowed to reach a sensitivity equivalent to the SGR 1935+2154 X-ray to radio luminosity rate. Flaring magnetar models are thus still consistent with being at the source of the observed FRBs (Scholz et al. 2017, 2020; Laha et al. 2022).

1.7 Thesis outline

This thesis, titled ‘‘Exploring the link between Neutron Stars and Fast Radio Bursts’’, started with the aim of advancing our knowledge on Fast Radio Bursts using real-time detections and multi-wavelength observations. At the time when I started this project, FRBs were very enigmatic, and little data was available to explore them. I have had the chance to participate in the Apertif time-domain survey since its start in July 2019 until the operations ceased in February 2022. In

this time, the field of FRBs has experienced a massive development, and in consequence the goals of this thesis have evolved, reflecting the progress in the field in order to contribute to it. The work presented in this thesis is mainly based on FRB searches and observations with Apertif; it also combines data from multiple instruments in order to study neutron stars, high-energy transients, and their link to FRBs, from a multi-wavelength approach.

In Chapter 2, we carried out LOFAR observations of four isolated neutron stars known to produce high-energy pulsations in X-rays or γ-rays. These neutron stars had all been previously observed in radio, generally at higher frequencies, but never detected before. At lower frequencies, the radio beam is expected to be wider. If the radio-quietness of these sources is due to a misalignment of the radio beam with Earth, LOFAR observations might be successful where other searches have failed before. These high-energy emitting neutron stars share properties with RRATS, X-ray Dim Isolated Neutron Stars (XDINSs), and radio-quiet magnetars, the latter being the most likely FRB progenitors. This suggests there might be an evolutionary link between these different neutron star types, and thus radio observations of high-energy isolated neutron stars might give some insight into the FRB emission. We did not find any periodic emission or single pulses from these four high-energy pulsars, but we set constraining upper limits on the radio flux.

In Chapter 3, we describe the EPIC-pn XMM-Newton Outburst Detector (EXOD) algorithm, that we developed to search for faint X-ray transients in XMM-Newton observations. Such faint transients could be, for instance, extragalactic magnetar bursts, or the X-ray counterparts of FRBs. We applied EXOD to all the observations taken with the EPIC-pn instrument included in the 3XMM-DR8 catalogue, and identified ~ 2500 variable sources. Of these, we explored the properties of 35 sources without a previous classification in order to determine their nature. We identified four of these sources as extragalactic type I X-ray bursters, a type of neutron star Low Mass X-ray Binaries (LMXBs) that experience thermonuclear bursts. These discoveries doubled the amount of identified NSs in the Milky Way neighbouring galaxy, Andromeda (M31).

Chapter 4 presents an extensive follow-up campaign of the periodic repeater FRB 20180916B that we took at two different radio frequencies, with Apertif and LOFAR. With Apertif, we collected a large dataset of 54 bursts in $\sim$400 h of observations. With LOFAR, we detected nine bursts down to 120 MHz, which represent the lowest frequency detections of an FRB. From these detections, and combining them with the available data from other instruments, we determined that the activity of FRB 20180916B, with a period of $\sim$16.3 days, peaks earlier and is narrower at higher frequencies than at lower frequencies. The presence of emission at such low frequencies and the absence of scattering additional to what we expect from the Milky Way reveals that FRB 20180916B lives in a clean environment. A narrower activity window at higher frequencies and the presence of emission at such low frequencies, are opposite to the predictions from models invoking free-free absorption. We could thus disfavour periodicity models of binary systems with strong companion winds shielding the radio emission.

In Chapter 5, we present a one-off FRB discovered with Apertif displaying five temporal components with quasi-periodic spacing. We performed a complex temporal analysis to determine the periodicity of this structure, and find it is marginally significant, at 2.5σ. We explored different scenarios that could be the source of such structure, and ruled out a compact object binary coalescence or the rotation of a neutron star as plausible explanations. Given the similarities between

the morphology of this FRB and some pulsars and magnetar single pulses, we determined the morphology to be likely caused by the magnetospheric structure of a magnetar.

Finally, in Chapter 6 we present the compilation of all one-off FRBs that were detected during the Apertif survey between July 2019 and February 2022, a sample of 24 bursts. At present, it is one of the largest single-instrument FRB samples at L band. We describe the properties of several FRBs of interest, and analyse the properties of the FRB sample as a population, including the all-sky rate, localisation regions, and propagation properties. Our sample includes the FRB with the second largest DM to date; an FRB displaying both scintillation and scattering that can constrain the distance to its scattering screen; and an FRB that we localised to its most likely host galaxy. We found one third of the bursts display several components. This is a much larger fraction of multi-component bursts than what CHIME/FRB has observed at 600 MHz, and we determined that scattering alone cannot account for such difference.

The final sections of this thesis include the bibliography, an overview of the co-author contributions, other publications, and a Spanish, English and Dutch Summary.

2

New upper limits on low-frequency radio emission from isolated neutron stars with LOFAR

I. Pastor-Marazuela, S. M. Straal, J. van Leeuwen, V. I. Kondratiev

To be submitted to Astronomy & Astrophysics

Abstract

Neutron stars that show X-ray and γ-ray pulsed emission must, somewhere in the magnetosphere, generate electron-positron pairs. Such pairs are also required for radio emission, but then why do a number of these sources appear radio quiet? Here, we carried out a deep radio search towards four such neutron stars that are isolated X-ray/γ-ray pulsars but for which no radio pulsations have been detected yet. These sources are 1RXS J141256.0+792204 (Calvera), PSR J1958+2846, PSR J1932+1916 and SGR J1907+0919. Searching at lower radio frequencies, where the radio beam is thought to be wider, increases the chances of detecting these sources, compared to the earlier higher-frequency searches. We thus carried a search for periodic and single-pulse radio emission with the LOFAR radio telescope at 150 MHz. We used the known periods, and searched a wide range of dispersion measures, as the distances are not well constrained. We did not detect pulsed emission from any of the four sources. However, we put very constraining upper limits on the radio flux density at 150 MHz, of $\lesssim 1.4$ mJy.

2.1 Introduction

Through their spin and magnetic field, neutron stars act as powerful cosmic dynamos that can generate a wide variety of electromagnetic emission. There thus exist many subclasses of neutron stars, with different observed behavior. The evolutionary links between some of the classes are established, while for others these connections are currently unknown. The largest group in this varied population is formed by the regular rotation-powered radio pulsars. The fast spinning, high magnetic field influx to this group are the young pulsars. These show a high spin-down energy loss rate $\dot{E}$, and a number of energetic phenomena such as radio giant pulse (GP) emission. The most extreme of these fast-spinning and/or high-field sources could potentially also power Fast Radio Bursts (FRBs; Pastor-Marazuela et al. 2022). On the long-period outskirts of the P-$\dot{P}$ diagram, slowly-rotating pulsars (Tan et al. 2018) and magnetars (Caleb et al. 2022; Hurley-Walker et al. 2022) sometimes continue to shine.

Some neutron stars, however, only shine intermittently in radio. The rotating radio transients (RRATs) burst very irregularly, and in the P-$\dot{P}$ diagram most are found near the death line (Keane et al. 2011). The exact evolutionary connection between RRATs and the steadily radiating normal pulsars is unclear, but they are most likely closely linked. Except for their intermittency, RRATs appear to mostly display the same spin-down characteristics as normal, albeit generally old, pulsars.

Finally, populations of neutron stars exist that appear to not emit in radio at all: radio-quiet magnetars such as most anomalous X-ray pulsars (AXPs) and soft gamma repeaters (SGRs), X-ray dim isolated neutron stars (XDINSs; Haberl 2007), and γ-ray pulsars (Abdo et al. 2013). These are able to produce high-energy emission but are often radio quiet.

Potentially, some of these could produce radio emission only visible at low radio frequencies. Detections of radio pulsations of the γ and X-ray pulsar *Geminga*, PSR J0633+1746, have been claimed at and below the 100 MHz observing frequency range (Malofeev & Malov 1997; Malov et al. 2015; Maan 2015), although a very deep search using LOFAR came up empty (Ch. 6 in Coenen 2013). Such low-frequency detections offer an intriguing possibility to better understand the radio emission mechanism of these enigmatic objects. Radio detections of a magnetar with LOFAR, complementary to higher-frequency studies such as Camilo et al. (2006) and Maan et al. (2022) for XTE J1810−197, could offer insight into emission mechanisms and propagation in ultra-strong magnetic fields.

XDINSs feature periods that are as long as those in magnetars, but they display less extreme magnetic field strength. The XDINSs form a small group of seven isolated neutron stars that show thermal emission in the soft X-ray band. Since their discovery with ROSAT in the 1990s, several attempts were made to detect these sources at radio frequencies, but they were unsuccessful (e.g. Kondratiev et al. 2009). As those campaigns operated above 800 MHz, a sensitive lower-frequency search could be opportune. It has been proposed (e.g. Komesaroff 1970; Cordes 1978) and observed (e.g. Chen & Wang 2014) that pulsar profiles are usually narrower at higher frequencies and become broader at lower radio frequencies. This suggests the radio emission cone is broader at low frequencies, and sweeps across a larger fraction of the sky as seen from the pulsar. If that is the case for all neutron star radio beams, chances of detecting radio emission from

γ- and X-ray Isolated Neutron Stars (INSs) increase at the lower radio frequencies offered through LOFAR. The earlier observations that resulted in non-detections could then have just missed the narrower high-frequency beam, where the wider lower-frequency beam may, in contrast, actually enclose Earth. In that situation, LOFAR could potentially detect the source.

Recently, a number of radio pulsars were discovered that shared properties with XDINSs and RRATs, such as soft X-ray thermal emission, a similar position in the P-$\dot{P}$ diagram, and a short distance to the solar system. These sources, PSR J0726−2612 (Rigoselli et al. 2019) and PSR J2251−3711 (Morello et al. 2020), support the hypothesis that XDINSs are indeed not intrinsically radio quiet, but have a radio beam pointed away from us. These shared properties could reflect a potential link between the radio and X-ray emitting pulsars with XDINSs and RRATs. A firm low-frequency radio detection of INSs would thus tie together these observationally distinct populations of neutron stars.

In this work we present LOFAR observations of four INSs that brightly pulsate at X-ray or γ-ray energies, but have not been detected in radio. These sources are listed below, and their parameters are presented in Table 2.1.

2.1.1 J1412+7922

The INS 1RXS J141256.0+792204, dubbed "Calvera" and hereafter J1412+7922, was first detected with *ROSAT* (Voges et al. 1999) as an X-ray point source, and subsequently with *XMM-Newton* (Pires et al. 2009). X-ray observations confirmed its neutron star nature through the detection of $P \simeq 59$ ms pulsations by Zane et al. (2011), and allowed for the determination of its spin-down luminosity $\dot{E} \sim 6 \times 10^{35}$ erg s^{-1}, characteristic age $\tau_c \equiv P/2\dot{P} \sim 3 \times 10^5$ years, and surface dipole magnetic field strength $B_s = 4.4 \times 10^{11}$ G by Halpern et al. (2013). Although these values are not unusual for a rotationally-powered pulsar, the source is not detected in radio (Hessels et al. 2007; Zane et al. 2011) or γ-rays (Mereghetti et al. 2021). The X-ray emission can be modelled with a two-temperature black body spectrum (Zane et al. 2011), similar to other XDINSs (Pires et al. 2014). However, J1412+7922 shows a spin period much faster than typically observed in XDINS. Since the source is located at high galactic latitudes and its inferred distance is relatively low ($\sim$3.3 kpc; Mereghetti et al. 2021) the path through the interstellar medium is not long enough to explain the radio non-detections by high Dispersion Measure (DM) or scattering values.

2.1.2 J1958+2846

Discovered by Abdo et al. (2009) through a blind frequency search of *Fermi-LAT* γ-ray data, INS PSR J1958+2846, hereafter J1958+2846, has shown no X-ray or radio continuum emission counterpart so far (Ray et al. 2011; Frail et al. 2016). Arecibo observations have put very constraining upper limits of 0.005 mJy at 1510 MHz (Ray et al. 2011). Searches for pulsations from the source using the single international LOFAR station FR606 by Grießmeier et al. (2021) also found no periodic signal.

The double-peaked pulse profile of J1958+2846 can be interpreted as a broad γ-ray beam. The earlier higher-frequency radio non-detections could be due to a narrower radio beam and to an

unfavourable rotation geometry with respect to the line of sight. If the radio beam is indeed wider at lower frequencies, LOFAR would have higher chances of detecting it. In that case, a setup more sensitive than the Grießmeier et al. (2021) single-station search is required.

Modeling by Pierbattista et al. (2015) indicates that the γ-ray pulse profile of J1958+2846 can be well fitted by One Pole Caustic emission (OPC, Romani & Watters 2010, Watters et al. 2009) or an Outer Gap model (OG, Cheng et al. 2000). In both cases, the γ-rays are generated at high altitudes above the NS surface. Each model constrains the geometry of the pulsar. For the OPC model, the angle between the rotation and magnetic axes $\alpha = 49^\circ$, while the angle between the observer line-of-sight and the rotational axis $\zeta = 85^\circ$. The OG model reports similarly large angles, with the NS equator rotating in the plane that also contains Earth, and an oblique dipole: $\alpha = 64^\circ,\ \zeta = 90^\circ$. If this model is correct, the low-frequency radio beam would thus need to be wider than $\sim$30° to encompass the telescope. As that is wider than most pulsar beams, a total-intensity detection would suggest to first order a geometry where α and ζ are closer than follows from Pierbattista et al. (2015), even if that suggestion would only be qualitative. Subsequent follow-up measurements of polarisation properties throughout the pulse, and fitting these to the rotating vector model (RVM; Radhakrishnan & Cooke 1969), can quantify allowed geometries to within a relatively precise combinations of α and ζ. As a matter of fact, in a similar study on radio-loud γ-ray pulsars, Rookyard et al. (2015) already find that RVM fits suggest that the magnetic inclination angles α are much lower than predicted by the γ-ray light curve models. This, in turn, affirms that deep radio searches can lead to detections even when the γ-ray light curves suggest the geometry is unfavorable.

2.1.3 J1932+1916

The INS PSR J1932+1916, hereafter J1932+1916, was discovered in *Fermi-LAT* data through blind searches with the *Einstein@Home* volunteer computing system. J1932+1916 is the youngest and γ-ray brightest among the four γ-ray pulsars presented from that effort in (Pletsch et al. 2013). The period is 0.21 s, the characteristic age is 35 kyr. Frail et al. (2016) find no continuum 150 MHz source at this position with GMRT above a 5σ limit on the period-averaged flux density of 27 mJy beam^{-1}. If the flux density they find at the position of the pulsar, 2.4$\pm$5.3 mJy beam^{-1}, is in fact the pulsed emission from J1932+1916, then a LOFAR periodicity search as described here should detect the source at a S/N of 15 if the duty cycle is 10%. Karpova et al. (2017) report on a potential pulsar wind nebula (PWN) association from *Swift* and *Suzaku* observations. However, no X-ray periodicity searches have been out carried before.

2.1.4 J1907+0919

The Soft Gamma Repeater J1907+0919, also known as SGR 1900+14, was detected through its bursting nature by Mazets et al. (1979). Later outbursts were detected in 1992 (Kouveliotou et al. 1993), 1998 (Hurley et al. 1999) and 2006 (Mereghetti et al. 2006). The August 1998 outburst allowed the detection of an X-ray period of ~ 5.16 s, and thus confirmed the nature of the source as a magnetar (Hurley et al. 1999; Kouveliotou et al. 1999). Frail et al. (1999) detected a transient radio counterpart that appeared simultaneous to the 1998 outburst, and they identified the radio source as a synchrotron emitting nebula. Shitov et al. (2000) claimed to have found radio pulsa-

tions at 111 MHz from four to nine months after the 1998 burst, but no other periodic emission has been found at higher radio frequencies (Lorimer & Xilouris 2000; Fox et al. 2001; Lazarus et al. 2012).

This paper is organized as follows: in Section 2.2 we explain how we used LOFAR (van Haarlem et al. 2013) to observe the sources mentioned above; in Section 2.3 we detail the data reduction procedure, including the periodicity and the single pulse searches that we carried; in Section 2.4 we present our results, including the upper limit that we set on the pulsed emission; in Section 2.5 we discuss the consequences of these non-detections for the radio-quiet pulsar population, and in Section 2.6 we give our conclusions on this work.

2.2 Observations

We observed the four sources with the largest possible set of High Band Antennas (HBAs) that LOFAR can coherently beam form. Each observation thus added 22 HBA Core Stations, covering a 78.125 MHz bandwidth in the 110 MHz to 190 MHz frequency range (centered on 148.92 MHz). The LOFAR beam-forming abilities allow us to simultaneously observe different regions of the sky (van Leeuwen & Stappers 2010; Stappers et al. 2011; Coenen et al. 2014). For our point-source searches of INSs, we used three beams per observation; one beam pointed to the source of interest, one on a nearby known pulsar, and one as a calibrator blank-sky beam to cross-check potential candidates as possibly arising from Radio Frequency Interference (RFI). The observations were carried out between 16 January 2015 and 15 February 2015 under project ID LC3_036. We integrated for 3 hours on each of our sources. The data were taken in Stokes I mode. Since the periods of the gamma-ray pulsars are known, the time resolution of each observation was chosen such to provide good coverage of the pulse period, at a sampling time between $0.16-1.3$ ms. The observation setup is detailed in Table 2.1.

2.3 Data reduction

The data was pre-processed by the LOFAR pulsar pipeline after each observation (Alexov et al. 2010; Stappers et al. 2011) and stored on the LOFAR Long Term Archive[1] in `PSRFITS` format (Hotan et al. 2004). The 1.5 TB of data was then transferred to one of the nodes of the Apertif real-time FRB search cluster *ARTS* (van Leeuwen 2014; van Leeuwen et al. 2022).

We performed a periodicity search as well as a single-pulse search using `Presto`[2] (Ransom 2001). The data was cleaned from RFI and searched for periodic signals and single pulses. We searched for counterparts around the known P and $\dot{P}$. Additionally, we performed a full blind search in order to look for potential pulsars in the same field of view, since many new pulsars are found at low frequencies (Sanidas et al. 2019) and chance discoveries happen regularly (e.g., Oostrum et al. 2020). Since the DM of our sources is unknown, we searched over a range of DMs going from 4 pc cm^{-3} to 400 pc cm^{-3}. The DM-distance relation is not precise enough to warrant a much smaller DM range, even for sources for which a distance estimate exists; and a wider DM

[1] LTA: https://lta.lofar.eu/
[2] Presto: https://www.cv.nrao.edu/~sransom/presto/

Table 2.1: Parameters of the observed pulsars and observational setup of the observations in the LC3_036 proposal. The beam of each observation was centered in the reported pulsar coordinates. Listed in the bottom rows are the earlier periodicity-search limits. The upper limits from Frail et al. (2016) described in the main text are period-averaged flux densities and are not listed here. The last row lists the limits from the current work, for S/N=5, with errors of 50% (Bilous et al. 2016).

	J1412+7922	J1958+2846	J1932+1916	J1907+0919
Right ascension, α (J2000)	14 12 56	19 58 40	19 32 20	19 07 14.33
Declination, δ (J2000)	+79 22 04	+28 45 54	+19 16 39	+09 19 20.1
Period, P (s)	0.05919907107	0.29038924475	0.208214903876	5.198346
Period derivative, $\dot{P}$ (s s^{-1})	3.29134×10^{-15}	2.12038×10^{-13}	9.31735×10^{-14}	9.2×10^{-11}
Epoch (MJD)	58150[a]	54800[b]	55214[c]	53628[d]
LOFAR ObsID	L257877	L258545	L259173	L216886
Obs. date (MJD)	55094	57046	57068	56755
Sample time (ms)	0.16384	1.31072	1.31072	0.65536
Test pulsar detected	B1322+83	B1952+29	B1933+16	B1907+10
Previous limits (mJy @ GHz).....	4 @ 0.385[e] 0.05 @ 1.36[f] 0.3 @ 1.38[e]	2.0 @ 0.15[g] 0.005 @ 1.51[b]	2.9 @ 0.15[g] 0.075 @ 1.4[c]	50 @ 0.111[h] 0.4 @ 0.43[i] 0.3 @ 1.41[i] 0.012 @ 1.95[j]
LOFAR sensitivity limit $S_{\rm lim}$ (mJy)	0.26 ± 0.13	0.53 ± 0.26	0.73 ± 0.36	1.39 ± 0.69

[a] Bogdanov et al. (2019), [b] Ray et al. (2011), [c] Pletsch et al. (2013), [d] Mereghetti et al. (2006), [e] Hessels et al. (2007), [f] Zane et al. (2011), [g] Grießmeier et al. (2021), [h] Shitov et al. (2000), [i] Lorimer & Xilouris (2000), [j] Lazarus et al. (2012)

range allows for discovery of other pulsars contained in our field of view. The highest DM pulsar detected with LOFAR has a DM = 180 pc cm^{-3} (Bilous et al. 2016). We thus searched up to twice this value to make sure that any detectable sources were covered. We determined the optimal de-dispersion parameters with `DDplan` from Presto. The sampling time variation between some of the four observations had a slight impact on the exact transitions of the step size but generally the data was de-dispersed in steps of 0.01 pc cm^{-3} up to DM = 100 pc cm^{-3}; then by 0.03 pc cm^{-3} steps up 300 pc cm^{-3} and finally using 0.05 pc cm^{-3} steps.

We manually inspected all candidates down to $\sigma = 4$, resulting in ~ 1400 candidates per beam. To verify our observational setup, we performed the same blind search technique to our test pulsars B1322+83 and B1933+16, which we detected. The test pulsar B1953+29 was not detected because the sampling time of the observation of J1958+2846 was not adapted to its ~ 6 ms period. However, we were able to detect B1952+29 (Hewish et al. 1968) in this same pointing. Even though it is located at >1° from the targeted coordinates, it is bright enough to be visible as a side-lobe detection.

The candidates from Presto's single pulse search were further classified using the deep learning classification algorithm developed by Connor & van Leeuwen (2018), which has been verified and successful in the Apertif surveys (e.g. Connor et al. 2020; Pastor-Marazuela et al. 2021). This reduced the number of candidates significantly by sifting out the remaining RFI. The remaining candidates were visually inspected.

2.4 Results

In our targeted observations we were unable to detect any plausible astronomical radio pulsations or single pulses. We determine new 150 MHz flux upper limits by computing the sensitivity limits of our observations. To establish these sensitivity limits, we apply the radiometer equation adapted to pulsars (Dewey et al. 1985), assuming a pulsar duty cycle of 10%. We determine the telescope parameters that are input to this equation by following the procedure[1] described in Kondratiev et al. (2016). That approach takes into account the system temperature (including the sky temperature), the projection effects governing the effective area of the fixed tiles, and the amount of time and bandwidth removed due to RFI, to produce the overall observation system-equivalent flux density (SEFD). To facilitate direct comparison to values reported in e.g., Ray et al. (2011) and Grießmeier et al. (2021), we use a S/N of 5. A more conservative option, given the high number of candidates per beam, would arguably be to use a limit of S/N=8. We did, however, review by eye all candidates with S/N>4; and the reader can easily scale the reported sensitivity limits to a different S/N value. We report these sensitivity limits, computed at the coordinates of the central beam of each observation, in Table 2.1. Even though all observations are equally long, the estimated $S_{\rm lim}$ values are different. That is mostly due to the strong dependence of the LOFAR effective area, and hence the sensitivity, on the elevation.

In Fig. 2.1, we compare our upper limits to those established in previous searches, mostly using the same techniques, and generally at higher frequencies (Hessels et al. 2007; Zane et al. 2011; Ray et al. 2011; Pletsch et al. 2013; Grießmeier et al. 2021). If we assume that these four pulsars have

[1] https://github.com/vkond/LOFAR-BF-pulsar-scripts/blob/master/fluxcal/lofar_fluxcal.py

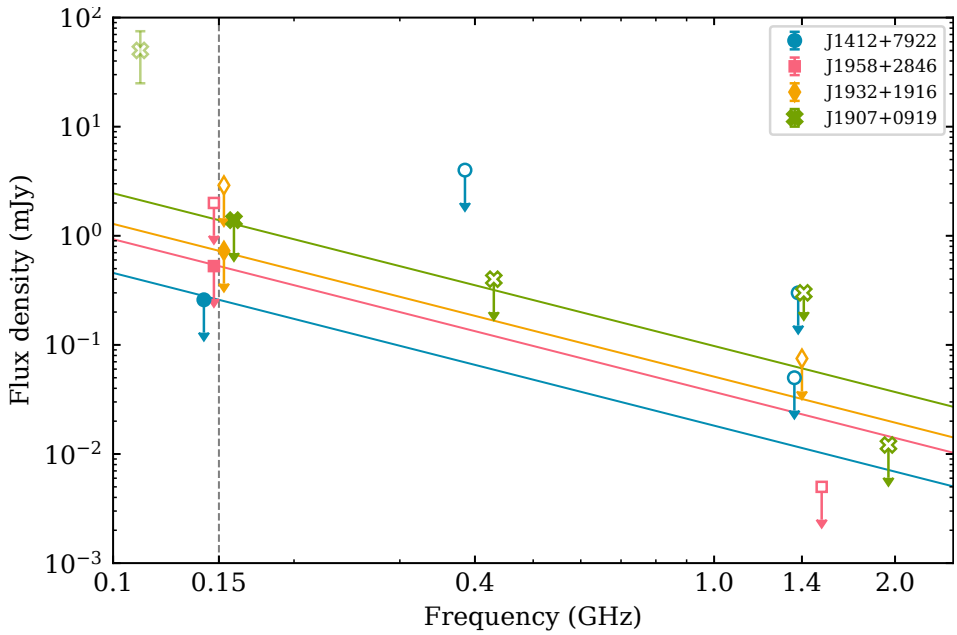

Figure 2.1: Flux density upper limits of this work at 150 MHz (filled symbols) with S/N = 5 for comparison to earlier searches of the same sources (empty symbols). Solid lines going through our upper limit estimates with spectral index $\alpha = -1.4$ are overlaid to show the scaling of our sensitivity limits. Our limits are plotted slightly offset from the 150 MHz observing frequency (dashed line) for better visibility.

radio spectra described by a single power-law $S_\nu \propto \nu^\alpha$ with a spectral index of $\alpha = -1.4$ (Bates et al. 2013; Bilous et al. 2016), the upper limits we present here for J1412+7922 and J1932+1916 are the most stringent so-far for any search. The upper limits on J1958+2846 (Arecibo; Ray et al. 2011) and J1907+0919 (GBT; Lazarus et al. 2012) are a factor of 2–3 more sensitive than ours.

2.5 Discussion

2.5.1 Comparison to previous limits

For J1958+2846 and J1932+1916, we can make a straightforward relative comparisons between our results presented here and the existing limit at 150 MHz, from the single-station LOFAR campaign by Grießmeier et al. (2021). Our 22 Core Stations are each 1/4th of the area of the FR606 station and are coherently combined, leading to a factor $\frac{A_\mathrm{core}}{A_\mathrm{FR606}} = \frac{22}{4}$ difference in area A for the radiometer equation and S_lim. The integration time t of 3 h is shorter than the FR606 total of 8.3 h (J1958+2846) and 4.1 h (J1932+1916), leading to a factor $\sqrt{\frac{t_\mathrm{core}}{t_\mathrm{FR606}}} = \sqrt{\frac{3}{8.3}}$ in the radiometer equation. Other factors such as the sky background and the influence of zenith angle on the sensitivity should be mostly the same for both campaigns. Our S_lim is thus $\frac{22}{4}\sqrt{\frac{3}{8.3}} = 3.3$

times deeper than the Grießmeier et al. (2021) upper limit for J1958+2846, and 4.7 times for J1932+1916. Those factors are in good agreement with the actual limits listed in Table 2.1.

2.5.2 Emission angles and intensity

Different pulsar emission mechanism models exist that predict simultaneously the radio and γ-ray emission.

The polar cap model assumes that the γ-ray emission is produced at the surface of the NS near the magnetic polar caps. The outer magnetosphere emission models, such as the outer gap and the slot gap, predict that the γ-ray emission is produced in the magnetosphere of the NS, within the extent of the light cylinder.

If the non-detection in radio of these INS is due to the fact that the radio beam does not cover the observer, it would favor the outer magnetospheric models, since these predict an extended γ-ray beam much broader than the radio beam. That narrower radio beam does not reach the line of sight.

Note that while it is instructive to discuss the coverage of the radio pulsar beam in binary terms – it either hits or misses Earth – this visibility is not that black and white in practice. The beam edge is not sharp. In beam mapping experiment enabled by the geometric precession in PSR J1906+0745 (van Leeuwen et al. 2015), the flux at the edge of the beam is over 100$\times$ dimmer than the peak, but it is still present and detectable (Desvignes et al. 2019). Deeper searches thus continue to have value, even if non-detections at the same frequency already exist.

That said, the detection of PSR J1732−3131 only at 327 and potentially even 34 MHz (Maan & Aswathappa 2014) shows that pulse broadening (or, possibly equivalently, a steep spectral index) at low frequencies is a real effect, also for γ-ray pulsars.

2.5.3 Emission mechanism and evolution

Most models explain the radio quietness of an NS through a chance beam misalignment, as above. It could, of course, also be a more intrinsic property. There are at least two regions in the P-$\dot{P}$ diagram where radio emission may be increasingly hard to generate.

The first parameter space of interest is for sources close to the radio death line (Chen & Ruderman 1993). XDINSs are preferably found there, which suggests these sources are approaching, in their evolution, a state in which radio emission generally ceases. From what we see in normal pulsars, the death line represents the transition into a state in which electron-positron pair formation over the polar cap completely ceases. Once the pulsar rotates too slowly to generate a large enough potential drop over the polar cap, required for this formation, the radio emission turns off (Ruderman & Sutherland 1975). The high-energy emission also requires pair formation, but these could occur farther out. We note that polar cap pair formation can continue at longer periods, if the NS surface magnetic field is not a pure dipole. With such a decreased curvature radius, the NS may keep on shining. Evidence for such higher-order fields is present in a number of pulsars, e.g., PSR J0815+0939 (Szary & van Leeuwen 2017) and PSR B1839−04 (Szary et al. 2020). This

would also influence the interpretation of any polarization information, as the RVM generally assumes a dipole field.

None of the sources in our sample are close to this death line (See Fig. 2.2), but SGR J1907+0919 is beyond a different, purported boundary: the photon splitting line (Baring & Harding 2001). In pulsars in that second parameter space of interest, where magnetic fields are stronger than the quantum critical field, of 4.4×10^{13} G (Fig. 2.2), pair formation cannot compete with magnetic photon splitting. Such high-field sources could then be radio quiet but X-ray or γ-ray bright. Given its spindown dipole magnetic field strength of 7×10^{14} G, our non-detection of SGR J1907+0919 supports the existence of this limit.

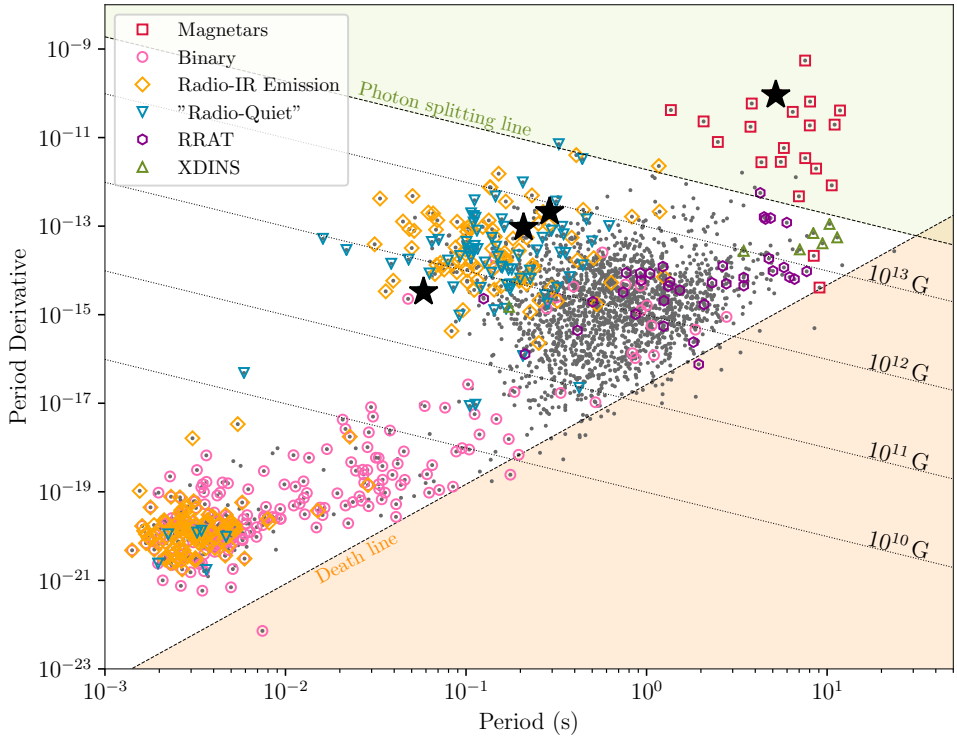

Figure 2.2: $P - \dot{P}$ diagram showing the location of the sources presented in this work. All pulsars from the ATNF Pulsar Catalogue (Manchester et al. 2005) are shown as grey dots, with different pulsar classifications encircled by different symbols. The sources discussed in this work are shown as black stars, from left to right: J1412+7922, J1932+1916, J1932+1916, and J1907+0919. The orange shaded region is delimited by the death line, while the green shaded region is delimited by the photon splitting line. Plot generated with `psrqpy` (Pitkin 2018).

2.6 Conclusion

We have conducted deep LOFAR searches of periodic and single-pulse radio emission from four isolated neutron stars. Although we validated the observational setup with the detection of the

test pulsars, we did not detect any of the four targeted pulsars. This can be explained with an intrinsic radio-quietness of these sources, as was previously proposed. It could also be caused by a chance misalignment between the radio beam and the line of sight.

With the new upper limits, we can rule out the hypothesis that INSs had not been previously detected at radio frequencies around 1 GHz, because of a steeper spectrum than that of regular radio pulsars.

Acknowledgements

This research was supported by the Netherlands Research School for Astronomy ('NOVA5-NW3-10.3.5.14'), the European Research Council under the European Union's Seventh Framework Programme (FP/2007-2013)/ERC Grant Agreement No. 617199 ('ALERT'), and by Vici research programme 'ARGO' with project number 639.043.815, financed by the Dutch Research Council (NWO). We further acknowledge funding from National Aeronautics and Space Administration (NASA) grant number NNX17AL74G issued through the NNH16ZDA001N Astrophysics Data Analysis Program (ADAP) to SMS. This paper is based (in part) on data obtained with the International LOFAR Telescope (ILT) under project code LC3_036. LOFAR (van Haarlem et al. 2013) is the Low Frequency Array designed and constructed by ASTRON. It has observing, data processing, and data storage facilities in several countries, that are owned by various parties (each with their own funding sources), and that are collectively operated by the ILT foundation under a joint scientific policy. The ILT resources have benefitted from the following recent major funding sources: CNRS-INSU, Observatoire de Paris and Université d'Orléans, France; BMBF, MIWF-NRW, MPG, Germany; Science Foundation Ireland (SFI), Department of Business, Enterprise and Innovation (DBEI), Ireland; NWO, The Netherlands; The Science and Technology Facilities Council, UK; Ministry of Science and Higher Education, Poland.

3

The *EXOD* search for faint transients in *XMM-Newton* observations: Method and discovery of four extragalactic Type I X-ray bursters

I. Pastor-Marazuela, N. A. Webb, D. T. Wojtowicz, J. van Leeuwen

Astronomy & Astrophysics, Volume 640, A124, August 2020

Abstract

XMM-Newton has produced an extensive X-ray source catalogue in which the standard pipeline determines the variability of sufficiently bright sources through χ^2 and fractional variability tests. Faint sources, however, are not automatically checked for variability, thus overlooking faint, short timescale transients. Our goal is to find new faint, fast transients in XMM-Newton EPIC-pn observations. To that end we have created the EPIC-pn XMM-Newton Outburst Detector (EXOD) algorithm, which we run on the EPIC-pn data available in the 3XMM-DR8 catalogue. In EXOD, we compute the whole-field variability by binning in time the counts in each detector pixel. We next compute the maximum-to-median count difference in each pixel to detect variability. We applied EXOD to 5,751 observations and compared the variability of the detected sources to the standard χ^2 and Kolmogorov-Smirnov (KS) variability tests. The algorithm is able to detect periodic and aperiodic variability, short and long flares. Of the sources detected by EXOD, 60-95% are also shown to be variable by the χ^2 and KS tests. We obtain a net number of 2,536 variable sources. Of these we investigate the nature of 35 sources with no previously confirmed classification. Amongst the new sources, we find stellar flares and AGNs; but also four extragalactic type I X-ray bursters that double the known neutron-star population in M31. This algorithm is a powerful tool to promptly detect variable sources in XMM-Newton observations. EXOD detects fast transients that other variability tests classify as non-variable due to their short duration and low number of counts. Finally, EXOD allows us to detect and identify the nature of rare compact objects through their variability. We demonstrate this through the discovery of four extragalactic neutron-star low mass X-ray binaries, doubling the number of known neutron stars in M31.

3.1 Introduction

XMM-Newton has been inspecting the X-ray sky since its launch in 1999. Its three on-board telescopes, each with a geometric effective area of $\sim 1550\,\mathrm{cm}^2$ at 1.5 keV, are combined to provide the largest total collecting area of any X-ray telescope launched (Jansen et al. 2001). This has allowed for the compilation of a very large catalogue of X-ray detections. We used the eighth data release of the *XMM-Newton* catalogue, 3XMM-DR8, which contains 775,153 detections (Rosen et al. 2016)[1].

The large majority of these detections are of steady, unvarying sources. Compared to this static sky, the dynamic sky remains relatively unexplored. Many violent and rare variable phenomena such as tidal disruption events and X-ray bursters can be observed, which can be used for studying (astro)physics, including strong gravity and thermonuclear explosions. The X-ray regime is one part of multi-messenger time-domain astronomy, which focuses on this dynamical sky. The detection of cosmic rays and neutrinos (e.g. Hirata et al. 1987), of extragalactic bursts in radio (Lorimer et al. 2007), type Ia supernovae in the optical (e.g. Riess et al. 1998), and of double neutron star mergers in gravitational waves (Abbott et al. 2017) show that transient surveys are of vital importance to understand the physics behind the explosive universe.

XMM-Newton was not built as a transient detector. However, the high sensitivity and high time resolution of its European Photon Imaging Cameras (EPIC) allow it to record fast X-ray transients. Nevertheless, the detection of these transients and potential follow-up with other instruments depends on the sensitivity and performance of the variability detection pipeline. The pipeline processing for the 3XMM catalogue includes such a variability study, for sources with total EPIC counts (including the detectors pn, MOS1 and MOS2) exceeding 100.

The variability of these brightest sources is studied through two complementary tests; the first is a simple χ^2 test where the time series are fitted to a constant model. The time bin width is the lowest integer multiple of 10 s for which the average number of counts is ≥ 18 counts/bin. Sources with a χ^2 probability of constancy $\mathrm{P}(\chi^2) \leq 10^{-5}$ are flagged as variable (Watson et al. 2009). The second method is the study of the fractional variability amplitude, F_{var}, as described in Rosen et al. (2016) and references therein. F_{var} is given by the square root of the excess variance normalised by the mean count rate. This provides the scale of the variability. Although F_{var} is given in the catalogue, it is not used to flag sources as variable.

The χ^2 statistic can be applied to binned data sets where the observed number of counts deviates from expectation approximately following a Gaussian distribution. Cash (1979) showed that when the number of counts per bin falls below ~10-20, the χ^2 statistic becomes inaccurate. This justifies the requirements for the light curve generation in *XMM-Newton*'s pipeline.

There are, however, some drawbacks to this technique. Faint, variable sources can easily go unnoticed, since their time series are not generated. Additionally, sources that are variable on timescales shorter than the duration of the time bins will not be flagged as variable, since one single data point with a very high count rate is likely to be disregarded by the χ^2 variability test.

[1] 3XMM-DR8 website: http://xmmssc.irap.omp.eu/Catalogue/3XMM-DR8/3XMM_DR8.html

A number of objects can display variability within a single *XMM-Newton* observation. These can be distinguished in multiple ways. In a sample containing stars, AGN and different compact object systems, the compact objects show a higher X-ray flux variation factor (Lin et al. 2012). Furthermore, the features in the light curves are usually specific to a particular type of object. Thus, a number of source classes have previously been detected and identified:

Type I X-ray bursts are outbursts lasting from seconds to minutes, emitted by low mass X-ray binaries (LMXB) with an accreting neutron star (NS; e.g. Parikh et al. 2013). One subclass of High mass X-ray binaries (HMXB) called supergiant fast X-ray transients (SFXT) are HMXB with a neutron star accreting the winds of its companion. These sources can present multiple X-ray flares that are visible for a few hours (see Sidoli 2013, for a review). Cool late-type stars can show flares, due to magnetic reconnection. These flares can last from minutes to hours and show an exponential rise and decay (e.g. Pye et al. 2015; Favata et al. 2005; Imanishi et al. 2003). Cataclysmic variables (CVs) show modulated light curves with periods between ~ 0.2 and ~ 1.5 h (e.g. Kuulkers et al. 2006; Southworth et al. 2011).

While some sources from the list above have been previously detected with *XMM-Newton*, a more sensitive algorithm could detect a higher number; improving population statistics, and increasing the chance of detection.

We also aim to detect rarer transients such as short gamma ray bursts (SGRBs), the electromagnetic counterpart to NS mergers, as well as long gamma ray bursts (LGRBs), believed to be emitted from the jets formed during the death of massive stars in core-collapse supernovae. Whilst GRBs generally have spectra that peak in the gamma-rays, the spectra are broadband and can also be observed in X-rays. For distant GRBs, the peak luminosity will be redshifted into the *XMM-Newton* energy range. If a GRB with a small angle between the jet and the line of sight is within the field of view (FoV) of an *XMM-Newton* observation, it could be detected as a very faint, short transient. A handful of distant LGRBs has been detected by the *Swift* mission (Salvaterra 2015, and references therein).

Short X-ray bursts may accompany fast radio bursts (FRBs) – the rare, extragalactic, millisecond radio transients. Such a connection is implied by the behaviour of Galactic magnetar SGR 1935+2154. That source is capable of emitting short FRB-like radio bursts with fluences as high as a MJy ms (Bochenek et al. 2020; CHIME/FRB Collaboration 2020) These radio bursts are accompanied by bright, short X-ray bursts (Mereghetti et al. 2020b; Tavani et al. 2020a; Zhang et al. 2020b; Ridnaia et al. 2020). Extragalactic FRBs may thus potentially also be accompanied by a transient X-ray counterpart (e.g. Kaspi & Beloborodov 2017; Metzger et al. 2019). Previous follow-up efforts and archival data searches so far have not found convincing X-ray counterparts to extragalactic FRBs (Scholz et al. 2016; Bhandari et al. 2018; DeLaunay et al. 2016). More observations, more sensitive instruments, or perhaps more sensitive algorithms applied to existing instruments could offer the step needed to detect a counterpart or to set more stringent limits on their existence.

Variability is thus a feature that can be used as a diagnosis tool to shed light upon the nature of a source and potentially allow the identification of new and rare compact objects. Hence, there is a

need for new algorithms that are computationally cheaper than the generation of individual light curves that can be applied to faint sources.

Previous attempts to detect faint transients in *XMM-Newton* data include the *EXTraS* project[1], which searched for transients and periodic variability (De Luca et al. 2015; Novara et al. 2020). The transient detection method employed there combines a source search on short time intervals with an imaging technique. The time intervals are defined through a modified Bayesian block algorithm (Scargle 1998; Scargle et al. 2013) that finds count-rate changes in the EPIC observations and runs a source detection algorithm on the time-resolved images.

In this paper, we present EXOD, a new algorithm that aims to detect short, faint transients by computing the variability of the whole FoV, then by detecting variable sources through an imaging technique. This can be used to promptly spot interesting sources that vary on timescales as short as 3 s. Due to the difference in the methodologies between *EXTraS* and EXOD (see Section 3.3), particularly in the way the time windows are defined and the stage at which the source detection algorithm is run, we expect to find different sources.

The remainder of this paper is organised as follows: Section 3.2 explains the data we used and how it was reduced. Section 3.3 details the EXOD algorithm and the variability detection technique as well as the comparison with other variability tests. Section 3.4 discusses the results and reports the detection of new variable sources. In Section 3.5, we discuss our work and potential applications and we give our conclusions in Section 3.6.

3.2 Data

3.2.1 Observation mode

We analysed the set of EPIC-pn observations contained in the 3XMM-DR8 catalogue performed in the full frame mode. The full frame mode was chosen for the following reasons: (1) The FoV covers a large surface of $27.2' \times 26.2'$ and thus contains a higher number of sources than other EPIC-pn observation modes. (2) A time resolution of 73.3 ms allows the study of short timescale variability. (3) EPIC-pn receives about twice the number of photons that fall on EPIC-MOS (Strüder et al. 2001b; Turner et al. 2001). These properties are key to finding new variable, faint sources. We analysed a total number of 5,751 observations with these characteristics.

3.2.2 Filtering observations

We filtered the EPIC FITS pn IMAGING mode event list (PIEVLI) files using the Science Analysis System (SAS) version 16.1.0[2] with the following criteria:

We limited the energy range to 0.5–12 keV. We filtered out the 0.2 – 0.5 keV energy range to avoid the spurious detections caused by low-energy noise (Watson et al. 2009).

In order to ignore high background count rates from soft proton flares we removed periods in which the 10 – 12 keV count rate exceeds a certain threshold. We tested the *XMM-Newton* Science

[1] http://www.extras-fp7.eu/index.php
[2] https://xmm-tools.cosmos.esa.int/external/xmm_user_support/documentation/sas_usg/USG/

Analysis System (SAS) task `bkgoptrate` for this. It computes the rate maximising the signal to noise ratio for a given source. However, we found that the rate computed by this function is not optimal to detect faint variable sources. Although this rate increases the number of counts per source, the sources present an extrinsic variability due to the proton flares.

Figure 3.1 is an example, showing the background count rate in observation 0112370801. One can see that the `bkgoptrate` optimal background rate (*green* solid line) is too high to filter out several background flares. Choosing this rate would thus imply keeping a contaminated observation, affecting the variability detection. The count rate recommended by the SAS for filtering EPIC-pn observations, $0.4\,\mathrm{cts\,s^{-1}}$ (pink dotted line) filters all the high background periods of this observation. However, this value could filter too many photons in the case of an observation with a higher low background rate or a source showing an extremely bright outburst. We thus chose a threshold of $0.5\,\mathrm{cts\,s^{-1}}$ (orange dashed line). This threshold filters most of the background flares that are also filtered with $0.4\,\mathrm{cts\,s^{-1}}$. The steepness of the light curve at the beginning and the end of the background flares implies that the difference of the good time intervals between count rates of 0.4 and 0.5 will be small. The threshold of $0.5\,\mathrm{cts\,s^{-1}}$ was adopted after testing it on $\sim$700 observations. Whilst a slightly refined value may be better for some observations, this value was found to be appropriate for the large majority of the observations studied. We used the extra precaution of removing all the time windows (see Section 3.3.1.1 for definition) where a background flare starts or ends to avoid contamination.

We used the SAS task `tabgtigen` with a count rate of $0.5\,\mathrm{cts\,s^{-1}}$ and time bins of 100 s to generate the good time interval (GTI) file and filtered the bad time intervals from the observations. Additionally, we applied the standard filters `#XMMEA_EP` and `PATTERN<=4`.

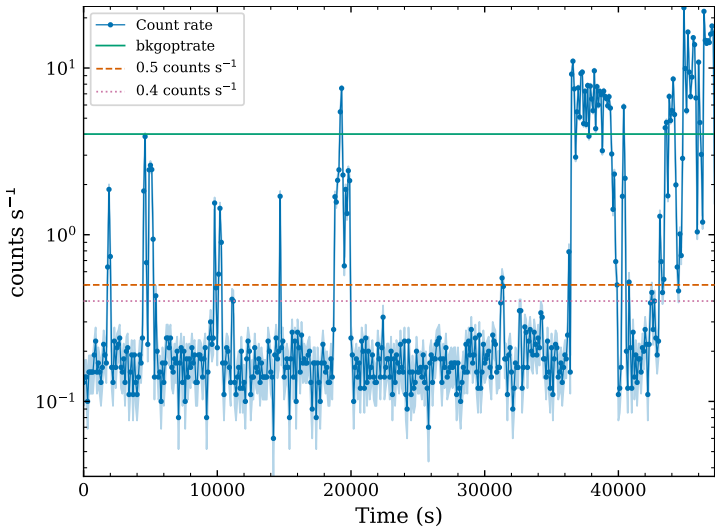

Figure 3.1: Count rate of observation 0112370801 between 10 – 12 keV as a function of time since the beginning of the observation. The vertical axis is in logarithmic scale and we use a time binning of 100 s. *Green* solid line: optimal rate as computed by `bkgoptrate`, in this case $\sim 4\,\mathrm{cts\,s^{-1}}$. *Orange* dashed line: $0.5\,\mathrm{cts\,s^{-1}}$. *Pink* dotted line: $0.4\,\mathrm{cts\,s^{-1}}$.

Table 3.1: Input parameters of the variability computation.

Symbol	Parameter	Accepted Values	Default Value	Function
DL	Detection level	$\Re^+$	10	Level above which an area is considered as being variable. A lower value allows the detection of more sources, but a higher proportion of the detected sources will be non-variable.
TW	Time window	$\Re^+$	100 s	Duration of the time windows. It is also the minimal timescale of the variability that can be explored.
b	Box size	[3,5,...,63]	5	Length in pixels of the detection box, limited by the size of the CCDs. It determines the extension of the variable area that we want to detect.
r_{GT}	Good time ratio	[0;1]	1.0	Critical (good time)/TW above which the time window will be taken into account. Choosing 1.0 will remove all time windows that have been partially or entirely contaminated by soft proton flares.

3.3 Method

3.3.1 The algorithm

Since the light curve generation is necessary for the variability computation of the sources in *XMM-Newton*'s pipeline, only the variability of the brightest sources is studied. In order to detect fast, faint transients coming from fainter sources within *XMM-Newton* observations, the whole FoV should be explored.

We developed EXOD, the EPIC-pn *XMM-Newton* Outburst Detector, an algorithm that detects fast and faint transients by computing the variability of every single EPIC-pn pixel from each observation, as we present below. The code is publicly available online[1].

The algorithm computes the variability as explained in the following section using the previously generated filtered events file and GTI file. The required input parameters used for the variability detection can be found in Table 3.1.

3.3.1.1 Variability computation

The variability computation can be divided in the steps depicted in Fig. 3.2 and explained next: (1) First, we extract the time and pixel of arrival of every event detected during the observation from the events file. (2) Secondly, photons detected in a 3×3 square around each pixel are added together to increase the signal-to-noise ratio and to reduce stochastic variability. (3) Next we bin the events per pixel into time windows (TW), whose duration we give as an input. (4) We then extract the data from the GTI file. (5) We compute the good time ratio of each time window, that is, the time belonging to the GTI of the considered time window divided by the duration of the time window. (6) Next we divide the number of counts per time window by the good time ratio. Only those time windows with the good time ratio above a critical value, r_{GT}, will be considered. This will normalise the number of photons that have been detected during a time window that has been shortened by the bad time periods. We note that the r_{GT} default value is 1 (see Table 3.1). This removes every time window that has been partially or totally contaminated by background

[1] https://github.com/InesPM/EXOD

flares, avoiding detecting these flares as variable sources. (7) Finally, the variability $\mathscr{V}$ of each pixel is given by:

$$\mathscr{V} = \begin{cases} \max(\mathscr{C}_{\max} - \tilde{\mathscr{C}}, |\mathscr{C}_{\min} - \tilde{\mathscr{C}}|)/\tilde{\mathscr{C}} & \text{if } \tilde{\mathscr{C}} \neq 0 \\ \mathscr{C}_{\max} & \text{if } \tilde{\mathscr{C}} = 0 \end{cases} \tag{3.1}$$

where $\mathscr{C}_{\max}$ and $\mathscr{C}_{\min}$ are, respectively, the maximal and minimal number of counts per time window for that pixel and $\tilde{\mathscr{C}}$ is the median number of counts over the time windows for the pixel. The expression $\mathscr{C}_{\max} - \tilde{\mathscr{C}}$ targets sources presenting outbursts, while $|\mathscr{C}_{\min} - \tilde{\mathscr{C}}|$ points to those sources with a period of lower flux. Considering the maximum between the two allows the detection of a wider variety of phenomena. The division by the median $\tilde{\mathscr{C}}$ gives the variability relative to the flux. The algorithmic notation is given in Appendix 3.C.

3.3.1.2 Variable source detection

The variable areas are detected with the sliding box technique, where a box of size $|b|^2$ pixels will move through all the pixels of the observation, with b representing an odd number.

This procedure has been broadly used in X-ray observatories, for instance the *Einstein* observatory (Gioia et al. 1990), *ROSAT*[1], and currently in *Chandra* (Calderwood et al. 2001) and *XMM-Newton* (Watson et al. 2009).

We first compute the median variability value $\tilde{\mathscr{V}}$ (Eq. 3.1) for all detector pixels. We next calculate the sum of the variability in a box of size $|b|^2$ to obtain $\mathscr{V}_{\text{box}}$. The central position of the box is then shifted to the contiguous pixel and the process is repeated until $\mathscr{V}_{\text{box}}$ has been calculated for every available position within the detector (based on Watson et al. 2009). The variability of a box $\mathscr{V}_{\text{box}}$ centered on the pixels x,y is given by the following equation:

$$\mathscr{V}_{\text{box (x,y)}} = \sum_{i=x-(b-1)/2}^{x+(b-1)/2} \sum_{j=y-(b-1)/2}^{y+(b-1)/2} \mathscr{V}_{i,j}, \tag{3.2}$$

Where b is the length of the box in raw pixel units. $\mathscr{V}_{\text{box}}$ will not be computed at the border of the CCDs, since the size of the box would be smaller than $|b|^2$.

If for a certain box $\mathscr{V}_{\text{box}}$ is above a chosen threshold, we consider the pixels contained in the box as variable. The value of this threshold is given by the following expression:

$$\mathscr{V}_{\text{box}} > DL \times |b|^2 \times \tilde{\mathscr{V}}, \tag{3.3}$$

where DL is the detection level. When two consecutive boxes are variable, the pixels of both boxes are joined into a single variable area.

The variable sources are located at the centre of the variable areas. The position of the (X,Y) coordinates in raw pixels is the mean value of the position of the pixels belonging to the variable areas. The raw pixel position and the number of the CCD of the variable sources are given

[1] https://heasarc.gsfc.nasa.gov/wgacat/

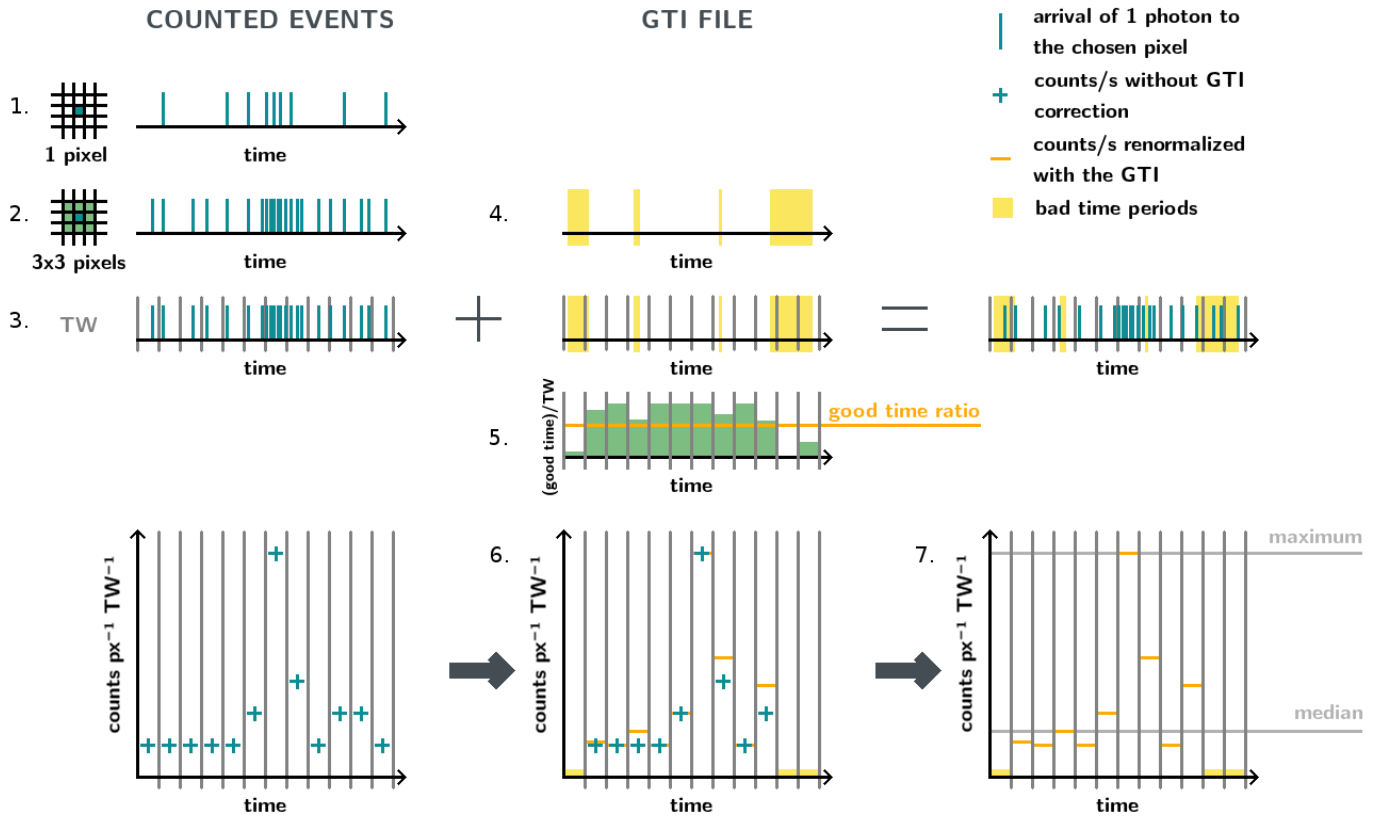

Figure 3.2: Diagram of the variability computation with the different stages of the algorithm. The vertical *blue* lines indicate the arrival time of the photons during the observation. The vertical *gray* lines represent the time bins. The *blue* crosses indicate the counts per time window per pixel without filtering for the GTI. The *yellow* shaded regions indicate the time periods contaminated by soft proton flares. The *green* rectangles show the good time over the duration of the time window for each time window. The *orange* horizontal lines show the counts per time window per pixel after renormalising with the GTI, and the yellow horizontal lines show the time windows that will not be taken into account because they are below the good time ratio. Finally, the *gray* horizontal lines indicate the maximum $\mathscr{C}_{max}$ and the median $\tilde{\mathscr{C}}$ counts that will be used to compute the variability.

Table 3.2: Parameters used for the variability computation, with Good Time Ratio $r_{GT} = 1.0$. For each time window (TW), the three respective detection levels (DL) were used, whereas the two given box sizes b were used for all the TW-DL combinations.

TW (s)	3	10	30	100
DL	5	6	7	8
	6	7	8	9
	7	8	9	10
b (pixels)	3		5	

as an output, as well as the distance from the centre to the outermost pixel belonging to the variable area, in pixels. We do not consider sources detected in CCD=4, RAWX=12; CCD=5, RAWX=12; CCD=10, RAWX=28 since these pixels are known to be damaged (Strüder et al. 2001a) and produce a high number of spurious detections.

3.3.2 Detection parameters

We applied the algorithm to the observations defined in Section 3.2 with different time windows, detection levels, and box sizes. We thus empirically determined the optimal parameters for finding most variable sources, while minimising spurious detections. The different values of the time windows check for variability on different timescales. We chose $TW = 3, 10, 30, 100$ s to optimise time variability with computation time.

We performed these variability tests with the parameters given in Table 3.2 and $r_{GT} = 1.0$ on a subset of 2,284 observations. These are the observations that were included in the incremental releases of the 3XMM-DR7 and 3XMM-DR8 catalogs. We used the optimal parameters obtained to analyse the light curves of the sources detected in the remaining observations.

3.3.3 Comparison with other variability tests

In order to determine the robustness of the algorithm, we needed a comparison with the existing variability tests. To do so, we determined the fraction of false positives as well as the fraction of false negatives.

To measure the fraction of false negatives, we performed a positional cross-match of the EXOD sources with the 3XMM-DR8 sources flagged as variable. For this we used the catalogue manipulation tool Topcat (Taylor 2005).

To measure the fraction of false positives, we first recreated for reference the standard variability measure of the EXOD-detected sources. We generated the light curve of the detected sources with the SAS function `evselect` and subsequently computed the probability of constancy with the χ^2 and Kolmogorov-Smirnov tests, P(χ^2) and P(KS) respectively, with the FTOOLS Xronos function `lcstats`. Comparisons with other test are found in Pastor-Marazuela (2018)[1]. We used the HEASOFT version 6.22.1 (Blackburn 1995).

[1] Searching for fast transients in *XMM-Newton* data. Master thesis: https://www.uva.nl/en/profile/p/a/i.pastormarazuela/i.pastor-marazuela.html

The χ^2 test can only be applied to data with a Gaussian distribution, which occurs when the number of counts per bin is $\gtrsim 18$. As we generated light curves regardless of the number of counts, not every light curve satisfies this criterion. We thus additionally apply the KS test, which makes no assumptions about the binning of the data and can be safely applied to sources with low counts[1].

If P(χ^2)$\leq 10^{-4}$ or P(KS)$\leq 10^{-4}$, we consider the source to be variable. P(χ^2)$\leq 10^{-4}$ gives a $> 4\sigma$ confidence level on the variability detection with the χ^2 test. We define the robustness of the algorithm as the ratio of sources detected with EXOD that are variable according to at least one of the variability tests χ^2 or KS.

The light curves were extracted automatically by giving the position in raw pixel units of the detected variable source, then using a set of SAS tasks described below that optimise the position and radius of the source. We used the TW duration as the bin size of the light curves. For these tasks, the SAS summary file and the EPIC FITS global background time series (FBKTSR) are needed additionally to the filtered observation and the GTI file.

Since we noted that extended sources, bright sources, or out-of-time (OOT) events can trigger spurious detections of variability within an observation, we only applied the automatic light curve generation when the number of detections per observation was less than six.

We determined this six-source threshold empirically, by noting that less than $\sim 2.6\%$ of the observations have more than five variability detections, and that these are usually spurious detections. However, we visually inspected the variability plots (such as the one shown in Fig. 3.9) of the fields of view with more than five detections in order to avoid missing interesting candidates.

Source region: From the raw pixel and CCD of the detected variable sources, we can determine the position in sky pixel space with the SAS task `ecoordconv`. The position and the radius of the source are corrected with the function `eregionanalyse` with `backval=0.1`. This function returns a circle containing 90% of the energy of the source.

It is known that the shape of the point spread function (PSF) in the EPIC-pn detector depends on its angle with respect to the centre of the detector (Read et al. 2011). Whereas a centered (on-axis) source is well approximated by a circular region, a non-centered (off-axis) source is elongated due to off-axis aberration (astigmatism), giving a larger, energy-dependent radius. Although elliptical regions increase the signal to noise ratio of the light curves, we chose circular extraction regions since this option is a sufficiently good approximation, especially when dealing with faint sources for which only a small number of pixels will be above the background level. We also find it to be more reliable in such an extensive study to automatically extract the counts of all the sources and find nearby background extraction regions. The selection of elliptical regions becomes of greater importance when performing spectral analyses.

Background region: To subtract the background from the source light curve, we use background regions determined with the SAS task `ebkgreg`. This task searches the optimal background region following only geometrical criteria. To avoid selecting a region containing sources, we extract the background from a filtered events file where we have removed the sources. We obtain the

[1] Kirkman, T.W. (1996) Statistics to Use. http://www.physics.csbsju.edu/stats/

positions of all the sources of the observation from the FBKTSR file. We choose the same radius as for the source region.

3.3.4 M31

There are some fields observed by *XMM-Newton* where we expect to detect more than five variable sources. In this work we have decided to focus on one specific field, M31. Because of its crowded field, M31 required analysis that was more manual than described above.

M31 is located at ~ 0.78 Mpc[1], and is the nearest spiral galaxy to the Milky Way. With an angular size of $\sim 200' \times 80'$, EPIC-pn's FoV covers its central region. This makes the study of M31 very interesting, since one observation contains a high number of extragalactic sources.

There is a total of 48 *XMM-Newton* EPIC-pn observations of M31 that have not been strongly polluted by high background flares. The high density of sources required selecting the extraction regions manually. In most observations, the number of detected sources exceeds the limit of five. We have thus made an exception for this limit for M31, where we expect to detect a higher number of variable sources.

3.3.5 Fast Radio Bursts

We know EXOD is sensitive to bursts lasting up to 100s (see, Sect. 3.4.3). There are now both theories and observations linking fast radio bursts (FRBs) with magnetars; and the latter are known to show X-ray flares lasting up to a few seconds. FRB theories such as those put forward by Beloborodov (2017) and Metzger et al. (2017) require young magnetars as the power source. Meanwhile, observations of SGR 1935+2154 show that Galactic magnetars can emit energetic flashes that show as both FRB-like radio bursts (Bochenek et al. 2020; CHIME/FRB Collaboration 2020) and X-ray bursts (Zhang et al. 2020b), simultaneously.

We thus tested whether EXOD could again find variability missed by standard tools. We reanalysed observations 0792382801 and 0792382901 of FRB 121102, the first known repeating FRB (Scholz et al. 2017). FRB 121102 was highly active in radio during these *XMM-Newton* observations (Chatterjee et al. 2017; Law et al. 2017), but Scholz et al. (2017) found no transient X-ray counterparts. Using our same optimal parameters defined in Section 3.3.2, we also found no sign of variability.

The energy upper limit estimates that Scholz et al. (2017) set on the X-ray emission of $10^{45} - 10^{47}$ erg at a distance of 972 Mpc (Tendulkar et al. 2017), remains several orders of magnitude lower than that of GRBs. The detection of an FRB afterglow with *XMM-Newton* could be possible only if its host galaxy was located at a lower redshift. Following up on non-repeating low-DM FRBs, such as FRB 110214 at 169 pc cm^{-3} (Petroff et al. 2018), could help to achieve a detection, especially if possible near real-time (cf. Maan & van Leeuwen 2017).

[1] M31 properties obtained from NASA/IPAC Extragalactic Database (NED): https://ned.ipac.caltech.edu/byname?objname=M31. The given distance is an average of the published distances.

3.4 Results

3.4.1 Detected sources

In this section, we present the sources EXOD detected in our set of observations. This includes the detected variable sources for which the light curves were automatically generated (less than six detections per observation) as well as those with more than five detections that we determined as non-spurious through a visual inspection.

There were 221 observations with more than five variability detections, with only 20 containing non-spurious detections. Among these non-spurious detections, we generated the light curve of 83 sources. We include these sources in the following analyses.

3.4.1.1 Variability

In Fig. 3.3, we show the results obtained after applying EXOD as described in the previous sections. By looking at the test parameters, one can see that the number of detected sources increases with decreasing detection level DL. Decreasing DL also increases the fraction of non-variable sources according to the χ^2 and KS tests, although this is accompanied by an increase of the net number of variable sources. In most cases a 3×3 pixel box results in a slightly higher fraction of variable sources than a 5×5 box.

In order to detect the highest possible number of previously unknown variable sources, we chose a low detection level with a box size of 3×3 pixels to analyse the full data set, accepting the accompanying increase in false positives. These final optimal parameters are given in Table 3.3, together with the number of sources detected among the 5,751 observations. The results are plotted in Fig. 3.3 as filled symbols, with the same color code as the test observations.

From these results, we can determine that the robustness of the algorithm as defined in Section 3.3.3 is between $\sim$60 and 95% and depends on the chosen parameters. For the optimal parameters, $\sim$84% of the sources are deemed to be variable using the χ^2 and KS tests for a time window $TW = 100$s. This percentage decreases when TW decreases, and reaches $\sim$64% for $TW = 3$s. EXOD is thus more robust for longer time windows.

The remaining fraction of sources are usually detected in short or highly polluted observations, notably when the net exposure time is below 5000 s, and can be clearly identified. We thus advise visually inspecting the results when using EXOD for such short exposure observations.

Although we perform a large number of independent trials (especially the number of TWs, in four trials $\times$ number of detection boxes), statistical fluctuations of sources that are not intrinsically variable are not a significant cause of false positives, given the high minimum detection levels we require.

When applying the optimal parameters to the whole set of observations, we find the fraction of non-variable sources to be higher than that in the test observations. We are investigating the cause for this but we suspect the later date of the DR7 and DR8 observations to play a role, as the average duration of the later observations has increased. Given the longer duration, the number of flares that can be present in an observation increases. In a shorter observation, the lower number

Table 3.3: Optimal parameters and detected sources. Parameters used to generate the light curves of all the observations, number of sources detected and percentage of variable sources according to the χ^2 and KS tests. $r_{GT} = 1.0$. Bottom line: sum of the detected sources and total number of sources after auto-correlation.

Property	Value			
TW (s)	3	10	30	100
DL	5	6	7	8
b (pixels)	3	3	3	3
Detected sources	1459	1707	1795	1831
Variable sources (%)	64.3	69.2	73.4	83.7
Sum 6792		Total		2961

of counts may give rise to a higher number of spurious detections due to the aforementioned outliers of the Poissonian fluctuations.

The sum of the sources detected with the optimal parameters is 6,649. Since some of the sources are detected with different time windows, we performed an auto-correlation on the position of the sources with Topcat. We searched for internal matches in a radius of $15''$ around the location of each source. This radius corresponds to the Half Energy Width (HEW) of EPIC-pn at 1.5 keV (Strüder et al. 2001b). After removing the duplicated selections, we obtain a grouped list with a total number of 2,961 sources detected among the 5,751 observations.

The *XMM-Newton* pipeline finds slightly more variable sources because it searches longer timescales than EXOD. Sources varying more slowly than our longest timescale of 100 s might not be detected.

Although EXOD may miss some variables found by the standard pipeline, it does find variable sources this pipeline missed. We investigate these in Sect. 3.4.3.

3.4.1.2 Cross-correlation with other catalogues

To determine the nature of the EXOD-detected sources, we queried them by position in the Simbad database[1] (Wenger et al. 2000), using `astroquery`. This returns the name, location and source type of the nearest catalogued source. We allowed a $15''$ radius around the detection coordinates. We then placed the sources in one of the categories listed in Table 3.4. These include six physical classes, one group of known extended sources, and two categories of unknowns: the ‘‘no identification’’ class for previously detected sources whose type is not known; and the ‘‘without counterpart’’ class where no detection has previously been made at all. If two sources were identified with the same Simbad entry, only one is counted. For that reason, the number of classified sources in Table 3.2 (2,961) differs from the total number of sources in 3.4 (2,907).

In a preliminary cross-correlation with Simbad, we found $\sim 1,200$ classified as ‘‘without counterpart’’. A visual inspection of these sources revealed that most of these belonged to one of the following categories: (1) Out of Time events, (2) detections in the PSF of a bright source,

[1] Simbad: http://simbad.u-strasbg.fr/simbad/

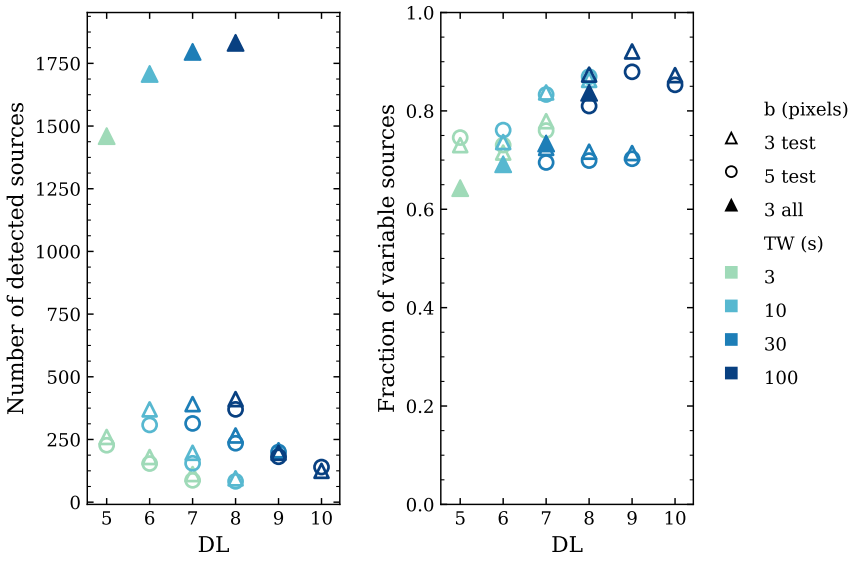

Figure 3.3: Properties of the sources detected by EXOD. Test observations with the detection parameters listed in Table 3.2: empty markers. All observations with the parameters in Table 3.3: filled markers. **Left:** Number of detected sources as a function of DL. **Right:** Fraction of sources confirmed to be variable through the χ^2 and KS tests among the detected ones as a function of DL. The colors correspond to different TW: light green for $TW = 3$ s, light blue for $TW = 10$ s, medium blue for $TW = 30$ s and dark blue for $TW = 100$ s. The shapes represent the box size: triangles for $b = 3 \times 3$ pixels and circles for $b = 5 \times 5$ pixels.

(3) detections in an extended source and (4) hot pixels. We thus cross-matched these with the 3XMM-DR8 catalogue with Topcat in a $15''$ radius around the detection position and the radius of the sources given in the catalogue to take into account their extension. The sources matching a 3XMM-DR8 source were added to the ‘‘no identification’’ (point-like sources) or the ‘‘extended sources’’ class ($> 6''$ radius). This reduced the number of ‘‘without counterpart’’ to ~ 400. A visual inspection of the remaining ‘‘without counterpart’’ sources showed that these were spurious detections.

Given our search criteria, we could have expected to find new sources through the variability search if they were faint and short enough to be drowned in the background noise and would thus not be included in the regular XMM catalogue. Whilst no completely new sources were identified here, further modifications to the detection parameters could still reveal such objects.

In Fig. 3.4, we show the result of the cross-correlation with Simbad for the four sets of parameters as thin bars. The cross-correlation of the grouped sources with Simbad and 3XMM-DR8 is shown as thick bars with a solid black contour. The cross-correlation only with Simbad is plotted as dashed black contours for comparison.

If we remove the number of spurious detections from our set of detected sources, we obtain a net count of 2,536 variable sources detected with EXOD.

Table 3.4: Source category classification. Naming of the categories used in Fig. 3.4, with a description of the objects included in each category and the number of sources detected for each.

Category	Description	Number of sources
Compact binaries	Cataclysmic variables, X-ray binaries, ULXs, novae.	153
Stars	Stars, pulsars	515
Stellar binaries	Binary stellar systems	66
ISM	Interstellar medium	66
Galaxies	Galaxies, AGNs, QSOs	504
Multiple objects	Galaxy clusters, groups of galaxies, stellar clusters or associations.	80
Extended sources	The angular distance d to the catalogued source satisfies $10'' \leq d \leq 15''$ and it belongs to the category ISM, galaxies or multiple objects.	430
No identification	Previously known source of unknown type.	668
Without counterpart	No association has been found within $15''$.	425

We can compare this number to the number of variable sources in the catalogue. 3XMM-DR8 contains 775,153 sources. 438,342 of these sources were detected in observations that we have analysed. 102,498 of these sources have generated time series. Finally, 3,418 sources are catalogued as variable, compared to the net 2,536 sources in this work.

However, the number of sources that are classified as variable in 3XMM-DR8 and EXOD simultaneously is 777. This corresponds to a false negative rate of 77.3%. The high rate of false negatives was expected, since we are targeting a very specific kind of short-term variability, and sources varying on longer timescales are not detected. Nevertheless, the light curve of 688 (27.1%) of the EXOD variable sources were not generated in 3XMM-DR8, so there was no previous available information about their variability. Lastly, Table 3.3 shows that EXOD detects a high number of variable sources according to the χ^2 or the KS tests, indicating that we are sensitive to a variability that the tests applied in *XMM-Newton*'s pipeline are not always adapted to detect.

3.4.1.3 Detected variability

Although EXOD was specifically designed to detect faint, short outbursts, the inspection of the detected sources showed that it is able to detect a large diversity of variable phenomena. In Fig. 3.5 we show a selection of six light curves from different variable sources. These light curves were extracted automatically. We also plot $\tilde{\mathscr{C}}$ and $\mathscr{C}_{max}$ to compare the light curves to the value of the variability obtained with EXOD.

These sources differ in their variability timescales (short and long flares), periodicity or aperiodicity, and speed of decline and rise. They also span a range of physical classes. In Fig. 3.5, we present the following sources: in (1), an ultra compact binary showing periodic oscillations whose maximal values seem to increase during the observation (Steeghs et al. 2006). In (2), a high proper motion star showing a flare during the observation (Kirkpatrick et al. 2016). In (3), we can see flares from a supergiant fast X-ray transient, aperiodic with varying maxima (Sidoli et al. 2012). In (4), an eclipsing binary of beta Lyr type (Bruch 2017). In (5), we see a magnetic cataclysmic variable whose periodic variability is due to variation in the opacity of the accretion curtain that comes into view as the system rotates (Mason 1985; Fuchs et al. 2016). In (6), an LMXB presents first an eclipse during which the flux decreases, then a type-I X-ray burst (in 't

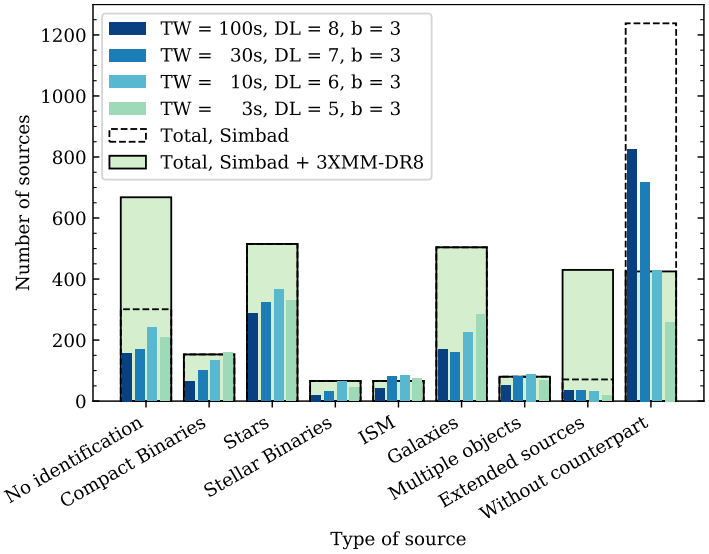

Figure 3.4: Classification of the sources detected by EXOD in source types. The thin bars show the Simbad association of the sources detected, from darker to lighter, with 100 s, 30 s, 10 s and 3 s respectively. The thick bars with a black dashed contour show the Simbad association of the grouped sources. The thick light green bars with a solid black contour show the Simbad association with the 3XMM-DR8 correction.

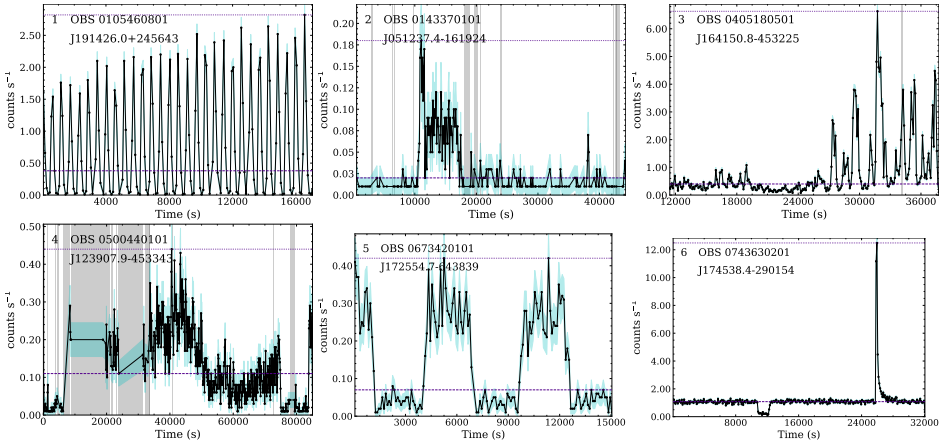

Figure 3.5: Example of light curves of sources with different types of variability detected by EXOD. The light curves are plotted in black with cyan shaded regions representing the 1σ error bars. In each plot we give the OBSID where it was detected and the 3XMM name of the source. The dashed purple line represents $\tilde{\mathscr{C}}$, the median number of counts. The dotted purple line represents $\mathscr{C}_{max}$, the maximal number of counts. The gray vertical shaded regions represent the bad time intervals. 1) RX J1914.4+2456, ultra compact binary showing periodic oscillations (Steeghs et al. 2006). 2) WISEA J051237.57-161925.2, high proper motion star showing a stellar flare (Kirkpatrick et al. 2016). 3) IGR J16418-4532, flares from a supergiant fast X-ray transient (Sidoli et al. 2012). 4) V* V1129 Cen, eclipsing binary of beta Lyr type (Bruch 2017). 5) LSQ J172554.8-643839, magnetic cataclysmic binary showing periodic eclipses (Fuchs et al. 2016) 6) AX J1745.6-2901, LMXB showing a type I X-ray burst (in 't Zand et al. 2019).

Table 3.5: Computation time fit parameters. Parameters of the fit to the computation time for the expression 3.4 for EXOD and the light curve generation.

	EXOD			light curve		
TW(s)	a	b	c	a	b	c
100	0.151	0.054	0.836	158.204	0.002	1.125
30	12.614	0.012	0.975	83.171	0.001	1.170
10	5.210	0.012	1.013	121.960	0.040	0.876
3	36.822	0.005	1.156	89.109	0.091	0.866

Zand et al. 2019). We note that we refiltered the last observation since the 0.5 cts s^{-1} `tabgtigen` threshold cut a part of the flare.

3.4.2 Computational performance of the algorithm

We measured the absolute computation time t_{comp} taken by EXOD to analyse each observation. Additionally, we measured the computation time for the generation of a single light curve for each detected variable source. Experiments were conducted on a virtual machine with 38 cores at 2.3 GHz and 320 GB of RAM. We fitted these values to a power law with the expression given in Eq. 3.4 as a function of the total duration of the GTI, t_{gti}. The result is plotted in Fig. 3.6,

$$t_{comp} = a + b \times t_{gti}^{c}, \tag{3.4}$$

where a, b, and c are the parameters determined by the fit. We computed these parameters by considering the computation time for all of the analysed observations with time windows of 3s, 10 s, 30 s and 100 s. These values are shown in Table 3.5.

The computation time of the algorithm includes the variability computation and the source detection time, whereas the computation time of the light curve includes some SAS and FTOOLS tasks that are required for the light curve generation: `cifbuild`, `eregionanalyse`, `ebkgreg`, `evselect`, `epiclccorr`, `lcstats` and `lcurve`.

The EXOD computation time increases for shorter TW, as expected given the increased number of data points. The light curve computation time is similar for 10, 30 and 100 s TW, and increases for $TW = 3$ s. For 100 and 30 s TW, EXOD can compute the variability of the whole observation before even a single light curve is generated. While for a shorter TW, the computation is slower than generating a single light curve, EXOD is faster than light curve generation when more than one source is present in the FoV.

3.4.3 Previously steady sources found to be variable

Since no completely new sources were found among the ‘‘unknown source’’ class (Sect. 3.4.1.2), we analysed the ‘‘no identification’’ sources in more detail. We collected the sources not flagged as variable by *XMM-Newton*’s pipeline and visually inspected these. We removed the sources misidentified in the automatic procedure or affected by high background rates. Since the outburst selection was based on a visual inspection, we checked the P(χ^2) and P(KS) of the pn light

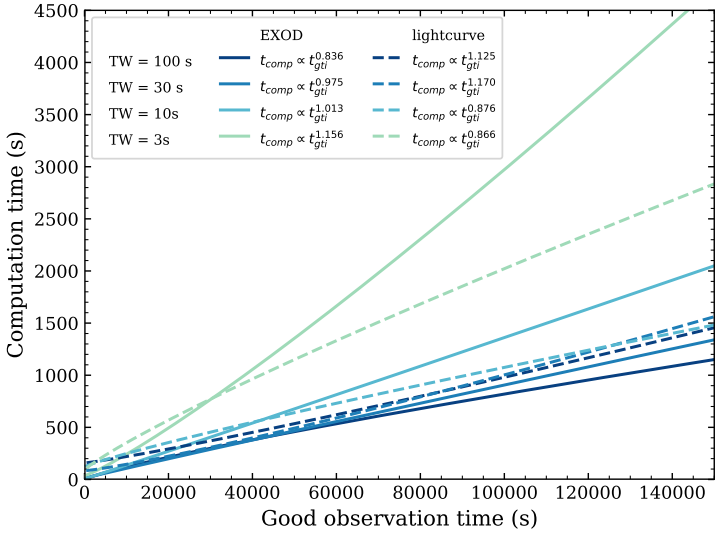

Figure 3.6: Computation time as a function of the observation time that has not been polluted by background flares (good time) fitted to a power law. The solid lines indicate the EXOD detector computation time. The dashed lines indicate the light curve computation time for one source. Blue (dark) is the computation time for a time window of 100 s, green (medium) for 30 s, orange (medium) for 10 s and pink (light) for 3s.

curves. When these probabilities of constancy were $> 10^{-4}$, we also computed them for the MOS1 and MOS2 light curves, and only kept the sources for which the P(χ^2) and P(KS) for pn, MOS1 or MOS2 were $< 10^{-4}$. We ended up with a subset of 26 sources, whose light curves are presented in Fig. 3.7. Among the M31 observations for which we manually selected the light curve extraction regions, we found a further 9 sources previously detected but not flagged as variable, plotted in Fig. 3.8. The properties of these sources are summarised in Table 3.6.

All the new transients were detected with $TW = 100$ s. Some of these transients were also detected by shorter TW, but no new sources were detected only with shorter time windows. If the duration of the transient is $\lesssim 100$ s, most of the photons will fall within the same time bin if $TW = 100$ s, increasing the signal to noise ratio. With a lower TW, the number of photons per time bin is lower, and thus has lower chances to reach the detection level. We found some interesting candidates that had been detected with $TW = 3$ s, but a closer look at these sources showed that they were damaged pixels. In particular, the pixel RAWX=1, RAWY=72, CCD=8 and the surrounding pixels were detected in ~ 20 observations as what looked like very short, bright outbursts. In some cases, these had been included in 3XMM-DR8 as real detections. The problem with the damaged pixels being detected as sources is addressed in 4XMM-DR9 (Webb et al., submitted), where there will be a flag to indicate that the source is likely to be spurious if it falls on or close to one of these pixels. Most of the sources detected with EXOD that turned out to have a probability of constancy $> 10^{-4}$ have in common that the net exposure time is less than 5000 s, that as mentioned in Section 3.4.1.1, cannot be ruled out as being due to statistical fluctuations.

While discussing the totality of the newly identified variable sources is beyond the scope of the paper, we analyse in more detail some particularly interesting candidates that show clear outbursts, some of them surprisingly undetected by *XMM-Newton*'s pipeline. In some cases this was done through the identification of a counterpart. In other cases, we extracted the spectra of the source and carried out spectral fitting using Xspec version 12.9.1p. We note however, that the low number of counts preclude us from performing a detailed spectral analysis, thus we use simple models like `powerlaw` and `bbody` to characterise the emission. We compute fluxes using the pseudo model `cflux` in Xspec. For the four transients found in M31 showing outbursts, we refine our analysis in extracting the spectra separately for the burst and the persistent emission by visually selecting the times for each period. We fit each spectra separately and compute the persistent luminosity L_{pers}, peak luminosity L_{peak} and luminosity ratio (L_{peak}/L_{pers}) to study the properties of the emission in each case, in order to put constraints on their nature. Again, due to the low number of counts, we rely on WebPIMMS[1] to compute this luminosity ratio. L_{pers} is estimated using the model of the persistent emission and the median count rate of the light curve while L_{peak} is computed with the burst model and the peak count rate of the light curve. Since the distance to M31 is known, we assume that the sources are located at the same distance, 0.78 Mpc, to obtain the luminosity. Below we give a detailed analysis and discuss the nature of the selected sources. The detailed results and the plots of the spectral fitting can be found in Appendix 3.D.

J173046.7+521846, OBS 0021750201, Source 1

This source, 2XMM J173046.8+521847 in Simbad, is classified as an active galactic nucleus (AGN) candidate (Lin et al. 2012). It shows an aperiodic variability within the duration of the observation (~ 3500 s). Long term X-ray variability (months/years) is common in AGNs, but short term variability (hours/days) has only been observed in Seyfert types 1.8 and 1.9 (e.g. Hernandez-Garcia et al. 2017 and references therein). We thus propose that this source belongs to one of those classes.

J083941.3+192901, OBS 0101440401, Source 4

Although the automatic Simbad query classified this source in the ''no identification'' group, we later found that the source is classified as a star in a cluster with a manual query of the Simbad database (Hambly et al. 1995). This source, Cl* NGC 2632 HSHJ 283 in Simbad, shows an outburst lasting ~ 3000 s, with a main burst lasting ~ 500 s. The flare was not detected by the *XMM-Newton* pipeline. Since we have not checked the totality of the source associations, we suspect there might be additional misidentifications like this one amongst the detected sources.

J015709.1+373739, OBS 0149780101, Source 6

We detected this ~ 800 s long outburst in the direction of the open cluster NGC 752, located at a distance of ~ 430 pc (Daniel et al. 1994; Giardino et al. 2008). We identify a potential blue counterpart at a distance of $0.92''$ with a magnitude of 22.83 in the Bj photographic band (NBXA027004, Lasker et al. 2008). The counterpart is point like; if it is a star in this open cluster, the X-ray transient could be a stellar flare that would correspond to a luminosity of 1.6×10^{30} erg s^{-1}.

[1] WebPIMMS: https://heasarc.gsfc.nasa.gov/cgi-bin/Tools/w3pimms/w3pimms.pl

While our paper was under review, Alp & Larsson (2020) also reported a discovery of this source that they refer to as XT 030206. The authors identify the counterpart as a starburst galaxy and infer a photometric redshift of $z = 1.17$ by fitting the SED of the optical spectrum. They conclude that the most likely explanation for this X-ray transient is a supernova shock breakout (SBO). As the SED fitting makes the analysis of Alp & Larsson (2020) more thorough we defer to their interpretation of the transient as an SBO. A new X-ray outburst of the source in the future would strengthen the case for the stellar flare.

J174610.8−290021, OBS 0202670701, Source 8

Although this observation is highly contaminated by soft proton flares, we detected a variable source with an outburst lasting ~ 100 s. Surprisingly, the light curve of this source was generated by *XMM-Newton*'s pipeline, and the burst is visible[1]. However, the source was not classified as variable by the χ^2 test, probably due to the short duration of the outburst. This source, CXOU J174610.8-290019 in Simbad, is classified as an ''X-ray source''. It is a perfect example of why EXOD is better adapted to detecting short transients than other variability tests.

This source is highly variable. Its flux decreased by more than a factor 10 between 2000 and 2004 and then was never detected again by Swift or *XMM-Newton*, even though these satellites returned to the field on numerous occasions as the source is towards the Galactic center. It has a very absorbed spectrum, typical of sources in the Galactic center, $n_{\rm H} \sim 1.6 \times 10^{23}\,{\rm cm}^{-2}$, indicating a distance of ~ 8 kpc.

The luminosity in the burst, assuming a distance of 8 kpc, reaches $\sim 10^{34}\,{\rm erg\,s}^{-1}$. Its non-flare spectrum shows indications of the presence of an emission line at ~ 6.66 keV, that we identify as an iron line or a cyclotron resonance line (See Appendix 3.D). The number of counts is too low to draw firm conclusions on the nature of this source, but it is most likely that it is an accreting neutron star in an X-ray binary. Whether it is an LMXB or an HMXB is not clear, since the search for an optical counterpart is complicated due to its location in a crowded region and the addition of the high extinction from the observed photoelectric absorption. A 100 s flare would be uncommon amongst HMXBs, but not unexpected due to the high variability that these sources present (see e.g. Chaty 2011, and references therein). A type I X-ray burst from an NS-LMXB, given the timing and spectral properties of the flare, could be an explanation.

J183658.4−072119, OBS 0606420101, Source 13

The outburst of this source lasts ~ 3000 s. It is located in a crowded region in the galactic plane and presents numerous optical/NIR counterparts within a $6''$ radius. We thus conclude that this source is most likely a star.

J081907.9−384302, OBS 0655650201, Source 15

This source shows an outburst that lasts ~ 300 s, but it is preceded and followed by higher flux periods before going back to its quiescent state. Including these periods, the outburst lasts ~ 2500 s.

[1] Automatically generated light curve of Source 8: http://xmm-catalog.irap.omp.eu/detection/102026707010084

This type of variability is also observed in stellar flares.

J175131.6−401533, OBS 0763700301, Source 24
This outburst, lasting 1000 s, is classified as a variable source in 3XMM-DR8, but it has no Simbad object associated. The source is however in a crowded region of the Galactic plane, indicating that this is most likely a star.

J113407.5+005223, OBS 0770380401, Source 25
This puzzling source has a burst that lasts only ~ 200 s, expected for type I X-ray burst, with some structure appearing in the burst. The burst spectrum appears to be fairly soft, although this is based on the joint fit of the persistent and burst emission due to the low number of counts.
Alp & Larsson (2020) presented also this source (under name XT 151219) as an SBO while our paper was under review. They associate the transient with a host galaxy located at redshift $z = 0.62$. Although the presence of four galaxies within a 15″ radius from the position of the X-ray source[1] casts some doubts on the identification of the host galaxy, Alp & Larsson (2020) find the flux and spectral properties of the source to be in good agreement with blue supergiant SBO predictions. In general, we too argue that this is likely an extragalactic source because it is located well outside the galactic plane and there is no clear bright counterpart other than background galaxies.

J022133.7−042346, OBS 0785101401, Source 26
This source shows a ~ 1000 s outburst, with a linear rise and an exponential decay. The source has a red-NIR counterpart at a distance of ~ 125 pc (Gaia Collaboration 2016; Gaia Collaboration et al. 2018; Bailer-Jones et al. 2018), indicating that it is a star.

J004307.5+412019, OBS 0109270101, Source M31-1
This outburst lasts ~ 400 s. The source, [ZGV2011] 23 in Simbad, had been previously classified as a low-mass X-ray binary (Zhang et al. 2011), but the nature of the accretor was unknown. We extracted the spectrum of the burst and the persistent emission separately, and fitted each one with an absorbed black body (tbabs*bbody in Xspec) and with an absorbed power law (tbabs*pow). The low number of photons does not allow for a clear preference for one of these models, although a power law gives a slightly better fit for both burst and persistent emission.

From persistent to burst emission, the resulting black body temperature increases from ~ 0.2 to ~ 0.3 keV, whereas the power law index Γ goes from ~ 3.3 to ~ 1.9 (See Appendix 3.D), indicating an apparent spectral hardening during the burst. From the power law indices and a count rate going from 0.01 cts s^{-1} to 0.14 cts s^{-1}, we computed a $L_{peak}/L_{pers} \sim 30$. A persistent flux of $\sim 0.3 \times 10^{-13}$ erg cm^{-2} s^{-1} scales to a luminosity of $\sim 2 \times 10^{36}$ erg s^{-1} at the distance of M31, 0.78 Mpc. This corresponds to a burst luminosity of $\sim 6 \times 10^{37}$ erg s^{-1}, around 30% of the Eddington luminosity for an NS ($\sim 1.8 \times 10^{38}$ erg s^{-1}). The presence of such a burst and the luminosity rise indicate that this is likely a type I X-ray burst and would, in this case, identify the

[1] NED query: https://ned.ipac.caltech.edu/

accretor as an NS. Such a source shows the power of EXOD since it allows one to identify the nature of a compact object.

J004215.6+411720, OBS 0650560201, Source M31-3

This outburst lasts ~ 300 s. The source is classified as an X-ray binary candidate (Lin et al. 2012). The spectral fitting seems to indicate a hardening of the source during the burst, with Γ going from ~ 1.6 in the persistent emission to ~ 0.7 during the burst, although still consistent within the error bars. These values are nevertheless hard for type I X-ray bursts, making it difficult to identify the nature of the compact object in the system. By using the aforementioned power law indices and the count rates from the persistent ($0.02\,\mathrm{cts\,s^{-1}}$) and burst ($0.13\,\mathrm{cts\,s^{-1}}$) emission, we calculate $L_{peak}/L_{pers} \sim 16$. The presence of such a burst makes the type I X-ray burster the most likely scenario, although with the present data we cannot robustly confirm its nature.

J004210.9+411248, OBS 0674210201, Source M31-6

The outburst lasts ~ 200 s, and it is followed by a higher flux period before going back to the quiescent state. Including this, the outburst lasts ~ 500 s. This type of outburst is consistent with a type I X-ray burst. The source, XMMM31 J004211.0+411247 in Simbad, where it is catalogued as an ''X-ray source'', has been detected in 44 *XMM-Newton* observations. It is so faint that its spectrum and time series have only been extracted in 3 out of 44 observations. The observation where we detected its variability was not included[1], and the source is thus not catalogued as variable.

We fitted the spectrum with an absorbed black body (tbabs*bbody) and an absorbed power law (tbabs*pow). The fitted power law gives $\Gamma \sim 2.4$ for the persistent emission and $\Gamma \sim 1.1$ at peak. However, there are only 30 available counts during the flare and the source was additionally located next to a chip gap in the pn detector, reducing the number of available photons for the spectral fitting. We obtain $L_{peak}/L_{pers} \sim 40$ for a count rate going from $0.01\,\mathrm{cts\,s^{-1}}$ to $0.13\,\mathrm{cts\,s^{-1}}$. The flare spectrum as well as the duration of the burst are all comprised within the typical values of type I X-ray bursts, and it makes this source an NS-LMXB candidate.

J004212.1+411758, OBS 0727960401, Source M31-8

This outburst lasts ~ 500 s. Previously identified as an LMXB named [ZGV2011] 27 (Zhang et al. 2011), it has been detected in 47 *XMM-Newton* observations. In order to identify the nature of the accretor, we fitted its persistent and burst spectrum with an absorbed black body (tbabs*bbody) and with an absorbed power law (tbabs*pow). This source was also located near a chip gap in the pn detector, considerably reducing the number of photons used for the spectral fitting, with only 20 available photons during the burst, and thus not enough to detect spectral shape deviations between the persistent and burst emission. However, the presence of a short burst reinforces the previous identification with an LMXB and makes an accreting NS the most likely explanation.

[1] Source M31-6: http://xmm-catalog.irap.omp.eu/source/201125704010111

Table 3.6: New variable EXOD sources. Detected with $TW = 100$ s. Column 1 gives the source ID in this paper. Column 2 the name of the source in 3XMM-DR8. Column 3 the observation ID in which the source was detected, columns 4 and 5 the RA and Dec. respectively. Column 6 the duration of the burst if there is one, column 7 in which instrument the light curve is variable (PN or MOS), and column 8 some comments, including the presence of a counterpart (ctp.). The top 30 are the general survey, the bottom 9 are in the direction of M31.

ID	Name	OBSID	RA (J2000)	Dec (J2000)	Burst dur. (s)	Var.	Comments
1	J173046.7+521846	0021750201	17:30:46.7	+52:18:46		PN	AGN candidate.
2	J160502.1+430401	0025740101	16:05:02.1	+43:04:01		PN	Short observation.
3	J191515.1+044348	0075140501	19:15:15.1	+04:43:48		PN	No Simbad object associated.
4	J083941.3+192901	0101440401	08:39:41.3	+19:29:01	3000	PN	Star in cluster.
5	J182929.4−092530	0135744801	18:29:29.4	−09:25:30		PN	Stellar flare. Off-axis detection.
6	J015709.1+373739	0149780101	01:57:09.1	+37:37:39	800	PN	Stellar flare.
7	J070509.8−112940	0201390201	07:05:09.8	−11:29:40		PN	Short observation. Star.
8	J174610.8−290021	0202670701	17:46:10.8	−29:00:21	100	PN	Type I X-ray burst candidate.
9	J010909.2+132337	0203280301	01:09:09.2	+13:23:37		PN	AGN candidate.
10	J015727.2−004041	0303110101	01:57:27.2	−00:40:41	200	PN	Short observation, off-axis detection.
11	J092927.6+504810	0556210401	09:29:27.6	+50:48:10		PN	Quasar candidate.
12	J233504.9−534751	0604870332	23:35:04.9	−53:47:51		PN	AGN.
13	J183658.4−072119	0606420101	18:36:58.4	−07:21:19	3000	PN	Close to CCD gap. Star.
14	J090150.9−015815	0655340159	09:01:50.9	−01:58:15	600	PN	Short observation. Blue ctp.
15	J081907.9−384302	0655650201	08:19:07.9	−38:43:02	2500	PN	IR-optical ctp. Star.
16	J221448.2+002707	0673000136	22:14:48.2	+00:27:07	400	MOS	QSO.
17	J090629.9−000911	0725300150	09:06:29.9	−00:09:11		MOS	Short observation. Star.
18	J090335.4+013224	0725300157	09:03:35.4	+01:32:24		PN	Short observation. Seyfert 1.
19	J011552.2−003058	0747400134	01:15:52.2	−00:30:58	300	PN	No Simbad object associated.
20	J012517.1−001829	0747410134	01:25:17.1	−00:18:29	300	PN	QSO.
21	J012351.6+000831	0747410144	01:23:51.6	+00:08:31		MOS	Short observation, highly contamined.
22	J014150.5+000754	0747430146	01:41:50.5	+00:07:54	400	PN	Optical-UV ctp.
23	J144506.2+685817	0763640601	14:45:06.2	+68:58:17	200	PN	Contamined observation. Blue ctp.
24	J175131.6−401533	0763700301	17:51:31.6	−40:15:33	1000	PN	var_flag=True. Optical ctp. Star.
25	J113407.5+005223	0770380401	11:34:07.5	+00:52:23	200	PN	No Simbad ctp.
26	J022133.7−042346	0785101401	02:21:33.7	−04:23:46	1000	PN	NIR-blue ctp. Star.
				M31			
1	J004307.5+412019	0109270101	00:43:07.5	+41:20:19	400	PN	Type I X-ray burst. NS-LMXB.
2	J004242.5+411657	0405320701	00:42:42.5	+41:16:57		PN	
3	J004215.6+411720	0650560201	00:42:15.6	+41:17:20	300	PN	Type I X-ray burst. NS-LMXB.
4	J004252.4+411648	0650560501	00:42:52.4	+41:16:48		PN	
5	J004209.5+411745	0674210201	00:42:09.5	+41:17:45		PN	
6	J004210.9+411248	0674210201	00:42:10.9	+41:12:48	500	PN	Type I X-ray burst. NS-LMXB.
7	J004215.1+411234	0674210301	00:42:15.1	+41:12:34		PN	
8	J004212.1+411758	0727960401	00:42:12.1	+41:17:58	500	MOS	Type-I X-ray burst. NS-LMXB.
9	J004231.2+411938	0727960401	00:42:31.2	+41:19:38		PN	

3.5 Discussion

3.5.1 Effectiveness and speed

We present a new algorithm that can be used as a tool to promptly detect interesting sources variable on short timescales in *XMM-Newton*'s EPIC-pn observations. EXOD is computationally inexpensive when compared to other variability tests, like χ^2 and KS. This makes EXOD faster than generating the light curve of all the sources in one observation.

The combination of the parameters $TW = 100\,\mathrm{s}$, $DL = 8$, $r_{GT} = 1$ and $b = 3$ pixels detects a higher number of variable sources according to the χ^2 and KS variability tests with a lower proportion of non-variable sources. We chose a low DL in order to detect a higher number of new variable sources, accepting the consequent increase in false positives. The variability of the whole observation with these parameters is computed faster than the generation of a single light curve with the SAS. This makes it optimal to find new variable sources. However, a visual inspection of the detected sources becomes necessary since the amount of detections in bright or extended sources is higher than with higher DLs, and the $TW = 100\,\mathrm{s}$ can lead to a worse localisation than with other TW.

With the optimal parameters applied to different time windows, the percentage of variable sources according to the χ^2 and KS tests varies between 64.3% and 83.7%. However, only 22.7% of the sources classified as variable in 3XMM-DR8 are detected. The high rate of false negatives is partially compensated by the fact that we get variability information from faint sources for which the light curves were not previously automatically generated (27.1% of the EXOD sources).

3.5.2 Contamination

The source detection with the sliding box technique gives the same problems when applied here as when applied to the source detection in *XMM-Newton*'s pipeline. It is a simple technique that usually gives good results, except in complicated cases where extended sources, bright sources, crowded regions or OOT events are present, since the spatial background can vary rapidly and give rise to spurious variability detections. These problems have been listed in Watson et al. (2009), and such sources have been flagged as spurious in the 3XMM-DR8 catalogue thanks to visual screening. Fortunately, it is easy to distinguish real sources from false detections with a visual inspection.

We are confident that the variability computation algorithm gives the desired results. Nevertheless, the number of spurious detections ($\sim$1/8 of the total) remains quite large due to the source detection procedure. A more sophisticated source detection algorithm could get rid of this problem, but it would probably be more computationally expensive. A comparison of different source detection procedures for *XMM-Newton* can be found in Valtchanov et al. (2001).

We have noted an additional issue for bright sources: the spikes of the PSF are instrumental features with considerable stochastic variability, and they give rise to spurious variable detections around sources with a high number of counts. In most of these cases, the centre of the PSF is detected as a low variability region. This can be visualised in Fig. 3.9.

3.5.3 Discoveries

EXOD computes the variability of the whole field of view, which uncovers the variability of faint sources with <100 counts. It also allows the identification of variable sources that had been classified as non variable by *XMM-Newton*'s pipeline due to a non-optimal time binning or to the short duration of the outburst, helping to unravel the nature of these sources.

Applying EXOD to 5,751 EPIC-pn observations in the full frame mode with different parameters led to the detection of a total of 2,961 sources. Of these, 2,536 were previously known sources in 3XMM-DR8 or Simbad, and we consider the remaining ones to be spurious detections. These variable sources belong to a wide variety of categories, including stellar flares, cataclysmic variables, type I X-ray bursts, supergiant fast X-ray transients, supernova shock breakouts, AGNs and more.

Finally we discuss 35 sources previously known, but not known to be variable among those classified as ''no identification'' with Simbad and not classified as variable in the 3XMM-DR8 catalogue. Some of the sources that were detected in observations with a net exposure time lower than 5000 s are not classified as variable by other variability tests. We thus recommend the EXOD user to be cautious when analysing such short observations.

Variability is a prominent feature that can be used for classification purposes. Earlier works aiming to identify unidentified sources in the *XMM-Newton* catalogue applied a position cross-match to catalogs at other wavelengths. Other known parameters, such as optical to X-ray flux ratio, are used afterwards to discriminate between source classes (Pineau et al. 2011; Lin et al. 2012). More recent works have applied machine learning algorithms where timing parameters are the major classifying feature (Lo et al. 2014; Farrell et al. 2015). Around 27.1% of the EXOD detected sources did not have a previously generated light curve and thus no variability classification. Additionally, many EXOD detections that were bright enough for a light curve generation were classified as non-variable by *XMM-Newton*'s pipeline, where the light curve showed a clearly visible outburst. EXOD thus provides an additional component that can be used to improve the classification of faint sources.

3.5.4 M31

We identified four transients in M31 that are likely to be neutron-star low mass X-ray binaries given their variability and spectra. These double the population of known NSs in M31.

Previous neutron star searches in M31 have used various techniques. Pietsch & Haberl (2005) found two NSs in LMXBs from *XMM-Newton* data, through their bursting nature. Esposito et al. (2016) and Zolotukhin et al. (2017) found a 1.2 s X-ray pulsar in M31, while Rodríguez Castillo et al. (2018) detected a 3 s X-ray pulsar.

Radio pulsar searches have also been carried out. Rubio-Herrera et al. (2013) used the Westerbork telescope at 328 MHz to detect six bursts at a similar dispersion measure (DM), suggesting a neutron star emitting as a rotating radio transient, but the periodicity searches have been unsuccessful, and the source has not been confirmed. Deep radio-pulsar searches with LOFAR at 150 MHz have been reported by Mikhailov (2018) and van Leeuwen et al. (2020), without detections.

That adds up to a total number of known neutron stars in M31 of only four. In this galaxy, more massive than the Milky Way, many more than these four must clearly exist.

Given the increased number of *XMM-Newton* observations of M31 since the detections of e.g. Pietsch & Haberl (2005), and the sensitivity of EXOD to outburst detections demonstrated in Section 3.4.3, additional type I X-ray bursters could be expected to be found through EXOD.

And, indeed, our four new type I X-ray burster candidates J004307.5+412019, J004215.6+411720, J004210.9+411248, and J004212.1+4111758 significantly increase the limited available population of known extragalactic neutron stars.

3.5.5 Further potential for discovery

EXOD has the potential to discover further examples similar to the tidal disruption event recently discovered with unexplained quasi periodic eruptions as it declines to quiescence (Miniutti et al. 2019). Whilst the data showing the quasi periodic eruptions was not in the 3XMM-DR8 catalogue, another similar source was included, RX J1301.9+2747 (Giustini et al. 2020). This source was not found during the initial study as the observation was taken in the Extended prime full window mode, a mode that was not included in our study. However, the source was detected highly significantly by a run of EXOD on this data. It was identified as a galaxy and therefore there may be more of these rare and unexplained objects in that category. Identifying them should provide data that will help us understand the nature of the quasi periodic eruptions. Our goal is to apply EXOD to *XMM-Newton* observations performed in the Extended Full Frame mode and the Large Window mode in the future, where we expect to find a high number of unknown transients.

The two sources referred as source 6 and 25 in this paper that were independently detected by Alp & Larsson (2020) and identified as SBOs while this paper was under review, represent exceptional examples of EXOD's extragalactic transient discovery potential.

It is very likely that there are other variable sources that have an inaccurate identification following the automatic Simbad query. Some could also have been eliminated by the $0.5\,\mathrm{cts\,s^{-1}}$ GTI rate threshold. Finding these would require manual perusal of the associations, and a visual inspection of all the detected sources. This will be pursued in future work.

EXOD can further be adapted to other existing X-ray observatories with similar detector properties, such as *Chandra*, *NuSTAR*, *Swift*, or *eROSITA*. It could also be applied to future missions like *Athena*.

3.6 Conclusions

In this work, we present EXOD, a new algorithm able to detect sources that vary within the duration of an *XMM-Newton* observation. It applies an imaging technique proven in optical and radio transient surveys. Its main strength is to detect the variability of faint sources for which no light curve has been generated by *XMM-Newton*'s automatic pipeline.

We tested its performance by applying it to 5751 observations and subsequently implementing the χ^2 and Kolmogorov-Smirnov variability tests on the detected sources. With this technique, we

were able to find a net count of 2,536 variable sources such as stellar flares, type-I X-ray bursts, supergiant X-ray transients, cataclysmic variables, AGNs, and QSOs.

Thirty-five of the sources detected in *XMM-Newton* archival data were unknown transients[1]. In spite of the low number of counts of these sources, usually <100, we performed spectral fitting to get a hint on their nature, and we searched for archival counterparts at other wavelengths.

We find that four of these sources are extragalactic type I X-ray bursters, located in M31. Other sources, in spite of having analysed their spectra and looked for counterparts at other wavelengths, continue to be unidentified since the number of photons of these sources remains too low to draw any firmer conclusions.

EXOD is a computationally inexpensive algorithm, making it particularly advantageous to rapidly find sources of interest in *XMM-Newton* observations and to provide additional information suitable to identify the nature of a transient source. It can be applied to future *XMM-Newton* observations, and we are looking to later adapt it to other X-ray observatories with similar detection techniques. This could yield discoveries of new transients and ease their multi-wavelength, even multi-messenger follow-up studies.

Acknowledgements

IPM thanks A. Gúrpide and the anonymous referee for their input and discussions. IPM, NAW & DTW are grateful to the CNES for financing this study. IPM further acknowledges funding from the Netherlands Research School for Astronomy (NOVA5-NW3-10.3.5.14). JvL received funding from the European Research Council under the European Union's Seventh Framework Programme (FP/2007-2013) / ERC Grant Agreement n. 617199 ('ALERT'), and from Vici research programme ''ARGO'' with project number 639.043.815, financed by the Netherlands Organisation for Scientific Research (NWO). This research has made use of data obtained from the 3XMM *XMM-Newton* serendipitous source catalogue compiled by the 10 institutes of the *XMM-Newton* Survey Science Centre selected by ESA; of the Simbad database, operated at CDS, Strasbourg, France; and of data from the European Space Agency (ESA) mission *Gaia* (https://www.cosmos.esa.int/gaia), processed by the *Gaia* Data Processing and Analysis Consortium (DPAC, https://www.cosmos.esa.int/web/gaia/dpac/consortium). Funding for the DPAC has been provided by national institutions, in particular the institutions participating in the *Gaia* Multilateral Agreement.

3.A Additional tables

Figures 3.7, and 3.8 show the lightcurves of the sources listed in Table 3.6 with 100 s time binning.

[1] Although two were identified with an independent transient search algorithm while this paper was under review.

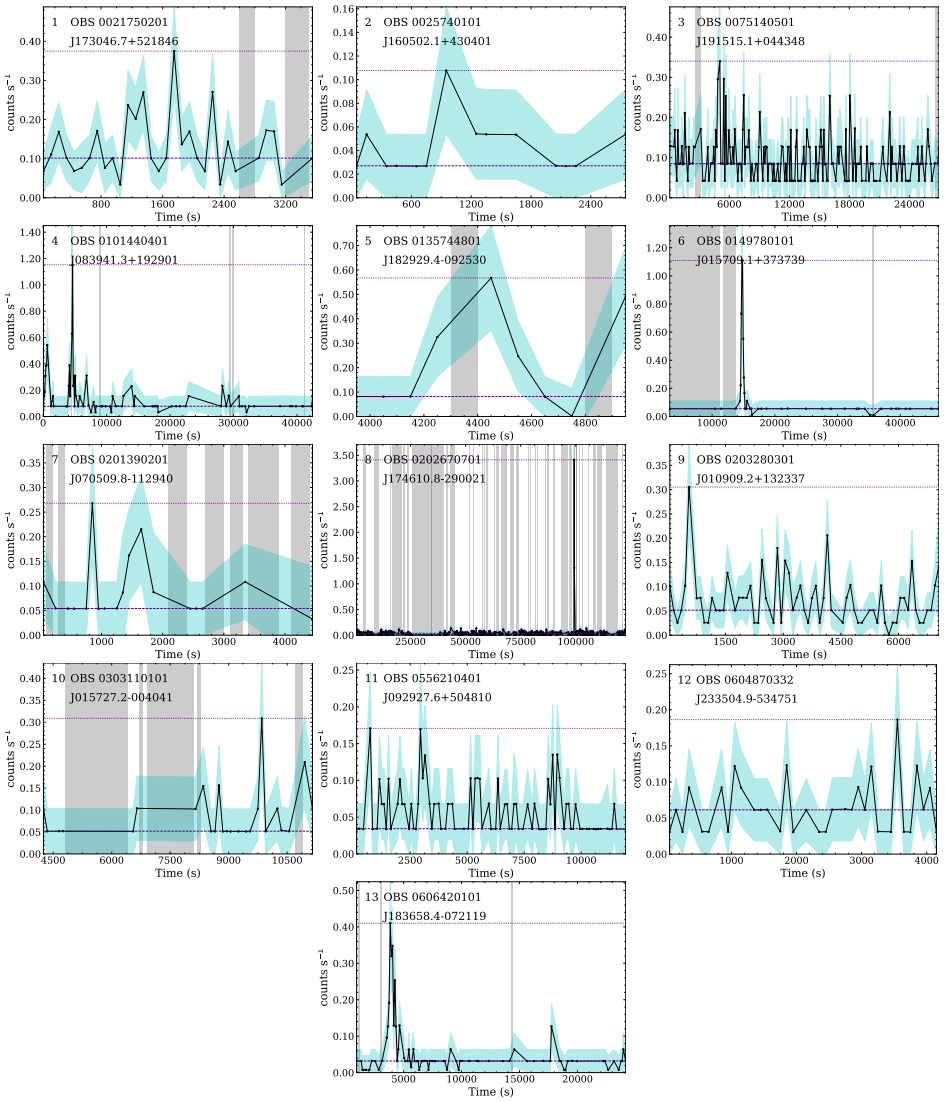

Figure 3.7: Light curves of sources detected with EXOD, present in 3XMM-DR8, but not classified as variable by the automatic pipeline. The light curves are plotted in black with cyan shaded regions representing the 1σ error bars. The dashed purple line represents $\tilde{\mathscr{C}}$, the median number of counts. The dotted purple line represents $\mathscr{C}_{max}$, the maximal number of counts. The gray vertical shaded regions represent the bad time intervals. Each plot gives the source ID, the OBSID in which it was detected and the 3XMM name of the source.

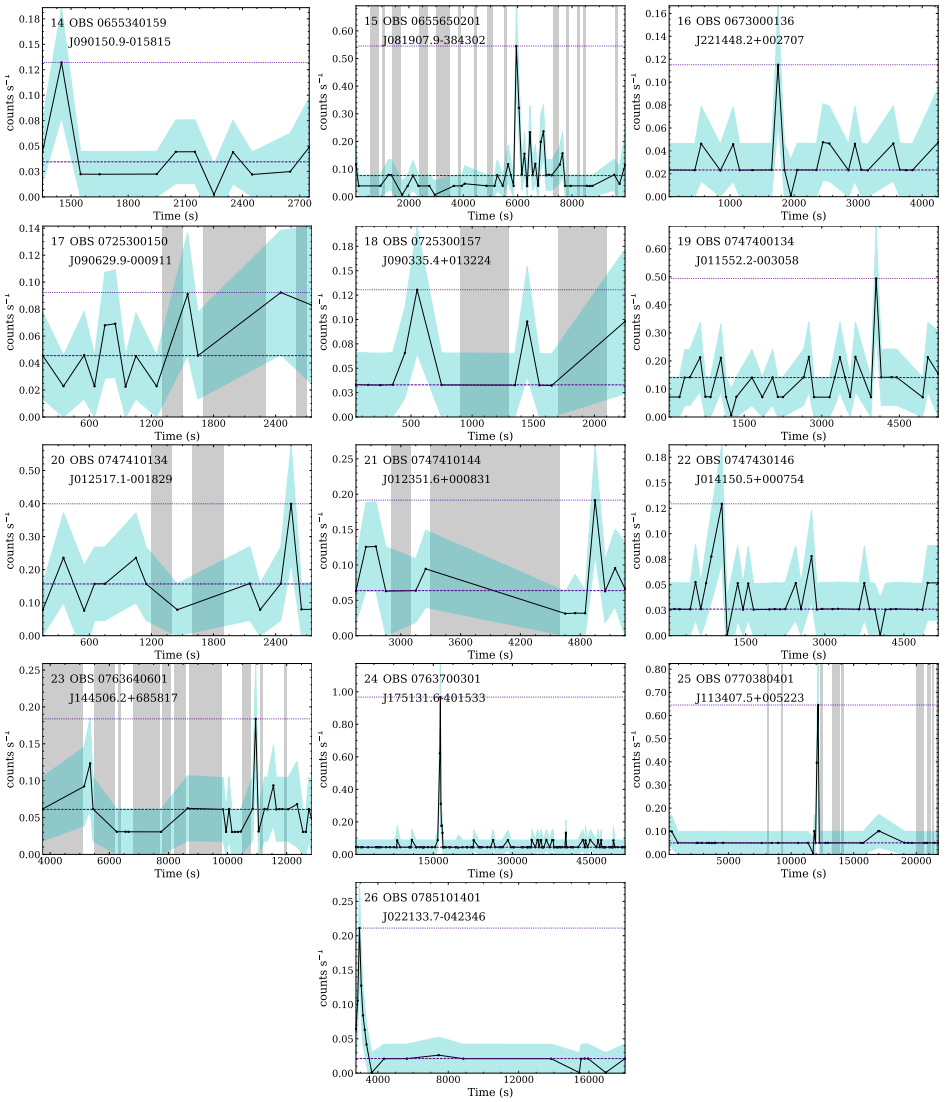

Figure 3.7: Continued.

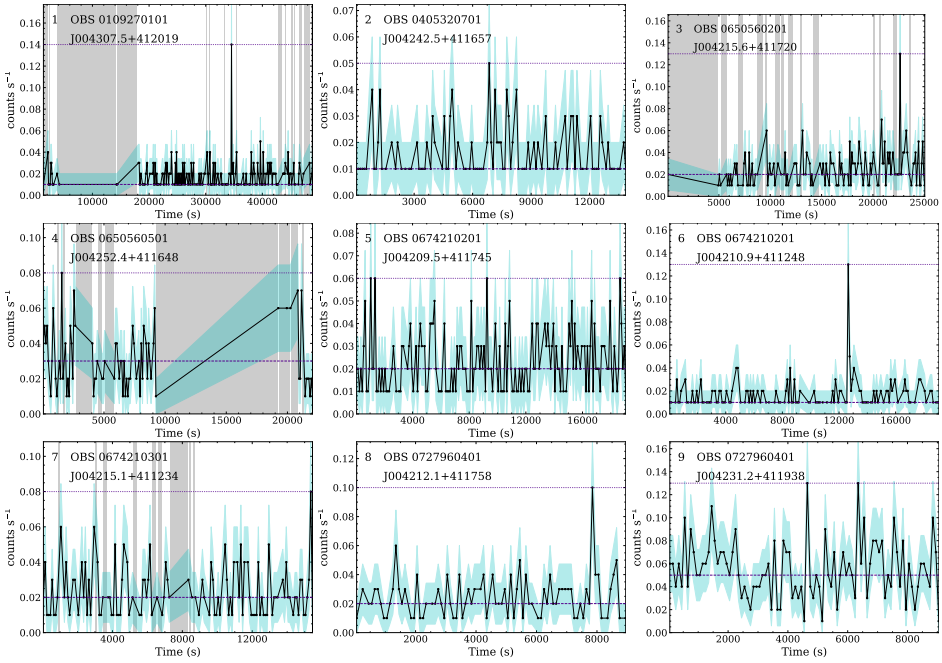

Figure 3.8: Same as Fig. 3.7, but with sources found in M31.

3.B EXOD output

In Fig. 3.9, we present an example of one of the M31 observations analysed with the four sets of parameters given in Table 3.3 to illustrate the output of EXOD and how the chosen time window affects the value of the variability.

In this particular observation, Pietsch & Haberl (2005) reported the detection of a type I X-ray burst in M31. Other sources are detected in the same field of view as being variable, amounting up to seven with $TW = 100\,\mathrm{s}$.

We can see that the sources detected with different TW can change. A remarkable fact is that some of the brightest sources that are variable on short timescales (3, 10 s) are seen as a low-variability centre embedded in a variable surrounding area at $TW = 100\,\mathrm{s}$.

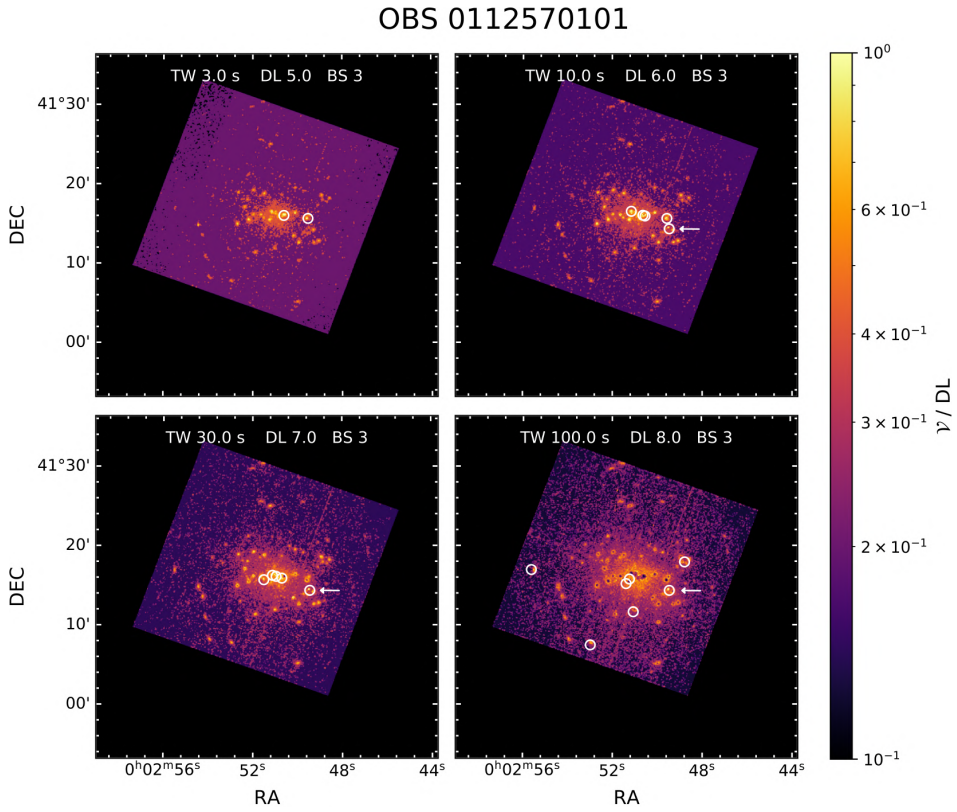

Figure 3.9: Variability of Observation 0112570101 of M31's central region. Computed with TW = 3 s (top left), 10 s (top right), 30 s (bottom left) and 100 s (bottom right). The colorbar is the same for all the plots and represents the variability divided by the detection level used for each time window, from less variable ($\mathscr{V}/DL = 0.1$, darker) to more variable ($\mathscr{V}/DL = 1$, lighter). The detected variable sources are marked by white circles. One of the sources that is detected with $TW = 100$ s, $TW = 30$ s and $TW = 10$ s in this observation was reported in Pietsch & Haberl (2005) as a type I X-ray burst, and is it marked here with white arrows.

3.C Algorithm

Algorithm 1 shows the variability computation explained in Section 3.3.1.1 with an algorithmic notation.

Algorithm 1: EXOD variability computation

Data: The events list $\mathscr{E} = \{< x,\ y,\ t >\}$, the good time intervals $GTI = \{< t_n,\ t_m >\}$, the list of TWs $T = \{< t_n,\ t_{n+TW} >\}$ and the good time ratio r_{GT}
Result: The variability per pixel, in $\mathrm{cts\,s^{-1}}$
begin
  /* Event count per pixel per time window */
  $\mathscr{C} \longleftarrow ()_{64,\ 254,\ |T|}$;
  foreach $x \in [0..64]$ **do**
    foreach $y \in [0..254]$ **do**
      foreach $tw \in T$ **do**
        $\mathscr{C}_{x,\ y,\ tw} \longleftarrow |\{\bigcup_{i\ =\ x-1}^{x+1} \bigcup_{j\ =\ y-1}^{y+1} \bigcup_{t\ \in\ tw} e_{i,\ j,\ t}\ \in\ \mathscr{E}\}|$;
  /* Good time ratio computation and TWs filtering */
  $tw \longleftarrow T_0$;
  foreach $g \in GTI$ **do**
    /* Deletion of the TWs outside GTIs */
    while $tw \cap g = \emptyset$ **do**
      if $r_{GT} \neq 0$ **then** remove tw in T, $\mathscr{C}$ and $\tilde{\mathscr{C}}$;
      $tw \longleftarrow next\ TW \in T$;
    /* Application of r_{GT} for each TW into a GTI */
    while $tw \cap g \neq \emptyset$ **do**
      $r_{GT}^{(tw)} \longleftarrow \frac{|tw\ \cap\ g|}{|tw|}$;
      if $r_{GT}^{(tw)} \geq r_{GT}$ **then**
        $\mathscr{C}_{\_,\ \_,\ tw} \longleftarrow (x_{i,\ j,\ tw} \times r_{GT}^{(tw)}\ :\ \forall\ i\ \in\ [0..64]\ \forall\ j\ \in\ [0..254])$;
      $tw \longleftarrow next\ TW \in T$;
  /* Variability computation */
  $\mathscr{V} \longleftarrow (0)_{64,\ 254}$;
  foreach $x \in [0..64]$ **do**
    foreach $y \in [0..254]$ **do**
      $\tilde{\mathscr{C}} \longleftarrow \mathrm{median}(\mathscr{C}_{x,\ y,\ tw} : \forall\ tw \in T)$;
      $\mathscr{C}_{\mathrm{max}} \longleftarrow \mathrm{max}(\mathscr{C}_{x,\ y,\ tw} : \forall\ tw \in T)$;
      $\mathscr{C}_{\mathrm{min}} \longleftarrow \mathrm{min}(\mathscr{C}_{x,\ y,\ tw} : \forall\ tw \in T)$;
      if $\tilde{\mathscr{C}} \neq 0$ **then**
        $\mathscr{V}_{x,\ y} \longleftarrow \mathrm{max}(\mathscr{C}_{\mathrm{max}} - \tilde{\mathscr{C}},\ |\mathscr{C}_{\mathrm{min}} - \tilde{\mathscr{C}}|)$;
      else
        $\mathscr{V}_{x,\ y} \longleftarrow \mathscr{C}_{\mathrm{max}}$;
  return $\mathscr{V}$;

3.D Spectral fitting

In this section, we give the detailed results of the spectral fittings performed with Xspec. The fitted spectra are shown in Fig. 3.10, and Table 3.7 shows the C-stat fit of the sources to an absorbed black body or an absorbed power law model. The spectra were generated with the SAS task `evselect` using standard filters as recommended. The spectra were rebinned to have at least five counts per spectral bin.

J174610−290021, without the photons emitted during the flare in observation 0202670701, was fitted with an absorbed black body with a Gaussian emission line (tbabs*(bbody+gaus)). The fitted parameters include the following:

$n_{\rm H} = 1.08^{+1.87}_{-1.08} \times 10^{22}$ atom cm^{-2}
kT $= 2.12^{+1.33}_{-0.78}$ keV
Gaussian energy $= 6.66^{+0.17}_{-0.13}$ keV
Gaussian $\sigma = 0.28^{+0.22}_{-0.12}$
Flux $= 1.175 \times 10^{-13}$ erg cm^{-2} s^{-1}
C-stat = 0.8 (9 dof)

We should note that the $n_{\rm H}$ value obtained by fitting the spectrum during the flare is an order of magnitude smaller than the value of the persistent emission. The large errors are due to the small number of data points. Both values are compatible at 3σ.

Table 3.7: Results from fitting different models to the pn spectra. Column (1) gives the name of the object in this paper and in 3XMM, (2) Time selection of the fit refers to all photons of the observation (A), the burst (B) or persistent (P) emission. Column (3) gives the interstellar absorption; columns (4) and (5) give the black-body temperature (kT) or the power law index (Γ) respectively; column (6) the goodness of fit measured using the C-statistic and the number of degrees of freedom; columns (7) and (8) give an estimate of the absorbed (F_{abs}) and unabsorbed (F_{unabs}) fluxes in the 0.2–10.0 keV band, respectively. All the errors are given for 90% confidence for one interesting parameter. For the fluxes, the errors are at 68% confidence.
* Values frozen for the fit.

(1) Object	(2) Time selct.	(3) n_H 10^{22} at. cm^{-2}	(4) kT (keV)	(5) Γ	(6) C-stat (dof)	(7) F_{abs} 10^{-13} erg cm^{-2} s^{-1}	(8) F_{unabs} 10^{-13} erg cm^{-2} s^{-1}
6 J015709.1+373739	A	< 0.12	$0.16\pm^{0.03}_{0.03}$	...	19.79 (19)	$0.16\pm^{0.03}_{0.03}$	$0.26\pm^{0.19}_{0.05}$
		< 1.14	...	$2.95\pm^{7.05}_{0.76}$	14.83 (19)	$0.20\pm^{0.12}_{0.09}$	$0.41\pm^{4208}_{0.19}$
8 J174610.8−290021	A	$23\pm^{44}_{11}$	$1.92\pm^{2.90}_{1.37}$	...	88.88 (90)	$1.81\pm^{0.36}_{0.33}$	$4.10\pm^{3.88}_{1.34}$
		$30\pm^{58}_{16}$	...	$1.74\pm^{3.28}_{0.72}$	88.69 (90)	$1.86\pm^{0.36}_{0.33}$	$9.17\pm^{47.8}_{5.22}$
25 J113407.5+005223	A	< 0.18	$0.30\pm^{0.07}_{0.08}$	...	36.30 (20)	$0.15\pm^{0.04}_{0.04}$	$0.17\pm^{0.04}_{0.04}$
		$0.31\pm^{0.39}_{0.23}$	...	$3.55\pm^{6.04}_{2.12}$	35.56 (20)	$1.89\pm^{75.8}_{1.51}$	$0.18\pm^{0.12}_{0.06}$
M31-1 J004307.5+412019	B	<0.50	$0.32\pm^{0.18}_{0.17}$	...	1.72 (2)	$0.83\pm^{0.54}_{0.39}$	$1.15\pm^{1.90}_{0.42}$
		<0.12	...	$1.91\pm^{1.02}_{1.04}$	0.68 (2)	$1.91\pm^{4.45}_{1.09}$	$2.68\pm^{4.07}_{1.02}$
	P	<0.16	$0.22\pm^{0.03}_{0.03}$	...	73.23 (51)	$0.23\pm^{0.03}_{0.03}$	$0.39\pm^{0.11}_{0.05}$
		$0.23\pm^{0.16}_{0.11}$	...	$3.31\pm^{1.11}_{0.72}$	56.71 (51)	$0.32\pm^{0.08}_{0.06}$	$2.03\pm^{8.91}_{1.16}$
M31-3 J004215.6+411720	B	<0.39	$0.68\pm^{0.56}_{0.23}$	...	2.72 (3)	$1.33\pm^{1.36}_{0.63}$	$1.47\pm^{1.32}_{0.66}$
		<0.54	...	$0.74\pm^{1.67}_{0.67}$	0.48 (3)	$3.55\pm^{3.86}_{2.31}$	$3.60\pm^{3.85}_{1.94}$
	P	<0.19	$0.65\pm^{0.20}_{0.13}$	...	50.42 (50)	$0.56\pm^{0.21}_{0.14}$	$0.61\pm^{0.21}_{0.13}$
		$0.25\pm^{0.20}_{0.14}$	...	$1.64\pm^{0.50}_{0.41}$	36.78 (50)	$0.96\pm^{0.27}_{0.23}$	$1.32\pm^{0.42}_{0.25}$
M31-6 J004210.9+411248	B	<3.86	$0.71\pm^{0.36}_{0.45}$	...	7.23 (2)	$3.22\pm^{2.29}_{1.00}$	$3.50\pm^{2.76}_{1.49}$
		<3.55	...	$1.15\pm^{0.42}_{0.47}$	5.87 (2)	$5.18\pm^{3.34}_{2.56}$	$5.18\pm^{3.34}_{2.56}$
	P	0.12*	$0.23\pm^{0.09}_{0.06}$	...	18.59 (23)	$0.13\pm^{0.05}_{0.04}$	$0.23\pm^{0.08}_{0.07}$
		0.12*	...	$2.38\pm^{0.67}_{0.59}$	21.39 (23)	$0.25\pm^{0.16}_{0.06}$	$0.47\pm^{0.17}_{0.17}$
M31-8 J004212.1+411758	B	0.12*	$0.43\pm^{0.17}_{0.12}$	...	0.28 (2)	$1.75\pm^{1.04}_{0.69}$	$2.15\pm^{1.06}_{0.76}$
		0.32*	...	$2.34\pm^{0.72}_{0.64}$	1.18 (2)	$2.51\pm^{1.84}_{1.10}$	$6.15\pm^{4.27}_{2.11}$
	P	<0.19	$0.73\pm^{0.11}_{0.11}$	...	31.21 (23)	$1.37\pm^{0.38}_{0.30}$	$1.48\pm^{0.39}_{0.30}$
		$0.32\pm^{0.22}_{0.17}$	...	$1.55\pm^{0.62}_{0.54}$	24.69 (23)	$2.27\pm^{0.95}_{0.69}$	$3.06\pm^{0.99}_{0.59}$

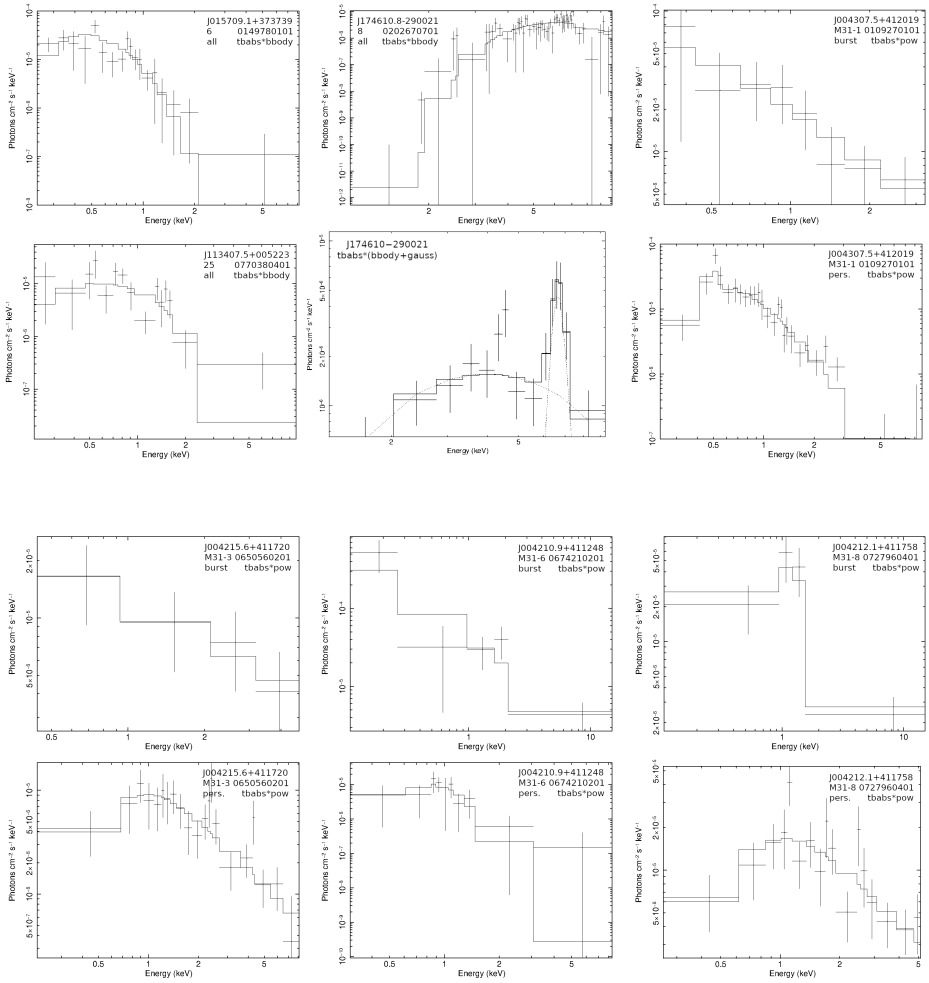

Figure 3.10: EPIC-pn fitted spectra in the 0.2–10 keV band. Beginning by first pair of rows and then second pair of rows, from left to right: 1) J015709.1+373739 fitted with a tbabs*bbody model. 2) J113407.5+005223 fitted with a tbabs*bbody model. 3) and 4) respectively: J174610.8−290021 fitted with a tbabs*bbody model and persistent emission fitted to a tbabs*(bbody + gauss) model. 5) and 6) J004307.5+412019 burst and persistent emission fitted with a tbabs*pow model. 7) and 8) J004215.6+411720 burst and persistent emission fitted with a tbabs*pow model. 9) and 10) J004210.9+411248 burst and persistent emission fitted with a tbabs*pow model. 11) and 12) J004212.1+411758 burst and persistent emission fitted with a tbabs*pow model.

4

Chromatic periodic activity down to 120 MHz in a Fast Radio Burst

I. Pastor-Marazuela, L. Connor, J. van Leeuwen, Y. Maan, S. ter Veen, A. Bilous, L. Oostrum, E. Petroff, S. Straal, D. Vohl, J. Attema, O. M. Boersma, E. Kooistra, D. van der Schuur, A. Sclocco, R. Smits, E. A. K. Adams, B. Adebahr, W. J. G. de Blok, A. H. W. M. Coolen, S. Damstra, H. Dénes, K. M. Hess, T. van der Hulst, B. Hut, V. M. Ivashina, A. Kutkin, G. M. Loose, D. M. Lucero, Á. Mika, V. A. Moss, H. Mulder, M. J. Norden, T. Oosterloo, E. Orrú, M. Ruiter, S. J. Wijnholds

Nature, Volume 596, Issue 7873, p.505-508, August 2021

Abstract

Fast radio bursts (FRBs) are extragalactic astrophysical transients (Lorimer et al. 2007) whose brightness requires emitters that are highly energetic, yet compact enough to produce the short, millisecond-duration bursts. FRBs have thus far been detected from 8 GHz (Gajjar et al. 2018) down to 300 MHz (Chawla et al. 2020), but lower-frequency emission has remained elusive. Some FRBs repeat (Spitler et al. 2016; CHIME/FRB Collaboration et al. 2019a; Fonseca et al. 2020), and one of the most frequently detected, FRB 20180916B (CHIME/FRB Collaboration et al. 2019c), has a periodicity cycle of 16.3 days (CHIME/FRB Collaboration et al. 2020). Using simultaneous radio data spanning over a factor 10 in wavelength, we here show that FRB 20180916B emits down to 120 MHz, and that its activity window is both narrower and earlier at higher frequencies. Binary wind interaction models predict a wider window at higher frequencies, the opposite of our observations. Our full-cycle coverage shows the 16.3 day periodicity is not aliased. We establish that low-frequency FRB emission can escape the local medium. For bursts of the same fluence, FRB 20180916B is more active below 200 MHz than at 1.4 GHz. Combining our results with previous upper limits on the all-sky FRB rate at 150 MHz, we find there are 3–450 FRBs $\mathrm{sky}^{-1}\,\mathrm{day}^{-1}$ above 50 Jy ms. Our results strongly disfavor scenarios in which absorption from strong stellar winds causes FRB periodicity. We demonstrate that some FRBs live in clean environments that do not absorb or scatter low-frequency radiation.

4.1 Results

We observed FRB 20180916B (also called FRB 180916.J0158+65) simultaneously with the Westerbork/Apertif and LOFAR radio telescopes, and detected multiple bursts with both facilities. Curiously, none occurred simultaneously at both frequency bands. The Apertif Radio Transient System (Maan & van Leeuwen 2017) observed between 1220−1520 MHz for 388.4 h, covering seven activity cycles. We recorded 48.3 h of simultaneous LOFAR (Stappers et al. 2011) observations between 110−190 MHz, during the predicted peaks of three cycles. The LOFAR data are public and are being analyzed independently (Pleunis et al. 2021b). We detected 54 bursts with Apertif and nine with LOFAR. (Fig. 4.1).

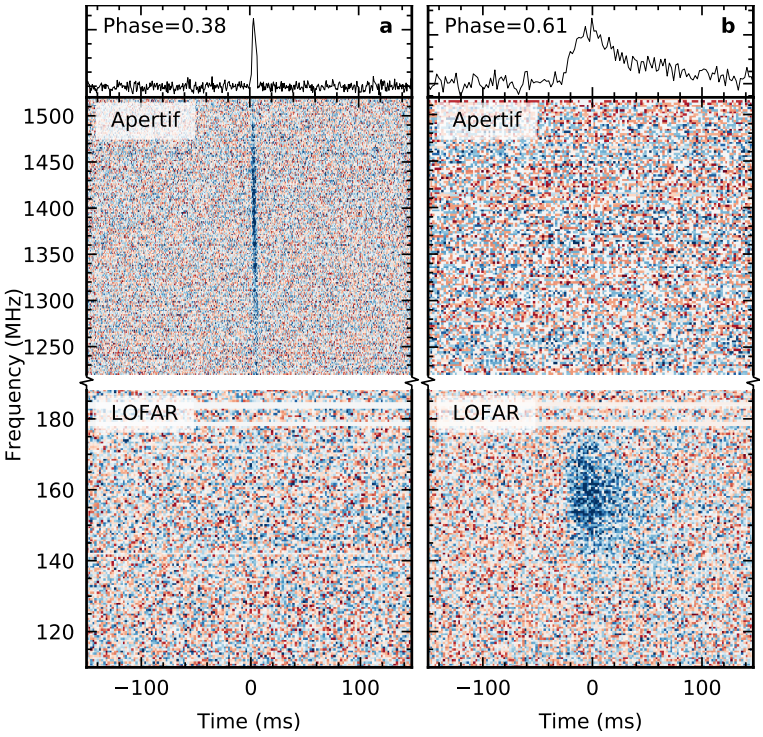

Figure 4.1: Two bursts at different phases. **a**−**b,** The bursts appear in either the Apertif (top) or LOFAR (bottom) bands of the dynamic spectra. **a,** Burst A13, detected at activity phase 0.38, is detected only at 1.4 GHz, with no emission below 190 MHz. **b,** Burst L06 occurred at phase 0.61 and is only detected by LOFAR.

No previous low-frequency searches, either all-sky (Coenen et al. 2014; Karastergiou et al. 2015) or targeting known repeaters (Chawla et al. 2020), detected any FRBs. Those strict limits on emission below 300 MHz fueled FRB theories in which local free-free absorption or strong intervening scattering was required. The nine LOFAR bursts presented here (Fig. 4.2 and Table 4.1) are the first FRB detections in this low-frequency range. All had simultaneous Apertif coverage, but none were detected there above our flux density limit of 1.7 Jy.

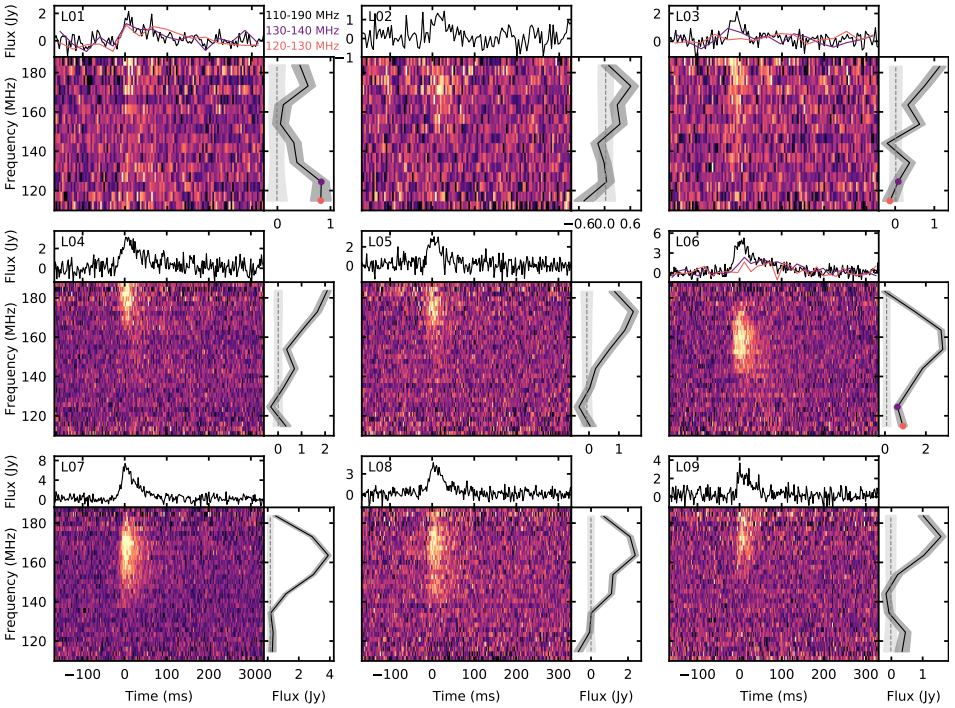

Figure 4.2: The nine LOFAR bursts. For each burst we show the calibrated pulse profile (top subpanel), dedispersed dynamic spectrum (bottom), and spectrum (right) . Bursts L01, L03, and L06 show emission below 140 MHz, and those subband profiles are plotted in purple and pink.

Remarkably, FRB 20180916B emits over 10× more bursts of the same fluence at 150 MHz than at 1.4 GHz (Fig. 4.5). Our detections allow for the first bounded FRB all-sky rate constraints below 200 MHz. A lower limit is obtained by assuming only FRB 20180916B is visible in the low-frequency radio sky. Combining this with previously published upper limits, we infer 3–450 burst $\mathrm{sky}^{-1}\,\mathrm{day}^{-1}$ above 50 Jy ms. A Euclidean fluence scaling then predicts 90–14,000 $\mathrm{sky}^{-1}\,\mathrm{day}^{-1}$ above 5 Jy ms at 150 MHz, promising for future low-frequency surveys.

The LOFAR bursts (see Fig. 4.2) are dominated by a sharp rise plus scattering tail. The scattering timescale τ_{sc}=46±10 ms at 150 MHz scales with frequency as $\tau_{\mathrm{sc}} \propto \nu^{-4.2\pm1.1}$, consistent with the ∼60 kHz scintillation seen at 1.7 GHz (Marcote et al. 2020). The scattering may explain why none of the millisecond-duration frequency-time subcomponents seen at higher frequencies (Hessels et al. 2019) are visible. The pulse broadening is consistent with Galactic scattering (Cordes & Lazio 2003), and no host galaxy contribution is required. The local environment notably scatters the FRB by $\lesssim 7\,\mu$s at 1.4 GHz. The dispersion measure (DM) of the LOFAR bursts, $\mathrm{DM_{LOFAR}}$=349.00±0.02 $\mathrm{pc\,cm^{-3}}$ (see Section 4.5.4), exceeds measurements taken 10 months prior at 1.7 GHz (Marcote et al. 2020), by ∼0.24 $\mathrm{pc\,cm^{-3}}$. We interpret this excess, again, as the presence of unresolved time-frequency subcomponents.

For bursts L01 and L07, FRB 20180916B emits down to 120 MHz (Fig. 4.2). We cannot confidently rule out the presence of emission below 120 MHz, given the reduced LOFAR sensitivity there. Our low-frequency detections show that free-free absorption and induced Compton scattering do not significantly impact burst propagation for this source. Combined with the small local rotation and dispersion measure contribution, and the lack of temporal scattering, these detections show that some FRBs reside in clean environments, a prerequisite for certain FRB applications to cosmology (McQuinn 2013).

In our Apertif campaign, we detected 54 bursts (Fig. 4.13 and Table 4.2). LOFAR co-observed 10 of these, but detected none above a 30 Jy ms fluence. All 26 bursts for which polarisation data was recorded are ∼100% linearly polarised. The polarisation position angle (PA) is constant within single bursts, and relatively flat both over activity phase, and between cycles. This observation can be used to constrain the FRB emission mechanism, and the origin of periodic activity.

After dedispersion by maximising the burst structure (Gajjar et al. 2018; Hessels et al. 2019) (see Section 4.5.4), a large fraction of 1.4 GHz bursts show multiple subcomponents that drift downward in frequency (see Fig. 4.10). That phenomenon seems common among repeating FRBs (Hessels et al. 2019; Gajjar et al. 2018; CHIME/FRB Collaboration et al. 2019a,c). For FRB 20180916B, drift rates had been estimated below 800 MHz, with $\dot{\nu} = -4.2 \pm 0.4\,\mathrm{MHz\,ms^{-1}}$ at 400 MHz (Chawla et al. 2020) and $-21 \pm 3\,\mathrm{MHz\,ms^{-1}}$ at 600 MHz (Chamma et al. 2021). The average drift rate we measure at 1370 MHz, of $-39 \pm 7\,\mathrm{MHz\,ms^{-1}}$, is nine times larger than at 400 MHz. The average drift rate values evolve linearly with frequency, as in FRB 20121102A (Josephy et al. 2019).

Our coverage (see Fig. 4.3) with LOFAR focused on peak days to maximise the detection probability, while Apertif observations spanned the entire 16.35 day activity cycle, to find or rule out any potential aliasing. The possibility of an aliased period remained, mostly driven by the brevity and daily cadence of the CHIME/FRB exposures (see Fig. 4.7). From periodograms (Aggarwal et al. 2020) based on our and previously published detections, we confirm the best period is $16.29^{+0.15}_{-0.17}$ days. This period minimises the activity width fraction for bursts detected between 110 MHz to 1765 MHz. We also searched for short periodicities within all our observations, but found none between 1 ms and 80 s.

Apertif bursts were found in six out of seven cycles. The LOFAR bursts occurred in a single cycle, with no 1.4 GHz detections, likely because Apertif observed at relatively late phase. Most Apertif bursts arrive before CHIME/FRB's activity peak day while LOFAR bursts arrive after. While previous observations of FRB 20180916B had hinted at a frequency dependent activity window (CHIME/FRB Collaboration et al. 2020), the scarcity of non-CHIME/FRB bursts prevented precise characterisation of the activity window with frequency. Using the Apertif, CHIME/FRB and LOFAR burst samples we have evaluated the 1400, 600 and 150 MHz activity windows. Folding the bursts arrivals at a 16.29 day period (Fig. 4.4, see Section 4.5.1), we determine the burst rate to phase relationship for each instrument. We find the activity window is narrower and peaks earlier at 1.4 GHz than at 600 MHz. The peak at Apertif occurs ∼ 0.7 days before CHIME/FRB, and the burst window is half as wide. LOFAR activity peaks ∼2 days later than CHIME/FRB, but the lower number of detections and the uneven phase coverage prevent a better activity window

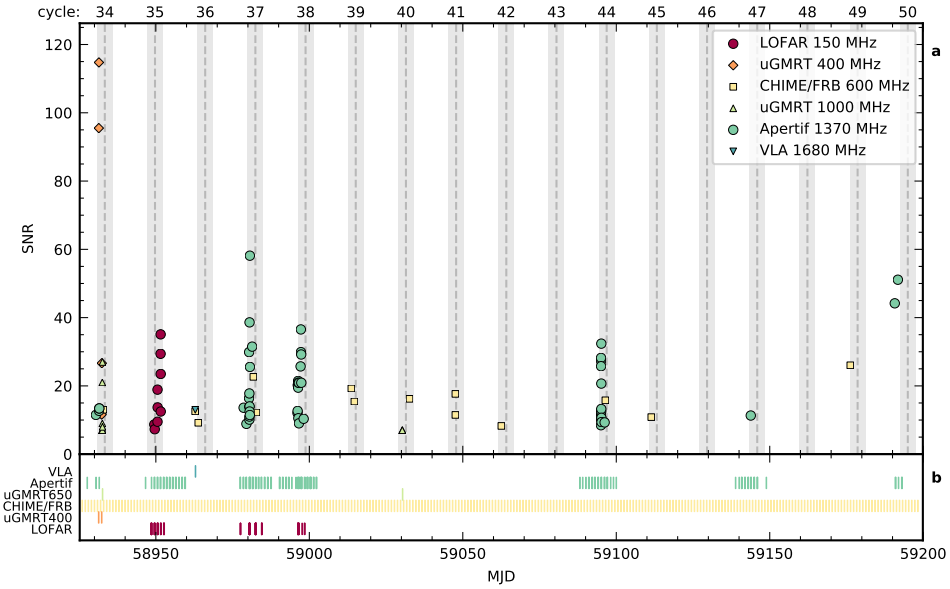

Figure 4.3: Coverage and detection times. **a.** The detection signal-to-noise ratios and **b.** observation epochs for our campaigns and other instruments(Sand et al. 2020; Marthi et al. 2020; Aggarwal et al. 2020) are plotted as a function of MJD (bottom axis) and CHIME/FRB cycle number (top axis). Here and in subsequent Figures, Apertif is shown in green and LOFAR in crimson. The predicted 16.35 day period active days are marked in gray.

width estimate. Thus, the overall FRB activity moves to ever lower frequencies throughout the phase. The similarity with the much shorter-timescale downward drifting emission within individual bursts is striking. We evaluated the likelihood of the bursts being drawn from the same distribution, taking into account the survey strategy. We are confident at the 4σ level that the Apertif and LOFAR bursts do not follow the same distribution. The CHIME/FRB and Apertif burst distributions, too, are different at 4σ confidence (see Section 4.5.2 and Fig. 4.8).

4.2 Interpretation

The discovery of periodic activity in FRB 20180916B, and subsequent report of 160-day periodicity in FRB 20121102A (Rajwade et al. 2020) led to many new FRB models with periodic aspects. One category places the engine of FRB 20180916B (a pulsar or magnetar) in a binary system with a $\sim$16-day orbital period. Free-free absorption in the wind from the companion (a massive star or another neutron star (Lyutikov et al. 2020; Ioka & Zhang 2020)) obscures the coherent radio emission from the engine for most of the orbit. Such models predict frequency-dependent activity windows, but as the absorption effects are stronger at low frequencies, the phase windows should be narrower there. We observe the opposite. Additionally, these models predict a DM evolution due to the dynamic absorption column, and a low-frequency cutoff. Our observations of a smaller phase range at higher frequencies, constant DM, and emission down to 120 MHz challenge all

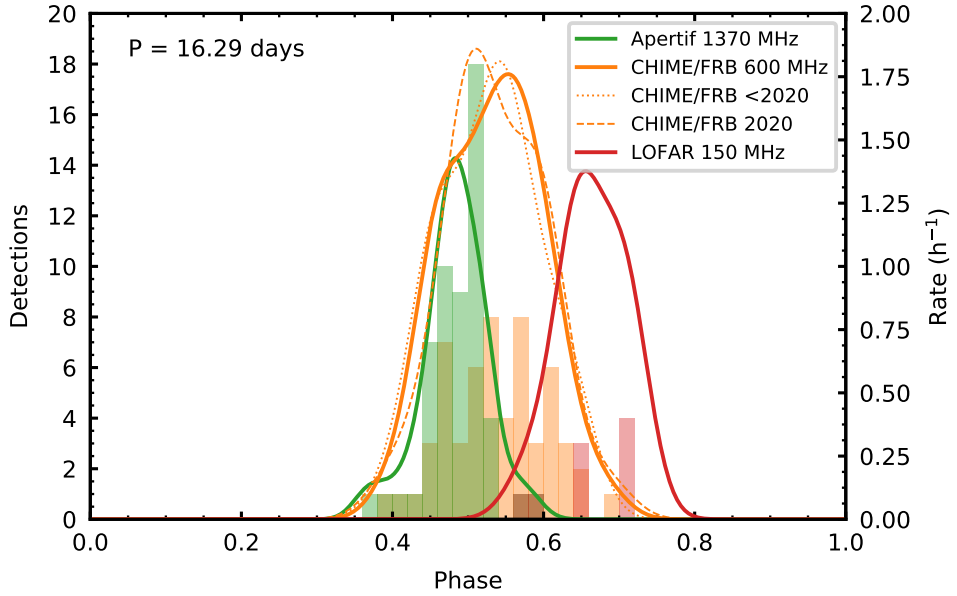

Figure 4.4: Frequency dependence of the FRB 20180916B activity windows. Burst activity windows versus phase for Apertif (green), CHIME/FRB (orange) and LOFAR (red) are shown. The histograms represent the detections, the solid lines are the rates obtained with kernel density estimates (KDEs). The KDEs for the pre-2020 and 2020 subsets of CHIME/FRB bursts (dotted and dashed lines) establish that the wider CHIME activity window is not due to a longer time baseline.

three predictions of these models. With the data presented in this work, simple absorptive binary wind models are highly disfavored as an explanation to the periodicity of FRB 20180916B.

In other models the periodic activity follows from magnetar precession. The precession is either free for isolated magnetars (Levin et al. 2020; Zanazzi & Lai 2020) or forced from e.g. a fallback disk (Tong et al. 2020). Precession models predict a second, shorter periodicity, from the neutron star rotation itself. We find no such intra-window periodicity. The spin noise, pulse profile instability, or dephased beams expected in young magnetars could, however, conceal this signal. FRBs produced from a rotating neutron-star beam should show a position angle (PA) sweep (Zanazzi & Lai 2020). We instead observe a flat PA. Furthermore, free precession models typically require young, hot, and highly active magnetars which may still be embedded in their birth environment. The limits we set on local scattering, absorption, and DM variation suggest, however, that FRB 20180916B is no longer surrounded by a dense supernova remnant and any remaining magnetar wind is not hampering radio propagation.

A precessing magnetar could also produce the required periodic coherent radio emission farther out. In synchrotron maser shock models (Metzger et al. 2019) a magnetar flare causes an ultra-relativistic shock when colliding with the neighbouring medium. The FRB emission is produced in this magnetized shock. This model predicts the flat, constant intra-burst PAs we observe, perpendicular to the upstream magnetic field of the surrounding material. But it is not clear if such models can power emitters as prolific as FRB 20180916B and FRB 20121102A. The

absence of short periodicity and DM variation with phase is consistent with the ultra-long period magnetar scenario (Beniamini et al. 2020). That model, however, requires expelling enough angular momentum to produce a period that is five orders of magnitude larger than any definitively-known neutron star rotation period.

4.3 Observations and burst search

4.3.1 Apertif

The Westerbork Synthesis Radio Telescope (WSRT) is a radio interferometer located in Drenthe, the Netherlands, consisting of twelve 25-m dishes in which a new system called Apertif (Aperture Tile in Focus) has recently been installed. Single receivers have been replaced by phased array feeds (PAFs), increasing its field of view to $\sim$8.7 square degrees (Oosterloo et al. 2010; Adams & van Leeuwen 2019). Apertif can work in time-domain observing mode to search for new FRBs (Connor et al. 2020) and follow-up known ones (Oostrum et al. 2020) using eight of the WSRT dishes. This capability is provided by a new backend, ARTS (the Apertif Radio Transient System (van Leeuwen 2014; Maan & van Leeuwen 2017; van Leeuwen et al. 2022)). ARTS covers the full Apertif field-of-view with up to 3000 tied-array beams, each with a typical half-power size of 25' by 25". In real-time FRB searches, the system records Stokes I data at a central frequency of 1370 MHz and a 300 MHz bandwidth with 81.92 μs and 195 kHz time and frequency resolution. The data are then searched in near-real time with our burst search software AMBER (Sclocco et al. 2014, 2020, 2019) and post-processing software DARC (Oostrum 2020). Raw FRB candidates are then filtered by a machine learning algorithm that assigns a probability of the candidate being of true astrophysical origin (Connor & van Leeuwen 2018) and later checked by human eyes. When AMBER identifies an FRB candidate with a duration $<$10 ms, a signal-to-noise ratio (S/N) $>$ 10 and a dispersion measure (DM) 20% larger than the expected Milky Way contribution to the DM in the pointing direction according to the YMW16 model (Yao et al. 2017), the full Stokes IQUV data of the candidate is saved. When following up known sources, the system also stores Stokes IQUV for any candidate with S/N $>$ 10 and a DM within 5 pc cm^{-3} of the source DM.

We carried out observations of FRB 20180916B with Apertif, resulting in 388.4 h on source. The observations covered seven cycles of the predicted 16.35-day activity period of FRB 20180916B, and the exposure times are visualised in the bottom panel of Fig. 4.3. The observations of the three activity cycles after our first detection (numbered 35, 37 and 38) ranged over the whole activity phase instead of only at the predicted active days in order to rule out or confirm any potential aliasing of the period (CHIME/FRB Collaboration et al. 2020). The later observations were scheduled at the confirmed activity peak days.

For 165 out of 388 observing hours, the high-resolution data were kept for a deeper offline search with PRESTO (Ransom 2001). After masking channels known to be affected by radio frequency interference (RFI) with `rfifind`, the data were dedispersed to DMs between 310 pc cm^{-3} and 397 pc cm^{-3} in steps of 0.3 pc cm^{-3}. Each time series was then searched for single pulses with S/N $>$ 8 and width $<$ 100 ms with `single_pulse_search.py`. After clustering the candidates in DM and time, the candidate with the highest S/N in each cluster was visualised and inspected by eye. A small fraction of the data were strongly affected by RFI, mainly in cycle 44 (as numbered in

Fig. 4.3) during 2020 September 3rd and 4th. These data were cleaned with `RFIClean`[1] and RFI was further masked with `rfifind`. A large fraction of channels was masked completely. Hence we cannot exclude the presence of faint or narrowband bursts that would have been above our sensitivity threshold without RFI.

In addition to the single pulse search, we searched the data for periodic signals with periods between 0.1 ms and 1 s using PRESTO's `accelsearch`. To account for any drift in the pulse frequency due to acceleration of the source in a putative orbit, an acceleration search was performed with a maximum Fourier-drift parameter of $z = 200$, corresponding to a maximum line-of-sight acceleration of $0.5\,\mathrm{m\,s^{-2}}$ for a periodicity of 1 ms and the typical observation duration of 3 hrs. The implicit assumption of constant acceleration holds as long as the orbit is longer than $\sim$30 hrs. All candidates were inspected visually.

4.3.2 LOFAR

The LOw Frequency ARray (LOFAR (van Haarlem et al. 2013; Stappers et al. 2011)) is an interferometric array of radio telescopes. Most LOFAR stations are located across the Netherlands, with a core in Drenthe, while 14 are distributed in neighbouring countries in order to increase its spatial resolution. The observations presented here used between 18 and 23 core (Dutch) stations, and used coherent Stokes mode at a time resolution of 983.04 μs and a frequency resolution of 3.052 kHz. Most data, including all detections, were recorded in intensity only (Stokes I). Data from 2020 May 27/28/29 were recorded in full polarisation (Stokes IQUV).

LOFAR was used to obtain 48.3 h of beam-formed data between 110 and 188 MHz, simultaneous to Apertif observations. LOFAR observations were taken at the predicted active days to increase the chances of detecting bursts that are broad band from 1.4 GHz to 150 MHz at both telescopes.

The observations were taken during commissioning of the transient buffer boards (TBBs) at LOFAR. In this observing mode, up to five dispersed seconds of raw sub-band data can be saved when a trigger is sent from another instrument. During the simultaneous Apertif-LOFAR observations, if AMBER detected a burst with S/N>10 and a DM within five units of $349.2\,\mathrm{pc\,cm^{-3}}$, Apertif sent a trigger to LOFAR. The dispersive delay of 40 s between 1220 MHz, the bottom of the Apertif band, and 188 MHz, the top of the band for the LOFAR High Band Antenna (HBA), gives enough time for the pipeline to find the candidate and send the alert, so that LOFAR can freeze the raw data in time.

The offline search for FRBs and periodic emission used PRESTO. The data were first sub-banded using Sigproc. In this process, every 25 consecutive channels were dedispersed using a DM of $349.5\,\mathrm{pc\,cm^{-3}}$ and averaged together, resulting in 1024 sub-bands across the full 78.1 MHz bandwidth. Strong periodic and other RFI were mitigated using `RFIClean` (Maan et al. 2020), and any remaining RFI were subsequently masked using PRESTO's `rfifind`. The data were then dedispersed to DMs between 342 and 358 $\mathrm{pc\,cm^{-3}}$ in steps of 0.03 $\mathrm{pc\,cm^{-3}}$. Each dedispersed time series was searched for single pulses with S/N > 7 and pulse-width < 250 ms using PRESTO's `single_pulse_search.py`. Similar to the offline search of the Apertif data, the candidates were clustered in DM and time, and the candidate with the highest S/N in each cluster

[1] https://github.com/ymaan4/rficlean

was visualized and examined by eye. Each of the dedispersed time series was also subjected to a periodicity search using PRESTO's `accelsearch`, with a maximum Fourier-drift parameter of $z = 128$. This value implies that, for an observing duration of 1 hour, we have searched for average accelerations of about 2.96 and 296 m s^{-2} of 1000 and 10 Hz signals, respectively. We note that our periodicity search is not sensitive to periods shorter than a few tens of milliseconds due to significant scatter-broadening at the LOFAR frequencies. For each observation, all the candidates with periods up to 80 s were folded and the corresponding diagnostic plots were examined by eye.

4.4 Detected bursts

During our observing campaign, we detected a total of 63 bursts, 54 with Apertif and 9 with LOFAR. None of these detections took place simultaneously at both instruments. Figure 4.3 shows the S/N of each detection as a function of modified julian day (MJD). It includes the detections by other instruments during the same time span for comparison, and the observation times in the bottom panel. The predicted activity days for a period of 16.35 days are illustrated as shaded regions in order to guide the eye, and the cycle numbers since the first CHIME/FRB detection are indicated on top.

4.4.1 Bursts detected with Apertif

We detected a total of 54 bursts with an S/N above 8 in 388.4 h of observations with Apertif. All Apertif bursts are given an identifier AXX, where XX is the burst number ordered by time of arrival within the Apertif bursts, from A01 to A54. Twenty-six of those bursts triggered a dump of the full-Stokes data. Eight of the bursts were not detected in real time, but in the later search of the filterbank observations with PRESTO. The number of IQUV triggers during cycle 44 is lower due to the incremented RFI environment that triggered IQUV dumps on RFI and avoided saving IQUV data on later real bursts. Table 4.2 summarises the main properties of the detected bursts. All detections took place in six out of the seven predicted activity cycles that our observations covered. In spite of observing FRB 20180916B during five days centered at the predicted Apertif peak day during cycle 47, only one burst was detected, revealing that the burst rate can fluctuate from cycle to cycle. Figure 4.13 shows the dynamic spectra and pulse profile of all bursts. Additionally, Stokes L and V are plotted for the bursts with full-Stokes data, together with the polarisation position angle (PA).

As shown in Fig. 4.3, all Apertif bursts were detected in a four-day window before the predicted peak day of the corresponding activity cycle, with none of the detections happening after the peak. There were no detections outside of a six-day activity window, even though they were largely covered by our observations. The late start of the observations around MJD 58950 with respect to the beginning of the predicted activity window could explain the non-detections in that cycle. However, the lack of emission at 1.4 GHz during that cycle cannot be discarded. After our detections and non-detections during the first four cycles, we refined the expected active window time at 1.4 GHz and scheduled the observations of the last three cycles accordingly, in five-day windows centered at the predicted Apertif peak day.

The detected bursts present a large variety of properties. Some display a single component, others show rich time-frequency structure with up to five components.

To estimate the fluence of all Apertif bursts, we obtained the mean pulse profiles using 21 ms time windows centered at each pulse's peak. This window duration is larger than the widest burst, except for A53 where a 42 ms window was needed to cover the whole burst duration. We normalised each pulse profile by the standard deviation of an off-burst region in order to convert the time series into SNR units. We determined the system-equivalent flux density (SEFD) by performing drift scans of the calibrator sources 3C147 and 3C286 whose flux densities are known (Perley & Butler 2017). Next we applied the radiometer equation (Cordes & McLaughlin 2003; Maan & Aswathappa 2014) to convert the pulse profile into flux units (Jy) using the SEFD, and integrated over the 21 ms or 42 ms time windows to obtain the fluence of each burst (Jy ms). We applied this technique in order to account for the burst structure. We assume 20% errors on the fluence based on the instability of the system over several days of observations.

The cumulative distribution function (CDF) of Apertif bursts fluences, presented in Fig. 4.5, can be fitted to a broken power-law with two turnovers. By applying a least squares minimisation technique and assuming Poissonian errors on the rate, we find the break fluences to be located at 3.2±0.2 Jy ms and 7.8±0.4 Jy ms. For bursts with S/N>10 displaying the typical burst width of 2 ms, our fluence completeness threshold is ∼1.7 Jy ms . The full range of widths for pulses near our S/N detection limit (Fig. 4.13) is between 1−5 ms, which leads to a fluence range of 1−3 Jy ms (Table 4.2). The lower-fluence turnover falls right above this range and we will thus assume that it is due to the Apertif sensitivity. The 7.8 Jy ms turnover is, however, above our completeness threshold and cannot be due to instrumental effects. CHIME/FRB bursts have been observed to show a turnover at 5.3 Jy ms that was associated to the sensitivity of the instrument (CHIME/FRB Collaboration et al. 2020). The potential presence of a turnover at 7.8 Jy ms intrinsic to the fluence distribution of FRB 20180916B could have been concealed by the sensitivity turnover. Each segment of the broken power law of the CDF follows $R(>F) \propto F^{\Gamma}$, where R is the rate (h^{-1}), F the fluence (Jy ms) and Γ the power law index. For F>7.8 Jy ms, we get $\Gamma = -1.4 \pm 0.1$. This index is consistent with the CDF of CHIME/FRB bursts, where they get $\alpha = \Gamma - 1 \sim -2.3$. For bursts with $3.2\,\mathrm{Jy\,ms} < F < 7.8\,\mathrm{Jy\,ms}$ we get $\Gamma = -0.7 \pm 0.1$, and for $F < 3.2\,\mathrm{Jy\,ms}$ we get $\Gamma = -0.2 \pm 0.1$. All errors represent the standard deviation of the fitted parameters.

4.4.2 Bursts detected with LOFAR

We detected a total of nine LOFAR bursts above a S/N of 7 in ∼48 h of observations. The bursts occurred on 10, 11 and 12 April 2020. Each burst is given an identifier LYY, where YY is the burst number ordered by time of arrival within LOFAR bursts, from L01 to L09. Table 4.1 summarises the properties of these bursts.

As shown in Fig. 4.3, all detections took place on the same predicted activity cycle in which there were no Apertif detections (cycle 35). The observations where the detections took place were performed in coherently beamformed Stokes I mode. Excepting the first two, all bursts arrived after the predicted peak day. There were thus no simultaneous bursts at 1.4 GHz and 150 MHz in the beamformed data nor the TBBs. From the dynamic spectra and pulse profiles displayed

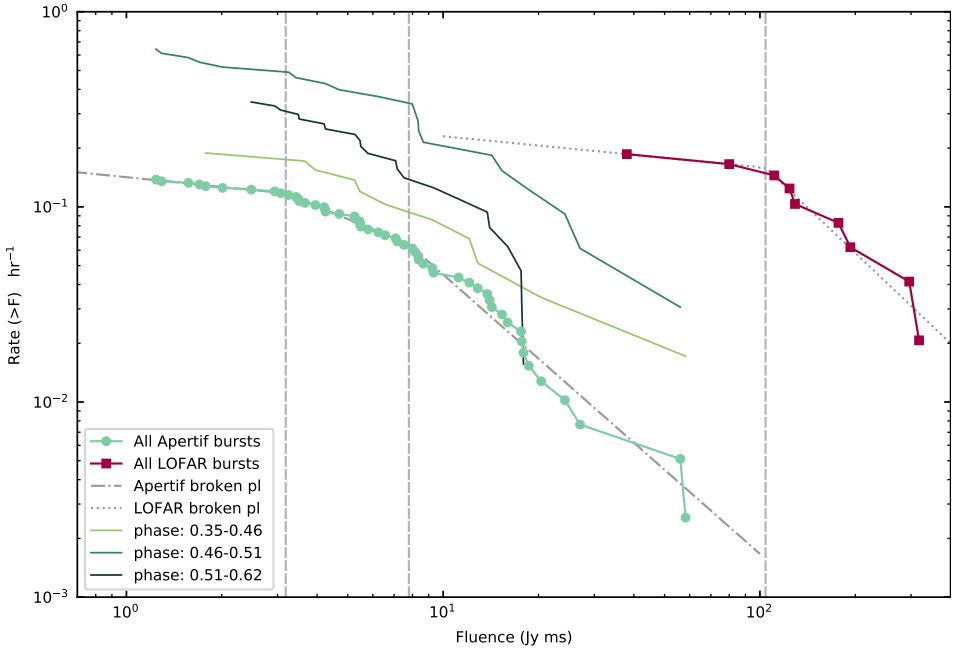

Figure 4.5: The FRB 20180916B fluence distribution, at Apertif and LOFAR. The light green markers show the cumulative distribution function (CDF) of all Apertif bursts, with dash-dotted, dotted and dashed lines giving the power-law fit respectively to bursts with fluences lower than 3.2 Jy ms, between 3.2 and 7.8 Jy ms and above 7.8 Jy ms. The coloured solid lines correspond to different phase ranges within the active window, with no discernible difference between them other than the rate scaling. The LOFAR fluence distribution is shown in crimson. The fit to a broken power law with a fluence turnover at 104 Jy ms is shown as a gray dotted line. For the same fluence, FRB 20180916B is more active at 150 MHz than 1370 MHz, even at the peak activity phases observed by Apertif.

in Fig. 4.2, there is no evidence of complex, resolved time-frequency structure. Nevertheless, a scattering tail is manifest in the pulse profiles of the brightest bursts. We will characterise the scattering timescale below. While the tail of burst L06 in Fig. 4.1 appears to plateau 25 ms after the main peak, hinting for a second subburst, a fit for multiple scattered bursts did not confidently identify a second component.

Generally, the LOFAR-detected bursts are brightest in the top of the band (see Fig. 4.2). Over the almost 2:1 ratio of frequency from the top of the band to the bottom, most bursts gradually become less bright. Although some previous targeted LOFAR FRB searches used wide bandwidths (Houben et al. 2019), most large-area searches were carried out in the lower part of the band, e.g., 119−151 MHz (Coenen et al. 2014; Sanidas et al. 2019) where the LOFAR beams are both more sensitive and larger, maximising the survey speed. Taking the sky background and the telescope sensitivity into account, a burst of the same fluence would have been detected with a 10% higher signal-to-noise ratio in that 32 MHz band from 119−151 MHz, than in same bandwidth at the top of the band, from 158−190 MHz. The behavior we see here was likely a factor in the earlier lack of detections.

The detections reported here already demonstrate there is no low-frequency cutoff above the LOFAR band. The individual bursts and the stacked profile (Fig. 4.12) also do not show a clear cutoff within the band. Two of the bursts (L01, L06) emit down to at least 120 MHz and thus cover the entire frequency range. These LOFAR burst spectra are compared to the telescope sensitivity limits in the right subpanels of Fig. 4.2. We averaged the flux densities for the bursts over fixed $[-50, +150]$ ms windows around the burst peak (dashed gray lines in the Fig. 4.2 subpanels), and contrast these against the off-burst windows (solid black lines in the same panels), given the $\pm 1\sigma$ telescope sensitivity limits (gray contours). These limits are calculated as the standard deviation of 3-s off-burst intervals, scaled to the 200-ms on-burst window. The LOFAR minimum detectable flux varies over the recorded band; it is higher at the band edges. The response (light gray contours) is relatively flat compared to the burst brightness. Seemingly significant negative pulse flux densities at low frequencies in e.g. L02 and L08 were caused by slowly-varying, low-level residual RFI that affected the baseline subtraction. Nevertheless, bursts L01 and L06 clearly show emission above the noise level, at the lower edge of the LOFAR band.

Furthermore, if we follow burst L06 from 150 to 120 MHz in decreasing frequency, the emission is ever more delayed with respect to the onset of the peak (see Figs. 4.1 and 4.2). Such behavior suggests unresolved time-frequency downward drift in the tail of the pulse. From this we conclude that the decrease in pulse peak brightness could be intrinsic, and is not due to a cutoff by intervening material. Bursts L04 and L05 show a similar hint of a delayed tail, at slightly higher frequencies.

The LOFAR flux density scale was derived from the radiometer equation, using information about frequency-dependent antenna and sky temperatures, models of telescope gain (frequency- and direction-dependent), number of performing stations/tiles, and RFI environment. It also takes the observing bandwidth, integration time, and number of summed polarizations into account. We estimate that imperfect knowledge of the system parameters introduces a 50% systematic uncertainty on the band integrated flux. The calibration procedure and flux uncertainty estimates are detailed in the LOFAR censuses of millisecond (Kondratiev et al. 2016) and normal (Bilous et al. 2016) pulsars.

Figure 4.5 shows the CDF of LOFAR bursts. It can be fitted to a broken power-law with the break fluence located at 104 ± 12 Jy ms. This fluence falls well within our LOFAR sensitivity limits, and we thus attribute the break to our completeness level. The power-law index of bursts with $F > 104$ Jy ms is $\Gamma = -1.5 \pm 0.2$, consistent with the Apertif and the CHIME/FRB power-law indices. However, the burst rate at the same fluence is two orders of magnitude larger for LOFAR bursts than for Apertif bursts. The power-law index for bursts with $F < 104$ Jy ms is $\Gamma = -0.2 \pm 0.2$.

4.5 Data analysis

4.5.1 Ruling out aliasing

As noted in the announcement of the FRB 20180916B periodic activity discovery (CHIME/FRB Collaboration et al. 2020), the best-fit cycle period could be an alias of the true period. The short CHIME/FRB exposures and their regular sidereal day sampling of $P_{\rm sid} = 0.99727$ days lead to a

degeneracy between the reported frequency $f_0 = (16.35\,\mathrm{days})^{-1}$ and aliases of this frequency at $f_N = (N f_{\mathrm{sid}} \pm f_0)$, with N a positive integer and $f_{\mathrm{sid}} = P_{\mathrm{sid}}^{-1}$. Some periodicity models, mainly those involving ultra-long period or precessing magnetars (Beniamini et al. 2020), fit better with the shorter periods involved when $N > 0$.

To maximise the chance of detection, follow-up instruments observed FRB 20180916B predominantly around its predicted activity peak (Chawla et al. 2020; Pilia et al. 2020; Aggarwal et al. 2020; Sand et al. 2020). The implied lack of coverage outside this purported peak could bias the derived activity cycle. Although detections of FRB 20180916B using multiple instruments and cadences have put strong constraints on allowed N values, aliasing has not been robustly ruled out until now.

To break this degeneracy, we scheduled observations covering all phases, during the first five activity cycles. Exposures lasted 3−9 hours. We next generated periodograms using `frbpa` (Aggarwal et al. 2020). We employed a Pearson's χ^2 test (PR3; CHIME/FRB Collaboration et al. 2020), an activity width minimisation algorithm (R20; Rajwade et al. 2020), and a quadratic-mutual-information-based (QMI) periodicity search technique (P4J; Huijse et al. 2018). We built periodograms using bursts from Apertif only; CHIME/FRB only; CHIME/FRB plus Apertif; and from all public, known bursts. Only CHIME/FRB and Apertif have coverage and detections over the whole activity phase. The periodograms span periods between 0.01−20 days to show all the aliased P_N periods for N between 0−37 (Fig. 4.6).

The CHIME/FRB periodograms (panels C, G, K of Fig. 4.6) show numerous peaks below eight days, at the predicted aliasing values (gray vertical lines), as expected for a transit instrument. In contrast, the Apertif periodograms (panels B, F, J) show no prominent periods below eight days beyond the broad 1-day peak in the R20 periodogram caused by the daily cadence. By next combining CHIME/FRB and Apertif bursts, the different observing cadence and exposure diminish the significance of most aliased peaks (panels D, H, L). We particularly focus on the activity width minimising plot (R20, panel H). The low values of the maximum continuous fraction indicate that bursts are detected across the whole activity phase for all periods below eight days, allowing us to rule out any potential aliased period. This is further confirmed when adding the bursts from FRB 20180916B that were detected by other instruments, in panel E. We conclude there is no aliasing.

To best estimate the period, we also generated wider, 1.57−60 day periodograms. The best-fit values of the peaks at ∼16 days are listed in all panels of Fig. 4.6. Error bars represent the full-width at half maximum (FWHM) of the peaks. The fewer cycles covered by Apertif observations translate as an uncertainty larger than one day in the period estimation with the PR3 and R20 techniques, in contrast with the period estimation using CHIME/FRB bursts only. The combination of CHIME/FRB and Apertif bursts gives a period of 16.29 days with the PR3 test. The activity width minimisation technique (R20) gives the most consistent period estimates when applied to different instrument combinations. We find the best-fit period is 16.29 days, where reference MJD 58369.9 centers the peak activity day at phase 0.5. This is the only period for which no bursts lie outside of a 6.1 day activity window.

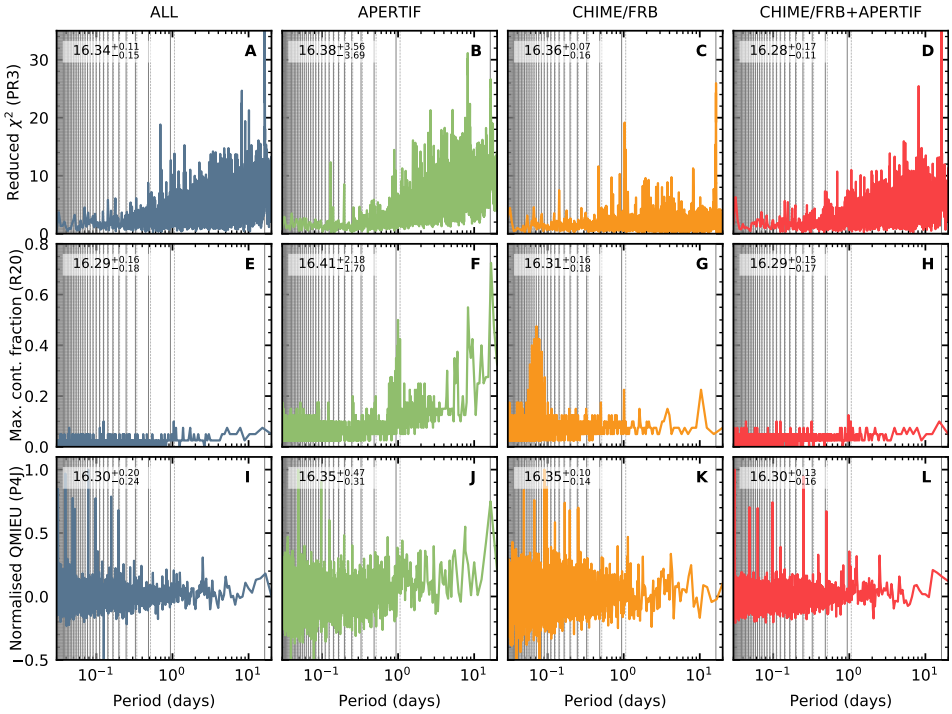

Figure 4.6: Finding the best period. **a**–**l,** The periodograms between 0.03 day and 20 day periods of four instrument combinations and three different period searching techniques. Each column corresponds, from left to right, to all detections combined (blue), Apertif detections (green), CHIME/FRB detections (yellow) and CHIME/FRB and Apertif detections combined (red). Each column corresponds to a different search technique, with Pearson's χ^2 test (CHIME/FRB Collaboration et al. 2019c) at the top, activity width minimisation center (Rajwade et al. 2020), and QMI method (Huijse et al. 2018) at the bottom. The vertical gray lines mark the position of the aliased periods, solid for $f_N = (N f_{\rm sid} + f_0)$ and dotted for $f_N = (N f_{\rm sid} - f_0)$. The number on the top left corner of each plot indicates the best period using the given burst data set and periodicity search method, with errors giving the full width at half maximum.

4.5.2 Activity windows

By using the aforementioned best period and reference MJD to compute the burst arrival phases, we have generated a histogram of detections versus phase on the top panel of Fig. 4.7. The cycle coverage by different instruments can be visualised on the bottom panel of the same figure, where it is manifest that CHIME/FRB and Apertif are the only instruments covering the whole activity cycle which have detected bursts. We have used data from all FRB 20180916B observations published thus far (CHIME/FRB Collaboration et al. 2020; Marcote et al. 2020; Scholz et al. 2020; Pilia et al. 2020; Chawla et al. 2020; Marthi et al. 2020; Aggarwal et al. 2020; Pearlman et al. 2020).

Several theoretical models have suggested the activity window may be frequency dependent (Lyutikov et al. 2020; Ioka & Zhang 2020; Beniamini et al. 2020). In absorptive wind models, for example, one expects a larger duty cycle at high frequencies due to heightened opacity at

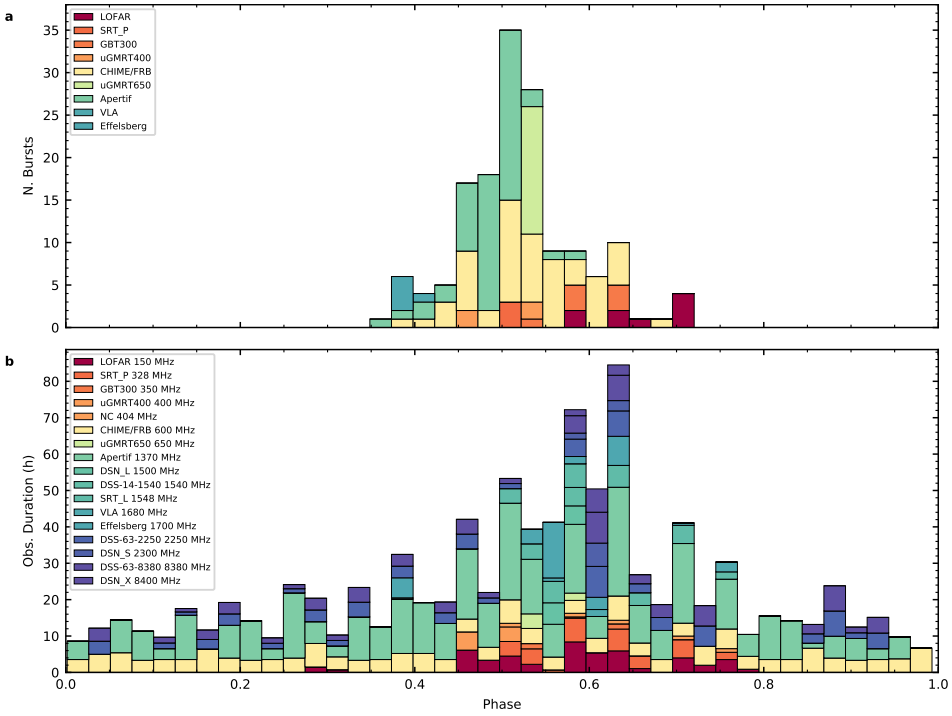

Figure 4.7: Observations and detections as a function of phase. Shown are histograms of **a,** burst detections and **b,** observation duration, both as a function of phase for the best period fitted to Apertif and CHIME/FRB data (16.29 days). In **a**—**b**, instruments are color-coded by central frequency, with blue for high frequencies and red for low frequencies. Figure was generated using an adaptation of the `frbpa` package (Aggarwal et al. 2020).

long wavelengths. There was also an observational hint that higher frequencies may arrive earlier, based on four EVN detections at 1.7 GHz (Marcote et al. 2020). By taking into account the bursts detected by Apertif, CHIME/FRB and LOFAR at 1.4 GHz, 600 MHz and 150 MHz respectively, we can obtain an estimate of the probability of the bursts being drawn from the same distribution at different frequencies.

To do so, we attempted to estimate the detection rate as a function of activity phase for the three different frequency bands. We estimate these activity windows by computing the probability density function (PDF) of detection rate for Apertif, CHIME/FRB and LOFAR using a weighted kernel density estimator (KDE). The KDE is a non-parametric smoothing technique in which a kernel is built at each data point from a sample and their contributions are summed in order to estimate an unknown probability density function. With $\{X_i : i = 1, 2, ..., n\}$ the observed data, a sample of n observations drawn from a distribution $f(x)$ with an unknown density, we define its weighted KDE in the general case as

$$\hat{f}(x) = \frac{1}{h} \sum_{i=1}^{n} p_i K\left(\frac{X_i - x}{h}\right), \tag{4.1}$$

with K the kernel function, $h > 0$ the bandwidth, and $\{p_i : i = 1, ..., n\}$ the probability weights of each data sample. In this case, the input data $\vec{X}$ are the activity phases of each of the n detections and the weights $\vec{p}$ are the inverse of the reciprocal observing time at that phase, and hence $\hat{f}(x)$ is the equivalent of a detection rate. We used a Gaussian function as kernel K and applied Scott's rule for bandwidth selection (Scott 2015), thus having

$$h = n_{\text{eff}}^{-1/(d+4)} = n_{\text{eff}}^{-1/5}, \tag{4.2}$$

with $d = 1$ the number of dimensions and n_{eff} the effective number of datapoints, that differs from n when applying a weighted KDE,

$$n_{\text{eff}} = \frac{(\sum_{i=1}^{n} p_i)^2}{\sum_{i=1}^{n} p_i^2}. \tag{4.3}$$

We applied the KDE separately to the Apertif, CHIME/FRB and LOFAR burst datasets. Based on the KDE estimation shown in Fig. 4.4, we find that higher frequencies appear to arrive earlier in phase, i.e. the activity peaks at a lower phase with larger frequencies. Additionally, the width of the activity window appears to be larger with CHIME/FRB. The KDE is useful for estimating probability distributions with a small number of samples, but it is non-parametric and does not easily allow us to compare the activity window widths between frequencies. For this we fit a Gaussian to the detection rate of FRB 20180916B for each instrument and find a full-width at half maximum (FWHM) of 1.2±0.1 days from the Apertif data at 1370 MHz and 2.7±0.2 days at 400–800 MHz using the CHIME/FRB bursts. The best-fit peak activity phase for Apertif is 0.494±0.002 and 0.539±0.005 for CHIME/FRB. The source activity window is therefore roughly two times wider at CHIME/FRB than at Apertif and its peak is 0.7 days later at CHIME/FRB.

The CHIME/FRB detections span multiple years, while the Apertif and LOFAR detections are all in 2020. Since an error of 0.05 days in a period ∼16 days could lead to a phase delay of ∼0.15 after two years and thus to a broadening of the resulting activity window, we compared the PDF including all CHIME/FRB bursts with what would be obtained only with the bursts detected before 2020 and during 2020. We observe that the three CHIME/FRB distributions are consistent with each other, and all are both wider and later in arrival phase than the Apertif profile.

We do not attempt to fit a Gaussian to the LOFAR bursts because of the small number of detections and our limited coverage in phase. However, we note that four out of the nine detected LOFAR bursts arrive later in phase than every previously detected CHIME/FRB burst. Therefore, the activity of FRB 20180916B at 150 MHz likely peaks later than at higher frequencies and the activity window may be wider as well. This is in stark contrast with the predictions of simple absorptive wind models where the activity ought to be wider at higher frequencies.

To quantify the statistical significance of the phase-window differences visible in Fig. 4.4, we compared each pair of burst ensembles from Apertif, CHIME/FRB and LOFAR, using Kolmogorov-Smirnov (KS) tests. For KS test p-values < 0.01 we can reject the null hypothesis that the observed samples are drawn from the same distribution. This is the case for all pairs: For Apertif versus CHIME/FRB samples, $p = 1.71 \times 10^{-7}$; for Apertif versus LOFAR, $p = 8.45 \times 10^{-10}$; and for CHIME/FRB versus LOFAR, $p = 7.64 \times 10^{-5}$.

We next investigate if the difference in observing strategies could cause these arrival differences. Although CHIME/FRB and Apertif cover the activity phase similarly, the per-cycle sampling function is different. After all, per day, the tracking Westerbork dishes can see FRB 20180916B for $\sim$12 hr, while the transit at CHIME/FRB lasts $\sim$20 minutes. We therefore test if selection effects influenced the inferred activity window, and if the different observing strategies led to other bias in the observed PDFs such as activity period jitter. To this end we simulated observed bursts drawn from a single Gaussian-distributed intrinsic population.

We first draw the number of bursts per cycle N from a normal distribution centered at the CHIME/FRB average rate, $R \sim 0.32\,\mathrm{h}^{-1} \sim 125\,\mathrm{cycle}^{-1}$, for a period $P = 16.29$ days, with standard deviation $R/5 \sim 25\,\mathrm{cycle}^{-1}$. We next draw burst arrival phases from a normal distribution centered at CHIME/FRB phase centre 0.52, with standard deviation 2.73 days or $\sim$0.17 in phase. We count the bursts Apertif, CHIME/FRB, and LOFAR would have detected at their respective observing sessions. We compare the resulting simulated periodograms between pairs of telescopes in the same way as we compared the actual periodograms. We perform this simulation 10^5 times (Fig. 4.8).

These activity-window selection effect simulations discard Apertif and CHIME/FRB burst samples as drawn from the same distribution at a 4.1σ level. The Apertif and LOFAR burst distributions are ruled out to be the same with 3.8σ confidence. For both, the actual p-values are well below 99.73% (3σ) of the simulated p-values (Fig. 4.8). The activity windows are indeed different and are not due to an observational bias. By itself, the observed CHIME/FRB-LOFAR p-value is at 2.7σ of the simulated p-values. The LOFAR detections are fewest, and the activity windows at CHIME/FRB and LOFAR are closer to one another. However, we note that four of the LOFAR detections in a single activity cycle arrive later in phase than any previously detected CHIME/FRB burst.

Thus, taking all observational biases into account, a frequency dependence of the activity window must exist to reproduce the observed burst distribution. It peaks earlier at higher frequencies. Additional LOFAR bursts have been reported (Pleunis et al. 2021b) that confirm the later activity phase at lower frequencies. The burst window is also $>2\times$ wider at low frequencies. This is opposite to the predictions from models where free-free absorption in the stellar wind of a binary companion directly produces the periodicity, where lower frequency emission windows should be narrower (Lyutikov et al. 2020; Ioka & Zhang 2020), not wider. Our results thus disfavour the cause of the periodicity to be free-free absorption in a binary system.

Bursts following radius-to-frequency mapping in an emitting magnetosphere swept back by binary orbital motion (Pleunis et al. 2021b) could exhibit the observed frequency-dependent phase delays. Such a model does not, however, produce the required reversal of the absorptive width versus frequency relationship. The absorption characteristics of the material outside the trailing funnel are unchanged. The radius-to-frequency mapping required to reproduce the delay relationship depends on highly localised emitting regions for each observed phase angle (Lyutikov 2020). It is yet unclear whether such models can easily produce the significant intrinsic widening observed for the emitting regions at later phase.

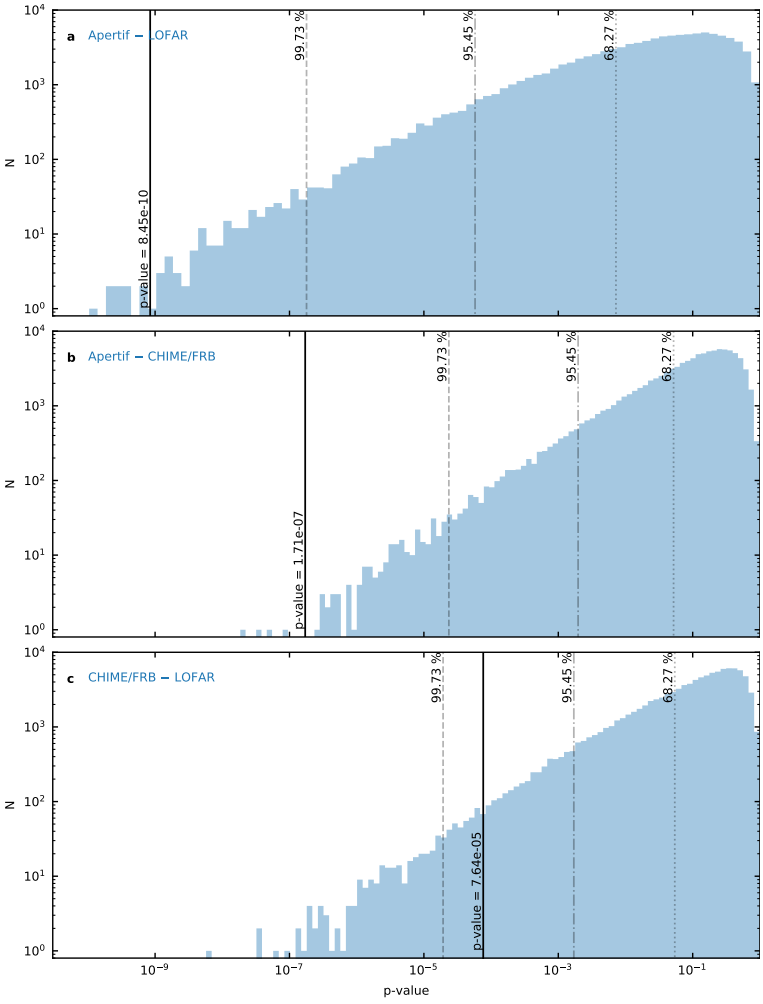

Figure 4.8: Comparison of simulated and observed activity window p-values. Each panel **a**—**c** compares the p-value obtained through the Kolmogorov-Smirnov statistic on two instrument burst samples. The vertical black lines give the observed p-value, whereas the histograms correspond to 10^5 simulations of the p-value that would be obtained if both instrument burst samples were drawn from the same distribution. Shown are comparisons of burst samples from **a,** Apertif and LOFAR. **b,** Apertif and CHIME/FRB **c,** CHIME/FRB and LOFAR. In **a**—**c,** the vertical gray dotted, dash-dotted and dashed lines show respectively the p-value where 68.27% (1σ), 95.45% (2σ) and 99.73% (3σ) of the simulations give a larger p-value.

4.5.3 Polarisation

Monitoring the polarisation position angle (PA) of FRB 20180916B over time and across cycles with Apertif is made easier by the fact that Westerbork is a steerable equatorial mount telescope. This stability of the system's response allows us to investigate the polarisation properties of FRB 20180916B within each pulse, within an activity cycle, and even between multiple periods.

The source is always in the same central beam and the on-sky feed orientation does not vary with parallactic angle. This eases the study of the intrinsic polarisation position angle. For lower-frequency surveys or higher-RM sources, such study is hampered by the covariance between RM and PA, where $\Delta\mathrm{PA} = 2\Delta\mathrm{RM}\lambda^2 \approx 5.5^\circ \left(\frac{\Delta\mathrm{RM}}{1\,\mathrm{rad\,m^{-2}}}\right)\left(\frac{\nu}{1370\,\mathrm{MHz}}\right)^{-2}$.

We calibrate the Apertif polarisation response by observing 3C286 and 3C147. The former is roughly 12% linearly polarised with a stable PA; the latter is known to be unpolarised, which allows us to solve for leakage from I into Q, U, and V. For the analysis, we dedisperse the bursts to 348.75 pc cm^{-3}. We use $\mathrm{RM} = -115\,\mathrm{rad\,m^{-2}}$, a value (Chawla et al. 2020) corroborated by Q/U fitting using RM-Tools (Purcell et al. 2020) and our own code. Compared to CHIME, our smaller $\Delta\lambda^2$ range limits our ability to identify RM variations in activity phase and across cycles. For our purpose of monitoring PA over time, we feel confident using this previously-determined RM value, especially since the Galactic Faraday foreground of $-115 \pm 12\,\mathrm{rad\,m^{-2}}$ likely dominates the total RM of FRB 20180916B (Ordog et al. 2019; CHIME/FRB Collaboration et al. 2019a).

We find the PA of FRB 20180916B to be flat within each burst, with ΔPA<20 deg, in agreement with other polarisation studies of the source (CHIME/FRB Collaboration et al. 2019c; Chawla et al. 2020; Nimmo et al. 2021). This is in contrast to most pulsars whose PAs swing across the pulse, in many cases with the S-shaped functional form predicted by the rotating vector model (RVM). In the classic picture, PA varies with the arctangent of pulse longitude and the amount of swing is proportional to the emission height but inversely proportional to the star's rotation period (Blaskiewicz et al. 1991). However, the flat PAs of FRB 20180916B are similar to other FRBs, notably FRB 20121102A whose intra-burst polarisation exhibits less than 11 deg of rotation (Gajjar et al. 2018). They are also similar to radio magnetars. FRB 181112 was the first source to show significant variation in the polarisation state within a burst and between sub-components of an FRB with temporal structure (Cho et al. 2020).

While the flat PAs within each FRB 20180916B burst are in line with previous measurements, we have found that its PA is also stable on average within an activity cycle and even between periods, with ΔPA<50 deg. In models that invoke precession as the origin of periodicity and magnetospheric emission as the origin of the FRBs, one generically expects a PA change as a function of activity phase. However, the amount of PA swing depends on the geometry of the system and well as the fraction of a precession period that is observable (Zanazzi & Lai 2020), so we cannot rule out precession with our polarisation measurements. In relativistic shock models, the synchrotron maser mechanism provides a natural path for flat PAs within a burst, but it is not clear how or if the polarisation state could be nearly constant within a cycle and over multiple months (Metzger et al. 2019; Beloborodov 2017). Given the duty cycle of FRB 20180916B appears to be just $\sim$10% in the Apertif band, it will be useful to observe the PAs of FRB 20180916B over at lower frequencies with a steerable telescope that can cover a full periodic cycle.

4.5.4 Dispersion

The Apertif real-time FRB detection pipeline AMBER reports the dispersion measure that maximises the S/N of a burst ($DM_{S/N}$). Any frequency-swept structure intrinsic to the pulse, as seen in a number of repeating FRBs, will be absorbed in this value. The discovery of multiple subcomponents showing a downward drift in frequency, in bursts from the first repeating FRB (FRB 20121102A) – and later in other repeaters – motivated the development of methods that maximise DM upon structure (DM_{struct}) rather than S/N (Gajjar et al. 2018; Hessels et al. 2019). As $DM_{S/N}$ assumes that the signal can be completely described by a ν^{-2} power law, DM_{struct} is more likely to represent the actual dispersive effect (Oostrum et al. 2020). If a burst shows a single component, the computed DM_{struct} is equivalent to $DM_{S/N}$. Hence, we report DM_{struct} for all Apertif bursts, which was determined using a modified version of `DM_PHASE`[1]. We define the best Apertif DM by computing the median DM_{struct} of bursts that were detected with S/N>20. We obtain $DM_{Apertif}$=348.75±0.12 pc cm^{-3}, where the errors represent the median absolute deviation. $DM_{Apertif}$ is consistent with values previously reported in the literature, and we use this value to create the dynamic spectra of the bursts shown in Fig. 4.13.

There is no evidence for a variation of DM with phase (Fig. 4.9, top panel). Within the error, the bursts are consistent with a constant DM=348.75 pc cm^{-3}. From a visual inspection of the dedispersed pulse profiles we find that the DM of outlier bursts A08, A19, A24 and A31 could be explained by the presence of unresolved subbursts.

The LOFAR bursts lack detectable time-frequency structure, but require separating the frequency-dependent scattering tails from the DM fit. After initial S/N-maximization DM fitting using `pdmp` (Hotan et al. 2004), we hence divided every profile into subbands, and fitted these with a scattered Gaussian each. The resulting Gaussian centers were time aligned using an additional $\tau_{DM} \propto \nu^{-2}$ correction. For the final LOFAR DM, obtained by averaging over all bursts with S/N>20 (Table 4.1), we find $DM_{LOFAR} = 349.00 \pm 0.02$ pc cm^{-3}, with the error reporting the standard deviation.

4.5.5 Sub-pulse drift rate

Several FRBs exhibit downward drifting sub-pulses, in which later sub-bursts in a pulse train arrive at ever lower frequencies. Thus far, there is currently no example of upward drift within a burst. In the first known repeater, FRB 20121102A, the subpulses drift downward faster at higher observing frequencies (Hessels et al. 2019; Josephy et al. 2019; Caleb et al. 2020). Several of our FRB 20180916B detections at Apertif show downward drifting sub-pulses, enabling us to make the first measurement of the drift rate $\dot{\nu}$ of FRB 20180916B above 1 GHz (Fig. 4.10).

As no scattering tails were seen above 350 MHz (CHIME/FRB Collaboration et al. 2019c; Marcote et al. 2020; Chawla et al. 2020) we represented each sub-burst as Gaussian in time. After dedispersing each burst to its DM_{struct}, we applied least-squares fitting to two, three, four, five, or twelve sub-burst Gaussians. Next, we defined each sub-pulse time component by taking the 2σ time area around each Gaussian peak, we next fitted each component as a Gaussian in frequency.

[1] https://www.github.com/DanieleMichilli/DM_phase

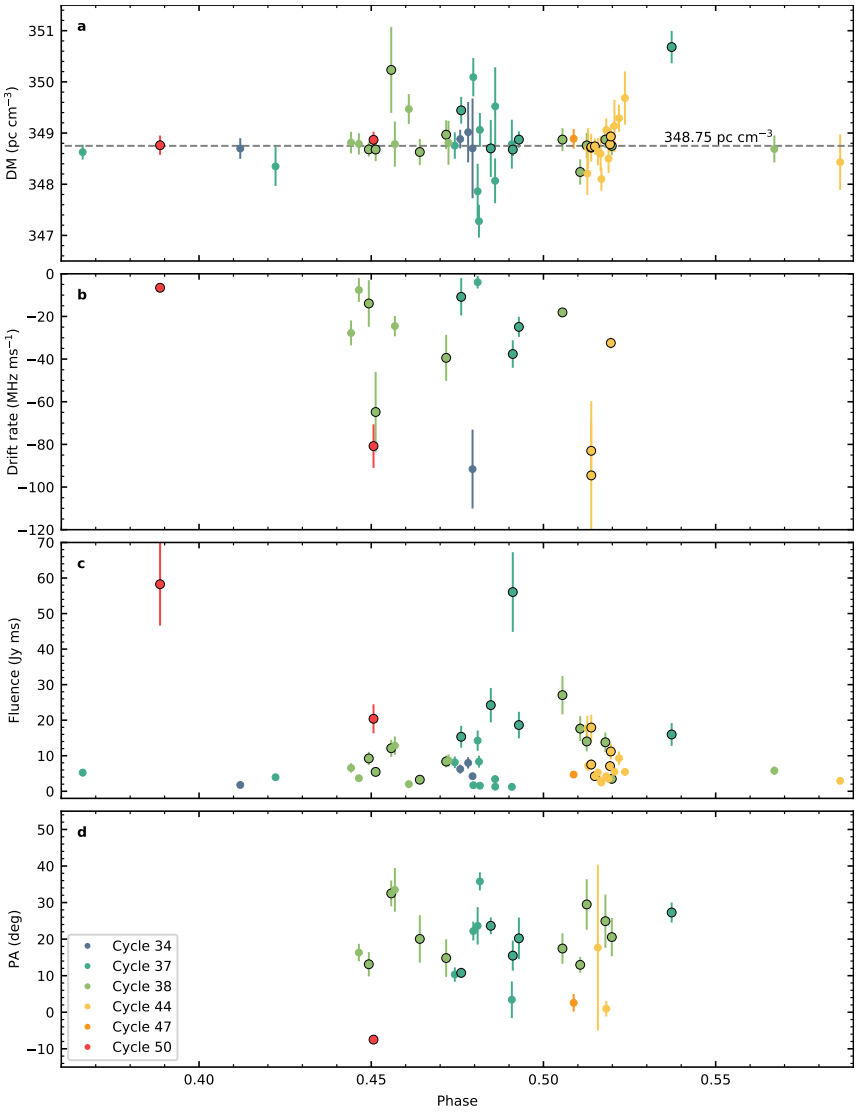

Figure 4.9: Apertif burst properties against phase. **a,** The structure-optimised dispersion measure, with the 348.75 pc cm^{-3} average as a reference. **b,** The drift rate of bursts with multiple components. **c,** The fluence. **d,** The average polarisation position angle of each burst. In **a**—**d,** Bursts are color-coded by activity cycle. Each color corresponds to a different activity cycle, and the data points with a black edge represent bursts with S/N>20. The error bars represent 1σ (s.d.) errors.

A linear fit to the resulting time-frequency sub-pulse centroids finally produced the burst drift rate. Figure 4.10 illustrates different burst morphologies and components counts.

We obtain an average sub-pulse drift rate of -39 ± 7 MHz ms^{-1} at 1370 MHz, where we quote the standard error on the mean. The standard deviation of the sample is 31 MHz ms^{-1}. This drift rate is nine times larger than e.g. the one reported at 400 MHz (Chawla et al. 2020) of ~ -4.2 MHz ms^{-1}. Figure 4.11 shows how the downward drift amplifies towards higher frequencies. We quantify the drift rate evolution by fitting a power-law $\dot{\nu} = k_p \nu^{\gamma}$, with k_p a constant and γ the power-law index, and a linear function $\dot{\nu} = k_l \nu$ with k_l a constant. Neither model allows drift rates to turn from negative to positive at a frequency $\nu > 0$, which we do not deem physically possible. A least squares minimisation fit to the power-law gives $\gamma = 0.7 \pm 0.4$ and $k_p = -0.2 \pm 0.6$, close to linear. The linear function itself is best fit as $k_l = -(2.9 \pm 0.4) \times 10^{-2}$. By scaling the fitted functions to the frequency of the LOFAR HBA, we would expect the drift rate to be around ~ -6 MHz ms^{-1} at 150 MHz. The apparent lack of multiple components in the LOFAR bursts do not allow us to confirm this. Overall, as in FRB 20121102A (Josephy et al. 2019), the drift rate evolution appears linear. As these two FRBs reside in significantly different environments, the behavior may be common across FRBs. The frequency-dependence and consistent sign of the drifting phenomenon will likely offer clues to the FRB emission mechanism (Metzger et al. 2019; Wang et al. 2019; Rajabi et al. 2020).

4.5.6 Scattering

Most of the LOFAR bursts (Fig. 4.2) exhibit an exponential tail, indicating the pulse-broadening due to scattering in the intervening medium. To quantify the scatter broadening timescale (τ_{sc}), we divided the dedispersed spectrograms of a few high S/N bursts into 4 or 8 sub-bands The burst profiles obtained from the individual sub-bands were modelled as a single Gaussian component convolved with a one-sided exponential function (Krishnakumar et al. 2017; Maan et al. 2019). The τ_{sc} thus obtained are presented in Table 4.1.

In order to obtain a more precise estimate of scatter-broadening timescale, we first divided the bandwidth of the stacked LOFAR bursts dedispersed to their DM$_{\rm LOFAR}$=349.0 pc cm^{-3} into eight frequency bands, for which we obtained separate pulse profiles and fitted each to a scattering tail as above. The results are shown in Fig. 4.12. We obtain the scattering timescale of 45.7$\pm$9.5 ms at 150 MHz, which is consistent with the measurements using individual bursts. We also characterize the scatter broadening variation with frequency as $\tau_{sc} \propto \nu^{-\alpha}$ and obtain the frequency scaling index $\alpha = -4.2 \pm^{1.1}_{1.0}$. This scatter-broadening is consistent with the upper limit of 50 ms at 150 MHz that was derived from GBT detections at 350 MHz (Chawla et al. 2020). By scaling the scatter broadening of LOFAR bursts to Apertif frequencies, we expect $\tau_{sc} \sim 6.6 \mu$s at 1370 MHz, which is an order of magnitude smaller than Apertif's temporal resolution.

The observed scattering time is within a factor of two of the predicted Galactic scattering (Cordes & Lazio 2003). Thus, we attribute this pulse broadening to scattering in the Milky Way interstellar medium (ISM) and not to plasma in the host galaxy. The fact that the ISM scattering is stronger in the Milky Way than in the host galaxy is not surprising, given FRB 20180916B is at a low galactic latitude, whereas its host is a nearly face-on spiral galaxy (Marcote et al. 2020).

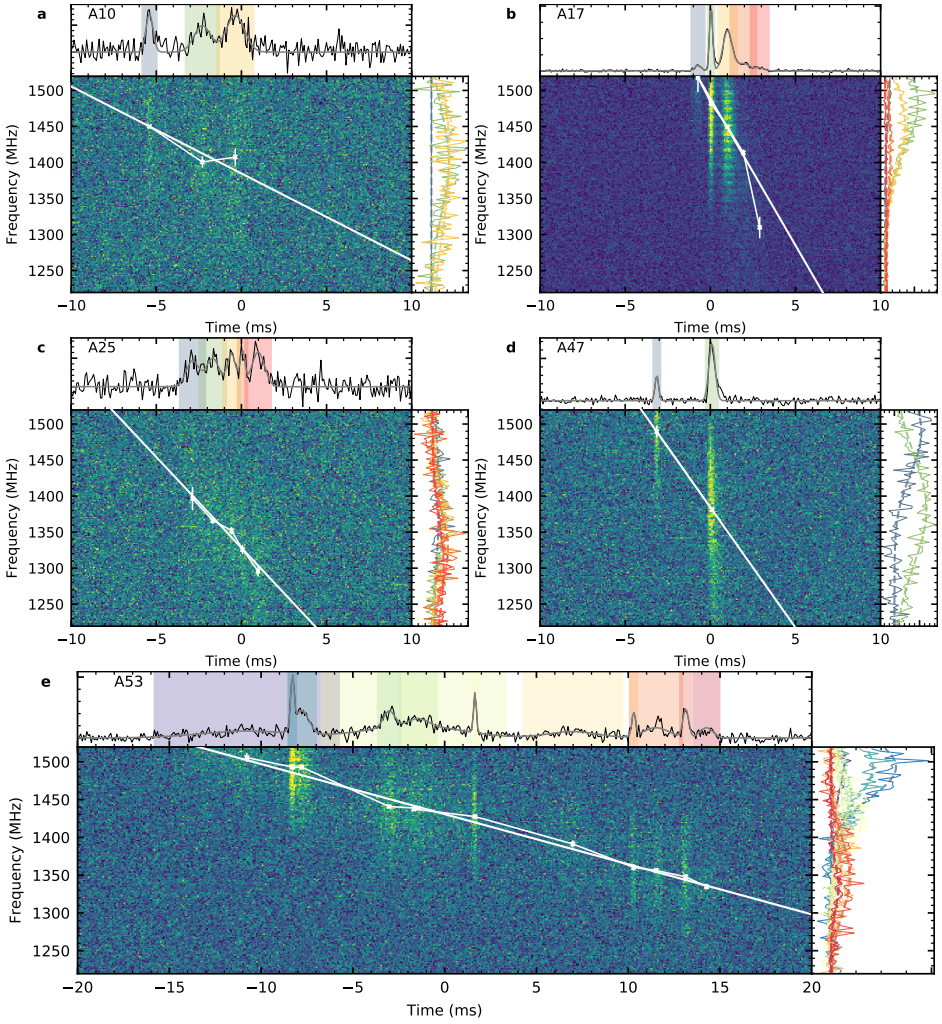

Figure 4.10: Five of the bursts with a measurable drift rate. **a**—**e,** For each burst, the top panel shows the pulse profile as a solid black line and the fitted multi-component Gaussian in gray. Coloured regions indicate the subcomponent position. The lower-left panels show the dynamic spectra, the subcomponent centroids with 1σ (s.d.) errors and the fitted drift rate (white line). The right panels display the spectra and the fitted Gaussian of each subcomponent, with the same color as the shaded region of the pulse profile.

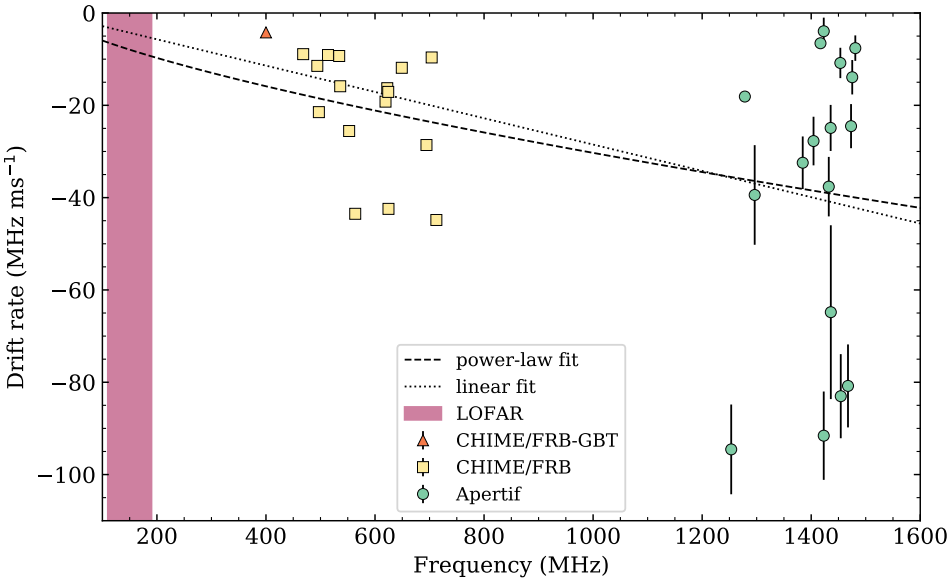

Figure 4.11: Comparison of drift rates at different frequencies. The green circles are the drift rate of bursts presented in this work, detected with Apertif. The yellow squares are drift rates from CHIME/FRB bursts (CHIME/FRB Collaboration et al. 2020; Chamma et al. 2021). The orange triangle is the simultaneous CHIME/FRB-GBT burst where a drift rate was reported (Chawla et al. 2020). The dashed line is a power law fit of the drift rate at different frequencies, $\dot{\nu} = -0.2\nu^{0.7}$. The dotted line is the linear fit of the drift rate, $\dot{\nu} = -2.9 \times 10^{-2}\nu$, and it is almost superposed to the power law fit.

4.5.7 Rates

Before our LOFAR detections, there existed only upper limits on the FRB sky rate below 200 MHz. Blind searches for fast transients at these low frequencies are difficult due to the deleterious smearing effects of intra-channel dispersion and scattering, which scale as ν^{-3} and ν^{-4}, respectively. This is amplified by the large sky brightness temperatures at long wavelengths, due to the red spectrum of Galactic synchrotron emission; pulsars are detectable at low frequencies because of their steeply rising negative spectra, but the spectral index of the FRB event rate is not known. We first consider the repetition rate of FRB 20180916B from our LOFAR and Apertif detections to determine its activity as function of frequency. We then convert that into a lower-limit on the all-sky FRB rate at 150 MHz and combine it with previous upper-limits at those frequencies to derive the first ever bounded constraints on FRB rates below 200 MHz.

We detected nine bursts in 48 h of LOFAR observing, giving a rate of $0.19 \pm 0.06\,\mathrm{h}^{-1}$. Since we only targeted LOFAR during simultaneous Apertif observations during the presumed activity window whose duty cycle is $\sim$0.25, we divide this rate by 4 to get its repetition rate averaged over time. Assuming a fluence threshold of 50 Jy ms and noting that the duration of all bursts from this source at 150 MHz is set by scattering and does not vary, we find $R_{150}(\geq 50\ \mathrm{Jy\,ms}) \approx (4.6 \pm 1.6) \times 10^{-2}\,\mathrm{h}^{-1}$. At 1370 MHz, Apertif detected 54 pulses in 388 hours of observing. Our coverage of FRB 20180916B was deliberately more uniform in activity phase, so only $\sim$149 h took

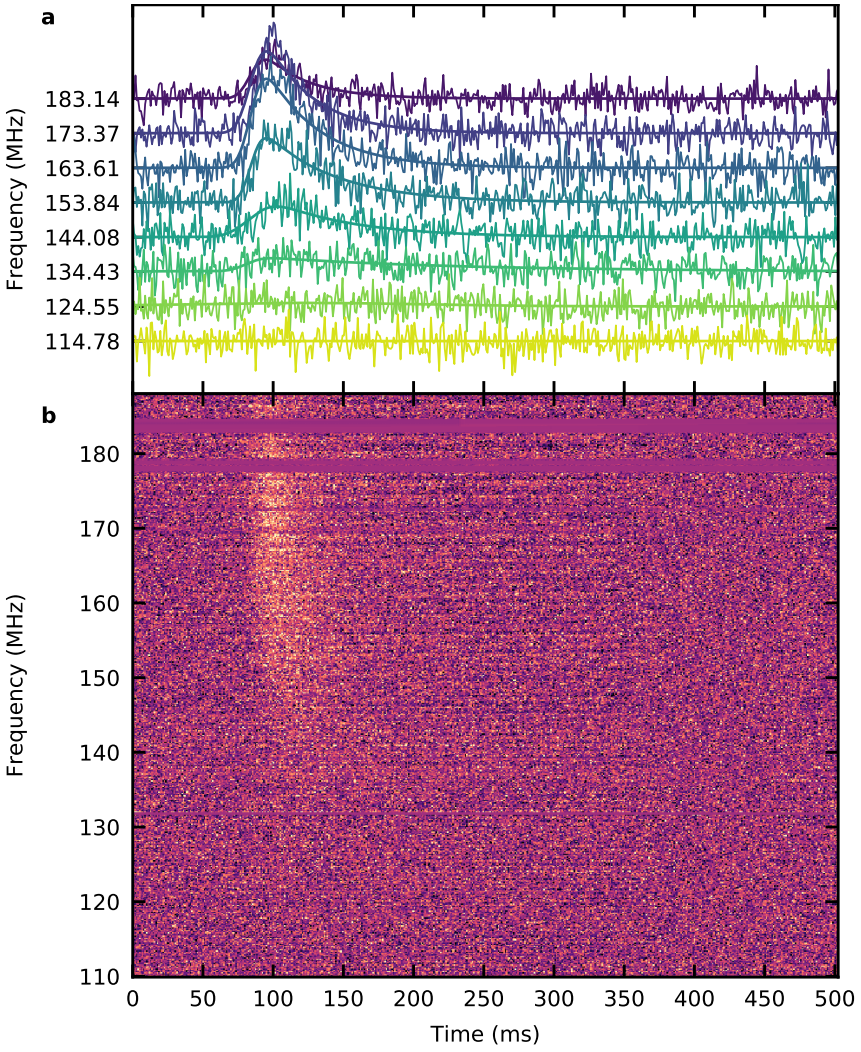

Figure 4.12: Stacked LOFAR bursts. After dedispersion to the S/N-maximising DM of 349.00 pc cm^{-3}, the individual bursts were co-added. **a.** The pulse profiles in eight different frequency bands of the co-added total, and fits to the scattering tail. The central frequency of the band is indicated on the vertical labels. **b.** The dynamic spectrum of the stacked bursts.

place during the active days. The phase range in which Apertif detected bursts gives a duty cycle of 0.22. This results in $R_{1370}(\geq 1\ \mathrm{Jy\,ms}) \approx (8.0 \pm 1.1) \times 10^{-2}\,\mathrm{h}^{-1}$. While the absolute detection rates by Apertif and LOFAR are similar, we note that the fluence threshold was much lower for Apertif than LOFAR. Scaling by the approximate fluence distribution of FRB 20180916B, $N(\geq \mathscr{F}) \propto \mathscr{F}^{-1.5}$ (CHIME/FRB Collaboration et al. 2020), we find $R_{1370}(\geq 50\ \mathrm{Jy\,ms}) \approx 2.3 \times 10^{-4}\,\mathrm{h}^{-1}$. We come to the remarkable conclusion that the FRB is two orders of magnitude more active at 150 MHz than at 1370 MHz at the relevant fluences.

The all-sky FRB event rate is a difficult quantity to determine for a myriad of reasons (Rane et al. 2016). Beam effects result in a pointing-dependent sensitivity threshold (Lawrence et al. 2017; Vedantham et al. 2016); Each survey has back-end dependent incompleteness, including in flux density and fluence (Keane & Petroff 2015) as well as in pulse duration and DM (Connor 2019). Nonetheless, meaningful constraints can be made if one is explicit about the region of parameter space to which the rate applies.

As the LOFAR bursts are the sole unambiguous FRB detections below 200 MHz, we and other teams (Pleunis et al. 2021b) can now provide the first bounded limits on the all-sky event rate at low frequencies. A lower limit on the FRB rate at 150 MHz can be obtained by assuming FRB 20180916B is the only source in the sky emitting at these wavelengths. This lower bound can be combined with previous upper bounds from non detections by blind searches at LOFAR and MWA (Karastergiou et al. 2015; Coenen et al. 2014; ter Veen et al. 2019; Tingay et al. 2015; Rowlinson et al. 2016; Sokolowski et al. 2018). The repetition rate of FRB 20180916B implies that there are at least $0.6\,\mathrm{sky}^{-1}\,\mathrm{day}^{-1}$ above 50 Jy ms at 110–190 MHz at 95% confidence. Assuming a Euclidean scaling in the brightness distribution that continues down to lower fluences, this is equivalent to more than $90\,\mathrm{sky}^{-1}\,\mathrm{day}^{-1}$ above 5 Jy ms. An earlier blind LOFAR search (Karastergiou et al. 2015) placed an upper limit of $29\,\mathrm{sky}^{-1}\,\mathrm{day}^{-1}$ above 62 Jy pulses with 5 ms duration. Combining these two limits, we obtain a 90% confidence region of 3–$450\,\mathrm{sky}^{-1}\,\mathrm{day}^{-1}$ above 50 Jy ms.

The lower-limit value may be conservative, as FRB 20180916B is in the Galactic plane at a latitude of just 3.7 deg, which is why its scattering time is 50 ms at 150 MHz. If the burst width were 5 ms before entering the Milky Way, then a factor of $\sim$3 was lost in S/N due to the low Galactic latitude of FRB 20180916B. Therefore, a similar FRB at a more typical offset from the plane would, in this example, be $\sim 3^{\gamma}$ times more active, where γ is the cumulative energy distribution power-law index, because the Galactic scattering timescale would only be a few milliseconds.

4.6 Data and code availability

Raw data were generated by the Apertif system on the Westerbork Synthesis Radio Telescope and by the International LOFAR Telescope. The Apertif data that support the findings of this study are available through the ALERT archive, http://www.alert.eu/FRB20180916B. The LOFAR data are available through the LOFAR Long Term Archive, https://lta.lofar.eu/, by searching for "Observations" at J2000 coordinates RA=01:57:43.2000, DEC=+65:42:01.020. The custom code used to generate these results is publicly available at https://doi.org/10.5281/zenodo.4559593.

Acknowledgements

This research was supported by the European Research Council under the European Union's Seventh Framework Programme (FP/2007-2013)/ERC Grant Agreement No. 617199 ('ALERT'), and by Vici research programme 'ARGO' with project number 639.043.815, financed by the Dutch Research Council (NWO). Instrumentation development was supported by NWO (grant 614.061.613 'ARTS') and the Netherlands Research School for Astronomy ('NOVA4-ARTS', 'NOVA-NW3', and 'NOVA5-NW3-10.3.5.14'). We further acknowledge funding from an NWO Veni Fellowship to EP; from Netherlands eScience Center (NLeSC) grant ASDI.15.406 to DV and AS; from National Aeronautics and Space Administration (NASA) grant number NNX17AL74G issued through the NNH16ZDA001N Astrophysics Data Analysis Program (ADAP) to SMS; by the WISE research programme, financed by NWO, to EAKA; from FP/2007-2013 ERC Grant Agreement No. 291531 ('HIStoryNU') to TVDH; and from VINNOVA VINNMER grant 2009-01175 to VMI.

IPM and YM thank M. A. Krishnakumar for providing a software module that was useful in estimating the scatter-broadening timescale. This work makes use of data from the Apertif system installed at the Westerbork Synthesis Radio Telescope owned by ASTRON. ASTRON, the Netherlands Institute for Radio Astronomy, is an institute of NWO.

This paper is based (in part) on data obtained with the International LOFAR Telescope (ILT) under project code COM_ALERT. These data are accessible through the LOFAR Long Term Archive, https://lta.lofar.eu/, by searching for ''Observations'' with the J2000 coordinates RA 01:57:43.2000 and DEC +65:42:01.020, or by selecting COM_ALERT in ''Other projects'' and downloading data which includes R3 in the ''Observation Description''. LOFAR (van Haarlem et al. 2013) is the Low Frequency Array designed and constructed by ASTRON. It has observing, data processing, and data storage facilities in several countries, that are owned by various parties (each with their own funding sources), and that are collectively operated by the ILT foundation under a joint scientific policy. The ILT resources have benefitted from the following recent major funding sources: CNRS-INSU, Observatoire de Paris and Université d'Orléans, France; BMBF, MIWF-NRW, MPG, Germany; Science Foundation Ireland (SFI), Department of Business, Enterprise and Innovation (DBEI), Ireland; NWO, The Netherlands; The Science and Technology Facilities Council, UK; Ministry of Science and Higher Education, Poland.

We acknowledge use of the CHIME/FRB Public Database, provided at https://www.chime-frb.ca/ by the CHIME/FRB Collaboration.

4.7 Extended data

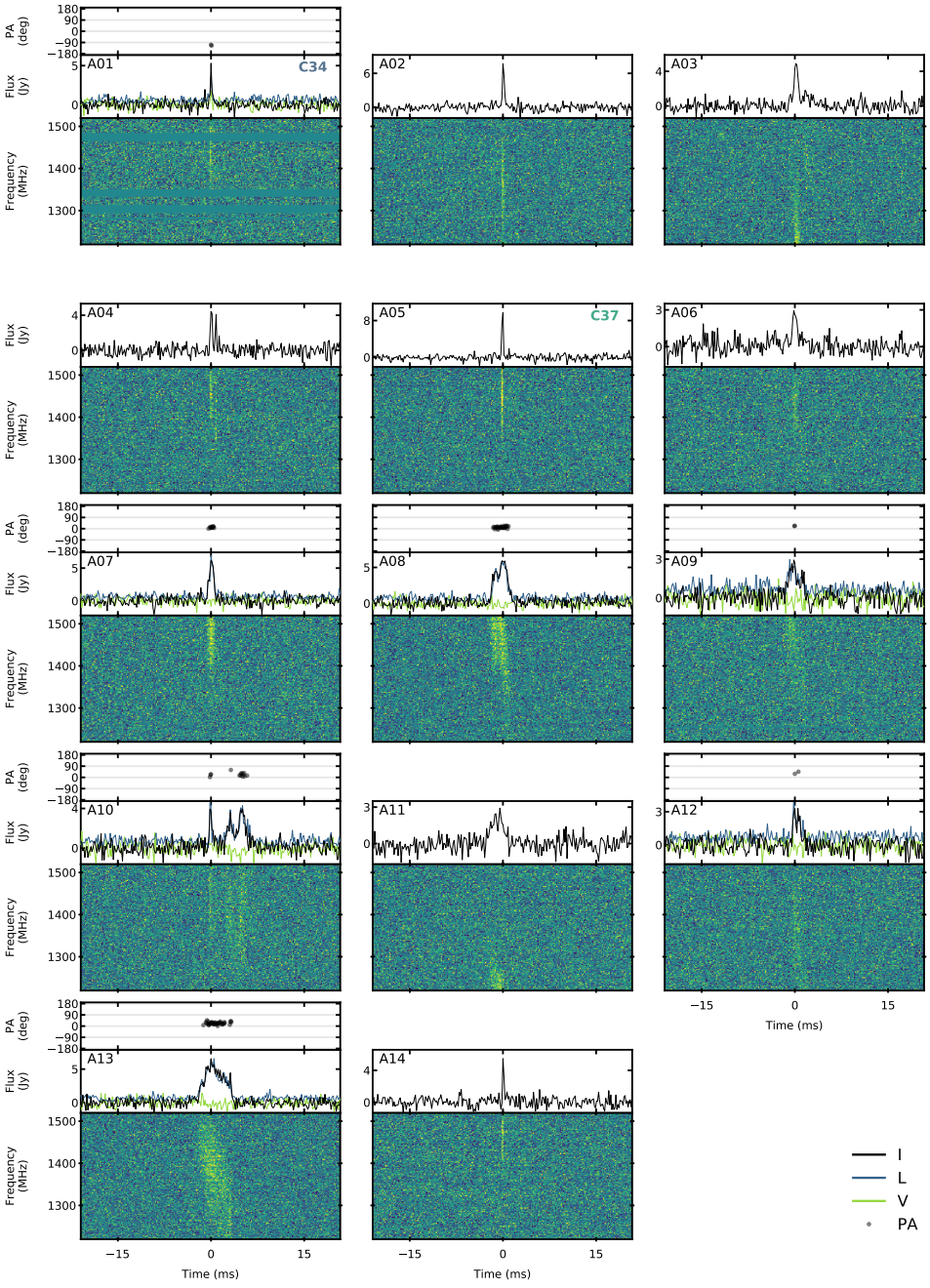

Figure 4.13: Dynamic spectra of Apertif bursts (A01-A14). We display PA (top panel), stokes parameters ILV (central panel) and dynamic spectra (bottom panel), for bursts with full-Stokes data (cf. A01). Bursts with only intensity data, such as A02, are limited to the total intensity profile. Burst identifiers are given in the top left corners, and activity cycle number in top-right. Dedispersed to DM=348.75 pc cm^{-3}, downsampled 2× and 8× in time and frequency.

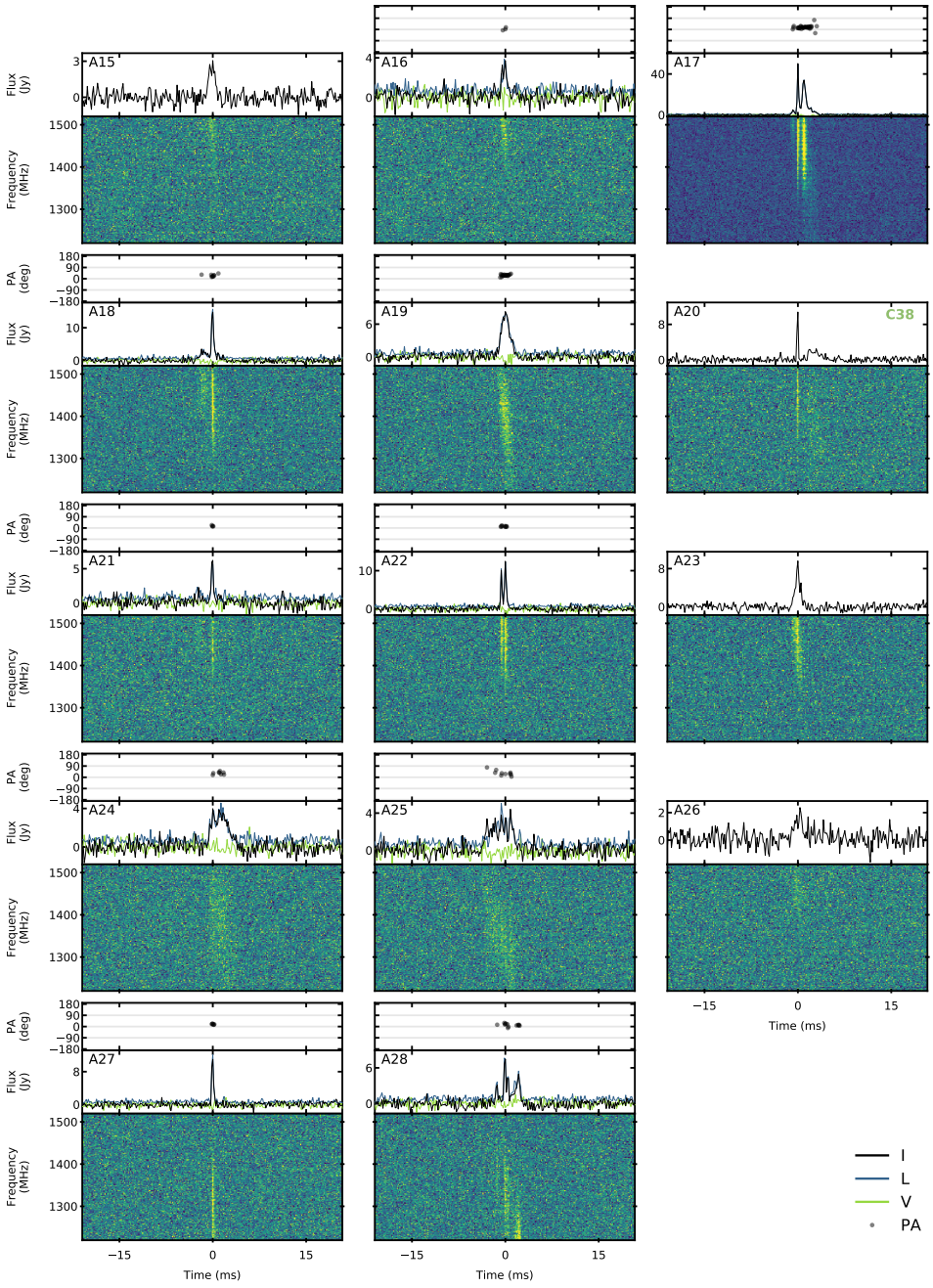

Figure 4.13: Continued, bursts (A15-A28).

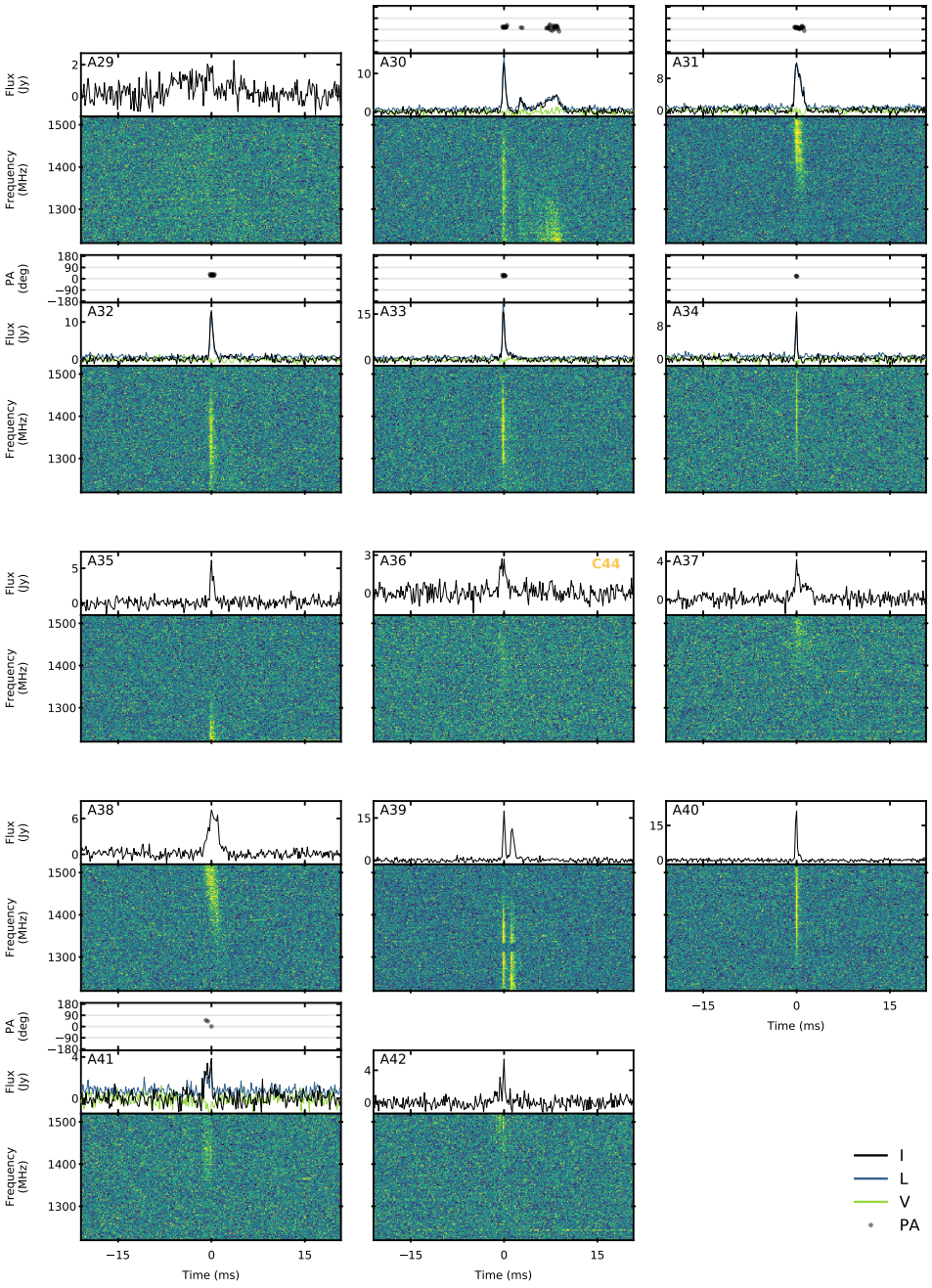

Figure 4.13: Continued, bursts (A29-A42).

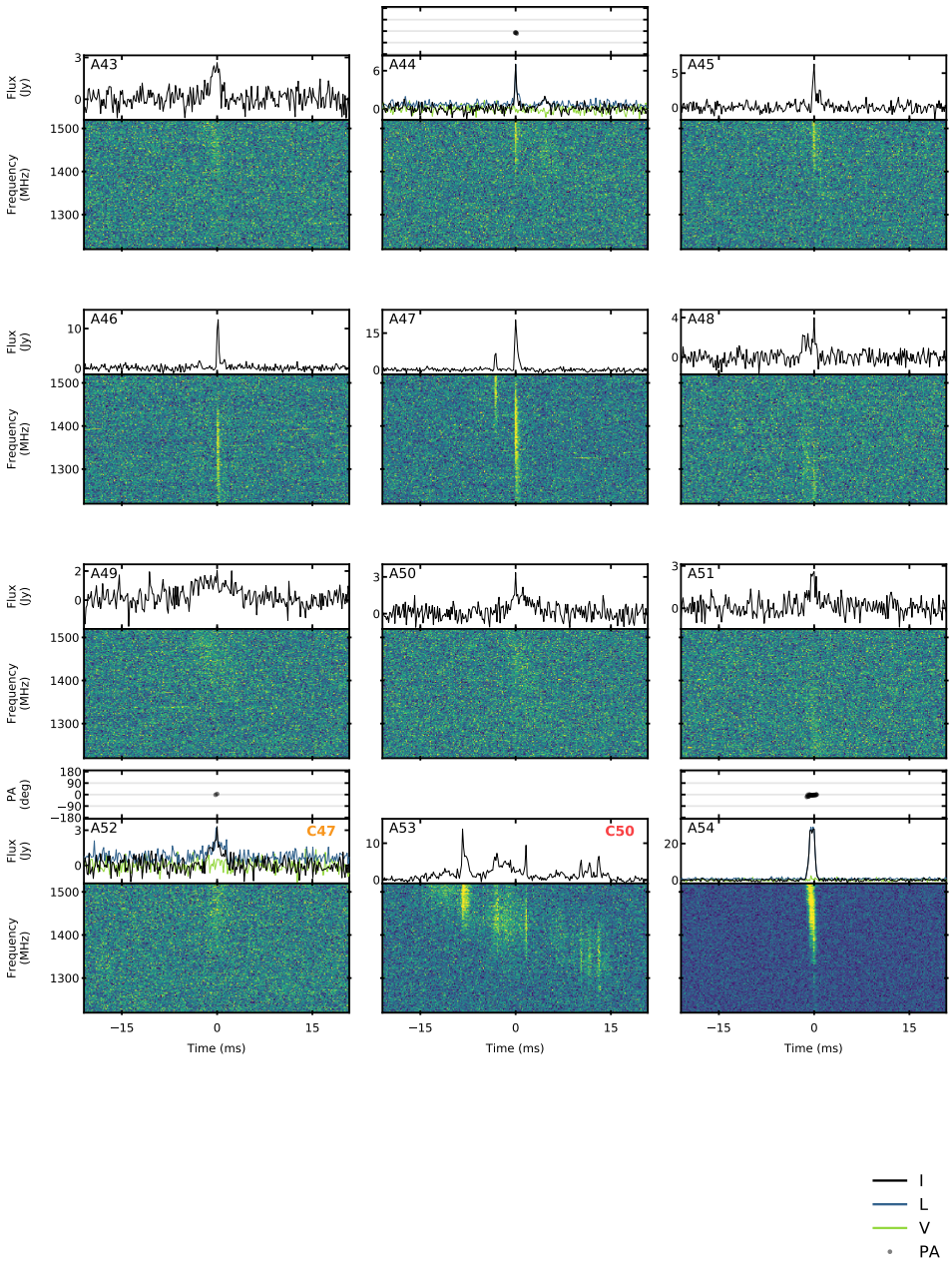

Figure 4.13: Continued, bursts (A43-A54).

Table 4.1: Summary of LOFAR burst properties.

Burst ID	OBSID	Arrival time (MJD)	Arrival time (UTC)	Detection S/N	DM ($\mathrm{pc\,cm^{-3}}$)	Fluence (Jy ms)	τ_{sc} at 150 MHz (ms)
L01	L775795	58949.53491816	2020-04-10 12:50:16.929	8.7	349.03±0.11	111±55	...
L02	L775801	58949.63987585	2020-04-10 15:21:25.273	7.3	348.94±0.08	38±19	...
L03	L775977	58950.52919335	2020-04-11 12:42:02.305	9.5	349.02±0.08	80±40	...
L04	L775977	58950.54130169	2020-04-11 12:59:28.466	18.9	349.41±0.03	177±88	...
L05	L775979	58950.58347838	2020-04-11 14:00:12.532	13.7	349.09±0.04	129±64	...
L06	L775953	58951.54162736	2020-04-12 12:59:56.604	29.4	349.03±0.05	318±159	48.2±16.6
L07	L775953	58951.55801455	2020-04-12 13:23:32.457	35.1	348.98±0.02	296±148	46.9±16.0
L08	L775955	58951.58470795	2020-04-12 14:01:58.767	23.5	348.99±0.03	193±96	36.2±19.0
L09	L775955	58951.59135120	2020-04-12 14:11:32.744	12.5	348.86±0.08	124±62	42.0±17.4

Table 4.2: Summary of Apertif burst properties.

Burst ID	Arrival time (MJD)	Arrival time (UTC)	Detection S/N	DM ($pc\,cm^{-3}$)	Fluence (Jy ms)	Drift rate ($MHz\,ms^{-1}$)
A01	58930.47097294	2020-03-22T11:18:12.062	11.5	348.70(20)	1.8	...
A02	58931.51122577	2020-03-23T12:16:09.907	12.7	348.88(18)	6.2	...
A03	58931.54877968	2020-03-23T13:10:14.564	13.4	349.02(59)	8.0	...
A04	58931.56964778	2020-03-23T13:40:17.568	13.4	348.70(97)	4.2	-91.58
A05	58978.59561357	2020-05-09T14:17:41.012	13.6	348.63(14)	5.2	...
A06	58979.50785914	2020-05-10T12:11:19.030	8.9	348.35(38)	4.0	...
A07	58980.35572077	2020-05-11T08:32:14.275	16.4	348.75(26)	8.2	...
A08	58980.38590828	2020-05-11T09:15:42.475	29.9	349.44(26)	15.3	-10.82
A09	58980.44318898	2020-05-11T10:38:11.528	13.9	350.09(37)	1.7	...
A10	58980.46375074	2020-05-11T11:07:48.064	17.8	347.86(54)	14.2	-3.95
A11	58980.46995949	2020-05-11T11:16:44.500	10.1	347.28(32)	8.3	...
A12	58980.47426015	2020-05-11T11:22:56.077	11.0	349.06(33)	1.6	...
A13	58980.52593337	2020-05-11T12:37:20.643	38.6	348.70(56)	24.2	...
A14	58980.54629988	2020-05-11T13:06:40.310	14.0	348.07(44)	3.4	...
A15	58980.54684270	2020-05-11T13:07:27.209	12.5	349.52(76)	1.3	...
A16	58980.62542392	2020-05-11T15:00:36.627	11.5	348.78(48)	1.2	...
A17	58980.62998094	2020-05-11T15:07:10.353	58.1	348.68(13)	56.0	-37.62
A18	58980.65889322	2020-05-11T15:48:48.374	25.6	348.87(16)	18.6	-24.90
A19	58981.38138907	2020-05-12T09:09:12.016	31.5	350.68(32)	16.0	...
A20	58996.15501128	2020-05-27T03:43:12.975	12.1	348.81(21)	6.6	-27.74
A21	58996.19203445	2020-05-27T04:36:31.776	12.7	348.79(21)	3.7	-7.61
A22	58996.23898191	2020-05-27T05:44:08.037	20.2	348.68(14)	9.2	-13.91
A23	58996.27129126	2020-05-27T06:30:39.565	20.9	348.68(23)	5.5	-64.82
A24	58996.34499129	2020-05-27T08:16:47.247	21.4	350.23(84)	12.1	...
A25	58996.36224320	2020-05-27T08:41:37.812	19.5	348.78(44)	12.8	-24.51
A26	58996.42810299	2020-05-27T10:16:28.098	10.5	349.47(29)	2.0	...
A27	58996.48015176	2020-05-27T11:31:25.112	21.0	348.63(25)	3.2	...
A28	58996.60480633	2020-05-27T14:30:55.267	20.9	348.97(28)	8.4	-39.42
A29	58996.61583838	2020-05-27T14:46:48.436	9.0	348.81(43)	8.7	...
A30	58997.15492630	2020-05-28T03:43:05.632	25.7	348.87(22)	27.1	-18.10
A31	58997.23883623	2020-05-28T05:43:55.450	36.5	348.24(25)	17.6	...
A32	58997.26968437	2020-05-28T06:28:20.730	29.9	348.76(25)	14.0	...
A33	58997.35800780	2020-05-28T08:35:31.874	29.2	348.87(17)	13.8	...
A34	58997.38837259	2020-05-28T09:19:15.392	20.9	348.75(18)	3.5	...
A35	58998.15708057	2020-05-29T03:46:11.761	10.4	348.69(26)	5.8	...
A36	59095.01258701	2020-09-03T00:18:07.518	8.5	348.21(42)	17.7	...
A37	59095.01647024	2020-09-03T00:23:43.029	10.3	348.70(40)	7.2	...
A38	59095.03083630	2020-09-03T00:44:24.256	27.4	348.71(27)	7.5	-83.02
A39	59095.03119917	2020-09-03T00:44:55.608	28.2	348.73(11)	17.9	-94.55
A40	59095.04813576	2020-09-03T01:09:18.930	25.8	348.74(16)	4.2	...
A41	59095.06242878	2020-09-03T01:29:53.847	11.4	348.64(26)	5.3	...
A42	59095.07525644	2020-09-03T01:48:22.156	12.7	348.59(34)	3.1	...
A43	59095.07913932	2020-09-03T01:53:57.637	11.5	348.10(23)	2.5	...
A44	59095.10211216	2020-09-03T02:27:02.491	12.6	349.06(23)	4.2	...
A45	59095.11289895	2020-09-03T02:42:34.469	13.2	348.50(28)	3.5	...
A46	59095.11989684	2020-09-03T02:52:39.087	20.7	348.78(14)	7.1	...
A47	59095.12368446	2020-09-03T02:58:06.337	32.4	348.93(23)	11.2	-32.44
A48	59095.14075045	2020-09-03T03:22:40.839	10.0	349.14(51)	5.5	...
A49	59095.16236684	2020-09-03T03:53:48.495	10.7	349.29(26)	9.3	...
A50	59095.19030365	2020-09-03T04:34:02.235	9.4	349.68(52)	5.5	...
A51	59096.20840871	2020-09-04T05:00:06.513	9.3	348.43(54)	2.9	...
A52	59143.81778929	2020-10-21T19:37:36.995	11.3	348.89(19)	4.7	...
A53	59190.73164688	2020-12-07T17:33:34.290	44.2	348.76(19)	58.3	-6.55
A54	59191.74125466	2020-12-08T17:47:24.403	51.1	348.87(16)	20.4	-80.80

5

A Fast Radio Burst with sub-millisecond quasi-periodic structure

I. Pastor-Marazuela, J. van Leeuwen, A. Bilous, L. Connor, Y. Maan, L. Oostrum, E. Petroff, S. Straal, D. Vohl, E. A. K. Adams, B. Adebahr, J. Attema, O. M. Boersma, R. van den Brink, W. A. van Cappellen, A. H. W. M. Coolen, S. Damstra, H. Dénes, K. M. Hess, J. M. van der Hulst, B. Hut, A. Kutkin, G. Marcel Loose, D. M. Lucero, Á. Mika, V. A. Moss, H. Mulder, M.J. Norden, T. A. Oosterloo, K. Rajwade, D. van der Schuur, A. Sclocco, R. Smits, J. Ziemke

Submitted to Astronomy & Astrophysics. arXiv e-prints, arXiv:2202.08002

Abstract

Fast radio bursts (FRBs) are extragalactic radio transients of extraordinary luminosity. Studying the diverse temporal and spectral behaviour recently observed in a number of FRBs may help determine the nature of the entire class. For example, a fast spinning or highly magnetised neutron star might generate the rotation-powered acceleration required to explain the bright emission. Periodic, sub-second components, suggesting such rotation, were recently reported in one FRB, and potentially in two more. Here we report the discovery of FRB 20201020A with Apertif, an FRB that shows five components regularly spaced by 0.415 ms. This sub-millisecond structure in FRB 20201020A carries important clues about the progenitor of this FRB specifically, and potentially about that of FRBs in general. We thus contrast its features to the predictions of the main FRB source models. We perform a timing analysis of the FRB 20201020A components to determine the significance of the periodicity. We compare these against the timing properties of the previously reported CHIME FRBs with sub-second quasi-periodic components, and against two Apertif bursts from repeating FRB 20180916B that show complex time-frequency structure. We find the periodicity of FRB 20201020A to be marginally significant at 2.5σ. Its repeating subcomponents cannot be explained as a pulsar rotation since the required spin rate of over 2 kHz exceeds the limits set by typical neutron star equations of state and observations. The fast periodicity is also in conflict with a compact object merger scenario. These quasi-periodic components could, however, be caused by equidistant emitting regions in the magnetosphere of a magnetar. The sub-millisecond spacing of the components in FRB 20201020A, the smallest observed so far in a one-off FRB, may rule out both neutron-star rotation and binary mergers as the direct source of quasi-periodic FRBs.

5.1 Introduction

Fast radio bursts (FRBs) are bright, millisecond-duration radio transients of extragalactic origin that have puzzled researchers since their discovery (Lorimer et al. 2007; see Petroff et al. 2019 and Cordes & Chatterjee 2019 for a review of properties). While most FRBs are only seen once (one-offs), around 24 have been seen to repeat (e.g. Spitler et al. 2016; CHIME/FRB Collaboration et al. 2019a). There is no consensus yet on whether these two observational classes are produced by the same types of sources or if they have different origins. Many models invoke compact objects as the source of FRBs (see Platts et al. 2019), and several observational clues point at magnetars as the progenitors of at least some FRBs (see Zhang 2020b, and references therein). After the detection of a bright radio burst from the Galactic magnetar SGR 1935+2154 (Bochenek et al. 2020; CHIME/FRB Collaboration 2020), we now know that at least some FRBs could be produced by magnetars.

Recently, the Canadian Hydrogen Intensity Mapping Experiment Fast Radio Burst Project (CHIME/FRB) published the largest catalog of FRBs detected with a single instrument to date (CHIME/FRB Collaboration et al. 2021a). While repeaters and non repeaters show similar sky distributions, dispersion measures (DM) and scattering timescales, repeaters have been seen to display a distinctive time and frequency structure commonly referred to as the ‘‘sad trombone effect’’ (Hessels et al. 2019), in which multi-component bursts drift downwards in frequency. On the other hand, one-off FRBs can present single-component bursts, either narrow or broadband, as well as multi-component bursts with similar frequency extent (Pleunis et al. 2021a).

Several works have carried out short-timescale timing analyses, including periodicity searches, in multi-component bursts from repeating FRBs. Nimmo et al. (2021, 2022a) find sub-component separations in FRB 20180916B and FRB 20200120E of just a few μs, but no evidence of periodicity. Meanwhile, Majid et al. (2021) find hints for a regular separation of 2-3 μs in the subcomponents of a burst from FRB 20200120E.

CHIME/FRB Collaboration et al. (2021b) recently reported the detection of a one-off FRB with $\geq$9 components, FRB 20191221A, showing a strict periodic separation of 216.8 ms between its components and a total duration of $\sim$ 3 s. This phenomenon is different from the long-term periodicity that two repeating FRBs have earlier been proved to show; FRB 20180916B with a period of $\sim$ 16.3 days (CHIME/FRB Collaboration et al. 2020), and FRB 20121102A with a period of $\sim$ 160 days (Rajwade et al. 2020; Cruces et al. 2020). These two repeating FRBs show a periodicity in their activity cycles, with a period $>$ 10 days, while FRB 20191221A shows a periodic structure within the subcomponents of the only detected burst, with a period $<$ 1 s. From here on, our use of the term ‘‘periodic’’ only refers to this latter, generally sub-second, fast periodicity. CHIME/FRB Collaboration et al. (2021b) report two additional one-off multi-component FRBs, FRB 20210206A and FRB 20210213A, with apparent periodic separations of 2.8 and 10.7 ms respectively, though at a lower significance. This hints to the potential existence of a new sub-group of one-off FRBs showing (quasi-)periodic sub-second components.

Prompted by the CHIME/FRB detections of FRB 20191221A, FRB 20210206A, and FRB 20210213A, we searched the Apertif FRBs for bursts with (quasi-)periodic structure. In this work, we report the detection of FRB 20201020A with the Apertif Radio Transient System (ARTS;

van Leeuwen 2014) installed at the Westerbork Synthesis Radio Telescope (WSRT; Adams & van Leeuwen 2019; van Cappellen et al. 2022). FRB 20201020A shows five components with a regular spacing of 0.415 ms. Furthermore, we perform a detailed timing analysis of the bursts A17 and A53 from FRB 20180916B that were first reported in Pastor-Marazuela et al. (2021), which also exhibit complex time and frequency structure that we compare to that of FRB 20201020A. In Section 5.2 we present the detection, observations and properties of FRB 20201020A, including its localisation, scintillation bandwidth and repetition rate upper limit. Section 5.3 explains the timing analysis of FRB 20201020A as well as the FRB 20180916B bursts A17 and A53. In Section 5.4 we discuss the interpretation of the temporal structure seen in FRB 20201020A, and assert that it belongs to the same morphological type as the CHIME FRBs 20210206A and 20210213A. Finally, we give our conclusions in Section 5.5.

5.2 Observations and data reduction

The Apertif Radio Transient System (ARTS) is currently carrying out an FRB survey which started in July 2019 (van Leeuwen et al. 2022) using ten 25-m dishes of the WSRT. In survey observing mode, we beamform 40 compound beams (CBs) covering a field of view (FoV) of 9.5 deg^2. Stokes I data is saved with a time resolution of 81.92 μs at a central frequency of 1370 MHz with 300 MHz bandwidth and a frequency resolution of 0.195 MHz (see Maan & van Leeuwen 2017; Oostrum et al. 2020, for further detail). The Stokes I data is then searched for transients in real-time with `AMBER`[1] (Sclocco et al. 2014, 2016, 2019). Next, a machine learning classifier assigns the probability to each candidate of it being a real FRB (Connor & van Leeuwen 2018), and the best FRB candidates are then sent in an email for human inspection.

FRB 20201020A was detected during a follow-up observation of the repeating FRB 20190303A (Fonseca et al. 2020). It was detected in three adjacent compound beams (CBs), with a maximum signal-to-noise ratio (SNR) of $\sim$53. Since its dynamic spectrum shows complex time-frequency structure, we used a structure maximisation algorithm (Gajjar et al. 2018; Hessels et al. 2019; Pastor-Marazuela et al. 2021) to get its optimal dispersion measure (DM) of 398.59(8) $\mathrm{pc\,cm^{-3}}$. The FRB properties are summarised in Table 5.1, and its dynamic spectrum is shown in Fig. 5.1.

The detection of bursts A17 and A53 from FRB 20180916B was originally reported in Pastor-Marazuela et al. (2021), where the observations and data reduction were already explained.

5.2.1 Burst structure

After dedispersing to the structure maximising DM, the pulse profile shows five distinct components with no visible scattering. In order to better characterise the intensity variation with time, we fitted the pulse profile to a five component gaussian and give the result in Table 5.2. The ToAs are given with respect to the arrival of the first component, and the component width is defined as the full width at half maximum (FWHM). The resulting burst component widths are unresolved due to intra-channel dispersive smearing, so given our time resolution the scattering timescale must be negligible. The total duration of the burst is 2.14(2) ms.

[1] https://github.com/TRASAL/AMBER

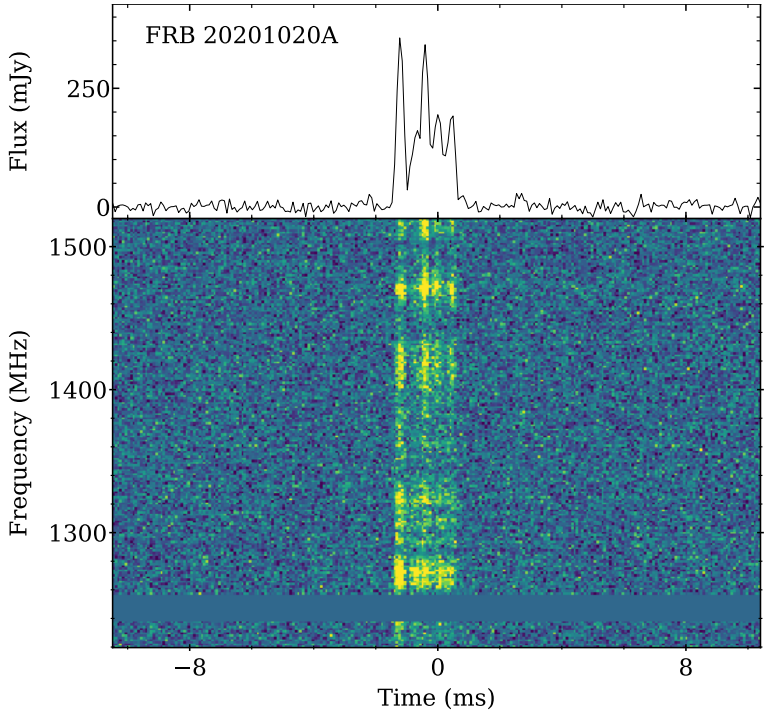

Figure 5.1: Dynamic spectrum of FRB 20201020A, dedispersed to a DM of 398.59 pc cm^{-3}. The top panel shows the average calibrated pulse profile of the burst, and the bottom panel the intensity of the burst in time versus frequency. The data has been downsampled in frequency by a factor 8.

Table 5.1: FRB 20201020A properties

FRB 20201020A properties	
Dispersion measure (DM)	398.59(8) pc cm^{-3}
Arrival time	2020-10-20 12:09:17.385
Barycentric MJD	59142.50645121
Detection SNR (CB29)	53.34
Right ascension (J2000)	$13^{\mathrm{h}}51^{\mathrm{m}}25^{\mathrm{s}}$
Declination (J2000)	$+49°02'06''$
Ellipse major and minor axes	$3.9' \times 17.2''$
Ellipse angle (N-E)	103.9°
Fluence	3.4(7) Jy ms
Peak flux	14.0(3) Jy
Total width	2.14(2) ms
Scintillation bandwidth	9.8(9) MHz
Rotation measure (RM)	$+110 \pm 69$ rad m^{-2}

Table 5.2: Properties of the five FRB 20201020A components. The first column gives the component number, the second the time of arrival in ms and the third the component width defined as the full width at half maximum (FWHM). Parenthesis give the one sigma uncertainties on the last digit.

Component	ToA (ms)	Width (ms)
0	0.000(4)	0.26(1)
1	0.50(2)	0.32(4)
2	0.810(7)	0.23(2)
3	1.222(9)	0.39(4)
4	1.664(7)	0.26(2)

The burst shows frequency-dependent intensity variations, as expected from scintillation produced by propagation through the turbulent interstellar medium (ISM) (see section 4.2.2 from Lorimer & Kramer 2004, and references therein). In order to measure the scintillation bandwidth, we generated the auto-correlation function (ACF) of the burst averaged spectrum, defined as follows:

$$\mathrm{ACF}(\Delta\nu) = \frac{\sum_{\nu}(S(\nu))(S(\nu+\Delta\nu))}{\sqrt{\sum_{\nu}(S(\nu))^2 \sum_{\nu}(S(\nu+\Delta\nu))^2}}, \tag{5.1}$$

where $S(\nu)$ is the burst averaged spectrum at frequency ν and $\Delta\nu$ the frequency lag. This is computed at the original frequency resolution. After removing the zero-lag value, we fitted the central peak of the ACF to a lorentzian. The scintillation bandwidth is often defined as the full-width at half-maximum (FWHM) of the fitted lorentzian (Cordes 1986). The YMW16 (Yao et al. 2017) and NE2001 (Cordes & Lazio 2003) models give the distribution of free electrons in the Milky Way (MW), and can thus be used to estimate the DM, scattering and scintillation contribution from the Galaxy. Comparing the resulting scintillation bandwidth of $\Delta\nu_{\mathrm{FRB}} = 9.8(9)$ MHz with the expected contribution from the MW in the direction of the FRB at 1370 MHz, we find that it is consistent both with the YMW16 model, where $\Delta\nu_{\mathrm{YMW16}} \sim 10.4$ MHz, and the NE2001 model, where $\Delta\nu_{\mathrm{NE2001}} \sim 16.0$ MHz[1]. The ACF and its fit to a lorentzian function are displayed in Fig. 5.2. By eye, all burst components seem to cover a similar frequency extent. In order to thoroughly check whether the subcomponents exhibit a downward drift in frequency, we computed the 2D auto-correlation function of the burst, which we ultimately fitted to a 2D ellipse whose inclination gives a good estimate of the drift rate (Hessels et al. 2019). The resulting 2D ACF, shown in Fig. 5.7, shows an inclination angle consistent with being vertical, which means there is no subcomponent frequency drift.

5.2.2 Localisation

Since the WSRT is an array in the East-West direction, it can localise any detected FRB to a narrow ellipse (cf. Connor et al. 2020). FRB 20201020A was detected in three adjacent CBs;

[1] Values estimated at 1370 MHz with the `pygedm` package: https://pygedm.readthedocs.io/en/latest/

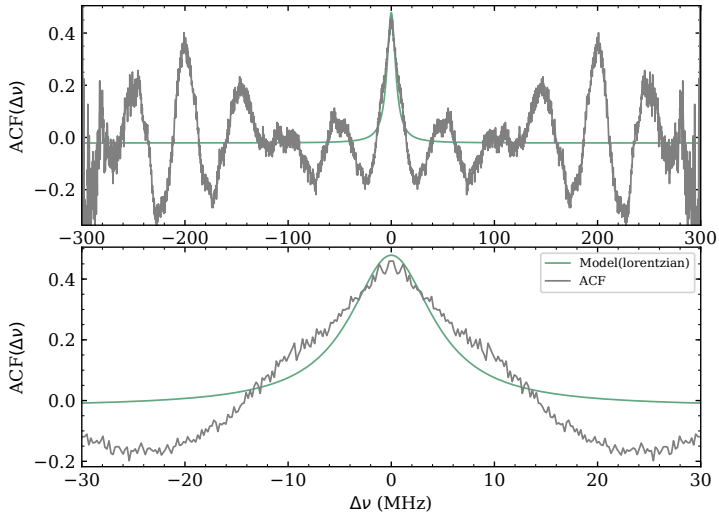

Figure 5.2: Auto-correlation function of the spectrum of FRB 20201020A. The grey line shows the ACF (see Eq. 5.1) and the green line the lorentzian fitted to the central peak. The top panel shows the ACF of the whole observing bandwidth, while the bottom panel is a zoom in on the central peak.

CB29, CB35 and CB28. Following the localisation procedure as described in Oostrum (2020)[1], we used the SNR of the burst in all synthesised beams (SBs) of all CBs where it was detected to get its 99% confidence region. We find the best position to be RA $=13^{\mathrm{h}}51^{\mathrm{m}}25^{\mathrm{s}}$ and Dec $=+49^{\circ}02'06''$. The localisation area is shown in Fig. 5.3, and it can be well described as $3.9' \times 17.2''$ ellipse with an angle of 103.9° in the North-to-East direction.

The DM expected from the MW in the direction of the FRB is $\sim 22\,\mathrm{pc\,cm^{-3}}$ according to the YMW16 model and $\sim 29\,\mathrm{pc\,cm^{-3}}$ according to NE2001. By assuming a MW halo contribution to the DM of $\sim 50\,\mathrm{pc\,cm^{-3}}$ (Prochaska & Zheng 2019), we find an extragalactic DM of $\sim 325\,\mathrm{pc\,cm^{-3}}$, that we use to estimate a redshift upper limit[2] of $z_{\mathrm{max}} \sim 0.43$ (Zhang 2018a; Planck Collaboration et al. 2020; Batten 2019)

We queried the NASA/IPAC extragalactic database (NED) to identify potential host galaxies of FRB 20201020A. We found five galaxies within the error region catalogued in the SDSS-IV MaNGA (Graham et al. 2018), which is based on the fourteenth data release of the sloan digital sky survey (SDSS-DR14, Abolfathi 2018) and has a 95% magnitude completeness limit of 22.2 in the g filter[3]. None of the five galaxies have a measured redshift or morphological type. Any of those five galaxies could thus be the host of FRB 20201020A, and there could be galaxies below the magnitude completeness of SDSS-DR14. The galaxies are listed in Table 5.4 of the Appendix 5.A.

[1] Localisation code can be found here: https://loostrum.github.io/arts_localisation/
[2] The redshift upper limit was computed with the `fruitbat` package assuming a Planck18 cosmology and the Zhang 2018 method: https://fruitbat.readthedocs.io/en/latest/
[3] See SDSS-DR14 information here: https://www.sdss.org/dr14/scope/

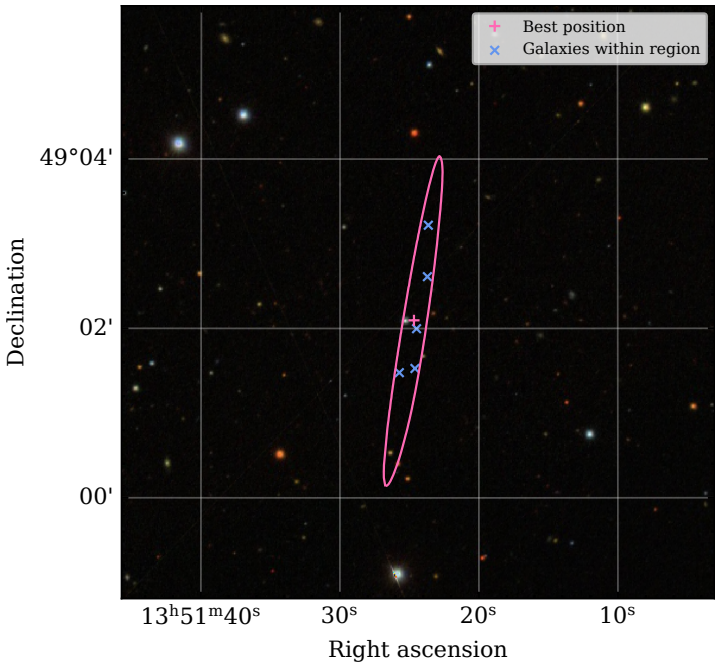

Figure 5.3: Localisation region of FRB 20201020A. The best position is indicated by a pink cross, and the 99% confidence interval contour is represented by the pink ellipse. Galaxies from the NED database within the error region are marked as blue crosses. The background is a composite color image from the Sloan Digital Sky Survey (SDSS, Blanton 2017).

5.2.3 Polarisation and rotation measure

The detection of FRB 20201020A triggered a dump of the full-Stokes data on CB29, allowing us to measure the polarisation properties of FRB 20201020A. We carried out calibration observations within 36 h after the FRB detection. We pointed at the unpolarised source 3C147 and the linearly polarised source 3C286 to correct for the difference in gain amplitudes between the x and y feeds and the leakage of Stokes V into Stokes U, respectively (cf. Connor et al. 2020). The polarisation properties of FRB 20201020A could provide us with essential information about the nature of this source. For instance, in the case of a rotating neutron star (NS), one would expect changes in the polarisation position angle (PPA) following the rotating vector model (RVM, Radhakrishnan & Cooke 1969).

Unfortunately, the polarisation calibration observations were corrupted by radio frequency interferences (RFI) and their poor quality does not allow for robust PPA measurements. Nevertheless, an estimate of the rotation measure (RM) can still be computed although with large uncertainties by assuming a constant value of Stokes V with frequency. From the resulting Stokes Q and U parameters, we obtain the best RM by applying RM synthesis (Burn 1966; Brentjens & Bruyn 2005), and we check the resulting RM by applying a linear least squares fit to the position angle

(PA) as a function of wavelength squared. We find an RM of $+110 \pm 69\,\mathrm{rad\,m^{-2}}$that can be visualised in Fig. 5.8 of the Appendix 5.C.

5.2.4 Repetition rate

The localisation region of FRB 20201020A has been observed for 107.8 h with Apertif since the beginning of the survey in July 2019. This observing time includes follow up observations of both FRB 20201020A and FRB 20190303A (Fonseca et al. 2020). We thus set a 95% upper-limit on the repetition rate of $\sim 3.4 \times 10^{-2}\,\mathrm{h^{-1}}$ assuming a Poissonian repetition process. This upper limit is roughly one order of magnitude lower than the average repetition rates observed in FRB 20121102A and FRB 20180916B in observations carried with Apertif (Oostrum 2020; Pastor-Marazuela et al. 2021). However, we note this limit may be less constraining if the FRB has non-poissonian repetition as has been seen for other FRBs (Spitler et al. 2016; Oppermann et al. 2018; Gourdji et al. 2019; CHIME/FRB Collaboration et al. 2020; Hewitt et al. 2021).

5.3 Timing analysis

We applied several timing techniques in order to determine the presence of a periodicity in FRB 20201020A, and the FRB 20180916B bursts A17 and A53. Initially, we obtained the power spectra of each pulse profile, defined as the Leahy normalised (Leahy et al. 1983) absolute square of the fast Fourier transform (FFT), to identify any potential peaks in the power spectrum of each burst.

Additionally, all three pulse profiles were fitted to multi-component gaussians in order to determine the time of arrival (ToA) of each burst subcomponent. The ToAs as a function of component number were subsequently fitted to a linear function using a weighted least squares minimization in order to determine the mean subcomponent separation P_{sc} as well as the goodness of fit using two different statistics. We used the statistic $\hat{S}$ as described in CHIME/FRB Collaboration et al. (2021b) in order to have a direct comparison between our sample and the FRBs presented there. Furthermore, we used the reduced χ^2 ($\mathrm{r}\chi^2$) statistic in order to take into account the statistical error on the ToAs. We also applied the $\mathrm{r}\chi^2$ statistic to CHIME FRBs 20210206A and 20210213A for comparison. Given the necessity of fitting a model to the tail of the distribution of the simulated statistics for FRB 20191221A in (CHIME/FRB Collaboration et al. 2021b) and the high significance found, we do not compare the statistics of FRB 20191221A with FRB 20201020A in this work. The $\mathrm{r}\chi^2$ statistic seems to be more adapted to the ToAs and errors obtained through our pulse profile fitting routine than the $\hat{S}$ statistic, and it does not significantly alter the periodicity significance of the CHIME FRBs 20210206A and 20210213A. We thus find it to be more robust when computing periodicity significances.

Lastly, we computed the significance of the potential periodicities by simulating the ToAs of 10^5 bursts following the procedure presented in CHIME/FRB Collaboration et al. (2021b). Figure 5.4 contains the relevant plots resulting from the timing analysis, and Table 5.3 gives the significance of the FRB periodicities.

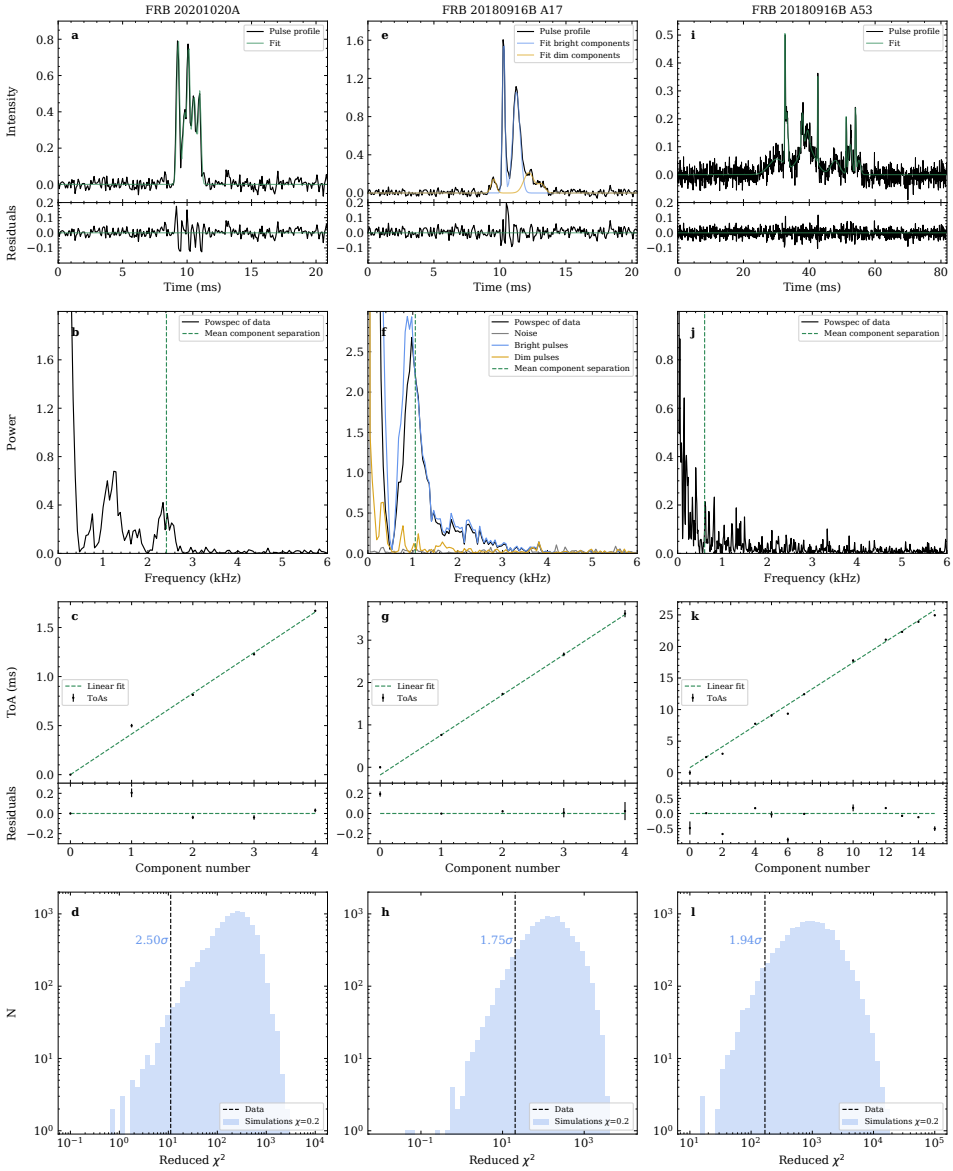

Figure 5.4: Timing analysis of FRB 20201020A (left column), A17 (central column) and A53 (right column). The top of panels a, e and i show the pulse profile of each burst (black) and the fitted multi-component gaussians in green for FRB 20201020A and A53; for A17 the bright components are shown in blue and the dim components in yellow. The bottom of panels a, e and i shows the residuals of the multi-component gaussian fit of each pulse profile. Panels b, f and j show the power spectra of each pulse profile in black. In b, the vertical dashed line indicates the average separation of the FRB 20201020A components. In f, the blue and yellow lines show respectively the power spectra of the bright and dim components. Panels c, g, and k show the ToAs of all subcomponents as a function of component number. The dashed green line in c, g, and k are linear fits to the ToAs, and the lower panels show their residuals. Panels d, h, and l show histograms of the simulated $r\chi^2$ statistic to compute the significance of the periodicity. The vertical lines correspond to the $r\chi^2$ of the linear fit to the data. The significance is indicated as blue text.

Table 5.3: Statistical significance of the FRB periodicities. Values computed for the FRBs presented in this paper as well as the FRBs below the 3σ significance threshold from CHIME/FRB Collaboration et al. (2021b). For each FRB considered, we give the component number vector ($n_{\rm comp}$), the quasi-period $P_{\rm sc}$ in milliseconds, the reduced χ^2 (rχ^2) with its respective significance σ_{χ^2}, and the value of the statistic $\hat{S}$ with its respective significance $\sigma_{\hat{S}}$ as recalculated in this work.

FRB	$n_{\rm comp}$	$P_{\rm sc}$ (ms)	rχ^2	σ_{χ^2}	$\hat{S}$	$\sigma_{\hat{S}}$
FRB 20201020A	(0,1,2,3,4)	0.415(6)	11.17	2.50	4.18	1.41
FRB 20180916B A17	(0,1,2,3,4)	0.95(3)	20.33	1.75	10.47	3.54
FRB 20180916B A53	(0,1,2,4,5,6,7,10,12,13,14,15)	1.7(1)	168.3	1.94	5.12	0.95
FRB 20210206A	(0,1,2,3,5)	2.8	2027.41	1.90	5.13	1.89
FRB 20210213A	(0,1,2,3,4,5)	10.8	270.80	2.96	7.42	2.56

5.3.1 FRB 20201020A

To get the mean subcomponent separation $P_{\rm sc}$, we fitted the ToAs given in Table 5.2 as a function of component number $n = (0, 1, 2, 3, 4)$. We get $P_{\rm sc}$= 0.415(6) ms, which we assume to be the period whose significance we want to examine.

The power spectrum of the FRB shows a peak at the frequency corresponding to the mean subcomponent separation, 2409 Hz. However, it also displays a peak with a higher amplitude at half the frequency corresponding to $P_{\rm sc}$. We argue that this peak is more prominent because of the higher amplitude of components 0, 2 and 4, which are spaced by twice the $P_{\rm sc}$. Additionally, the ToA of component 1 is delayed with respect to the others, as can be seen in Fig. 5.4 panel c, thus lowering the power of the peak at 2409 Hz. Red noise could also play a factor in increasing the peak amplitude. We thus consider 2409 Hz to be the fundamental frequency, and interpret the 1200 Hz peak as a lower-frequency harmonic.

By using the rχ^2 as the reference statistic and applying it both to the data and the simulations, we obtain a significance of 2.50σ. The different steps of the analysis are plotted in Fig. 5.4, panels a-d. While σ_{χ^2} and $\sigma_{\hat{S}}$ are not significant enough for a conclusive periodicity detection, this FRB is visually analogous the CHIME FRBs 20210206A and 20210213A. This suggests that these three bursts belong to the same morphological class of FRBs that present quasi-periodic components in time, with all subcomponents showing a similar frequency extent.

5.3.2 FRB 20180916B A17

The pulse profile of A17 can be well fitted by a five component gaussian, with the second and third components being much brighter than the others. Its power spectrum shows a bright peak at ∼1000 Hz. Since the separation between the second and third components is ∼1 ms, we tested whether the power spectrum was dominated by these two bright subcomponents instead of arising from an intrinsic periodicity. To do so, we created fake pulse profiles of the ‘‘bright’’ and ‘‘dim’’ components. The pulse profile of the bright components was created by subtracting the gaussian fit of the first, fourth and fifth components from the data, and the pulse profile of the dim components by subtracting the fit of the second and third components from the data. Next we generated power spectra of the ‘‘bright’’ and ‘‘dim’’ pulse profiles, both over-plotted in Fig. 5.4, panel f. Since the power spectrum of the bright components largely overlaps with the power spectrum of the

original pulse profile, we conclude that the peak in the power spectrum is dominated by the two brightest components.

We further fitted the ToAs to a linear function and compared the resulting rχ^2 and $\hat{S}$ statistics to simulations. While $\sigma_{\chi^2} = 1.75\sigma$ is below the 3σ threshold, $\sigma_{\hat{S}} = 3.54\sigma$ is not. Due to this discrepancy, we cannot confirm nor rule out the presence of a periodicity in A17. The steps of the timing analysis are plotted in Fig. 5.4, panels e-h.

5.3.3 FRB 20180916B A53

A53 is the widest FRB 20180916B burst and with the highest number of components (≥ 11) presented in Pastor-Marazuela et al. (2021), making it a good candidate for periodicity analysis. Although the ToAs plotted as a function of component number show irregularities in the spacing between bursts, we still carried out the fit to a linear function and the significance computation by associating the larger "gaps" to missing components, resulting in a component number vector $n = (0, 1, 2, 4, 5, 6, 7, 10, 12, 13, 14, 15)$. We find $\sigma_{\chi^2} = 1.94\sigma$ and $\sigma_{\hat{S}} = 0.95\sigma$.

The power spectrum of A53 is well fitted by a power law and all fluctuations are consistent with noise. We do not find a significant peak in the power spectrum at the average component separation of 1.7 ms. We thus conclude that A53 does not show a significant periodicity in its structure. All steps of the analysis are shown in Fig. 5.4, panels i-k.

5.4 Discussion

We next consider which mechanism can best explain the periodicity in FRB 20201020A: the rotation of an underlying sub-millisecond pulsar (§5.4.1), the final orbits of a compact object merger (§5.4.2), crustal oscillations after an X-ray burst (§5.4.3), or equidistant emitting regions on a rotating neutron star (§5.4.4). We also comment on whether these FRBs represent a new morphological type.

5.4.1 Sub-millisecond pulsar

One of the potential origins of the periodic structures in FRB 20201020A and the CHIME FRBs 20210206A and 20210213A discussed in CHIME/FRB Collaboration et al. (2021b) is the rotation of a neutron star with beamed emission, analogous to Galactic radio pulsars. While the period range observed in the aforementioned FRBs is compatible with Galactic pulsars, the quasi-period of FRB 20201020A $P_{\rm sc}$~0.415 ms is in the sub-millisecond regime.

A spin rate of such magnitude is interesting because it could provide the energy required for the highly luminous radio emission seen in FRBs in general. For a rotation-powered neutron star, the spin rate ν and surface magnetic field strength $B_{\rm surf}$ determine the potential of the region that accelerates the particles that generate the radio bursts. For example, giant pulses are only common in those pulsars with the highest known values of $\nu^3 B_{\rm surf}$, interpreted as the magnetic field strength at the light cylinder $B_{\rm LC}$ (where $B_{\rm LC} > 2.5 \times 10^5$ G, Johnston & Romani 2004; Knight 2006). Clearly the spin frequency is an important driver powering such luminous emission.

Fast radio bursts lasting for over 5 ms seem to be at odds with a sub-millisecond NS interpretation. However, these bursts could consist of subcomponents that are blended together due to scattering or observational limitations such as temporal resolution and intra-channel smearing. In the general population, the intrinsic width of the emitted FRBs is not well constrained (Gardenier & van Leeuwen 2021). A rotating millisecond neutron star or magnetar may thus explain the bright emission of an FRB, even when only a single burst is observed. Although the component separation in FRB 20191221A is two orders of magnitude larger than in FRB 20201020A, the number of FRBs with regularly spaced sub-second components is so small at the moment that one should aim for a single explanation. Overall, a sub-millisecond neutron star is a highly interesting hypothesis to test.

The FRB 20201020A quasi-period is shorter than that of the fastest spinning pulsar confirmed so far, with $\sim$1.4 ms (Hessels et al. 2006), and would be the smallest known neutron-star spin period. The maximum rotation rate an NS can achieve can set important constraints on the NS equation of state (EoS) (e.g. Shapiro et al. 1983). This maximum rotation rate is given by the mass-shedding frequency limit, above which matter from the outer layers of the NS is no longer gravitationally bound and is thus ejected. Haensel et al. (2009) establish an empirical formula for the mass-shedding frequency $f_{\rm max}$ given by the mass and radius of the NS, with $C \sim 1$ kHz,

$$f_{\rm max}(M) = C \left(\frac{M}{M_\odot}\right)^{1/2} \left(\frac{R}{10{\rm km}}\right)^{-3/2}. \tag{5.2}$$

Figure 5.5 shows a mass-radius diagram based on Demorest et al. (2010), including typical EoSs, the physical limits set by causality, finite pressure and general relativity (Lattimer 2012), and observational constraints given by the two most massive known NSs (Cromartie et al. 2020; Fonseca et al. 2021; Demorest et al. 2010) and the fastest spinning NS at 716 Hz (Hessels et al. 2006). In order to check whether the quasi-period of FRB 20201020A could be explained by the rotation of a NS, we plot the mass-radius relation using Eq. 5.2 assuming the mass-shedding frequency to be given by FRB 20201020A, $f_{\rm max} = 1/0.415$ ms$\sim$ 2409 Hz. Since no EoSs remain in the white region of the diagram, we conclude that the quasi-period of FRB 20201020A is incompatible with being due to the rotation of a NS using typical EoSs.

If, given the similar morphological properties of FRB 20201020A with the CHIME/FRB FRBs FRB 20191221A, FRB 20210213A and FRB 20210206A, the four FRBs are originated by the same type of progenitors, the periodicity of the burst components is unlikely to be due to the rotation of a NS.

5.4.2 Compact object merger

Merging compact objects have been hypothesised to produce FRBs through magnetic interaction between the two bodies in the system, including binary neutron star systems (BNS, Piro 2012; Lyutikov 2013; Totani 2013; Wang et al. 2016; Hansen & Lyutikov 2001), black hole-neutron star systems (BHNS, McWilliams & Levin 2011; Mingarelli et al. 2015; D'Orazio et al. 2016), and white dwarfs (WD) with either a neutron star or a black hole (Liu 2018; Li et al. 2018). The presence of multiple peaks in the FRB pulse profile could be explained by a magnetic outburst extending through successive orbits of the binary system, and thus the subcomponent frequency

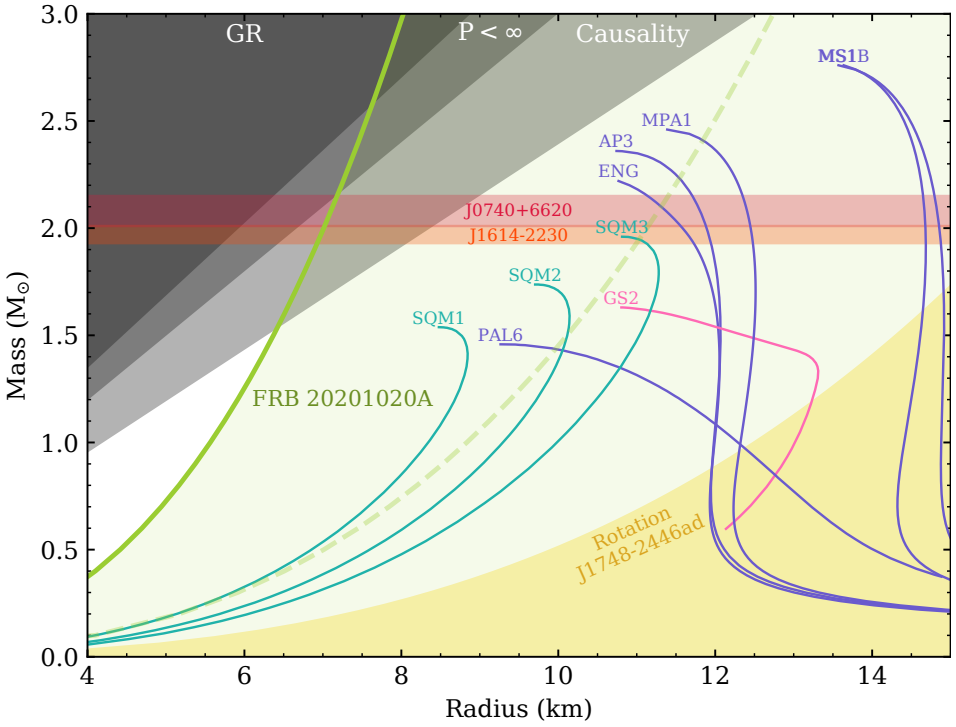

Figure 5.5: Neutron star mass-radius diagram. The solid lines represent the mass-radius relationship of typical EoSs. The gray shaded regions are forbidden by the general relativity (GR), finite pressure ($P < \inf$) and Causality. The yellow shaded region is forbidden by the rotation of the fastest spinning pulsar J1748−2446ad (Hessels et al. 2006). The red shaded region shows the mass of J0740+6620 (Cromartie et al. 2020; Fonseca et al. 2021) and the orange region the mass of J1614-2230 (Demorest et al. 2010), the two heaviest known NSs. Valid EoSs need to cross those regions. The green line and green shaded region would be forbidden if the quasi-period of FRB 20201020A was produced by the rotation of a NS at 2409 Hz, and the dashed green line if the rotation was at 1205 Hz.

should match half the gravitational wave (GW) frequency if one object in the system produces bursts, or the GW frequency if both of them do. The maximal GW frequency is attained when the binary reaches the mass-shedding limit for an NS (Radice et al. 2020). This frequency is given by the EoS of the merging NS, which is expected to be between 400 and 2000 Hz (Bejger et al. 2005; Dietrich et al. 2021; Hanna et al. 2009). The frequency seen in the components of FRB 20201020A of 2409 Hz is above the typical limits and it could only be explained by a very soft EoS.

This FRB frequency could only be produced at the very last moments of the inspiral, right before the merger. At this stage, the frequency derivative would be very high, which translates as a perceptibly decreasing spacing between burst subcomponents. Following (Cutler & Flanagan 1994, equation 16), we can derive the analytical expression for the phase of the gravitational waveform as a function of time, $\phi(t)$, by solving the differential equation of $\frac{df}{dt}$ and integrating $f(t) = \frac{d\phi}{dt}(t)$, where $f(t)$ is the GW frequency. We compute the maximal number of orbits that

could be completed between the time when the system reaches the FRB frequency and the time of the merger through the maximal phase difference $\Delta\phi_{\rm max}$, where one orbit equals 2π rad, with the steps of the computation detailed in Appendix 5.D. We find the following expression:

$$\Delta\phi_{\rm max} = \frac{1}{16\pi^{5/3}} \left(\frac{G\mathscr{M}}{c^3}\right)^{-5/3} f_{\rm FRB}^{-5/3} \tag{5.3}$$

Here, $\mathscr{M} \equiv \mu^{3/5} M^{2/5}$ is the chirp mass, with $M = M_1 + M_2$ the total mass of the system and $\mu = M_1 M_2 / M$ the reduced mass. G is the gravitational constant and c the speed of light in the vacuum. We have computed $\Delta\phi_{\rm max}$ for three values of $M_1 = 0.2, 1.4, 100\,{\rm M}_\odot$, and a range of M_2 values between 0.2 $\rm M_\odot$ (close to the lowest mass WD; Kilic et al. 2007) and 100 $\rm M_\odot$. We have tested both f_0 =2409 Hz and 4818 Hz as initial GW frequencies.

As shown in Fig. 5.6, only a WD-WD system could complete four rotations ($\Delta\phi_{\rm max} = 8\pi$) after reaching $f_{\rm FRB} = 4818$ Hz. However, given the typical WD radius of 5000-10000 km, this is not a realistic scenario. Indeed, we can get an estimate of the distance between the two compact objects in the system when they reach the FRB frequency using Kepler's third law, $r = \frac{(GM)^{1/3}}{(\pi f)^{2/3}}$. For a binary WD system of $\sim 1\,{\rm M}_\odot$ each, the expected separation would be ~ 16 km, well below the typical WD radius. Since none of the systems with masses corresponding to a BNS or BHNS system could reach $\Delta\phi_{\rm max} = 8\pi$, we can discard the pre-merger scenario as an explanation for FRB 20201020A.

The quasi-period of FRB 20210206A is also challenging to explain within this model (CHIME/FRB Collaboration et al. 2021b). Since only a small fraction of the known FRBs show regularly spaced components, we argue that these belong to the same class of progenitor and hence disfavour compact object merger models as the progenitors of FRBs with this type of morphology.

5.4.3 Crustal oscillations

If FRBs are a result of short X-ray bursts from a magnetar, the quasi-periodicity we observe could be explained through crustal oscillations of said neutron star. These oscillations would result from the same X-ray burst that also caused the FRB (Wadiasingh et al. 2020). The sub-bursts of FRB 20201020A suggest an oscillation frequency of ∼2400 Hz. Wadiasingh et al. (2020) examine if FRB sub-pulses can be a result of torsional crustal oscillations during a short X-ray burst. If so, their simulations show that the fundamental eigenmodes with low multipole number (corresponding to frequencies between 20–40 Hz) would be more prevalent than the higher frequencies that we observe. We conclude the difference in frequencies is too large, and disfavour crustal oscillations as the source of the periodicity.

5.4.4 Ordered emission regions on a rotating magnetar

The burst morphology and time scales of FRB 20201020A are very similar to two types of quasi-periodic behaviour seen in regular pulsars: subpulses and microstructure. Below we discuss scenarios where the FRB is produced in a similar manner, but on a magnetar instead of a purely rotation-powered pulsar.

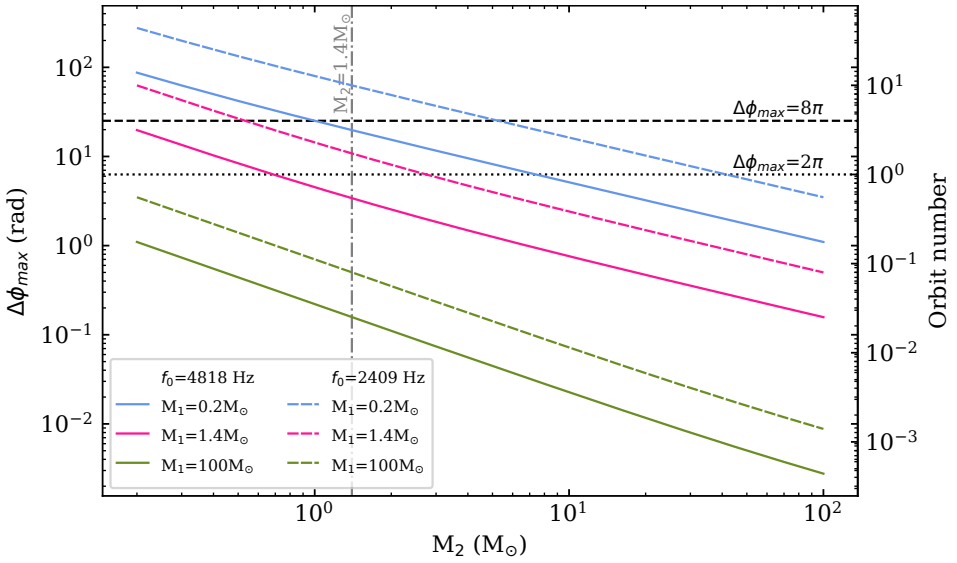

Figure 5.6: Maximal orbital phases a binary system can complete before a merger after reaching a GW frequency of 2409 Hz (solid lines) and 4818 Hz (dashed lines). The dashed and dotted black horizontal lines mark respectively phases of 8π (four rotations) and 2π (one rotation), required to see five and three FRB subcomponents respectively. The orbital phases have been computed for binary systems with the mass of the first compact object being M_1=0.2 $M_\odot$ (blue), 1.4 $M_\odot$ (pink) and 100 $M_\odot$ (green), while the mass of the second object M_2 ranges between 0.2 and 100 $M_\odot$. The dot-dashed gray vertical line indicates $M_2 = 1.4\,M_\odot$.

5.4.4.1 The analogue of pulsar subpulses

Like the components in FRB 20201020A, the individual pulses of rotation-powered pulsars are usually composed of one or more sub-pulses. Subpulse widths lie in the range of $1^\circ - 10^\circ$ of the spin longitude (Table 16.1 in Lyne & Graham-Smith 2012), thus broadly spanning $0.3 - 140$ ms for pulsars with spin periods of $0.1 - 5$ s. This qualitatively fits the individual components widths of observed FRB structures.

For a substantial fraction of these pulsars (mostly those with longer periods) the position or intensity of these subpulses changes in an organized fashion from one spin period to another (Weltevrede et al. 2007; Basu et al. 2019). The most widely accepted theory of drifting subpulses interprets these as emission from distinct plasma columns originating in a rotating carousel of discharges within the polar gap (Ruderman & Sutherland 1975). As the neutron star spins, these ordered, regularly spaced emission regions (“sparks”) produce quasi-periodic bursts in our line of sight. In this case, the burst morphology directly reflects the spatial substructure of the distinct emission regions. Given the similarity in appearance, we hypothesize here that a magnetar produces the components in FRB 20201020A in the same way that a pulsar produces subpulses.

This carousel rotation causes subpulses to appear at progressively changing longitudes[1]. Every period may contain one or few individual subpulses roughly equidistant from each other. These regular subpulses cause a stable second periodicity on top of the primary, rotational periodicity. In the most regular cases, the resulting drifting subcomponents behave quite periodically; in PSR B0809+74, the textbook example (van Leeuwen et al. 2003), the spark rotation and spacing were recognised early on to be steady to over 1 part in 250 (Unwin et al. 1978). Overall, the spark regularity is sufficient to produce the quasi-periodicity we observe here.

The residuals in the timing fit of FRB 20201020A (Sect. 5.3.1) have an analogue in pulsar subpulses, too. There, the deviation from strict periodicity within a single pulsar rotation is well-documented for some of the sources with more stable drift and is well described by the curvature of the line-of-sight path through the emission cone (Edwards & Stappers 2002; van Leeuwen et al. 2002). At least for some sources the drifting rate can be measured with good precision (indicating prominent periodic modulation) and it has been shown that it can slowly vary with time (Rankin & Suleymanova 2006), jitter on small timescales (van Leeuwen & Timokhin 2012), and change rapidly during a mode switch (Janagal et al. 2021). Several drift periodicities can even be present at the same time at different spin longitudes (bi-drifting, Szary et al. 2020).

Pulsar subpulses are not only similar to the components in FRB 20201020A, the CHIME FRBs 20210206A and 20210213A and A17 with respect to their regular spacing; also the number of sub-bursts agrees. Quite a few pulsars, such as B0329+54 (Mitra et al. 2007) B1237+25 (Srostlik & Rankin 2005), and B1857−26 (Mitra & Rankin 2008), show both a similarly high number of distinct subpulses and quasi-periodically spaced single pulse profiles.

One concern in this analogy might be the timescale of the ‘‘on-mode’’ for FRBs. If the FRBs we discuss here come from a single neutron-star rotation, the absence of fainter bursts nearby means the subpulses pattern flares for one period, and then turns off. This may seem problematic. Yet, for pulsars that display nulling, or different modes of emission, the spark pattern is known to establish itself very quickly, at the timescale of less than a spin period (Bartel et al. 1982). Furthermore, pulsars such as J0139+3336 (a 1.25 s pulsar that emits a single pulse only once every ∼5 minutes; Michilli et al. 2020) and the generally even less active RRATS (McLaughlin et al. 2006) show that a population of only very sporadically, but brightly, emitting neutron stars exists.

Overall, while the amount of information available for FRBs is limited, their behaviour falls within the (admittedly broad) range of features exhibited by subpulse drift.

5.4.4.2 The analogue of pulsar/magnetar microstructure

In pulsars, the individual subpulses mentioned in the previous sections themselves often contain yet another level of μs−ms, substructure (Kramer et al. 2002). Often narrow micropulses are observed in groups of several spikes riding on top of an amorphous base pulse; although deep modulation, down to to zero intensity, has also been observed (Cordes et al. 1990). This so-called microstructure is about 3 orders of magnitude narrower ($\sim \mu$s) than the enveloping subpulses

[1] There is also non-drifting, intensity-modulated periodicity, but that requires a spin period smaller than the observed periodicity, which we have ruled out in §5.4.1.

(∼ms), and the spacing between spikes is quasi-periodic. A linear relation between the periodicity of the microstructure and the pulsar spin period, has been established: first for pulsar spanning the period range $0.15 - 3.7$ s (Mitra et al. 2015), and next extended to millisecond pulsars (De et al. 2016). Recent observations of the 5.5-second magnetar XTE J1810−197 also generally agree with the linear microstructure-period relationship (Maan 2019). The relation strongly suggests a physical origin, but the exact mechanisms for the microstructure remains unclear. There are two main theories: a geometrical one, based on distinct tubes of emitting plasma; and a temporal one, based on modulation of the radio emission (see the discussion in Mitra et al. 2015).

Even if the FRB sub-component resemblance to pulsar microstructure does not immediately allow for their physical interpretation, we can still apply the empirical periodicity-period relation from Mitra et al. (2015) to these FRBs. Their observed sub-component periodicities lead to tentative neutron-star spin periods between 0.3 and 10 s.

In microstructure, an increase of pulsar period is met by a linear increase in the component periodicity, as we have just discussed. A similar relation with the spin period is seen for the micropulse *widths* (Cordes 1979; Kramer et al. 2002). If we, again, consider the different components in FRB 20201020A as micro-structures, we can also apply this relation. In FRB 20201020A, the average intrinsic component width (i.e., after accounting for the inter-channel dispersion smearing and the finite sampling time), defined as the full width at half maximum (FWHM), is 250 ± 30 μs, suggesting a tentative NS spin period in the range $0.3 - 0.6$ s. Given their required intrinsic brightness, FRBs might actually be more closely related to the giant micropulses as seen in the Vela pulsar (Johnston et al. 2001). On average, those have even narrower widths (Kramer et al. 2002). The bright single pulses from magnetar XTE J1810−197, however, could be giant micropulses; and still these agree with the standard linear relationship between the normal micropulse width and spin period (Maan 2019). There thus appears to be some scatter in these relations. We do conclude that if FRB 20201020A consists of such giant micropulses, the tentative neutron-star spin period may increase, and fall on the higher side of the above estimated period range.

One characteristic feature of microstructure is that linear and circular components of emission closely follow quasi-periodic total intensity modulation. This is also true for FRB 20210213A from CHIME/FRB Collaboration et al. (2021b), the only one with polarized data presented. Unfortunately, as mentioned in §5.2.3, we were not able to obtain a robust Stokes parameters calibration, which would have been useful to compare to typical pulsar microstructure features.

5.4.4.3 The magnetar connection

The microstructure that was previously known only in pulsars, has recently also been observed in radio emission from magnetars, especially in the radio-loud magnetar XTE J1810-197. This suggests a further expansion into FRBs is worth considering. The 2018 outburst of XTE J1810-197 led to high-resolution detections and studies, at a number of epochs and radio frequencies (Levin et al. 2019; Maan 2019; Caleb et al. 2021). The magnetar exhibits very bright, narrow pulses; and for discussions on the classification of these, we refer to Maan (2019) and Caleb et al. (2021). The source also exhibits multi-component single pulses that show quasi-periodicity is the separation between different components. If we assume FRBs originate from magnetars, it is possible that

the quasi-periodicity that is seen in the sample presented in this paper can be tied to a similar underlying emission mechanism, on a different energy scale. Much of the available energy budget is determined by the period and magnetic field. The spin-period range we find covers the periods of the known magnetars. Magnetars with a relatively short period, of about $\gtrsim 2\,\mathrm{s}$, plus a strong surface magnetic field of $> 10^{14}\,\mathrm{G}$, would produce a larger vacuum electric field (due to the rotating magnetic field) than normal, slower, magnetars. This field in turn generates stronger particle acceleration and larger Lorentz factors, as required for FRB luminosities. It would be interesting to compare the FRB luminosity of sources with different supposed spin periods, in this model.

5.4.5 A new FRB morphological type

Based on the first CHIME/FRB catalog, Pleunis et al. (2021a) identified four FRB types based on their morphology. These classes are simple broadband, simple narrowband, temporally complex and downward drifting. Downward drifting bursts are commonly associated with repeating FRBs (Hessels et al. 2019), and A17 and A53 are unequivocal examples of this morphological type. Bursts classified as temporally complex are those presenting more than one component peaking at similar frequencies, but with no constraint on the separation between components. This class makes up for 5% of the FRBs presented in the CHIME/FRB catalog, but $\lesssim 0.5\%$ of the FRBs show five or more components.

With the detection of FRB 20191221A, FRB 20210206A and FRB 20210213A, CHIME/FRB Collaboration et al. (2021b) propose the existence of a new group of FRBs with periodic pulse profiles. FRB 20201020A is the first source detected by an instrument other than CHIME/FRB showing a quasi-periodic pulse profile, thus adding a new member to this nascent FRB morphological type. It is not clear yet if these sources are produced by the same progenitors as the other types of FRBs or not.

All three FRB 20201020A, and the CHIME FRBs 20210206A and 20210213A have ≤ 6 components, and none of these FRBs reach the 3σ significance threshold for the periodicity. This could be explained by the structure of the magnetosphere of magnetars, formed by emission regions roughly equally spaced. The higher number of components in FRB 20191221A might reduce the effect of jitter in each single components and thus increase the significance of the periodicity. Alternatively, given its longer period, envelope duration, and higher periodicity significance, FRB 20191221A could have been produced by a magnetar outburst lasting several rotations or a single burst comprising crustal oscillations.

Considering the scarcity of FRBs with a regular separation between components, the detection of FRB 20201020A is remarkable, given the number of events detected with Apertif is a few orders of magnitude lower than CHIME/FRB. This suggests that a larger fraction of FRBs with quasi-periodic components might be visible at higher frequencies. Certain astrophysical and instrumental effects could play a role at blurring together multi-component bursts at lower frequencies. This includes interstellar scattering, which evolves as $\tau \sim \nu^{-4}$, as well as intra-channel dispersive smearing, which scales as ν^{-3} and finite sampling of existing instruments that prevent detection

of components narrower than the sampling interval. Searches of multi-component FRBs with a regular spacing might thus be more successful at higher frequencies.

The bursts A17 and A53 from FRB 20180916B discussed in this work, although similar by eye to FRB 20201020A, do not show conclusive evidence for periodicity in their subcomponents. This, added to the downward drift in frequency of the subcomponents, common in bursts from repeating FRBs, differs from FRB 20201020A and the CHIME/FRB FRB 20191221A, FRB 20210206A, and FRB 20210213A. This might suggest the presence of a different emission process between the bursts from repeating FRBs and the FRBs with quasi-periodic components or an additional mechanism modulating the bursts.

5.5 Conclusions

In this paper, we have presented a new fast radio burst detected with Apertif, FRB 20201020A. This FRB shows a quasi-periodic structure analogous to the three FRBs presented in CHIME/FRB Collaboration et al. (2021b). The average spacing between its five components, however, is ~ 0.415 ms, in the sub-millisecond regime. We have performed a timing analysis of the FRB, and we conclude that the significance of the periodicity is $\sim 2.5\sigma$, below the standard 3σ threshold, but comparable to the significance of the CHIME FRBs 20210206A and 20210213A. Given the scarcity of FRBs with quasi-periodic structure detected so far, they have been likely produced via the same mechanism, and we postulate that they constitute a new FRB morphological type.

Additionally, we have performed a timing analysis of bursts A17 and A53 from Pastor-Marazuela et al. (2021), the bursts with the highest number of visible subcomponents. We find no conclusive evidence of periodicity in these bursts, although the periodicity significance of A17 is above 3σ according to the $\sigma_{\hat{S}}$ test. In A53, a burst with ≥ 11 components, we find an average subcomponent spacing of ~ 1.7 ms. For the five-component burst A17, the average subcomponent separation is ~ 1 ms. These timescales are of the same order of magnitude as the subcomponent separation in FRB 20201020A.

We have discussed several interpretations of the quasi-periodicity, and we rule out the sub-millisecond pulsar and the binary compact object merger scenarios as potential progenitors to FRB 20201020A. However, its morphology is comparable to pulsar subpulses and pulsar microstructure, and similar structures have been observed in single pulses from radio-loud magnetars. We thus conclude that the structure in the magnetosphere of a magnetar could be at play in producing bursts such as FRB 20201020A and the CHIME FRBs 20210206A and 20210213A. On the other hand, given the high significance of the period detected in FRB 20191221A, as well as the higher burst separation of ~ 200 ms, the structure seen in this CHIME/FRB burst could have been produced by a magnetar outburst lasting several NS rotations.

Acknowledgements

We thank Kendrick Smith for helpful conversations. This research was supported by the European Research Council under the European Union's Seventh Framework Programme (FP/2007-2013)/ERC Grant Agreement No. 617199 ('ALERT'), by Vici research programme 'ARGO' with project number 639.043.815, financed by the Dutch Research Council (NWO), and through

CORTEX (NWA.1160.18.316), under the research programme NWA-ORC, financed by NWO. Instrumentation development was supported by NWO (grant 614.061.613 'ARTS') and the Netherlands Research School for Astronomy ('NOVA4-ARTS', 'NOVA-NW3', and 'NOVA5-NW3-10.3.5.14'). PI of aforementioned grants is JvL. EP further acknowledges funding from an NWO Veni Fellowship. SMS acknowledges support from the National Aeronautics and Space Administration (NASA) under grant number NNX17AL74G issued through the NNH16ZDA001N Astrophysics Data Analysis Program (ADAP). DV and AS acknowledge support from the Netherlands eScience Center (NLeSC) under grant ASDI.15.406. KMH acknowledges financial support from the State Agency for Research of the Spanish MCIU through the ''Center of Excellence Severo Ochoa'' award to the Instituto de Astrofísica de Andalucía (SEV-2017-0709) and from the coordination of the participation in SKA-SPAIN, funded by the Ministry of Science and innovation (MICIN). JMvdH and KMH acknowledge funding from the European Research Council under the European Union's Seventh Framework Programme (FP/2007-2013)/ERC Grant Agreement No. 291531 ('HIStoryNU'). This work makes use of data from the Apertif system installed at the Westerbork Synthesis Radio Telescope owned by ASTRON. ASTRON, the Netherlands Institute for Radio Astronomy, is an institute of NWO. This research has made use of the NASA/IPAC Extragalactic Database, which is funded by the National Aeronautics and Space Administration and operated by the California Institute of Technology.

5.A Galaxies within FRB error region

In this appendix we give Table 5.4 with the galaxies identified within the 99% confidence interval on the localisation of FRB 20201020A.

Table 5.4: Galaxies within the error region of FRB 20201020A. These galaxies were queried from the NED database. None have a measured redshift.

Object name	Magnitude and filter
SDSS J135123.63+490313.1	21.9g
SDSS J135123.70+490236.7	22.3g
SDSS J135124.48+490159.8	22.8g
SDSS J135124.60+490131.7	23.5g
SDSS J135125.72+490128.7	22.1g

5.B 2D auto-correlation functions of FRB 20201020A, A17 and A53

In this section we show the two-dimensional auto-correlation functions (AFC)[1] of FRB 20201020A, A17 and A53. After computing the ACFs they were fitted to two-dimensional gaussians with an inclination angle. This inclination angle gives us a robust drift-rate estimate of the burst subcomponents Hessels et al. (2019). We obtained the time and frequency ACFs by averaging in frequency and time respectively.

[1] Computed with the `signal.correlate2d` function of the SciPy python package.

The FWHM of a lorentzian fitted to the central peak of the frequency ACF gives the scintillation bandwidth of the FRB. In addition, any structure in the temporal ACF can provide with information about any dominant timescales in the pulse structure.

5.C Rotation measure

In this section we show the results from the polarisation and Faraday rotation calibration, shown in Fig. 5.8. Note that the best RM of $110 \pm 69\,\mathrm{pc\,cm^{-3}}$ is close to the lower limit of what Apertif can measure given its central frequency and bandwidth.

5.D Maximal number of orbits in binary merger

To get the expression for the maximal orbital phase a binary system can complete after reaching a certain frequency, $\Delta\phi_{\mathrm{max}}$ as given in Equation 5.3, we start with Eq. 16 from Cutler & Flanagan (1994):

$$\frac{df}{dt} = \frac{96}{5}\pi^{8/3}\left(\frac{G\mathscr{M}}{c^3}\right)^{5/3} f^{11/3} = \mathbb{M} f^{11/3}. \tag{5.4}$$

We define $\mathbb{M} \equiv \frac{96}{5}\pi^{8/3}\left(\frac{G\mathscr{M}}{c^3}\right)^{5/3}$, where $\mathscr{M} \equiv \mu^{3/5}M^{2/5}$ is the chirp mass, $M = M_1 + M_2$ the total mass of the system and $\mu = M_1 M_2/M$ the reduced mass. G is the gravitational constant and c the speed of light in the vacuum (note that we do not make the replacement $G = c = 1$). We solve the differential equation to find $f(t)$:

$$f(t) = \left(f_0^{-8/3} - \frac{8\mathbb{M}}{3}t\right)^{-3/8}. \tag{5.5}$$

Here, f_0 is the frequency at $t = 0$. To get the orbital phase, we solve the differential equation $\frac{d\phi}{dt} = 2\pi f(t)$ and we get:

$$\phi(t) = -\frac{6\pi}{5\mathbb{M}}\left(f_0^{-8/3} - \frac{8\mathbb{M}}{3}t\right)^{5/8} + \mathscr{C}. \tag{5.6}$$

The value of $\mathscr{C}$ is given by the initial conditions; $\phi(0) = 0$ so we get $\mathscr{C} = \frac{6\pi}{5\mathbb{M}}f_0^{-5/3}$. In the simplest scenario where we assume the objects in the binary system to be point-like sources, the merger will happen when $\frac{8\mathbb{M}}{3}t - f_0^{-8/3} = 0$, from which we define the maximal orbital phase $\Delta\phi_{\mathrm{max}} = \mathscr{C}$. Finally, we get:

$$\Delta\phi_{\mathrm{max}} = \frac{1}{16\pi^{5/3}}\left(\frac{G\mathscr{M}}{c^3}\right)^{-5/3} f_0^{-5/3}. \tag{5.7}$$

Since we take our initial frequency to be the frequency corresponding to the FRB subcomponent separation, we get Eq. 5.3.

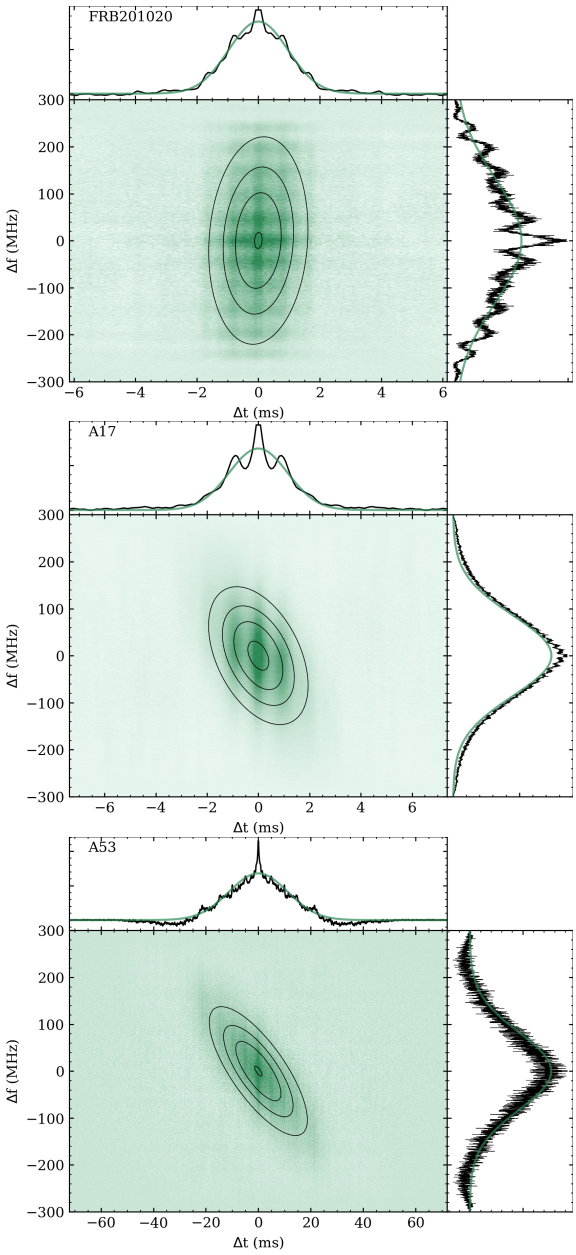

Figure 5.7: 2D ACFs of FRB 20201020A, A17 and A53 from top to bottom. The lower left panel of each bursts shows the 2D ACF in green, and the 2D gaussian fit as black elliptical contours. The top panel of each bursts shows the frequency-averaged temporal ACF in black and the gaussian fit in green. The left panels show the time-averaged frequecial ACF in black and the gaussian fit in green.

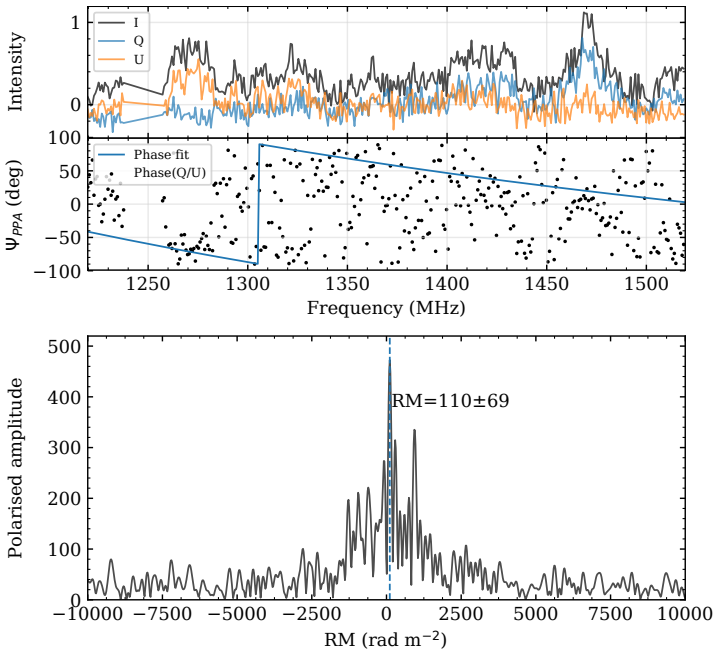

Figure 5.8: Measured polarisation properties of FRB 20201020A. The top panel shows the Stokes parameters I (black), Q (blue) and U (orange) as a function of frequency, calibrated by assuming Stokes V to be zero. The second panel shows the measured phase between Q and U (black dots) and its fit. The bottom panel shows the RM-synthesis solution, with the polarised amplitude as a function of RM. The dashed blue line marks the position of the maximum, at RM=$+110 \pm 69$ pc cm^{-3}.

6

Morphological evolution with frequency in Fast Radio Bursts as exposed by the Apertif survey

I. Pastor-Marazuela, J. van Leeuwen, L. Oostrum, E. Petroff, A. Bilous, L. Connor, Y. Maan, S. Straal, D. Vohl, P. Atri, O. M. Boersma, K. Rajwade, ARTS Builders, Apertif Builders

To be submitted to Astronomy & Astrophysics

Abstract

Understanding the origin of the energetic fast radio bursts (FRBs) is the main science driver of recent instrumentation development for several dedicated FRB surveys. One such instrument is Apertif, installed at the Westerbork Synthesis Radio Telescope (WSRT) in the Netherlands. It carried out an FRB survey, ALERT, at 1370 MHz between July 2019 and February 2022. Here we report the detection of 18 new FRBs with Apertif, and we study the properties of the entire 24 burst sample that were detected during the survey. This is one of the largest FRB samples above 1 GHz to date. About a third of the FRBs display multiple components; a fraction much larger than the 5% found by CHIME/FRB at 600 MHz. We find this difference cannot be explained by the increased scattering at lower frequencies alone, implying it might be intrinsic to the FRBs. The bursts have a dispersion measure distribution similar to the Parkes and UTMOST samples. One of the bursts, FRB 20200719A, is the second most dispersed FRB known to date, and its rest frame shows FRB emission frequencies reach 6 GHz. We localise a different burst, FRB 20211024B, to a host galaxy at >90% likelihood, thus determining its redshift to be z=0.21. The Apertif FRBs reveal a population of highly scattered bursts. Given the observing frequency and time resolution, the scattering of most FRBs is likely to have been produced in the circumburst environment, suggesting some FRBs are embedded in complex scattering media such as star forming regions or supernova remnants. We determine an FRB all-sky rate of 436^{+204}_{-150} sky^{-1} day^{-1} above a fluence limit of 2.8 Jy ms, and a fluence cumulative distribution with a power law index $\alpha = -1.23 \pm 0.06 \pm 0.2$, which appears to differ from the Euclidean Universe predictions. We conclude that FRB searches above 1 GHz are important to understand the FRB population through the study of multi-component and highly-scattered FRBs.

6.1 Introduction

The field of Fast Radio Bursts (FRBs) – extragalactic radio flashes of millisecond duration with extreme luminosities (Lorimer et al. 2007; Petroff et al. 2019; Cordes & Chatterjee 2019) – has been rapidly evolving in recent years. The number of published FRBs is now in the hundreds, twenty have been localised to their host galaxies, and two dozen are known to repeat (Petroff et al. 2022). Although these discoveries have not yet fully unveiled the origin of FRBs, the detection of a bright radio burst from the galactic magnetar SGR 1935+2154 demonstrated that at least some FRBs may be produced by magnetars (Bochenek et al. 2020; CHIME/FRB Collaboration 2020). These findings have been possible thanks to the increased number of observations and surveys dedicated to FRB searches in recent years.

The current published sample of both repeating and seemingly one-off FRBs is dominated by sources discovered by the CHIME/FRB project, which searches in the 400 – 800 MHz band (CHIME/FRB Collaboration et al. 2021a). Given the large sample size, population studies have been possible with the CHIME data to look at properties such as the bulk burst morphology of a large FRB sample. In studies of this sample, Pleunis et al. (2021a) find four burst archetypes: single component FRBs, classified under either narrow or broadband; multi-component bursts with each component spanning a similar frequency extent; or multi-component bursts with 'sad-trombone-like' downward drifting structure. A population study of burst properties in the first CHIME/FRB Catalog by Chawla et al. (2022) also reports the overabundance of scattering detected in this sample. Additionally, injections performed for the catalog analysis confirm CHIME detections are biased against highly scattered events, hinting at the presence of a wider FRB population with large scattering timescales to which CHIME/FRB is less sensitive (CHIME/FRB Collaboration et al. 2021a).

Several observed properties of FRBs including dispersion measure (DM), scattering, scintillation, and polarisation are highly frequency-dependent. While the CHIME/FRB sample is by far the largest, studies at higher (and lower) radio frequencies are essential to probe the full extent of the FRB population across all parameters, including DM and scattering. One-off FRBs discovered at frequencies of $\sim$1 GHz by the Murriyang Telescope at the Parkes Observatory and the Australian Square Kilometre Array Pathfinder (ASKAP) also show evidence of scatter broadening and multiple components (Day et al. 2020; Champion et al. 2016), some of which might be beyond the width detection threshold at CHIME/FRB frequencies.

The best-studied FRBs by far have been the small but productive sample of repeating FRB sources. Both the low (120 MHz; Pastor-Marazuela et al. 2021) and high (8 GHz; Gajjar et al. 2018) frequency detections of FRBs have been made through targeted observations of known prolific repeaters. Comparing activity of the repeating FRB 20180916B at 120 MHz and 1.4 GHz simultaneously has shown frequency-dependent activity of this particular source (Pastor-Marazuela et al. 2021). For one-off FRBs, direct comparisons of behaviour at high and low frequencies may not be possible. As such, assembling large samples of one-off FRBs at different radio frequencies may prove the most fruitful in uncovering frequency-dependent properties. Comparing the observed distributions of DM, scattering, flux, fluence, and scintillation of FRB samples from different instruments will provide insight into the underlying FRB population distribution, as well as the properties of the burst environment and host galaxy.

In this paper we present the sample of 24 one-off FRBs discovered with the Apertif system on the Westerbork Synthesis Radio Telescope (WSRT), during the Apertif-LOFAR Exploration of the Radio Transient sky survey (ALERT; van Leeuwen et al. 2022). Its high spectro-temporal resolution search has yielded a self-contained sample of FRBs for which we report DM, burst morphology, frequency structure, scattering, and scintillation. In Section 6.2 we present the bursts in the sample as well as the observing strategy for Apertif. In Section 6.3 we present the data analysis method of the detected bursts. In Section 6.4 we present the detected FRB properties and the results of population analysis across DM, propagation effects, and morphology; we discuss further in Section 6.5. We conclude in Section 6.6.

6.2 Observations

Apertif, the APERture Tile in Focus, is a front-end instrument installed at the Westerbork Synthesis Radio Telescope (WSRT), in twelve of the 25 m dishes of the interferometer (van Cappellen et al. 2022). It is located in the Netherlands. Apertif consists of phased array feeds (PAFs), with each dish forming 40 compound beams (CBs) on the sky and thus increasing the original Field of View (FoV) of the WSRT to 8.2 $\deg^2$ (Adams & van Leeuwen 2019). Apertif has carried out an imaging and time domain survey between July 2019 and February 2022. The Apertif Radio Transient System (ARTS) was designed to carry out the time domain survey, as described in van Leeuwen et al. (2022). The CBs from each dish are coherently beamformed into 12 tied-array beams (TABs, see Maan & van Leeuwen 2017), and these are next recombined in frequency to form 71 synthesised beams (SBs) per compound beam (van Leeuwen et al. 2022). The SBs of all CBs generate a total of 2840 Stokes I, Q, U and V data-streams at a central frequency of 1370 MHz and a bandwidth of 300 MHz, with a time and frequency resolution of 81.92 μs and 195 kHz respectively. The Stokes I data-streams are then searched for single-pulses with the software `AMBER`[1] (Sclocco et al. 2014, 2016, 2019). The data post-processing is implemented with the Data Analysis of Real-time Candidates from the Apertif Radio Transient System (`DARC` `ARTS`[2], Oostrum 2020), and includes real-time candidate classification (Connor & van Leeuwen 2018) through a neural network. The single pulse searches and data post-processing are run on a 40-node graphics processing unit (GPU) cluster at the WSRT.

ARTS has proven its FRB searching capabilities at high time and frequency resolution through the follow-up and detection of known repeating FRBs (Oostrum et al. 2020; Pastor-Marazuela et al. 2021), as well as through the discovery of new one-off FRBs (Connor et al. 2020; Pastor-Marazuela et al. 2022; van Leeuwen et al. 2022). Here, we present the discovery of a new population of, as of yet, one-off FRBs that have been detected in the ARTS time domain survey.

6.2.1 Pointings and sky exposure

The priority source list and thus pointing definition evolved during the ALERT survey, in order to adapt to the latest FRB discoveries. While only two repeating sources were known at the beginning of the survey in July 2019 (Spitler et al. 2016; CHIME/FRB Collaboration et al. 2019a),

[1] `AMBER`: https://github.com/AA-ALERT/AMBER
[2] `DARC`: https://github.com/loostrum/darc

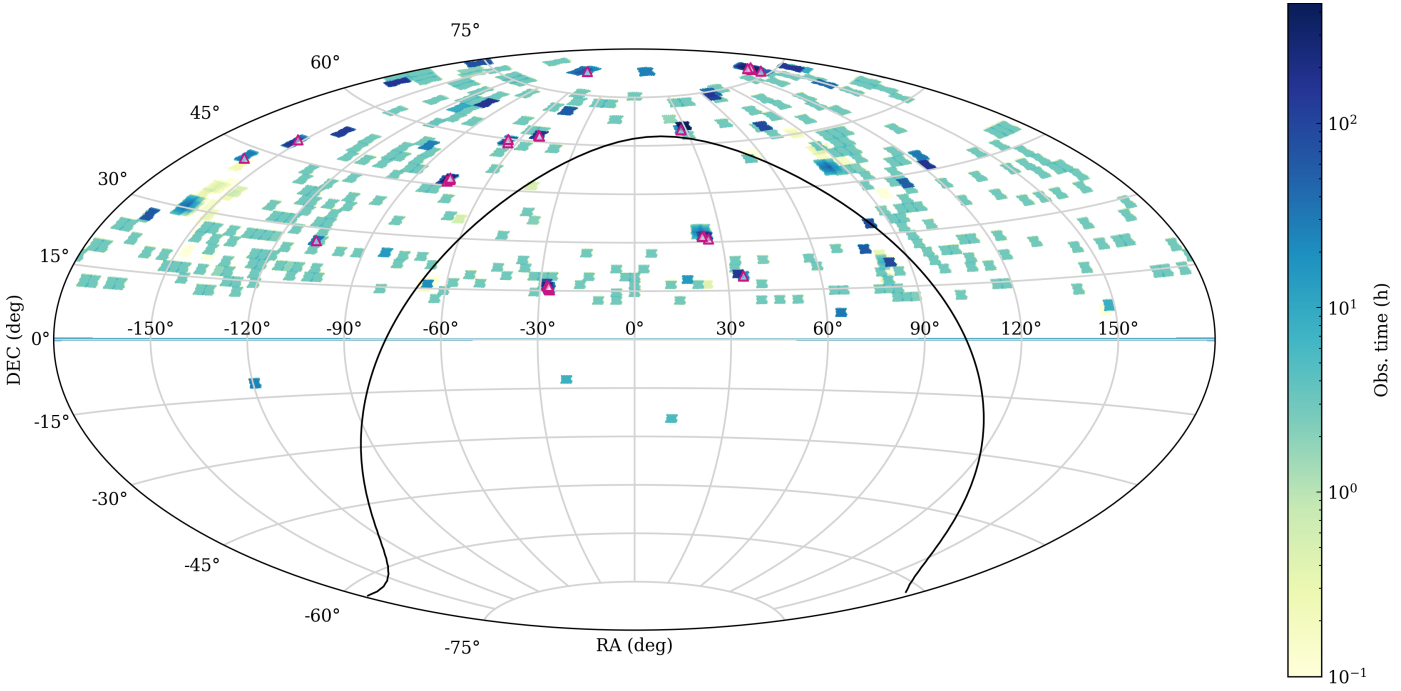

Figure 6.1: Exposure time per sky area in equatorial coordinates. Dark blue regions correspond to larger exposure times, and white regions have not been observed. The position of the detected FRBs is marked by magenta triangles. The galactic plane is indicated by the black line.

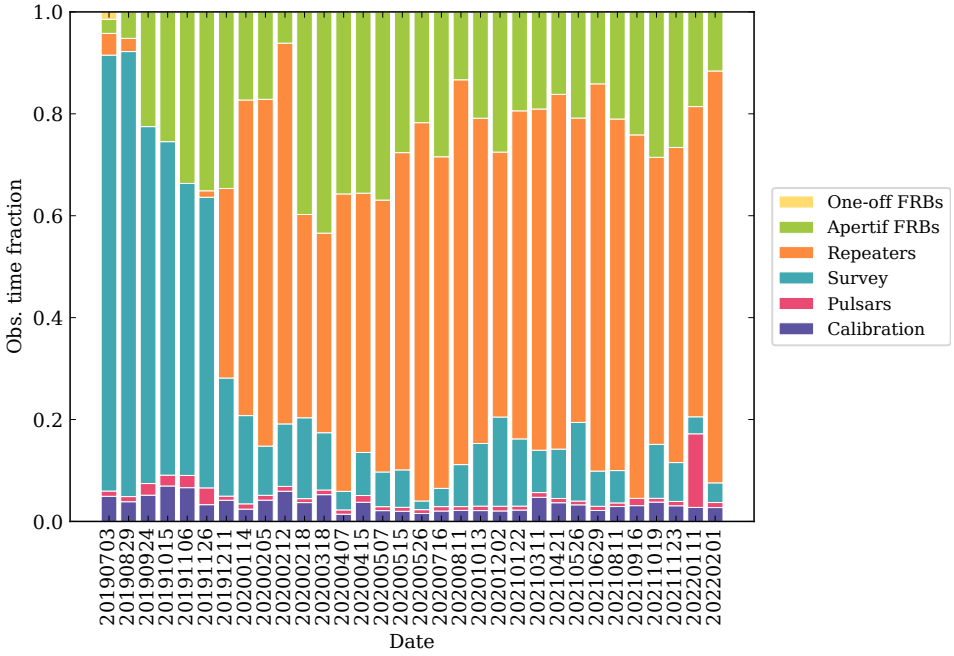

Figure 6.2: Fraction of the time spent on different target field classes per observing run. Each vertical bar corresponds to a different observing run, with the start date indicated below in YYYYMMDD format. Purple corresponds to the fraction of the time for calibration observations, pink for pulsar observations, blue for fields with no known FRBs defined in the original Apertif Survey, orange for known repeating FRBs, green for previously detected Apertif FRBs, and yellow for one-off FRBs discovered by other instruments.

several new repeaters were reported soon after (CHIME/FRB Collaboration et al. 2019c; Fonseca et al. 2020). Simultaneously, the number of Apertif detections was increasing. From 2020 onward, the observing shifted away from fields with no known FRBs in order to prioritise the follow up of repeaters and Apertif-discovered FRBs. Given the isotropic sky distribution of FRBs (Bhandari et al. 2018), one-off FRBs should be detected blindly at the same rate in pointings with and without known FRBs.

Figure 6.1 shows the exposure time per sky region in equatorial coordinates and the location of the newly discovered FRBs, while Fig. 6.2 shows the fraction of time spent on survey pointings, repeating FRBs, one-off FRBs, new FRBs discovered with Apertif, pulsars and calibration observations. During the 2019 observations $\sim$ 70% of the time was spent on the Apertif survey pointings, while the remaining $\sim$ 30% was divided between follow up of known and newly discovered one-off FRBs and calibration observations. The evolution in pointing strategy in 2020 and 2021 to prioritise the follow up of known repeaters and newly discovered Apertif FRBs is reflected in Fig. 6.2, where the changes implement around Jan 1 of each calendar year are visible. Roughly 60% of the time was dedicated to repeater follow up, 20% to the follow up of Apertif FRBs and the remaining 20% in survey pointings and calibration observations.

6.3 Data analysis

In this section, we detail the post-processing data analysis performed on the bursts that resulted from the AMBER and DARC searches and candidate selection (as described in van Leeuwen et al. 2022). Here we describe the methods to determine the burst properties, including dispersion measure, scattering, scintillation, flux calibration, morphology, frequency structure and localisation. The results of these analyses are presented in Section 6.4. Although for some discoveries the analysis and the results are somewhat intertwined, separating the analysis into its own Section here allows for easier back reference later, when we discuss the results.

6.3.1 Dispersion measure and redshift estimation

Each FRB candidate detected by the AMBER pipeline has an associated DM that maximises the signal-to-noise ratio (S/N) at the given downsampling factor. Some of the detected FRBs present multiple components, and we thus used an algorithm based on Hessels et al. (2019)[1], and already put to test in Pastor-Marazuela et al. (2021), to find the DM maximising the structure of the burst. For faint and/or scattered bursts with no signs of multi-component structure, we used pdmp[2] instead, since it maximises S/N and in these cases this method is more robust at determining the correct DM. The measured DMs of all FRBs presented in this paper are given in Table 6.3 of Appendix 6.A.

In order to determine the redshift upper limit for each FRB, we first estimate the extragalactic DM (DM_{EG}) from the observed DM_{obs}. We predict the Milky Way (MW) contribution to the DM (DM_{MW}) from the NE2001 (Cordes & Lazio 2003) and YMW16 (Yao et al. 2017) galactic electron density models, and take the lowest of the two to avoid underestimating the redshift. Since the galactic halo can also significantly contribute to the DM, we adopt the model from Yamasaki & Totani (2020) to compute the MW halo DM (DM_{halo}) in the direction of each FRB. The extragalactic DM will thus be $DM_{EG} = DM_{obs} - DM_{MW} - DM_{halo}$. Next we apply the DM–$z$ relation from Zhang (2018a) and assume the cosmological parameters from Planck Collaboration et al. (2020) to obtain the redshift upper limit. For this, we use the python package fruitbat[3] (Batten 2019). We assume a negligible host galaxy contribution to the DM. The measured DMs and estimated redshifts of our FRB sample are detailed in Section 6.4.4.1.

6.3.2 Flux calibration

To perform the flux calibration of all FRBs, we scheduled drift scan observations of the bright calibrator sources 3C147, 3C286, and/or 3C48 at the beginning and the end of each observing run. The flux densities of these sources are known (Perley & Butler 2017), and they can thus be used as calibrators to obtain the system-equivalent flux density (SEFD). For each FRB, we used the drift scan taken during the same observing run that was the least affected by radio frequency interference (RFI). To convert the pulse profile into flux units, we applied the radiometer equation using the obtained SEFD. We define the peak flux as the maximum flux value at the instrument

[1] DM_phase: https://github.com/danielemichilli/DM_phase
[2] pdmp: http://psrchive.sourceforge.net/manuals/pdmp/
[3] fruitbat: https://fruitbat.readthedocs.io/en/latest/

time resolution (0.08192 ms), and it is thus a lower limit. Finally we integrated over a time window covering the whole burst duration to obtain the FRB fluences in units of Jy ms. Based on the measured stability of the system, we assume 20% errors on the fluence. The resulting fluxes and fluences are given in Table 6.3 and detailed in Section 6.4.3.

6.3.3 Localisation and host identification

To determine the localisation of the detected FRBs, we implement the localisation method described in van Leeuwen et al. (2022). The method consists of creating a model of the telescope response in sky coordinates and comparing it to the observed response pattern as follows: first, a model of the Compound Beams (CBs) is created based on drift-scan data. From this we construct the TABs and SBs, consequently obtaining a model of the SB sensitivity in Right Ascension (RA) and Declination (Dec). To localise a burst, we next compare its S/N per SB detection pattern against the predicted SB model. We define the best position of each burst as the resulting 99% confidence regions, which have narrow elliptical shapes since the WSRT is an East-West array. The size of the confidence region decreases with higher detection S/N and the number of CBs where the burst was detected. The orientation of the ellipse depends on the hour angle of the detection due to the Earth rotation.

For each FRB, we looked for known galaxies within the localisation error region and below the redshift upper limit (Section 6.3.1) using two galaxy catalogues: the NASA/IPAC extragalactic database (NED) and the GLADE v2.3 catalogue (Dálya et al. 2018). However, in most cases the total error region is of order 7 arcmin^2, which is too large to unambiguously identify a unique FRB host galaxy (Eftekhari & Berger 2017). Although some FRB error regions might contain more than one known host galaxy candidate, there are probably more that are too faint to be detected. FRBs have been localised to galaxies of different types spanning a broad range of masses (see Bhandari et al. 2022, and references therein), from the dwarf galaxy hosts of FRB 20121102A (Chatterjee et al. 2017) and FRB 20190520B (Niu et al. 2022), to massive galaxies reaching close to $10^{11}\,M_\odot$ in the case of FRB 20200120E, which has been localised to a globular cluster of M81 (Bhardwaj et al. 2021; Kirsten et al. 2022). Following Petroff et al. (2018) and van Leeuwen et al. (2022), we estimate the expected number of galaxies within the comoving volume determined by the error region and the redshift upper limit of each burst. We adopt a dwarf galaxy number density of $n = (0.02-0.06)\,\mathrm{Mpc}^{-3}$ for galaxy masses $4\times10^7\,M_\odot < \mathrm{M_{stellar}} < 10^{10}\,M_\odot$ (Baldry et al. 2012; Haynes et al. 2011), and a massive galaxy number density of $n = (1.5-2.0)\times10^{-3}\,\mathrm{Mpc}^{-3}$ for galaxy masses $\mathrm{M_{stellar}} > 10^{11}\,M_\odot$ (Faber et al. 2007). The expected number of galaxies within the comoving volume V_co is simply $N_\mathrm{gal} = nV_\mathrm{co}$. The results of this analysis are given in Section 6.4.2.

6.3.4 Burst morphologies

We characterise the morphology of all FRBs by fitting their dedispersed pulse profiles to a single or multi-component model through minimisation of residuals. The number of components is determined by eye. Each burst is fitted to a single or multi-component Gaussian model given by Eq. 6.1, with and without a convolution with an exponential decay given by Eq. 6.2 to represent scattering, thus assuming the scattering timescale to be the same for all components. After fitting the scattered and unscattered models, the model with the lowest Bayesian information criterion

(BIC) is selected, with $\mathrm{BIC_g}$ for the Gaussian, unscattered model, and $\mathrm{BIC_{sc}}$ for the scattered model. The resulting expression for the fitted pulse profile $I(t)$ is given by Eq. 6.3.

$$G_i(t) = A_i \exp\left(-\frac{(t-t_i)^2}{2\sigma_i^2}\right) \tag{6.1}$$

$$F(t) = \begin{cases} e^{-t/\tau_{\mathrm{sc}}}, & \text{if } t \geq 0 \\ 0, & \text{otherwise} \end{cases} \tag{6.2}$$

$$I(t) = \begin{cases} \sum_{i=0}^{n} G_i(t), & \text{if } \mathrm{BIC_{sc}} > \mathrm{BIC_g} \\ F(t') \circledast \sum_{i=0}^{n} G_i(t'), & \text{otherwise} \end{cases} \tag{6.3}$$

Scattering is not the only explanation for the exponential broadening of the burst; intra-channel dispersive smearing is an instrumental effect that can also produce such broadening. While scattering is proportional to $\sim \nu^{-4}$, intra-channel smearing is proportional to ν^{-3} (Petroff et al. 2019, Section 4.1.2), and it becomes significant when the burst width is not resolved at the time-frequency resolution of the instrument. When possible, we compute the frequency-dependent exponential broadening in order to get the dependence on frequency and determine whether it is an instrumental or a propagation effect. However, bursts with low S/N or narrowband bursts do not allow for such an analysis. We thus determine whether the bursts are resolved in time, by comparing the fitted Gaussian width of the detected FRBs to simulated bursts at different DMs with different widths. We use the python library `simpulse`[1] to simulate bursts in a grid of varying intrinsic widths and DMs. We next use the burst fitting algorithm to determine the width that would be observed, and compare this to the actual FRB fitted Gaussian width. If the observed width corresponds to a simulated burst with a narrower intrinsic width, we consider the burst to be unresolved and thus unscattered at the Apertif time and frequency resolution.

We define the width of each burst component as the full width at tenth maximum (FWTM) of the fitted Gaussian for consistency with the First CHIME/FRB Catalog (CHIME/FRB Collaboration et al. 2021a), plus a factor $\tau_{\mathrm{sc}} \ln 10$ to take into account the scattering broadening. The total width of the burst is defined as follows in the general case of a multicomponent burst:

$$\mathscr{W}\ (\mathrm{ms}) = t_f - t_0 + (\mathrm{FWTM}_0 + \mathrm{FWTM}_f)/2 + \tau_{sc} \ln 10, \tag{6.4}$$

where t_0 and t_f are respectively the arrival time of the first and last subcomponents of the burst, and FWTM_0 and FWTM_f the full width at tenth maximum of the first and last components, respectively. For a single component burst and the independent burst subcomponents, the total width is defined as:

$$\mathscr{W}\ (\mathrm{ms}) = \mathrm{FWTM} + \tau_{sc} \ln 10. \tag{6.5}$$

If the scattering timescale of the FRB is unresolved, the term depending on τ_{sc} in Eq. 6.4 and 6.5 equals zero. Section 6.4.5 details the results of this analysis.

[1] `simpulse`: https://github.com/kmsmith137/simpulse

6.3.5 Frequency structure

The frequency structure of the detected FRBs provides information about the intrinsic burst spectrum and bandwidth, as well as phase modulations that could be intrinsic or produced by the propagation of the radio waves through the turbulent interstellar medium (ISM), known as scintillation. We obtain the FRB spectra $S(\nu)$ by averaging their frequency structure over the total burst duration W defined in Section 6.3.4. In the case of bursts with a frequency extent narrower than the observing bandwidth, we fit the averaged spectrum to a Gaussian. We define the burst peak frequency and the burst bandwidth respectively as the center and the FWTM of the fitted Gaussian.

To determine the scintillation bandwidth, we compute the auto-correlation function (ACF) of all burst spectra removing the zero-lag frequency value, and fit the central peak to a Lorentzian. We define the scintillation bandwidth $\Delta\nu_{\rm sc}$ as the full width at half maximum (FWHM) of the fitted Lorentzian. The ACF is defined as follows (see Section 4.2.2 from Lorimer & Kramer 2004, and references therein):

$$\mathrm{ACF}(\Delta\nu) = \frac{\sum_{\nu}(S(\nu))(S(\nu+\Delta\nu))}{\sqrt{\sum_{\nu}(S(\nu))^2 \sum_{\nu}(S(\nu+\Delta\nu))^2}}, \tag{6.6}$$

where $S(\nu)$ is the burst averaged spectrum at frequency ν and $\Delta\nu$ the frequency lag. In the case of multi-component bursts, we assume the scintillation to be the same for all subcomponents, since the subcomponent separation is small compared to the typical scintillation timescales of a few minutes observed in galactic pulsars (Narayan 1992; Bhat et al. 1998). The scintillation analysis results are summarised in Section 6.4.4.3.

For every FRB that is detected away from boresight, the spectrum we analyze is provided by an SB that is composed from the bands of several TABs (cf. Sect. 6.2). The number of combined TABs ranges from 0 (the central SB) to 8 (an outer SB). These TABs overlap but have some roll-off (see van Leeuwen et al. 2022). Variations in S/N with frequency of order 10% may be introduced throughout the band, between the edge and peak of each subsequent TABs.

6.4 Results

Between July 2019 and February 2022, a total of 24 new FRBs were discovered within the ALERT survey, including FRB 20190709A, FRB 20190926B, FRB20191020B, FRB 20191108A, FRB 20191109A, and FRB 20201020A from previous publications (van Leeuwen et al. 2022; Connor et al. 2020; Pastor-Marazuela et al. 2022). This is one of the largest samples of one-off FRBs above 1 GHz. The dynamic spectra and fitted pulse profiles of all 24 FRBs are presented in Fig. 6.3. All FRBs were followed up with Apertif observations for 30 h up to 450 h, but none were seen to repeat. The bursts display different morphologies, including broadband and narrowband single components, and a high fraction of bursts with multiple components peaking at the same frequency. These morphologies are typical of the one-off FRBs in the First CHIME/FRB catalogue

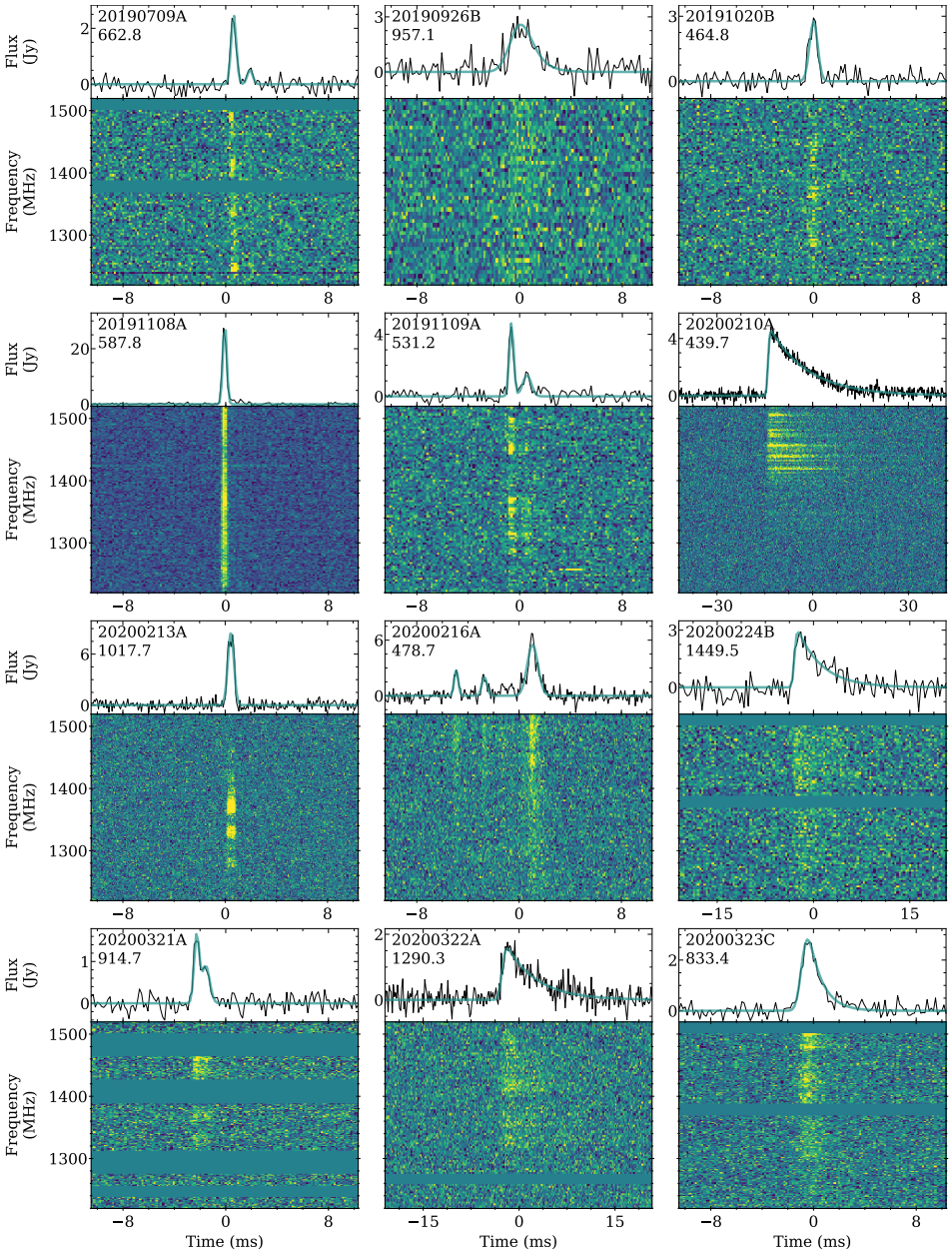

Figure 6.3: Dynamic spectra of all FRBs detected with Apertif. Each top panel shows the averaged pulse profile in black, and the fitted pulse profile in teal. The FRB TNS name is indicated on the top left corner, and the DM ($\mathrm{pc\,cm^{-3}}$) it has been dedispersed to below the name. Each bottom panel shows the dynamic spectrum of the FRB, with the data rebinned in time and frequency to optimise the visibility of the bursts.

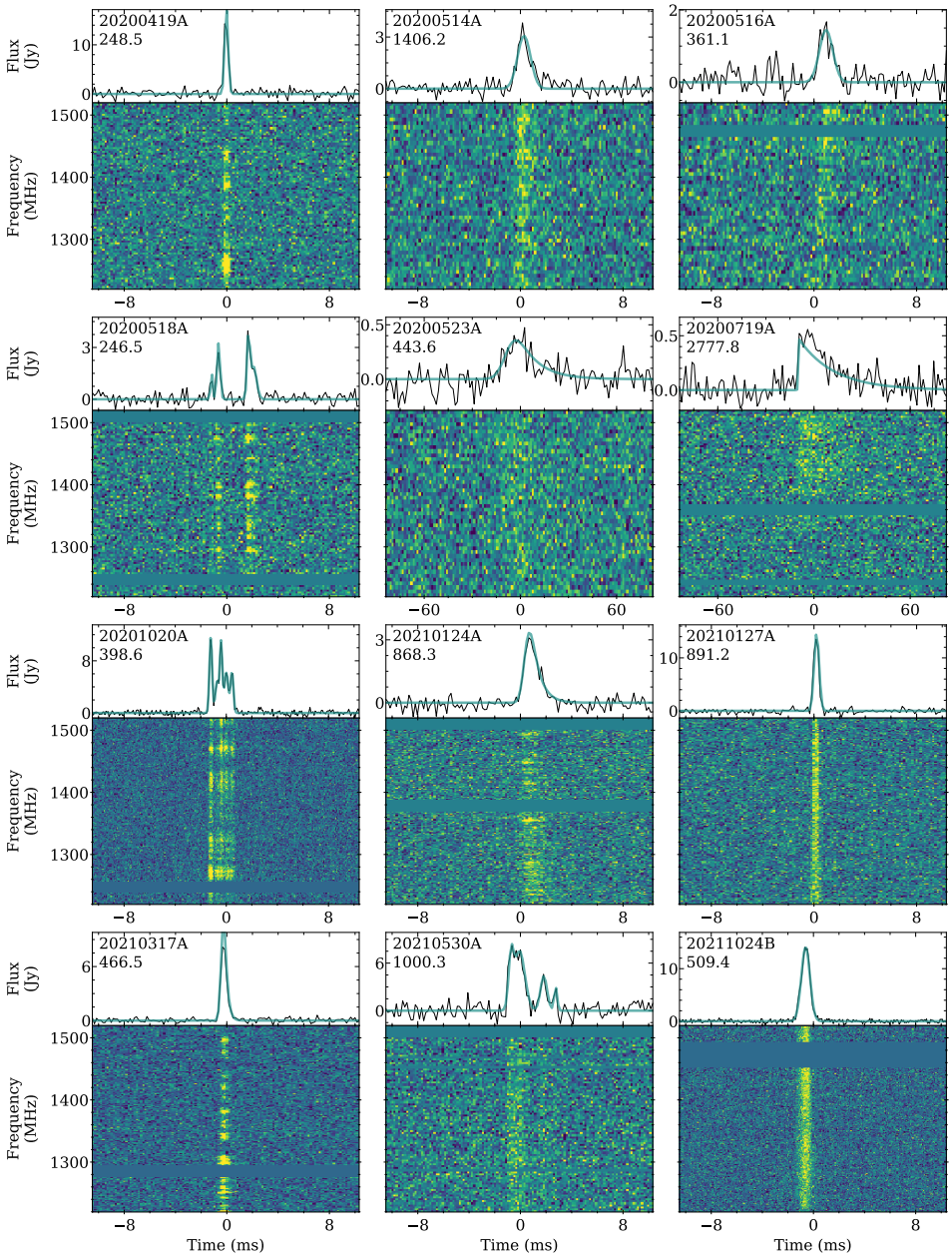

Figure 6.3: Continued

(Pleunis et al. 2021a); the lack of observed repetitions thus reinforces this apparent relation between morphology and repetition. Additionally, the bursts display a broad range of propagation properties that we will discuss below. In this Section, we first describe in detail the properties of some of the FRBs in our sample with remarkable features (Section 6.4.1), and next the properties of the FRB ensemble from Section 6.4.2 onwards.

6.4.1 FRBs of special interest

This section describes individual FRBs in our sample ordered by detection date, with the exception of three FRBs with similar features grouped in a single subsection at the end.

6.4.1.1 FRB 20200210A

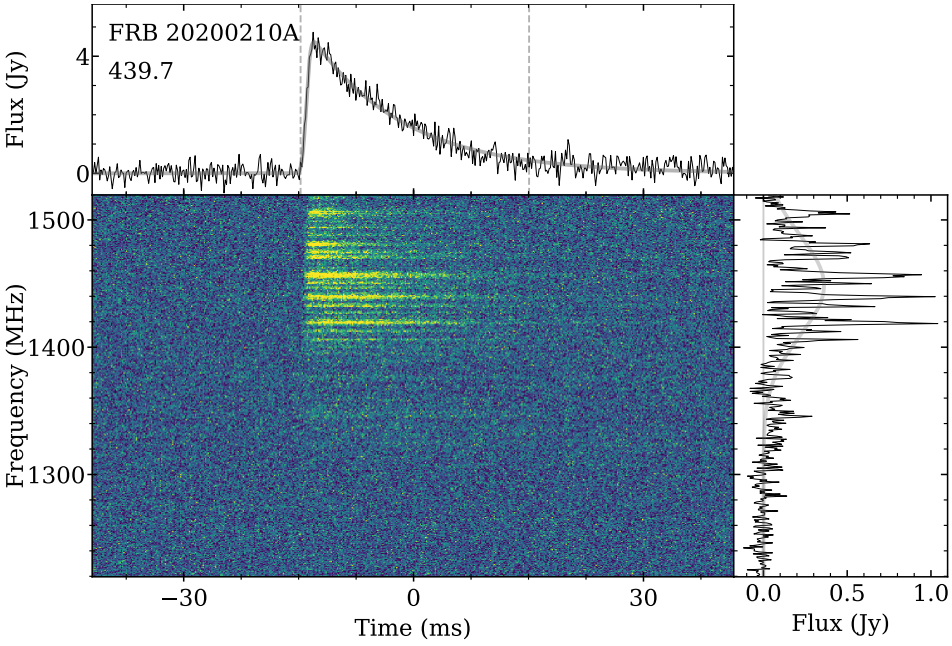

Figure 6.4: Dynamic spectrum of FRB 20200210A. The top panel shows the average pulse profile , with a transparent grey line representing the fit to a scattered gaussian, and the vertical dashed lines the initial and final times of the burst from which the spectrum is extracted. The text indicates the TNS name and the DM ($\mathrm{pc\,cm^{-3}}$) of the burst. The bottom right panel shows the spectrum extracted between the two dashed lines in the pulse profile, and its fit to a gaussian in grey. We associate the large intensity fluctuations to scintillation in the Milky Way. The bottom left panel is the dynamic spectrum.

This FRB presents a set of rare properties. It displays both temporal broadening from multi-path propagation, with $\tau_{\mathrm{sc}} = 12.6 \pm 0.3$ ms, as well as a scintillation pattern with $\Delta\nu_{\mathrm{sc}} = 1.6 \pm 0.1$ MHz, which indicates the burst has traveled through two distinct scattering screens. Furthermore, it is a narrowband burst, with a bandwidth of ~ 170 MHz. The scattering timescale is uncommonly

large for its DM of 439.7 pc cm^{-3}. Such a large scattering timescale at 1370 MHz cannot be explained by the Intergalactic Medium (IGM) or an intervening galaxy halo; we thus associate the first scattering screen with the host galaxy. The scintillation bandwidth falls within the expected ranges from the YMW16 (Yao et al. 2017) and NE2001 (Cordes & Lazio 2003) electron density models; the scattering screen producing scintillation is thus likely to be located in the Milky Way.

Scintillation can only occur when the scattering diameter of the first scattering screen is unresolved by the second, and this permits us to put constraints on the distance between the FRB and the first scattering screen (Masui et al. 2015; Cordes & Chatterjee 2019). Cordes & Chatterjee (2019) determine the source size requirements for scattering and scintillation to be present at the same frequency band:

$$\tau_X \tau_G < \frac{1}{(2\pi\nu)^2} \frac{d_{so}^2}{L_X L_G} \simeq (0.16 \text{ ms})^2 \left(\frac{d_{so}^2}{\nu^2 L_X L_G} \right), \tag{6.7}$$

where τ_X and τ_G are respectively the extragalactic and galactic scattering timescales in ms, ν is the observing frequency in GHz, d_{so} the source to observer angular diameter distance in Gpc, and L_X and L_G are respectively the distances of the lenses to the source and the observer in kpc. We want to determine the distance upper limit between the source and its host galaxy scattering screen, L_X. Scintillation bandwidths can be converted to scattering timescales with the following equation:

$$\tau_{\text{sc}} = C_1 / 2\pi \Delta\nu_{\text{sc}}, \tag{6.8}$$

where C_1 is a constant with a value close to unity that depends on the medium scattering properties, and we assume $C_1 = 1$ for a thin scattering screen (Eq. 8 from Cordes & Rickett 1998; Lorimer & Kramer 2004, Section 4.2.3).

In the case of FRB 20200210A at a frequency $\nu = 1.37$ GHz, we have the extragalactic scattering timescale $\tau_X = 12.6 \pm 0.3$ ms, and the Galactic scintillation bandwidth $\Delta\nu_{\text{sc}} = 1.6 \pm 0.1$ MHz, which yields $\tau_G = 0.1$ μs. Given the galactic latitude of the FRB, the scintillation is likely produced in the Milky Way thick disk, at $L_G \sim 1$ kpc (Ocker et al. 2022b). From the extragalactic DM of the FRB alone, we set a redshift upper limit of $z = 0.37$, and thus an angular diameter distance upper limit of $d_{so} = 1.09$ Gpc. By using these values in Eq. 6.7, we find an upper limit on the distance between the FRB and the scattering screen at its host galaxy of $L_X \lesssim 13$ kpc. However, the presence of scattering allows us to use a joint scattering-dispersion redshift estimator. We do this by applying the method described in Cordes et al. (2022), and assume a lognormal probability density function (PDF) for the scattering parameter $\phi_\tau \equiv \tilde{F}G$. We find the estimated median redshift to be $z = 0.11$, which corresponds to an angular diameter distance of $d_{so} = 0.43$ Gpc. With this new redshift constraint, we find the distance upper limit between the FRB and its scattering screen to be just 2 kpc. This is fully consistent with scattering in the host galaxy, even for a dwarf host, although it is not constraining enough to determine if the scattering originated in the circumburst environment.

6.4.1.2 FRB 20200213A

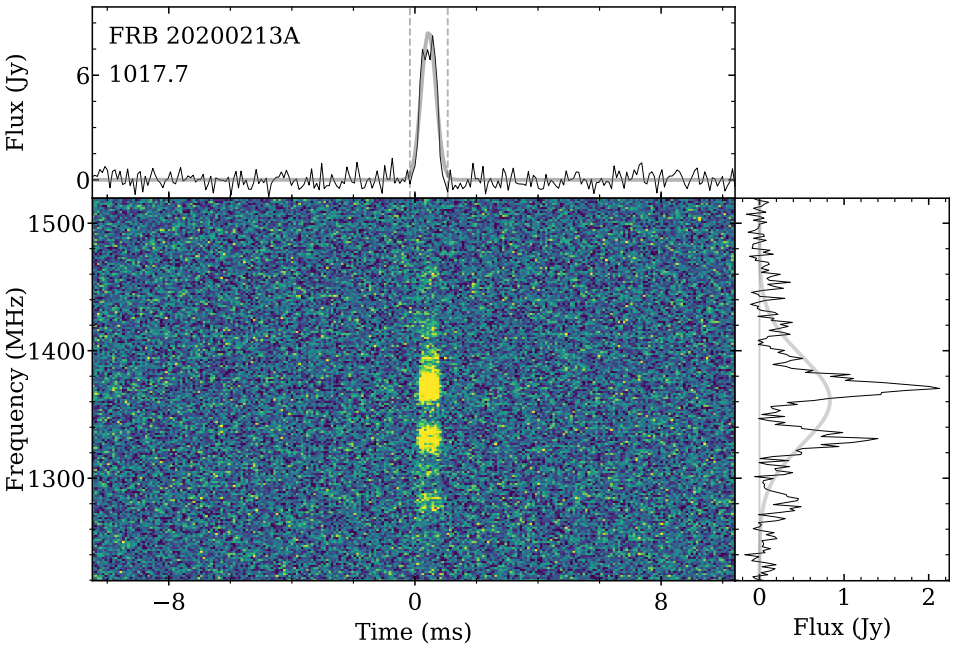

Figure 6.5: Dynamic spectrum of FRB 20200213A. The pulse profile and the spectrum are both fitted to a gaussian.

This FRB is the most narrowband of the sample. It has a bandwidth of 145 MHz, less than half of the total observing bandwidth. Additionally, it displays a strong frequency modulation, with two main patches of similar intensity and an array of lower intensity patches above and below the central ones. The frequency modulation has a 19 MHz bandwidth, significantly larger than the 4 MHz $\Delta\nu_{sc}$ predicted by the NE2001 model (YMW16 predicts 1 MHz). This suggests that either the Galactic ISM is more uniform than predicted by the electron density models, or that the frequency structure is intrinsic to the source. The temporal structure of the burst presents a single component with a flat peak. Given the DM of 1017.7 pc cm^{-3} and the instrument frequency resolution of 195 kHz, the FRB width is close to the dispersion broadening (Petroff et al. 2019). The flat peak could thus be a result of instrumental smearing instead of the intrinsic structure of the burst, or be the signature of a second or even third component indistinguishable from the first.

6.4.1.3 FRB 20200216A

This FRB consists of a bright main burst subcomponent with two narrow precursors of about a third of the amplitude of the main. The separation between the two precursors is ~ 2.2 ms, while the main component arrives ~ 3.8 ms after the second precursor. The pulse profile presents two bumps between the second precursor and the main component, but their amplitude is too low

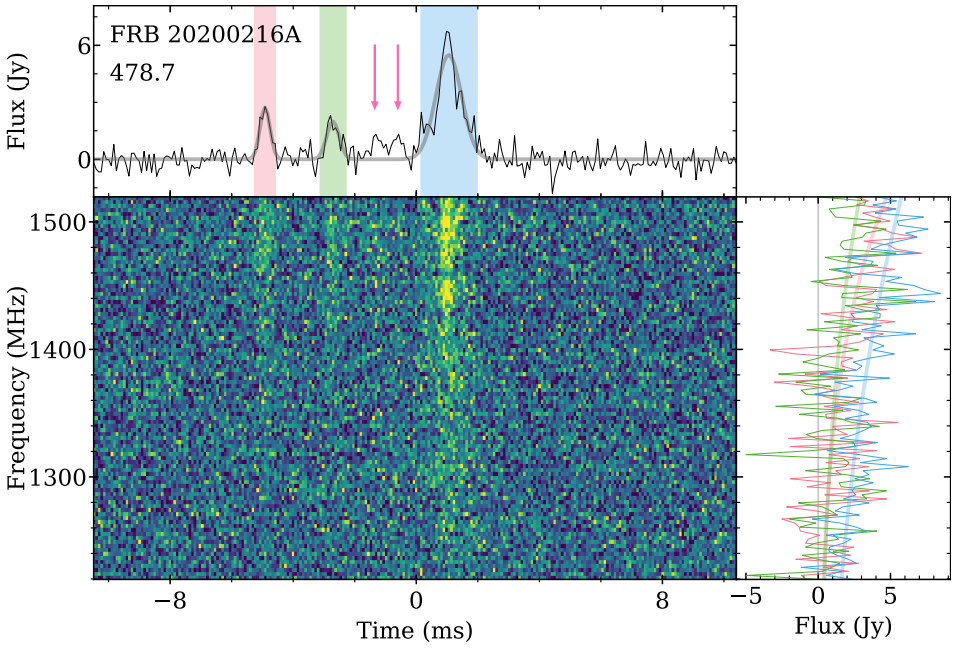

Figure 6.6: Dynamic spectrum of FRB 20200216A. On the pulse profile (top panel), each colored shaded region shows a distinct component and fitted to a gaussian. Their respective spectra are shown on the bottom right panel with the same color, and fitted to a power law (transparent solid lines). The two pink arrows on the pulse profile indicate the position of the two potential subcomponents between the precursors and the main component.

to be identified as real subcomponents. We carried out a timing analysis as the one described in (Pastor-Marazuela et al. 2022) to determine the presence of a periodicity FRB 20201020A, including the power spectrum analysis and the time separation between subcomponents, but we find no evidence of periodicity in this FRB.

The spectrum of each of the FRB 20200216A subcomponents can be well fitted by a power law. The power law spectral indices of the first, second, and third components are respectively 11.6, 8.7 and 5.6. The precursors seem to peak at higher frequencies than the main subcomponent, which might appear to be a reminiscent of the downwards drifting effect typically observed in repeating FRBs (e.g. Hessels et al. 2019). However, the main subcomponent is brighter at the top of the band. The lack of visible emission at the bottom of the band of the two precursors could be simply explained by their lower amplitude, which is below the noise level at lower frequencies. The emission of each component is likely to peak at similar frequencies, but above the highest observing frequency. We thus identify the morphology of this FRB as a multi-component burst with components peaking at the same frequency (Pleunis et al. 2021a).

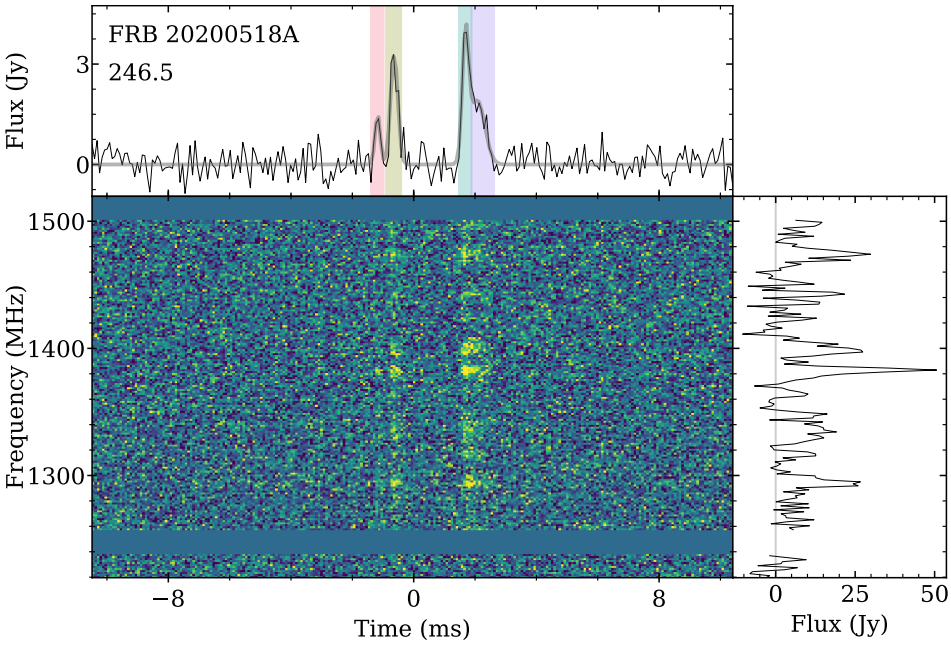

Figure 6.7: Dynamic spectrum of FRB 20200518A. On the pulse profile, each of the four components is marked by a coloured shaded region, and fitted to a gaussian. The spectrum on the bottom right panel is the sum of all components.

6.4.1.4 FRB 20200518A

This FRB consists of two groups of two narrowly spaced subcomponents each. The space between the two groups is ~ 2.3 ms, while the space between the subcomponents of each group is 0.54 ms on the first and 0.34 ms on the second. In the first group, the second component has a larger amplitude, while the first component of the second group is the brightest of all four. The power spectrum of the average pulse profile presents several peaks, but each one corresponds to the separation between different components. The timing analysis does not provide evidence for the presence of a periodicity.

All four subcomponents present a similar frequency extent. The peak frequency of the emission cannot be easily determined since the burst presents a frequency structure that we associate with scintillation, with a bandwidth of $\Delta\nu_{\rm sc} = 10 \pm 4$ MHz. This matches the expected Milky Way contribution from NE2001 (Cordes & Lazio 2003) within errors. The burst presents no evidence of broadening at the Apertif resolution.

With a DM of 246.5 pc cm^{-3}, its redshift upper limit is $z_{\rm max} = 0.18$, and the burst is localised to a 2.96 arcmin^2 error region. We can thus determine the expected number of galaxies contained within the comoving volume of the localisation region to be only ~ 2 dwarfs and ~ 0.1 massive galaxies. Any galaxy within the error region is thus likely to be the host. We found no potential

host galaxies in the NED and GLADE galaxy catalogs. Deep optical or near-infrared observations thus have a high chance of identifying the potential host where this FRB was produced.

6.4.1.5 FRB 20200719A

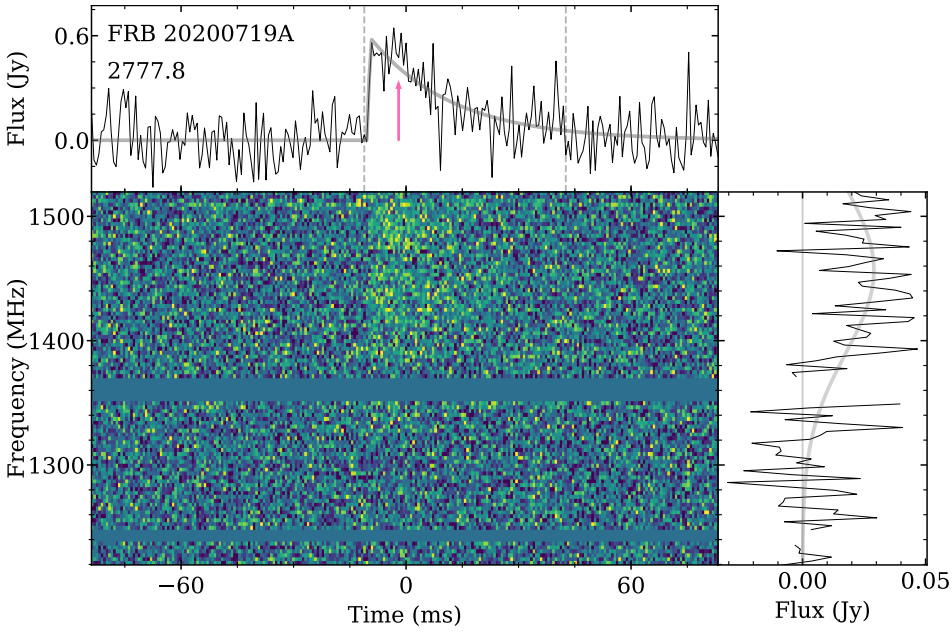

Figure 6.8: Dynamic spectrum of FRB 20200719A. The pulse profile is fitted to a scattered gaussian. The pink arrow indicates the position of an excess emission that might be explained by a second component merged to the first by scattering. The spectrum is fitted to a gaussian.

FRB 20200719A, with a DM of 2778 pc cm^{-3}, is the most dispersed FRB of our sample, as well as the most scattered, with τ_{sc}=21 ms. It differs by more than 1000 pc cm^{-3} from the Apertif FRB with the second largest DM. Compared to the FRBs in the TNS, it is the FRB with the second largest DM known to date, after CHIME/FRB source FRB 20180906B with a DM of 3038.1 pc cm^{-3}. The inferred redshift upper limit of FRB 20200719A is $z_{max} \sim 3.2$. The large scattering timescale might however be an indication of a significant contribution to the DM from the host galaxy and the circumburst environment (Cordes et al. 2022; Ocker et al. 2022b), which would place the FRB at a lower redshift. Nonetheless, since the host galaxy contribution to the observed DM evolves as $\mathrm{DM_{host}} = \mathrm{DM_{host,loc}}/(1+z)$ (Deng & Zhang 2014), even a large host local DM contribution would be diluted at high redshift. We can estimate what the redshift lower limit would be assuming the host galaxy has a DM contribution as large as the repeating FRB 20190520B (Niu et al. 2022). The host galaxy of this FRB has a contribution to the observed DM of $\mathrm{DM_{host}} = 902$ pc cm^{-3}. Since the host is located at $z = 0.241$, the local DM contribution in the host frame is $\mathrm{DM_{host,loc}} \sim 1119$ pc cm^{-3}. If we assume the host galaxy of FRB 20200719A

has a contribution to the DM as large as FRB 20190520B, its redshift would be $z_{\rm min} \sim 2.85$. This highly constraining lower limit still places the FRB at very large cosmological distances.

The probability of intersecting a foreground galactic halo increases with distance. For instance, the most highly dispersed FRB 20180906B from the CHIME/FRB sample (CHIME/FRB Collaboration et al. 2021a) was shown to intersect within 1.4 Mpc of a galaxy cluster (Connor & Ravi 2021). For FRB 20200719A, the possibility of intersecting foreground galaxies is not negligible. We follow Prochaska & Zheng (2019) to determine how likely this FRB is of intersecting an intervening galaxy with a mass greater than the Milky Way within the line of sight (LoS). We use the Aemulus halo mass function (McClintock et al. 2019) to generate galaxy halos with masses between $10^{12}\,{\rm M}_\odot$ (roughly the MW mass) and $10^{16}\,{\rm M}_\odot$. Next, we compute the average number of halos expected to occupy the comoving volume at the redshift upper limit of this FRB, $z_{\rm max} = 3.2$. If we consider an intersection within the virial radius of the galaxies within the comoving volume, which is the distance at which e expect a foreground galaxy to have a significant contribution to the DM, we find the average number of galaxies to be $N(z) = 2.633$. However, in order to have a significant contribution to scattering, the impact parameter must be lower (Ocker et al. 2021). If we consider 0.15 times the virial radius (roughly 10 times the half mass radius, and between 20 and 40 kpc depending on the mass, Kravtsov 2013), we find $N(z) = 0.089$. Assuming the location of the foreground galaxies within the comoving volume follows a Poisson distribution, the probability that the LoS crosses k halos is given by:

$$P(k|N(z)) = \frac{N^k e^{-N}}{k!}. \tag{6.9}$$

The probability of intersecting at least one foreground halo is thus given by $P(k \geq 1|N(z)) = 1 - e^{-N}$. We find the probability of at least one intersection within the virial radius of the foreground galaxy to be $\sim 93\%$, and within 0.15 times virial radius it is $\sim 8.5\%$. Foreground galaxies are thus very likely to contribute to the DM of this FRB, while the contribution to scattering is less likely.

The localisation region contains no known galaxies from the NED and GLADE databases, but at such a high redshift upper limit, roughly 10^3 dwarfs and ~ 50 massive galaxies are expected to be contained within the localisation comoving volume. Determining a potential host galaxy is thus unfeasible.

The spectrum of the FRB can be fitted to a gaussian peaking at $\nu_{\rm obs} = 1460$ MHz and with a bandwidth (FWTM) of 260 MHz. Part of the emission thus happens at frequencies above the observing bandwidth. The pulse profile fitted to a single scattered component shows excess of emission after the peak. This might be the signature of a second component that is blurred together with the first due to scattering. By fitting a two-component scattered model, we find a potential component separation of 5.95 ms. However, the BIC of the single component model is marginally lower and hence it is preferred.

Given the large distance at which this FRB was emitted, its peak frequency is highly redshifted towards lower frequencies. The observed frequencies evolve as $\nu_{\rm obs} = \nu_0/(1+z)$, which means the peak frequency in the host galaxy frame would have been between 5.6 and 6.2 GHz for $z_{\rm min}$

and $z_{\rm max}$ respectively. As it will be further discussed in Section 6.5.4, and shown in Fig. 6.23, this is the highest inferred rest frame frequency of a one-off FRB to date. The implications of such a high DM FRB are reviewed later in Section 6.5.1.4.

6.4.1.6 FRB 20210530A

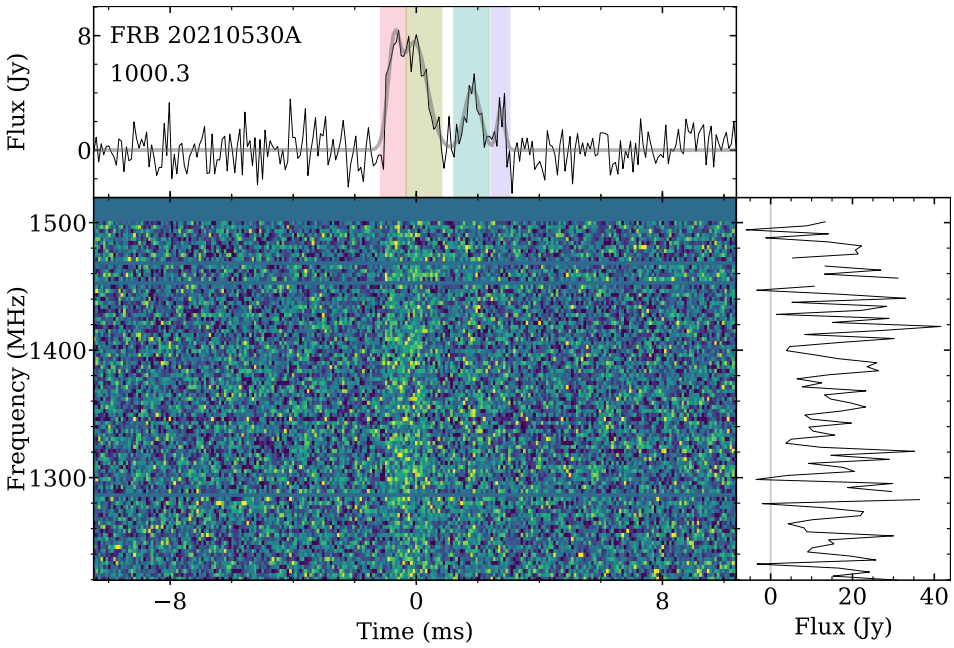

Figure 6.9: Dynamic spectrum of FRB 20210530A. The pulse profile is fitted to four gaussian components, each of them marked by coloured shaded regions. The added spectrum of all four components remains constant throughout the whole bandwidth.

The pulse profile of this FRB consists of a main, broad component with a flat top with two postcursors, but it is well fitted by four gaussian components. The first two gaussians model the profile of the main component, and they have a similar amplitude and a separation of 0.67 ms. The two postcursors have a separation of 1.89 ms and 0.93 ms with respect to their preceding subcomponents each. A timing analysis does not reveal evidence for periodicity.

6.4.1.7 FRB 20211024B

This FRB consists of a single discernible component with a FWTM of 1.45 ms. The burst presents a slight asymmetry, with the intensity increasing more slowly than it decreases later. This could be an intrinsic property of the burst, or a hint of a precursor that is not resolved. The burst was detected with a DM of 509.4 $\rm pc\,cm^{-3}$, and after removing the MW and halo contribution, we find

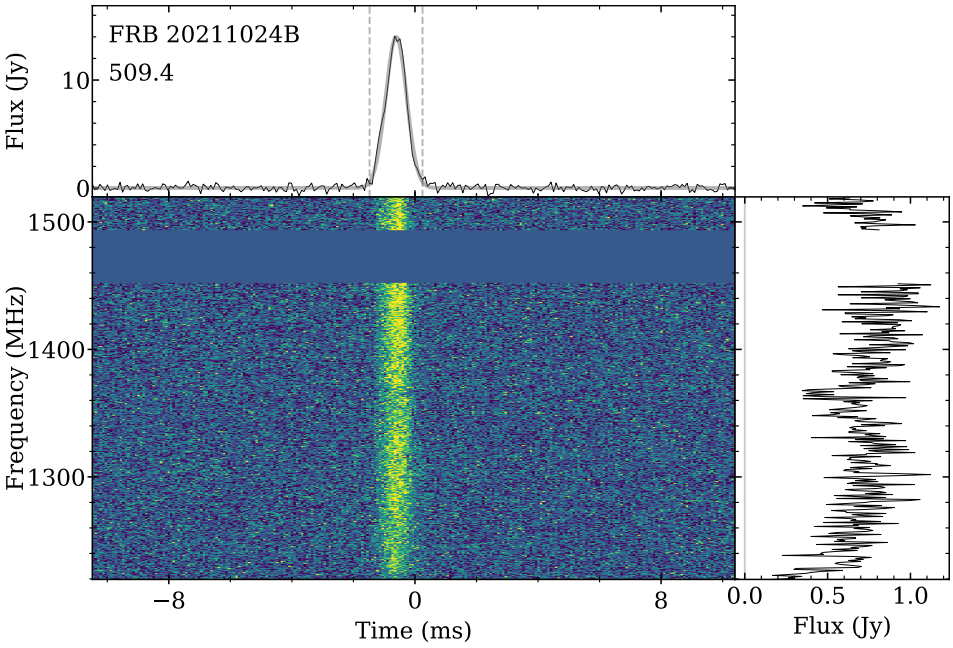

Figure 6.10: Dynamic spectrum of FRB 20211024B. The spectrum shows a morphology that cannot be well fitted to a gaussian nor a power law, but that could be of instrumental origin: the FRB was detected in SB 40 (Table 6.4), which is composed of 2 TABs (see Section 6.3.5).

a redshift upper limit of $z = 0.51$. This FRB has a small localisation region of 0.69 arcmin^2, where the estimated number of galaxies is 3–9 dwarfs and 0.2–0.3 massive galaxies. Four galaxies from the NED extragalactic database are known to occupy the localisation area, and all their photometric redshifts fall within the estimated FRB upper limit. The FRB localisation region and potential host galaxies are shown in Fig. 6.11. In order to determine what the probability for each galaxy of being the host of FRB 20211024B is, we applied the Probabilistic Association of Transients to their Hosts (PATH) analysis (Aggarwal et al. 2021), adopting the recommended assumptions, thus weighting the priors by the brightness of each galaxy and by a decreasing exponential probability density function for the offset of the FRB from the galaxy. We assumed the probability that the FRB host is unseen $P(U)$ to be 0%. The results from the analysis are given in Table 6.1. From our assumptions, we find the posterior probability of the galaxy SDSS J132034.68+422927.8 to be the host is $> 99.999\%$. Of the four, this is the lowest redshift, brightest galaxy, which also has the largest angular size. While other priors could potentially reduce this final probability, we conclude with >90% confidence that this galaxy is the host where FRB 20211024B was produced.

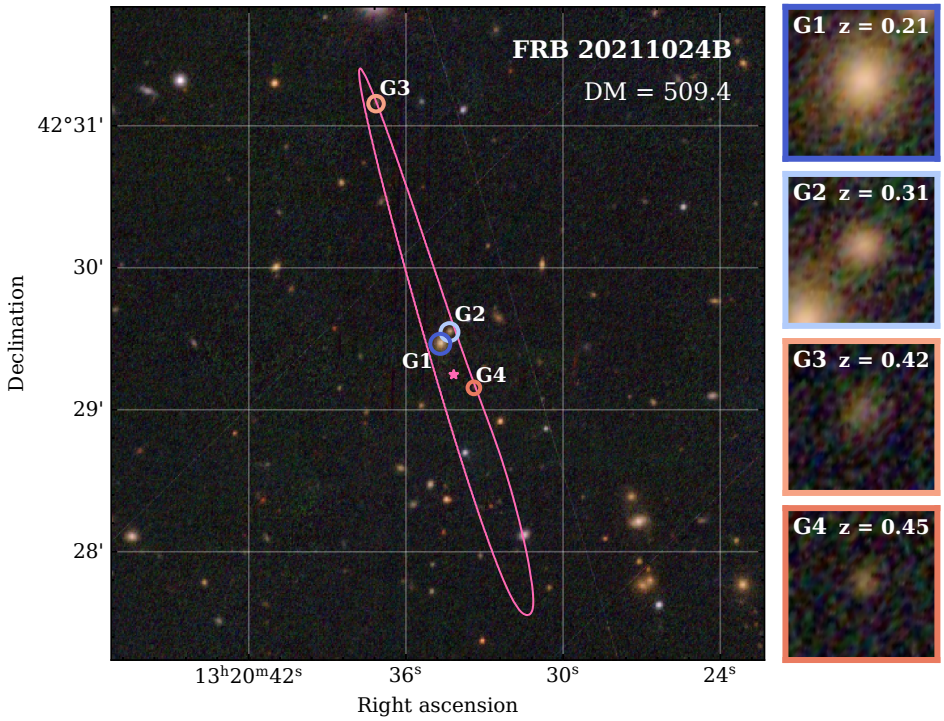

Figure 6.11: Localisation region of FRB 20211024B. The error region is marked by the pink contour, and the four galaxies within the region are marked by empty circles with bluer edge colors for lower redshifts and redder for higher redshifts, and the galaxy ID (same as in Table 6.1) is indicated next to each circle. The subplots on the right are a zoomed images of the four galaxies within the region (10″ FoV), where the spine colours are the same as the circles on the main image, each galaxy ID is written on the to left corner, and the photometric redshift is indicated on the top right corner.

6.4.1.8 Bicomponent bursts

Three bursts manifest two components, where the first is brighter than the second. Two of the FRBs, FRB 20190709A and FRB 20191109A, were originally presented in van Leeuwen et al. (2022). As discussed there, the subcomponents of FRB 20190709A have a separation of 1.3 ms, and the amplitude of the first is roughly five times larger than the second. Each has a FWTM of ~ 0.9 ms, and no scattering at the instrument resolution. The first component is broadband and shows intensity variations in frequency consistent with the expected scintillation in the MW. The second component is mainly visible at the bottom of the band, coincident in frequency with a bright scintillation 'patch' from the first component. Similarly, the subcomponents of FRB 20191109A have a separation of 1.2 ms, the main component has a width of 0.7 ms and it is ~ 3.5 larger in amplitude than the second, with a width of 1.4 ms.The pulse profile shows a bump about a millisecond after the first component, but its S/N is too low to confidently associate it with a third component. The two components have a similar frequency extent. The emission extends from

Table 6.1: Results from the PATH analysis for FRB 20211024B.
[a] SDSS galaxy name giving the right ascension (hhmmss) and declination (+ddmmss) of each galaxy. [b] Photometric redshift. [c] Magnitude in the r filter. [d] Petrosian radius in the r filter. [e] PATH priors. [f] PATH posteriors.

ID	Galaxy name[a]	$z_{\rm phot}$[b]	m_r[c]	r_r[d]	$P(O)$[e]	$P(O\|x)$[f]
G1	SDSS J132034.68+422927.8	0.2117	18.384	3.97	0.701682	> 0.99999
G2	SDSS J132034.33+422932.8	0.3072	20.077	2.53	0.205769	2×10^{-9}
G3	SDSS J132037.14+423109.3	0.4171	20.846	3.43	0.065606	$< 10^{-10}$
G4	SDSS J132033.40+422909.2	0.4455	21.889	1.71	0.026943	$< 10^{-10}$

the top of the band down to 1280 MHz. There appears to be a gap in emission between 1370 and 1440 MHz, but we associate it to an instrumental effect (lower sensitivity at those frequencies during the observation) rather than to an intrinsic property of the burst. FRB 20200321A is the last burst with two components. The observation where this burst was detected was highly affected by RFI, and almost half of the observing bandwidth had to be masked. The subcomponent separation is 0.7 ms, while the widths are 0.9 ms and 1.3 ms for the first and the second subcomponents respectively. The subcomponents are thus nearly merged together. From the limited available bandwidth, the two components appear to be narrowband, with a frequency extent of ~ 230 MHz at a peak frequency 1435 MHz, with both subcomponents extending the same range of frequencies.

6.4.2 Localisation

The Apertif localised FRBs have an average error region of $\sim 7\,\mathrm{arcmin}^2$ and a median of $\sim 3\,\mathrm{arcmin}^2$. Figure 6.12 displays the 99% confidence levels on the localisation of the new Apertif FRBs with a localisation area $< 6\,\mathrm{arcmin}^2$, as well as the galaxies identified within the error regions. Depending on the redshift upper limit determined through the extragalactic DM contribution, we estimate the number of dwarf and massive galaxies expected to be contained in the comoving volume $V_{\rm co}$ of the localisation region, as shown in Fig. 6.13.

For several of the Apertif FRBs, the expected number of dwarf galaxies within the error region computed as described in Section 6.3.3 is <5, while the number of expected massive galaxies is $\ll 1$. For these FRBs, namely FRB 20200518A, FRB 20210317A, FRB 20200419A and FRB 20201020A, deep optical observations of the localisation region might help identifying a short list of host galaxy candidates. Of these, only FRB 20201020A (Pastor-Marazuela et al. 2022) contains known galaxies from the NED and GLADE galaxy catalogues.

All FRBs were found with galactic latitudes $|l| > 12^\circ$ with the exception of FRB 20200514, with $l = 2.48^\circ$, which was detected in an observation of the repeating FRB 20180916B.

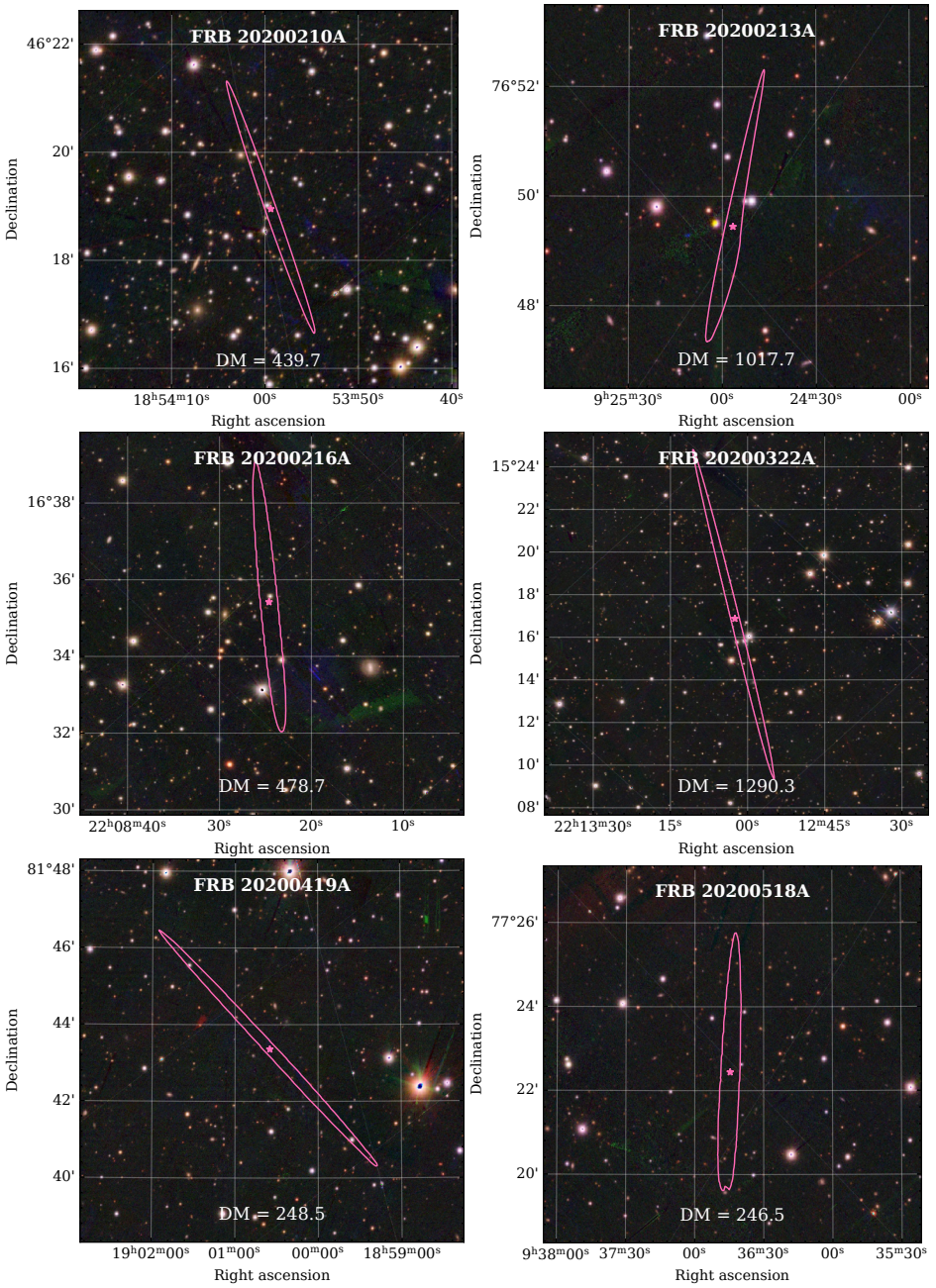

Figure 6.12: Localisation regions of the new Apertif FRBs. In each subplot, the pink contour represents the 99% confidence region of the localisation, and the pink star the centroid of the error region. The blue cross in FRB 20211024B represents the galaxy identified within the error region and redshift upper limit in the NED catalogue. The text on top of each plot gives the TNS identifier of each FRB, and the bottom text the DM in units of $\mathrm{pc\,cm^{-3}}$. The background images are from the PanSTARRS DR1 (Chambers et al. 2019). In each plot, the grids are spaced by 2 arcmin in declination.

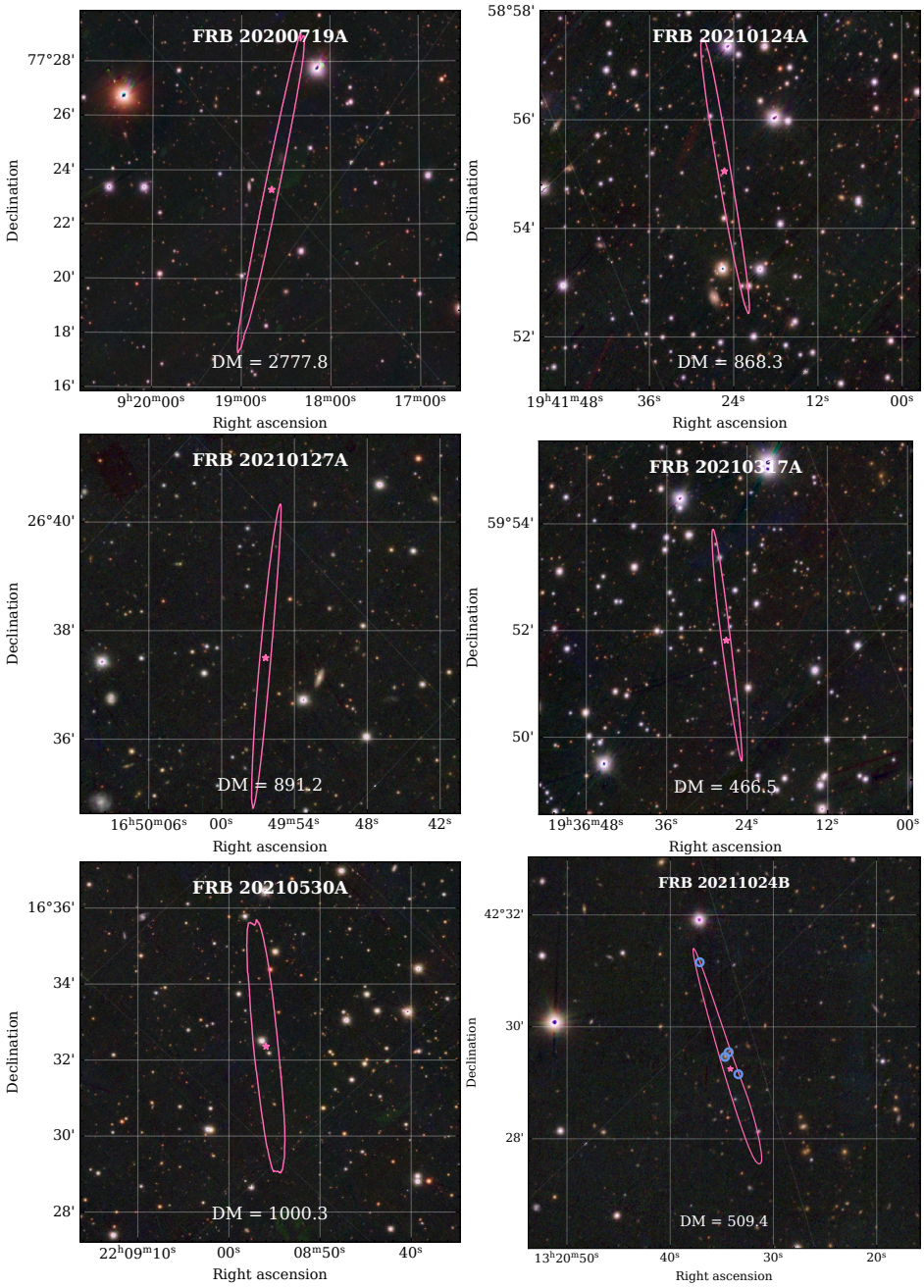

Figure 6.12: Continued

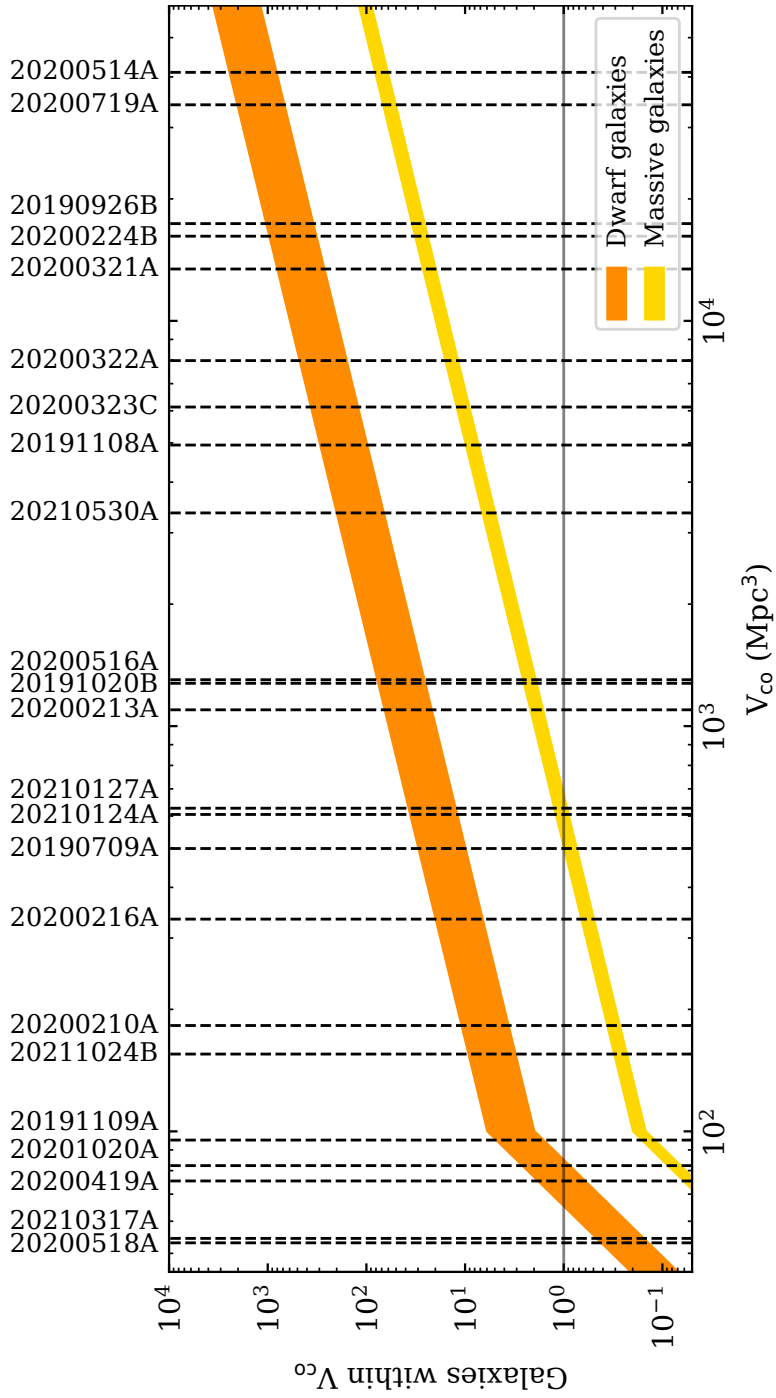

Figure 6.13: Expected galaxies within the comoving volume of the FRB localisation. The orange and yellow shaded regions give the expected number of dwarf and massive galaxies respectively within the localisation region and redshift upper limits. Each vertical dashed line gives the upper limit on the comoving volume of an FRB, whose TNS identifiers are given on top. The horizontal line shows the one galaxy limit.

6.4.3 Event rate and fluence distribution

Within the Apertif FRB survey, we have discovered 24 new one-off FRBs in 5259 h of observing time. This corresponds to an average of one FRB every 9.1 days. Following van Leeuwen et al. (2022), we assume an effective Apertif FoV of 8.2 deg^2, which already accounts for the sensitivity of the CBs. The all-sky rate for N detected FRBs is expressed as follows:

$$R\,(\mathrm{sky}^{-1}\mathrm{day}^{-1}) = N \times \frac{24\ \mathrm{h\ day}^{-1} \times 41253\ \mathrm{deg}^2\mathrm{sky}^{-1}}{5259\ \mathrm{h} \times 8.2\ \mathrm{deg}^2} \tag{6.10}$$

With $N = 24$ FRBs, this yields an Apertif all-sky FRB rate of 551^{+218}_{-171} sky^{-1} day^{-1}, with 90% Poisson errors (Gehrels 1986).

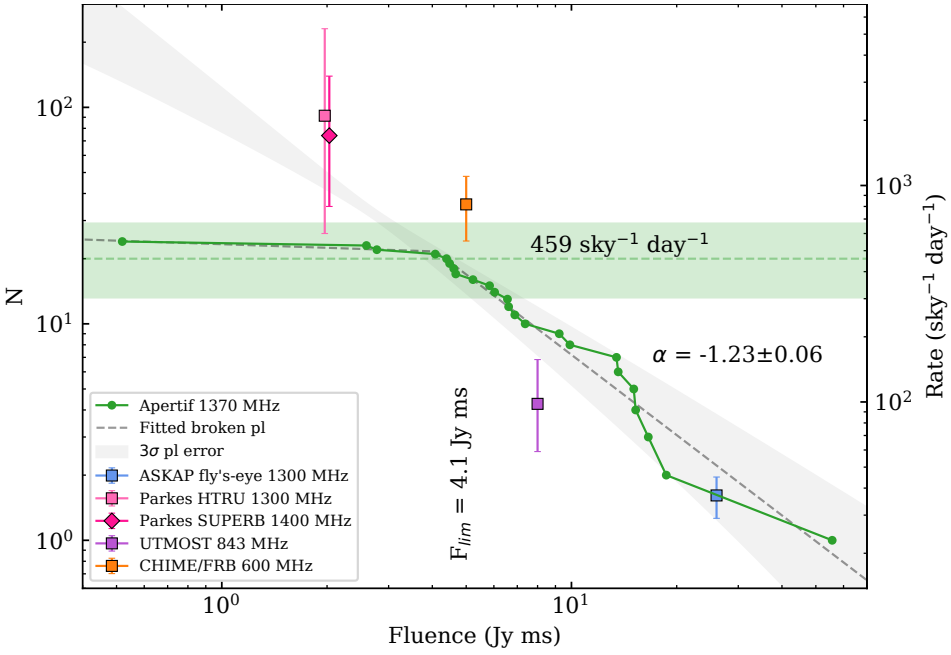

Figure 6.14: Cumulative fluence distribution of the Apertif FRBs. The left y axis gives the number of FRBs, and the right y axis its conversion to an all sky rate using Eq. 6.10. The green dots give the measured FRB fluences, and the grey dashed line their fit to a broken power law. The diagonal grey shaded region gives the 3σ confidence interval of the power law above the fluence limit extrapolated to other fluences. The vertical grey shaded region is below the fluence completeness threshold of 4.1 Jy ms, while the horizontal green shaded region gives the all-sky FRB rate above that fluence, with Poissonian 95% confidence limits. The power law above the completeness threshold has an index of $\alpha = -1.23$. The markers give the all-sky rates estimated by other surveys; cyan square for ASKAP fly's-eye (Shannon et al. 2018), light pink square for Parkes HTRU (Champion et al. 2016), dark pink diamond for Parkes SUPERB (Bhandari et al. 2018), orange square for CHIME/FRB (CHIME/FRB Collaboration et al. 2021a), and purple square for UTMOST (Farah et al. 2019).

Burst rates are only meaningful when given together with the fluence completeness threshold of the instrument, which can be highly variable. In van Leeuwen et al. (2022), we determined

this threshold from the typical SEFD of the system. Here we take a complementary approach; we build a cumulative fluence distribution of the Apertif FRBs (See Fig. 6.14), and fit it to a broken power law, assuming the break in the power law corresponds to the fluence completeness threshold;

$$N(>F) = \begin{cases} C(F/F_{\rm lim})^{\alpha_0}, & \text{if } F < F_b \\ C(F/F_{\rm lim})^{\alpha}, & \text{otherwise,} \end{cases} \tag{6.11}$$

where C is a constant, $F_{\rm lim}$ is the fluence completeness threshold, and α_0 and α are respectively the power law indices before and after the completeness threshold. This way, we recompute the all-sky rate for the FRBs above the completeness threshold and determine the power-law index of the fluence distribution. We find a fluence completeness threshold of $F_{\rm lim} = 4.1 \pm 0.2$ Jy ms, with $N = 20$ FRBs above the threshold. Using Eq. 6.10, this yields an FRB all-sky rate at 1370 MHz of $R_{1370}(F \geq 4.1 \text{ Jy ms}) = 459^{+208}_{-155}$ sky^{-1} day^{-1}, with 90% Poisson errors. Furthermore, we determine a fluence distribution power law index of $\alpha = -1.23 \pm 0.06$, where we quote the 1σ statistical error from the fit. We estimate a systematic error of 0.2 on α.

We use the resulting power law to compare our subsequent all-sky rate to the estimates made by other surveys at their respective fluence completeness thresholds. In Fig. 6.14 we plot the all-sky rates from the ASKAP fly's-eye search ($F > 26$ Jy ms; Shannon et al. 2018), the Parkes HTRU ($F > 2$ Jy ms; Champion et al. 2016) and SUPERB ($F > 2$ Jy ms; Bhandari et al. 2018) surveys, the UTMOST survey ($F > 8$ Jy ms; Farah et al. 2019) and the First CHIME/FRB Catalog ($F > 5$ Jy ms; CHIME/FRB Collaboration et al. 2021a). The comparison between the Apertif FRB all-sky rate and other surveys will be discussed in Section 6.5.3.

6.4.4 Propagation effects

The Apertif FRB sample displays a large variety of propagation effects. In this section we describe the observed dispersion measures, scattering timescales and scintillation bandwidths, and compare them to the FRB samples collected by other instruments and to the expected Milky Way contribution (queried from NE2001 and YMW16 at 1370 MHz using `pygedm`; Price et al. 2021).

6.4.4.1 Dispersion measure

The FRB sample presented here has observed DMs ranging from 246 pc cm^{-3} to 2778 pc cm^{-3}, with an average of ~ 800 pc cm^{-3} and a median of ~ 625 pc cm^{-3}. The expected MW and halo contribution in our FRB sample varies between 70 pc cm^{-3} and 300 pc cm^{-3}. We compare the Apertif DMs to other instruments with burst samples larger than ten listed in the Transient Name Server (TNS) database[1]; here we select the FRBs reported by CHIME/FRB (CHIME/FRB Collaboration et al. 2021a), ASKAP (Bannister et al. 2017; Shannon et al. 2018; Macquart et al. 2020), Parkes (Lorimer et al. 2007; Keane et al. 2012, 2016; Thornton et al. 2013; Burke-Spolaor & Bannister 2014; Petroff et al. 2015a, 2017; Ravi et al. 2015, 2016; Champion et al. 2016) and UTMOST (Caleb et al. 2017; Farah et al. 2018, 2019).

[1] TNS database: www.wis-tns.org

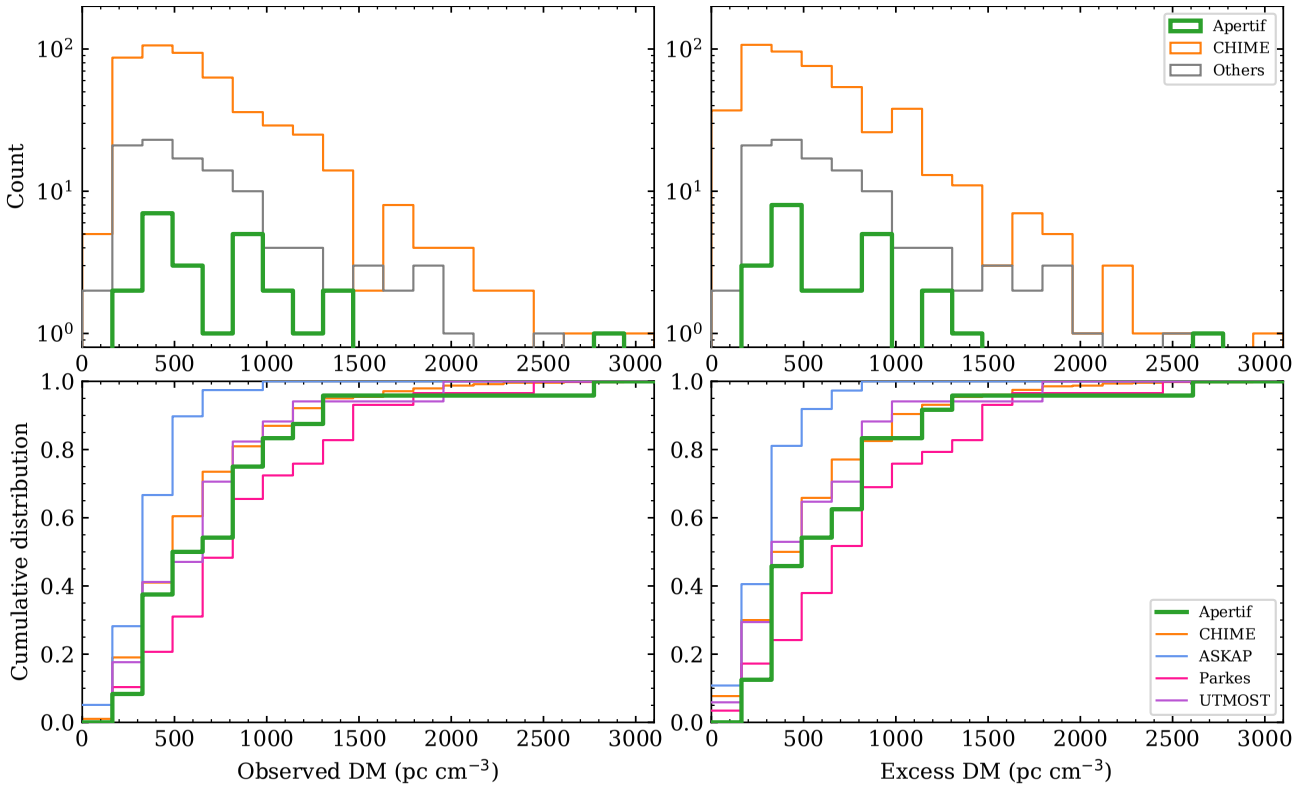

Figure 6.15: Distribution of Apertif FRB DMs compared to other FRB samples. The top left and right panels show respectively histograms of the observed and excess DMs with respect to the Milky Way contribution, with Apertif in green, CHIME/FRB in orange, and all other FRBs in the TNS in gray. The bottom left and right panels show respectively the cumulative distribution of observed and excess DMs of different single instrument FRB samples, with Apertif in green, CHIME/FRB in orange, ASKAP in cyan, Parkes in pink, and UTMOST in purple.

Table 6.2: Comparison of Apertif DMs to other instrument samples.
Observed and extragalactic DM medians of Apertif, CHIME/FRB, ASKAP, Parkes and UTMOST FRB samples, and KS two-sample p-value (p_{KS}) of Apertif against all other samples.

Instrument	Observed DMs		Extragalactic DMs	
	Median	p_{KS}	Median	p_{KS}
Apertif	625		615	
CHIME	563	0.271	489	0.058
ASKAP	403	0.005	361	0.002
Parkes	826	0.449	694	0.916
UTMOST	665	0.592	484	0.266

The top panels of Fig. 6.15 show histograms of the observed and excess DMs of the Apertif FRBs compared to the First CHIME/FRB Catalog, and to all other FRBs contained in the TNS database. The cumulative distributions of the observed (DM_{obs}) and excess ($DM–DM_{MW}$) dispersion measures of Apertif, CHIME/FRB, ASKAP, Parkes and UTMOST are also shown in the lower panels. Table 6.2 gives the median of the observed and extragalactic DMs for each of the aforementioned surveys. To know whether the Apertif DMs could be drawn from the same distribution as any of the other surveys, we perform a Kolmogorov-Smirnov two sample test and obtain the p-value p_{KS}. If $p_{KS} < 0.01$, we cannot reject the hypothesis that the DMs of the two surveys being compared have been drawn from different distributions.

We find the Apertif DM distribution to be compatible with Parkes, UTMOST and CHIME/FRB given the obtained p-values. The median observed and extragalactic DMs are comparable, with Parkes having the highest median DM and CHIME/FRB DMs being slightly lower than Apertif. ASKAP, however, has the lowest median DM of all surveys, and a $p_{KS} < 0.01$ on both the observed and extragalactic DMs when compared to Apertif. The difference in DMs is also discernible in the cumulative distribution of Fig. 6.15. This indicates Apertif is sensitive to a more dispersed, and thus more distant population of FRBs than ASKAP.

6.4.4.2 Scattering

Out of the 24 detected FRBs, nine have measurable scattering, with values ranging between 0.2 ms and 21 ms at the central frequency of 1370 MHz. A histogram of the measured values is shown in green on the left panel of Fig. 6.16. The measured scattering timescales are two to four orders of magnitude higher than what we expect from the Milky Way (MW) contribution according to the NE2001 (Cordes & Lazio 2003) and the YMW16 (Yao et al. 2017) models, as shown in Fig. 6.17. The scattering is thus likely produced in the host galaxy or the local environment of the FRB, or alternatively in an intervening galaxy in the Line of Sight (LoS) of the burst.

For a radio wave propagating through a thin scattering screen, the scattering timescale evolves with frequency as $\tau_{sc} \propto \nu^{-4}$ (Lorimer & Kramer 2004). We can thus compare the scattering timescales seen with CHIME/FRB at 600 MHz to the Apertif scattering timescales. Due to detection biases quantified with an injection pipeline (CHIME/FRB Collaboration et al. 2021a), the CHIME/FRB

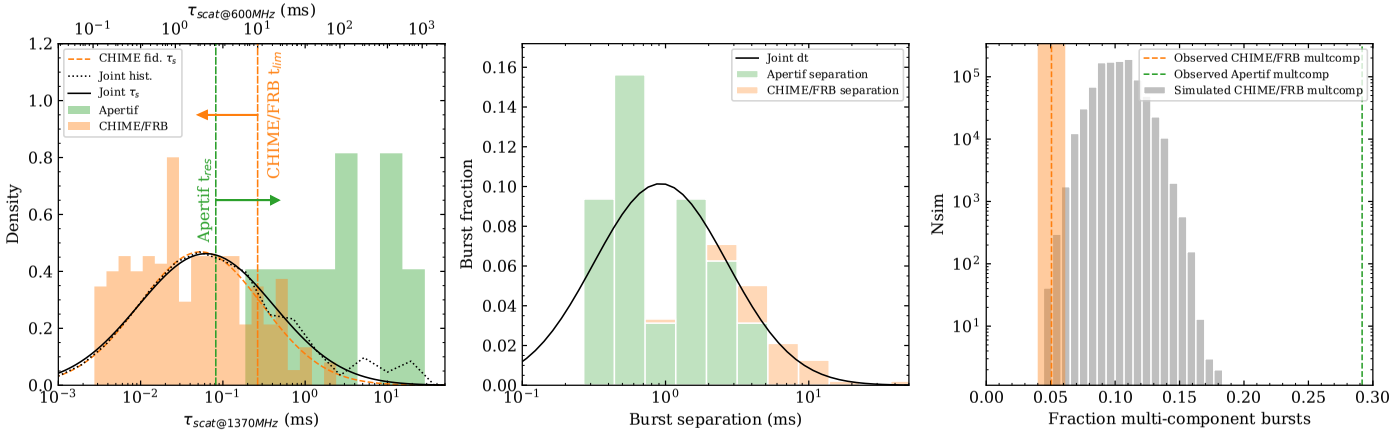

Figure 6.16: Observed scattering and results of the multi-component analysis. **Left:** Histogram of observed scattering timescales in CHIME/FRB and Apertif FRBs. The dashed orange line represents the fiducial scattering timescale distribution of CHIME/FRB FRBs. The dotted black line shows the joint scattering timescale distribution of Apertif and CHIME/FRB, and the solid black line its fit to a lognormal distribution. The dashed green and orange lines and arrows indicate respectively where Apertif and CHIME/FRB are sensitive to scattering. **Center:** Joint stacked histogram of observed subcomponent separations. The green histogram represents the Apertif separation distribution normalised by the total number of components in the FRB sample. The orange histogram is the same for CHIME/FRB. The black line shows a fit of the joint histogram to a lognormal distribution. **Right:** Result from the CHIME/FRB subcomponent separation simulations. The grey histogram shows the simulated fraction of observed multi-component FRBs. The orange vertical region shows the observed fraction of CHIME/FRB multi-component bursts with binomial errors. The green vertical line shows the observed Apertif multi-component fraction.

population of FRBs with τ_{sc}>10 ms at 600 MHz is incomplete, which corresponds to about 0.37 ms at 1370 MHz. The most scattered FRBs detected by CHIME/FRB thus slightly overlap with the low end of the Apertif sensitivity to scattering. This reveals that Apertif can detect a population of highly scattered bursts which are unlikely to be detected by CHIME/FRB due to the lowered S/N at lower frequencies through scattering.

In order to roughly estimate how the Apertif scattered bursts modify the intrinsic FRB scattering distribution, we build a joint scattering distribution. To do so, we add the Apertif scattering histogram normalised by the number of Apertif bursts to the CHIME/FRB fiducial scattering model (CHIME/FRB Collaboration et al. 2021a), and next we fit it to a lognormal model. This effectively skews the distribution towards higher scattering values. The equation for the lognormal distribution with the x axis in logarithmic scale is given by:

$$p(x) = \frac{m}{\sigma\sqrt{2\pi}} \exp\left(-\frac{\ln(x/m)^2}{2\sigma^2}\right), \tag{6.12}$$

where the shape σ is a frequency-independent value and m is the frequency-dependent scale in ms. For the joint distribution, we find $\sigma = 1.88 \pm 0.07$ and $m = 0.087 \pm 0.006$ ms at 1370 MHz or $m = 2.4 \pm 0.2$ ms at 600 MHz (same σ). This resulting distribution is a rough estimate, since correcting for observational biases and determining the intrinsic FRB scattering distribution is out of the scope of this paper.

6.4.4.3 Scintillation

Scintillation is measurable in eleven out of the 24 FRBs, with $\Delta\nu_{sc}$ values ranging from 1.5 to 15 MHz. In most cases, the observed scintillation bandwidths are larger than the expected Milky Way contribution at 1370 MHz predicted by the YMW16 (Yao et al. 2017) and NE2001 (Cordes & Lazio 2003) models, but they still fall within the 40% error assumed for these models. Figure 6.17 shows the measured scintillation bandwidths and their comparison to the expected Milky Way contribution. The scintillation bandwidth is converted to scattering timescales using Eq. 6.8. These results will be further discussed in Section 6.5.1.5.

6.4.5 Multi-component bursts

Seven out of the 24 detected bursts display more than one discernible component. Our system thus finds $\sim$ 29% of the bursts at 1370 MHz are multi-component. In the morphology study of the First CHIME/FRB Catalog bursts, however, Pleunis et al. (2021a) find that only about 5% of one-off bursts contain multiple components. This scarcity of apparent multi-component bursts at lower frequencies could be intrinsic to the FRB underlying properties. It could also be an effect of increased scattering at lower frequencies blurring together separate components into one, or an instrumental effect. Simulations suggest CHIME/FRB can determine the intrinsic width of single-component bursts down to $\sim 100\,\mu$s, but bursts containing multiple components separated by less than the instrument time resolution of 0.98 ms could still be perceived as single.

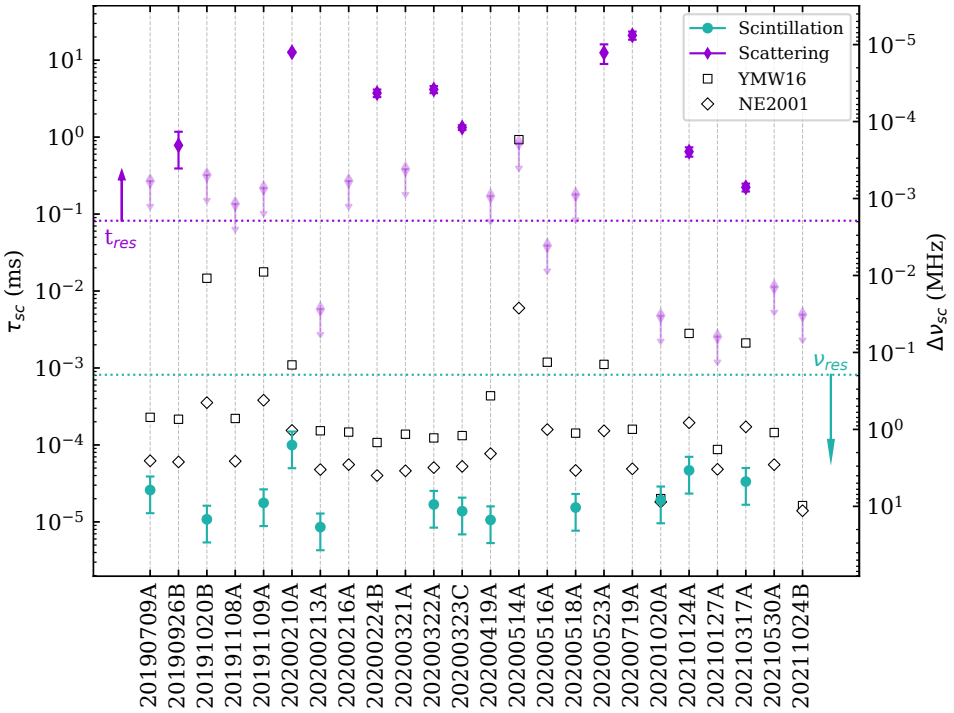

Figure 6.17: Scattering timescales and scintillation bandwidth of Apertif FRBs. Each vertical line corresponds to a different FRB, arranged by detection date. The left axis gives the scattering timescale and the right axis the corresponding scintillation bandwidth at 1370 MHz, using the conversion given by Eq. 6.8. Purple diamonds with error bars give the measurable scattering timescales or corresponding scintillation bandwidth, and purple diamonds with arrows the scattering timescale upper limits. Cyan circles with error bars give the measured scintillation bandwidth when measurable. The white squares and diamonds give respectively the expected Milky Way contribution to scattering from the YMW16 and NE2001 models at 1370 MHz. The horizontal dotted pink and cyan lines show respectively the Apertif time and frequency resolution.

The discrepancy between the multi-component burst fraction of the two instruments can be quantified with a Fisher's exact test. It returns the probability that we would observe this or an even more imbalanced ratio of multi-component bursts by chance, and it is valid for small sample sizes (Fisher 1922, 1934)[1]. The resulting p-value of 3×10^{-4} indicates there is a very low probability that we would observe such disparate ratios of multi-component bursts by chance.

To check whether the reduced multi-component burst fraction at lower frequencies can be explained by the increased scattering timescales, we performed a set of simulations. We test if the observed CHIME/FRB multi-component fraction can be reproduced from the observed Apertif burst properties as follows:

- First we determine the frequency-agnostic subcomponent separation distribution. We build a histogram of all Apertif subcomponent separations and divide it by the total number

[1] Applied with python package `scipy`, function `stats.fisher_exact`

of subcomponents in the Apertif sample (39 subcomponents); we do the same for the CHIME/FRB sample (506 subcomponents). We add the two normalised histograms and fit them to a lognormal distribution (Eq. 6.12), where we find the parameters $m = 0.70 \pm 0.18$ ms and $\sigma = 1.07 \pm 0.26$. The resulting histogram and distribution are plotted in the central panel of Fig. 6.16.

- Next we determine the scattering distribution for the simulations. We use the aforementioned fiducial CHIME/FRB scattering distribution at 600 MHz: a lognormal distribution with $m = 2.02$ ms and $\sigma = 1.72$ (Eq. 6.12, see Table 4 from CHIME/FRB Collaboration et al. 2021a). If we would have used the joint Apertif-CHIME/FRB distribution, scattering would have been even further increased at 600 MHz and some of the simulated bursts might be too scattered to be realistically detected by CHIME/FRB. This is an important distinction because the scattering timescale is one of the dominant selection effects in CHIME/FRB (Merryfield et al. 2022).
- We simulate samples of bursts and determine the number of multi-component among those from a binomial distribution, with $n = 474$ (number of one-off bursts in CHIME/FRB catalogue) and $p = 7/24 = 0.292$ (fraction of multi-component bursts in Apertif sample). For each multi-component burst, we draw a random scattering timescale $\tau_{\rm sc}$ and subcomponent separation dt from the previously described distributions. If $\tau_{\rm sc} \leq dt$, we consider it to be detected as a multi-component burst, and if $\tau_{\rm sc} > dt$ as a single component burst. Finally we count the fraction of detected multi-component bursts.
- We perform the previous simulation 10^6 times to determine the simulated distribution of multi-component burst fraction, and compare this to the actual CHIME/FRB fraction of multi-component bursts.

The resulting simulated fraction of multi-component FRBs is displayed on the right panel of Fig. 6.16. The distribution has an average of 10.2% with a standard deviation of 1.4%. The observed fraction of multi-component bursts in the CHIME/FRB catalogue differs by $> 4\sigma$ from the simulations towards the lower end. If we adopt the joint Apertif-CHIME/FRB scattering distribution – which will be more conservative in results, but it is less realistic – the simulated and observed multi-component FRB fractions still differ by $> 3\sigma$.

The results of these simulations rely on two main assumptions. First, we assumed the subcomponent separation follows the same distribution at all frequencies. In pulsars, the radius-to-frequency mapping (RFM) effect increases the subcomponent separation at low frequencies, as well as the subcomponent width. The average Apertif subcomponent width is ~ 0.5 ms, while for CHIME/FRB it is ~ 1 ms. Whether this difference is significant is yet to be determined with higher time-resolution studies at low frequencies. Assuming an increased separation at lower frequencies would have resulted in a larger difference between the observed CHIME/FRB multi-component fraction and the simulations. Our assumption is thus more conservative.

Second, we assumed single and multi-component bursts follow the same scattering distribution. None of the Apertif multi-component bursts exhibit a scattering tail, which might suggest they are produced in environments with different scattering properties. We thus compared the measured scattering values of the single and multi-component CHIME FRBs through a Kolmogorov-

Smirnov two-sample test. The resulting p-value = 0.4 indicates the scattering of single and multi-component bursts are likely to be drawn from the same distribution, which justifies our assumption.

From our results, we thus conclude the lower fraction of observed multi-component bursts at lower frequencies cannot be explained by scattering alone. Multi-component profiles appear to be intrinsically more prevalent at higher frequencies. This is an important feature and test for theories of e.g. FRB physical emission mechanisms. Alternatively, this might be an effect of the different time resolution. This result will be further discussed in Section 6.5.2.

6.4.6 Spectral properties

About two thirds of the Apertif FRBs are broadband, i.e. they have emission from the bottom to the top of the observing bandwidth at roughly the same intensity. The spectra of the remaining bursts can be classified in two different categories. Four have emission at the top of the band, and can be well fitted by a power law with a positive spectral index si, ranging from 5.4 to 11.6. The remaining five are narrowband and their spectra can be well fitted by a gaussian. Although the broadband bursts are likely to have, in reality, a gaussian or power law spectrum, the limited fractional bandwidth of Apertif (~ 0.2) and the presence of structure in frequency from scintillation impedes a complete characterisation of the spectral properties. The burst spectral properties are detailed in Table 6.4.

6.5 Discussion

6.5.1 Propagation effects

6.5.1.1 Scattering compared to other surveys

Scattering timescales are a frequency dependent quantity, $\tau_{\rm sc} \propto \nu^{-x}$ with x the scattering index. The choice of x is important when comparing FRB surveys observing at different frequencies. The theoretical values of the scattering index are $x = 4$ for a simple thin screen model and $x = 4.4$ for a propagation of the radio waves through a turbulent medium. Estimates of FRB scattering indices are still scarce, and although they are closer to $x = 4$ on average, they are compatible with $x = 4.4$ (e.g. Thornton et al. 2013; Burke-Spolaor & Bannister 2014; Ravi et al. 2015; Masui et al. 2015; Day et al. 2020; Qiu et al. 2020; Pastor-Marazuela et al. 2021). For galactic pulsars, Bhat et al. (2004) determine an average scattering index $x \sim 3.86$. In this work, we assume a scattering index $x = 4$, compatible both with galactic pulsars and FRB observations. This allows us to compare the scattering timescales reported by several surveys observing at different frequencies.

The CHIME/FRB scattering distribution is the most extensive to date, but it is incomplete above $\tau_{\rm sc}$>10 ms at 600 MHz (CHIME/FRB Collaboration et al. 2021a). This corresponds to about 0.37 ms at 1370 MHz. There is thus a slight overlap between the high end of CHIME and the low end of the Apertif scattering distributions. The Apertif FRBs thus represent a population of highly scattered bursts. Even though we have not performed a burst injection procedure to estimate our

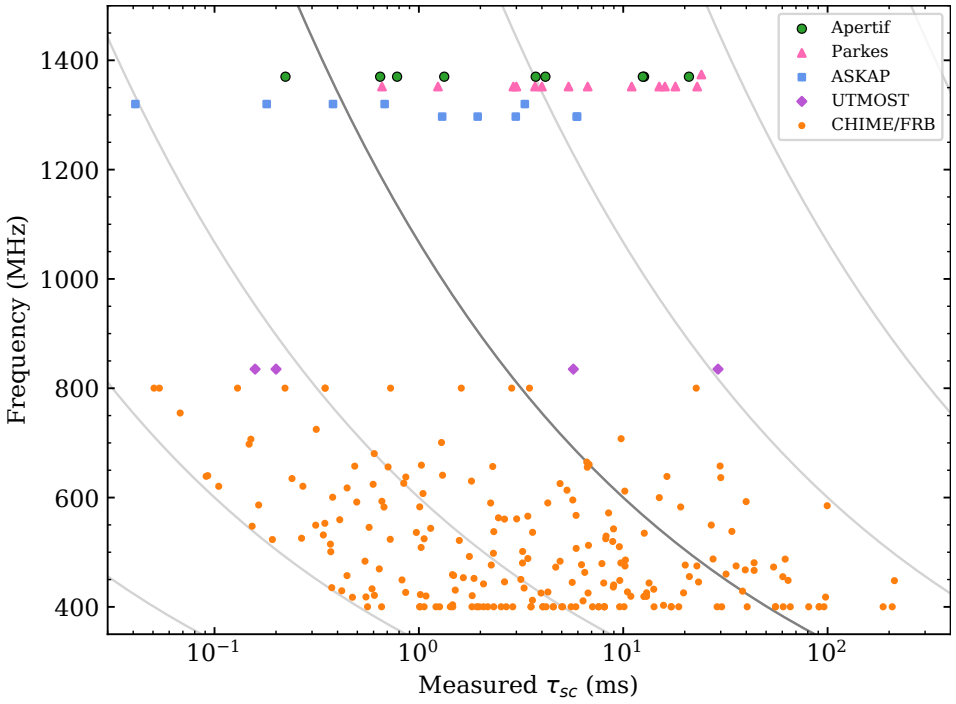

Figure 6.18: Observed scattering timescales from different instruments at different frequencies. Green circles represent Apertif (this work), pink triangles Parkes, blue squares ASKAP, purple diamonds UTMOST and orange circled CHIME. The values are queried from the TNS database and the First CHIME/FRB Catalog. Grey lines are a reference for the $\tau_{sc} \propto \nu^{-4}$ relation. The darkest grey line corresponds to the CHIME/FRB scattering sensitivity limit of 10 ms at 600 MHz. Apertif, Parkes, ASKAP and UTMOST τ_{sc} are shown at their respective central observing frequencies, while the CHIME/FRB τ_{sc} are shown at the peak frequency of the burst.

biases against detecting FRBs with different properties, the large fraction ($\sim$ 38%) of Apertif FRBs with measurable scattering demonstrate the existence of a large fraction of highly scattered FRBs in the population.

This highly scattered population is further supported by the results of other surveys above 1 GHz. This can be visualised in Fig. 6.18, where the scattering timescales measured at different frequencies by different surveys are shown. Amongst the ASKAP bursts with measurable scattering (Day et al. 2020; Qiu et al. 2020), more than half have scattering timescales above the CHIME/FRB sensitivity limit, accounting for the frequency difference. Storing data in high time and spectral resolution mode has enabled ASKAP to measure the exponential decay of two FRBs with a lower scattering timescale than any of the Apertif FRBs, down to τ_{sc}=0.041 ms for FRB 20190102C. The most scattered ASKAP FRB is FRB 20180130A with τ_{sc}=5.95 ms, well below the most scattered Apertif FRB (See Section 6.4.1.5). On average, the ASKAP FRBs are less scattered, with an average $\tau_{sc} \sim$ 2 ms compared to the Apertif average of $\tau_{sc} \sim$ 6 ms.

The Parkes FRBs with measurable scattering all fall above the CHIME/FRB sensitivity limit (Lorimer et al. 2007; Ravi et al. 2015; Petroff et al. 2015a; Champion et al. 2016; Bhandari et al. 2018; Osłowski et al. 2019; Price et al. 2019). Compared to Apertif, the Parkes FRBs show a marginally larger scattering than Apertif, with an average $\tau_{sc} \sim 9$ ms.

Although UTMOST observes at 843 MHz, which is a considerably lower frequency than Apertif, the measured scattering timescales in four FRBs do not significantly differ from Apertif and Parkes (Farah et al. 2019). This could potentially be explained by the high time resolution of $\sim 10\,\mu$s, but it is remarkable to note the similarities between UTMOST, Parkes and Apertif both in the measured dispersion measures and scattering timescales. When accounting for the frequency difference, though, the UTMOST FRBs probe a sample of less scattered bursts than Apertif and Parkes, but similar to ASKAP.

6.5.1.2 Correlation between dispersion and scattering

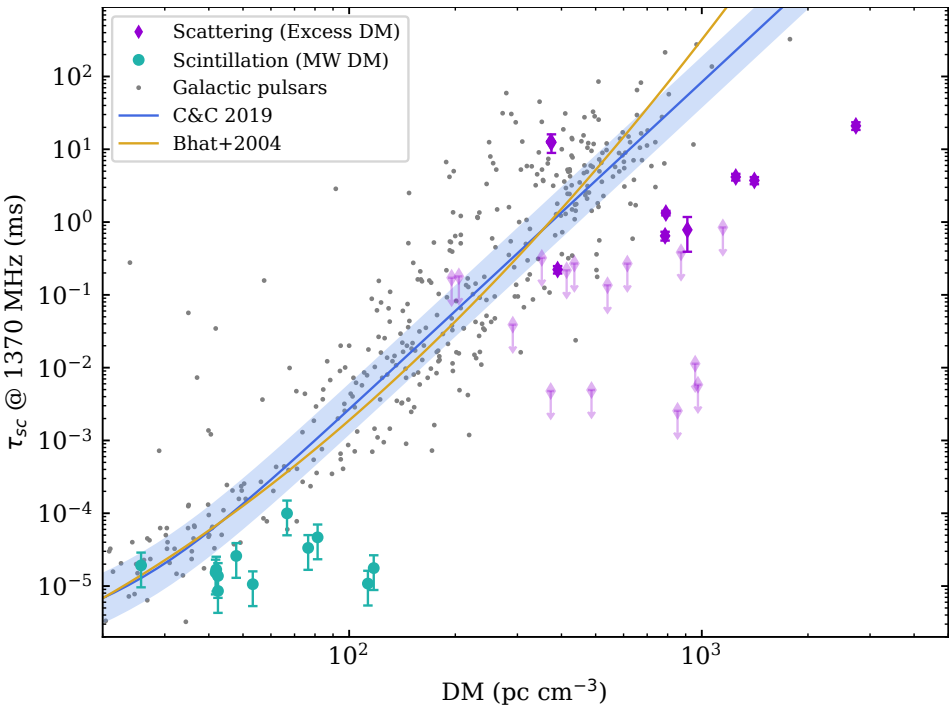

Figure 6.19: Scattering as a function DM of Apertif FRBs compared to galactic pulsars. The measured Apertif τ_{sc} as a function of extragalactic DM is shown as purple diamonds (higher transparency for upper limits). The cyan circles correspond to the measured scintillation converted to scattering as a function of the expected galactic DM. The grey dots are the known pulsar τ_{sc} at 1370 MHz as a function of measured DM. The blue line with shaded region is the τ_{sc}–DM relation from Cordes & Chatterjee (2019), and the yellow line the τ_{sc}–DM relation from Bhat et al. (2004).

Since galactic pulsars show a correlation between their DMs and scattering timescales, we investigated the presence of such a correlation in the Apertif FRBs. Figure 6.19 shows the scattering timescales of the FRBs, including upper limits, as a function of excess DM, since we expect the origin of scattering to be extragalactic. The measured DMs and scattering timescales of galactic pulsars are plotted for comparison, as well as the τ_{sc}–DM relations established by Cordes & Chatterjee (2019) and Bhat et al. (2004). We also plot the scintillation bandwidth of the FRBs converted to scattering timescales as a function of the expected DM_{MW}, since the measured scintillation bandwidths match the expected galactic contribution. By eye, scattering timescales seem to increase with DM, and thus we carried out further correlation analyses.

In order to determine the correlation coefficient between the excess DM and τ_{sc} of the Apertif FRBs, including τ_{sc} upper limits, we compute the Kendall τ correlation coefficient using the `cenken` function of the CRAN `NADA` package[1], following Feigelson & Babu (2012, Chapter 10.8.3 and references therein). The Kendall τ correlation coefficient is a non-parametric correlation test and it is robust on small sample sizes with censored data (Helsel 2004; Oakes 1982), and it is thus applicable to our case. This function also computes a p-value whose null hypothesis is the absence of correlation. We find a weak correlation coefficient of $\tau = 0.19$, and a p-value$= 0.19$ above the conventional 0.01, which indicates there is no evidence for a correlation between the excess DM and τ_{sc} of Apertif FRBs.

The lack of evidence for correlation is in agreement with previous FRB observations (Qiu et al. 2020; Petroff et al. 2019; Cordes & Chatterjee 2019). This further supports earlier claims that the IGM does not significantly contribute to scattering (Cordes et al. 2016; Xu & Zhang 2016; Zhu & Feng 2021).

6.5.1.3 Origin of scattering

Although only FRBs presenting both scattering and scintillation allow us to set upper limits on the distance between the source and the scattering screen, we can determine that the scattering of Apertif FRBs, when present, is much more likely to have been produced at the host galaxy and not in the halo of an intervening galaxy within the LoS. In their Eq. 8, Ocker et al. (2021) determine a relationship between scattering, the electron density fluctuations of the medium, and a geometric factor that depends on the distances between FRB, scattering medium and observer:

$$\tau_{sc}(\mathrm{DM}, \nu, z) \simeq 48.03 \text{ ns} \times \frac{\tilde{F}(z_l)\mathrm{DM}_l^2}{(1+z_l)^3\nu^4} \left[\frac{2d_{sl}d_{lo}}{Ld_{so}}\right], \tag{6.13}$$

where $\tilde{F}(z)$ in $\mathrm{pc}^{-2/3}\,\mathrm{km}^{-1/3}$ quantifies the electron density variations of the scattering lens, DM_l is the DM contribution from the scattering lens, z_l is the redshift of the scattering lens and ν is the observing frequency in GHz. d_{sl}, d_{lo}, and d_{so} are angular diameter distances in Gpc, with d_{sl} the source to lens distance, d_{lo} lens to observer, d_{so} source to observer. L is the thickness of the layer in Gpc, and the geometric boost factor $G_{sc} \simeq 2d_{sl}d_{lo}/Ld_{so}$. When either the source or the observer are embedded in the scattering medium and the source to observer distance d

[1] CRAN NADA package: https://cran.r-project.org/web/packages/NADA/index.html

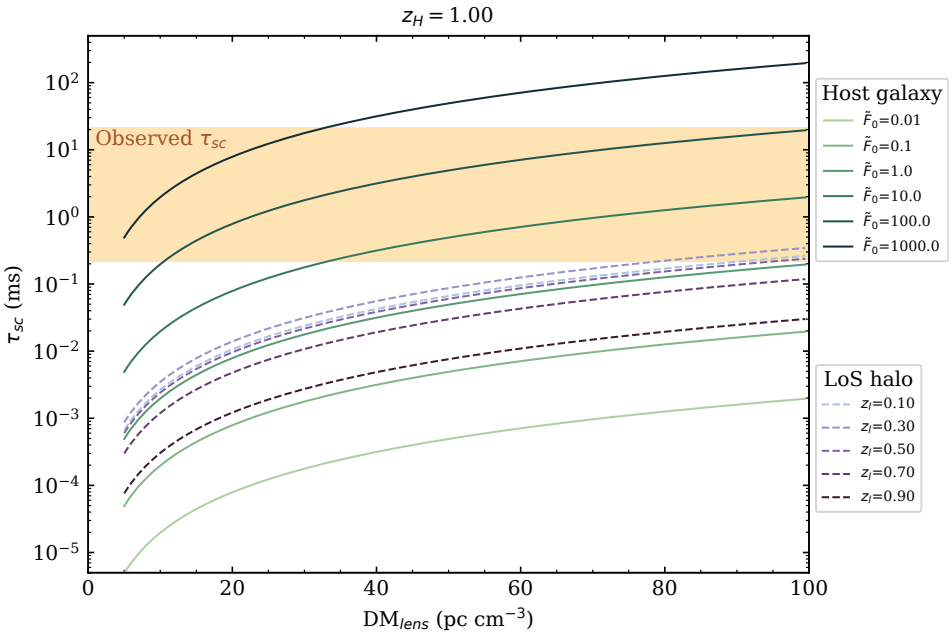

Figure 6.20: Expected contribution to scattering at 1370 MHz for different lens DMs from an FRB host galaxy at $z_H = 1$ and an intervening galaxy halo within the line of sight. The solid lines show the expected host galaxy contribution for different electron density variations and a geometric boost factor $G_{\rm sc} = 1$. The dashed lines show the expected contribution from an intervening galaxy halo with a thickness $L = 30$ kpc and $\tilde{F}_0 = 10^{-4}\,{\rm pc}^{-2/3}\,{\rm km}^{-1/3}$ located at different redshifts. The orange shaded region represents the observed Apertif $\tau_{\rm sc}$ range.

is much larger than the medium's thickness L, $G_{\rm sc} = 1$. The electron density fluctuations vary with redshift following the cosmic star formation rate (CSFR) as follows (Eq. 21 in Ocker et al. 2022a):

$$\tilde{F}(z) \simeq \tilde{F}_0 \times \frac{(1+z)^{2.7}}{1+1[(1+z)/2.9]^{5.6}}. \tag{6.14}$$

If the scattering lens is located in the host galaxy ($z_l = z_{\rm host}$), $\tilde{F}_0$ can vary from 10^{-2} to $10^3\,{\rm pc}^{-2/3}\,{\rm km}^{-1/3}$ by extrapolation from observations of MW pulsars in the Galactic plane. In this case, the FRB would be embedded in the scattering medium and $d_{\rm so}$ is much larger than the medium's thickness L, thus $G_{\rm sc} = 1$. If instead the scattering lens is a galactic halo falling within the FRB LoS, the electron density fluctuations are much lower. Galactic pulsars located in the Milky Way thick disk (10–20 kpc distances) exhibit an $\tilde{F}_0 \sim 10^{-3}\,{\rm pc}^{-2/3}\,{\rm km}^{-1/3}$. An FRB traversing an intervening galactic halo would encounter a much more homogeneous medium, with $\tilde{F}_0 \sim 10^{-4} - 10^{-5}\,{\rm pc}^{-2/3}\,{\rm km}^{-1/3}$. Although the geometric boost factor is much larger for an intervening galaxy halo than for the medium where the source or the observer are embedded, the turbulence of the intervening halo is very small unless the FRB passes with a small impact parameter with respect to the galaxy center.

In Figure 6.20, we compare the expected τ_{sc} produced by the host galaxy medium and by an intervening galactic halo as a function of the lens DM contribution. We compute these values at 1.37 GHz for an FRB located at $z = 1$, the average redshift upper limit of scattered Apertif FRBs. For the host galaxy, we test a range of electron density fluctuations from 10^{-2} to 10^{3}. For a scattering lens within the LoS of the FRB with a thickness of $L = 30$ kpc, we assume $\tilde{F}_0 = 10^{-4}$ pc$^{-2/3}$ km$^{-1/3}$ and test the τ_{sc} contribution at different distances varying from 10% to 90% the host galaxy redshift.

We find the observed Apertif scattering timescales to be much more easily produced in the host galaxy rather than by an intervening galaxy halo located in the LoS of the burst. This is in agreement with Cordes et al. (2022), and it is further supported by the lack of observable scattering in other FRBs which are known to travel through the halos of foreground galaxies. This is the case for FRB 20191108A, which passes through the halos of M33 and M31 with an impact parameter of 18 kpc from M33 (Connor et al. 2020) and FRB 20190709A passing $\gtrsim 25$ kpc away from the M33 center (van Leeuwen et al. 2022), as well as the localised FRB 20181112A (Prochaska et al. 2019; Cho et al. 2020), and FRB 20190608B (Simha et al. 2020).

By modelling the dispersion and scattering produced throughout the travel path of an FRB, Chawla et al. (2022) find that circumburst environments with strong scattering properties are required in order to reproduce the FRBs from the first CHIME/FRB catalogue with τ_{sc}>10 ms at 600 MHz. This corresponds to ~ 0.37 ms at 1370 MHz, which roughly matches the lowest measured Apertif scattering timescale. Although Chawla et al. (2022) suggest intervening galaxies within the burst LoS as an alternative explanation, we have determined above that this scenario is more unlikely given the low fluctuation parameter observed in the MW halo (Ocker et al. 2021). A very low impact parameter with respect to the center of the intervening galaxy ($\lesssim 10$ kpc for a MW-like galaxy, or roughly $\lesssim 15\%$ of the virial radius as assumed in Section 6.4.1.5) would be required in order to produce significant scattering.

A correlation between τ_{sc} and DM might have been an indication of a significant contribution to scattering from the IGM or intervening host galaxies. Meanwhile, scattering in the host galaxy would be highly dependent on the type of galaxy and its inclination, hence no correlation would be expected. The lack of a significant τ_{sc}–DM correlation supports an origin of scattering in the FRB host galaxies. We can thus conclude that the Apertif FRBs with measurable scattering are likely to be embedded in an environment with extreme properties. Such extreme environments could for instance be star-forming regions or supernova remnants, as has been previously suggested in the literature (Masui et al. 2015; Connor et al. 2016; Xu & Zhang 2016).

6.5.1.4 Dispersion

In Fig. 6.21, we display the fluence against the extragalactic DM of the Apertif FRBs compared to other surveys. For guidance, the grey lines represent the equivalent isotropic energy density that FRBs would have assuming the IGM DM contribution from Zhang (2018a) and the cosmological parameters from Planck Collaboration et al. (2020). We adopt an observed host galaxy contribution to the DM of $50/(1 + z)$. The fluence-DM plane has been used in previous works to show that bright, nearby FRBs have comparable energies to the more distant, fainter FRBs (Shannon et al.

2018; Farah et al. 2019; Niu et al. 2021). The Apertif sample is no different; the FRBs are located between the Parkes and the UTMOST FRB samples within the fluence-excess DM plane, while overlapping the FRBs from the First CHIME/FRB Catalog. This is in agreement with the DM distributions shown in Fig. 6.15 and the fluence-dependent rates presented in Fig. 6.14.

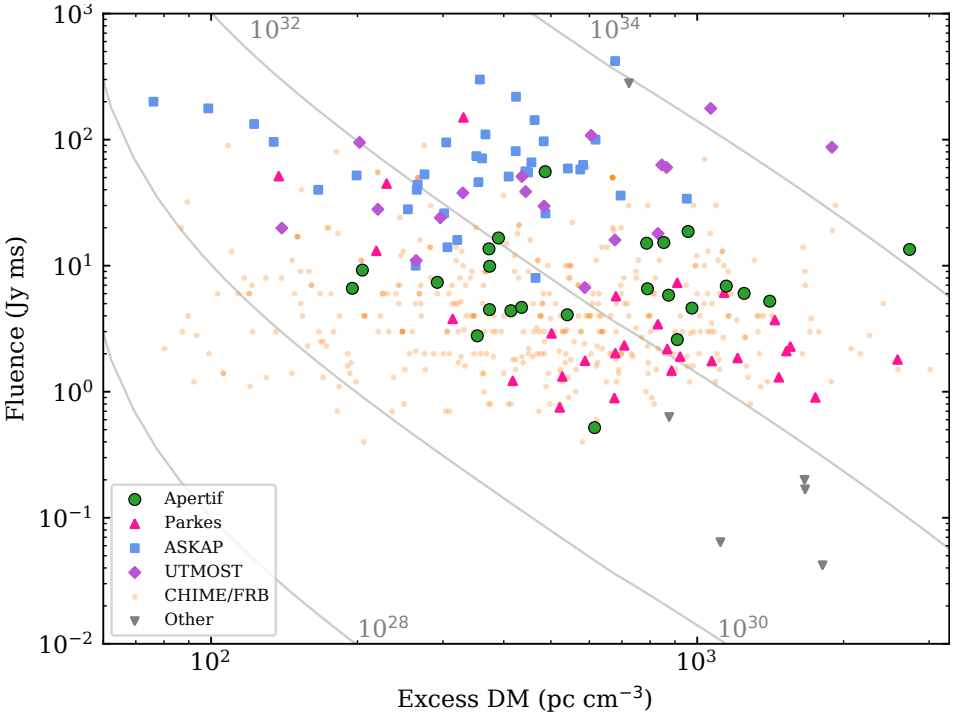

Figure 6.21: Fluence–excess DM diagram of Apertif and all other FRBs in the TNS. Apertif is shown as green circles, Parkes as pink upward triangles, ASKAP as blue squares, UTMOST as purple diamonds, CHIME/FRB as orange dots with a high transparency for better visualisation, and all other FRBs as grey downward triangles. Lines of constant spectral energy density are shown as grey lines for reference, with their labels indicating their value in erg Hz^{-1}.

The Apertif sample contains the FRB with the second largest DM known to date. The maximum cosmic star formation rate (CSFR) took place at $z \sim 2$ (Madau & Dickinson 2014); FRB 20200719A was thus emitted beyond the SFR peak. Previous works have compared the CHIME/FRB DM distribution to cosmic evolution models, and have found it does not appear to track the star formation history of the Universe (Qiang et al. 2022; Zhang & Zhang 2022). The multi-survey population synthesis of Gardenier et al. (2019) was also unable to show the FRB number density follows either the CSFR or the stellar mass density. As most FRB progenitor models are based on or related to stellar populations, and given that the CSFR decreases by over an order of magnitude from its peak to the current era, we find those results surprising. Detecting additional FRBs like FRB 20200719A at very large DMs and thus redshifts will better constrain the FRB rate evolution with redshift. Comparing the FRB host galaxy properties to that of other

astrophysical transients has proved useful in constraining the potential FRB progenitors (Heintz et al. 2020; Safarzadeh et al. 2020; Mannings et al. 2021; Bhandari et al. 2022); the redshift distribution could provide with additional information to rule out some of the current FRB progenitor models. However, the detection of some classes of transients is currently observationally challenging. Long Gamma-ray bursts (LGRBs) have been identified with redshifts up to $z \sim 9$ mainly with the Swift satellite (Cucchiara et al. 2011; Lan et al. 2021), while the most distant short Gamma-ray burst (SGRB) was found at a redshift of $z \sim 2.2$ (Selsing et al. 2018). This can be explained by a lower Swift sensitivity to high redshift SGRBs compared to LGRBs (Guetta & Piran 2005). The detection of distant optical transients is also limited; the most distant type Ia supernova has a redshift of only $z \sim 1.9$ (Jones et al. 2013), while core-collapse supernovae (CCSN) have been found up to $z \sim 2.4$ (Cooke et al. 2009) and superluminous supernovae (SLSN) up to $z \sim 3.9$. If a link is established between FRBs and any of these transients, high DM bursts might help establishing the cosmic evolution of their progenitors.

6.5.1.5 Scintillation

For FRBs with a measurable scintillation bandwidth, it falls within the errors of the expected NE2001 contribution, but in most cases it is larger than the predictions. This might indicate the electron density along the LoS fluctuates less than predicted by these models. The YMW16 predicted scintillation is generally lower than the Apertif measured values. This may be explained by the way the model predicts the scattering/scintillation values; it uses the τ_{sc}–DM relation instead of modelling the electron density fluctuations along the LoS (Yao et al. 2017). The scintillation measurements of Apertif FRBs can thus prove useful in better constraining the Milky Way electron distribution, especially at high galactic latitudes where there is a dearth of pulsars.

In Fig. 6.19, the Apertif scintillation bandwidths converted to scattering timescales through Eq. 6.8 are plotted as a function of the expected galactic contribution to DM, since we expect the scintillation to be produced in the MW. The measured values do not follow the τ_{sc} – DM relation from (Cordes & Chatterjee 2019) and (Bhat et al. 2004) observed in galactic pulsars. Since pulsars generally lay on the galactic plane, they probe a more inhomogeneous medium than the galactic halo encountered by most FRBs (Ocker et al. 2021). It is thus understandable that FRBs do not follow the same relation as pulsars.

6.5.2 Multi-component bursts

In the Apertif FRB sample, we find $\sim$ 30% of the bursts to display multiple components, a significantly higher fraction than the $\sim$ 5% of multi-component bursts in the First CHIME/FRB catalogue. We have shown through simulations presented in Section 6.4.5 that this difference cannot be explained by the increased scattering at lower frequencies alone. Even with a 0.98 ms time resolution, CHIME/FRB can accurately measure burst widths down to $\sim$ 100 μs if only one component is present. In the ASKAP FRB sample detected in fly's eye mode at 1.3 MHz with a time resolution of 1.26 ms, only one burst exhibits a second component identifiable by eye (FRB 20180119A; Shannon et al. 2018). However, in the coherent mode with a $\sim$ μs time

resolution, roughly half of the bursts display multiple components (Cho et al. 2020; Day et al. 2020).

Based on the fraction of multi-component one-off bursts in the Apertif sample, we predict that the true fraction of multi-component FRBs at CHIME frequencies should be higher than the fraction detected in the First CHIME/FRB Catalog. From our simulations of smearing effects due to scattering, we estimate a true fraction of multi-component FRBs at CHIME frequencies of $10.2 \pm 4.2\%$ (3σ). A higher time resolution search at CHIME frequencies, for example with the CHIME/FRB baseband pipeline (Michilli et al. 2021), should reveal a higher fraction of multi-component events. Similarly, other high time resolution FRB searches at 1 GHz, such as with the Deep Synoptic Array 110 (DSA-110; Kocz et al. 2019), should detect a similar fraction of multi-component bursts to Apertif (30%).

If high time resolution studies at lower or higher frequencies detect fewer or more multi-component bursts, respectively, at a level inconsistent with smearing due to scattering or instrumental effects, this would support the existence of frequency-dependent morphology for the population of one-off FRBs that we determined through our simulations. Such frequency-dependent effects are seen for pulse components of radio pulsars due to the different emission heights of different radio frequencies in the pulsar beam, so-called radius-to-frequency mapping (e.g. Cordes 1978). The RFM has been suggested to explain the drift rate evolution with frequency observed in repeating FRBs (Lyutikov 2020; Tong et al. 2021). Observing a similar frequency-dependent relationship in one-off FRB pulse components would provide further evidence for a neutron star origin for FRB emission.

The Apertif FRB components have an average width of $\sim$0.5 ms; at CHIME it is $\sim$1 ms. If we compare this to the observed profile (and component) width evolution in pulsars over this same frequency range of 1.4 to 0.4 GHz, we see an increase by $\sim$20% (Table 1 in Kijak & Gil 1997). If this difference persists when CHIME/FRB collects a larger sample of FRBs with baseband data, this would indicate the evolution of FRB component width versus frequencies is of at least the same scale, if not more, as that seen in pulsars.

We note that the Apertif sample consists entirely of one-off FRBs that have not been seen to repeat. While many previous studies of morphology have focused on samples of bursts from known repeaters (Hewitt et al. 2021; Platts et al. 2021; Sand et al. 2021), the large fraction of multi-component bursts in a self-consistent sample of one-off FRBs is novel. Ultimately, larger samples of high time resolution one-off FRBs detected by other facilities will be needed to fully contextualize the Apertif sample, as no further studies can be done with Apertif itself. However, we encourage other surveys to further explore the morphological properties of one-off FRBs.

6.5.3 All-sky FRB rates and fluence distribution

From the ALERT survey, we compute an all-sky FRB rate at 1370 MHz of $R_{1370}(F \geq 4.1 \text{ Jy ms}) = 459^{+208}_{-155}$ sky^{-1} day^{-1}, with 90% Poisson errors. From the resulting power law index fitted to the fluence cumulative distribution above the 4.1 Jy ms completeness threshold, we can compare this rate to other surveys with different sensitivity limits (See Fig. 6.14). Additionally, the resulting power law index for bursts above the fluence completeness threshold is

$\alpha = -1.23 \pm 0.06$. Note that the reported error on α is a result of the fit, and we estimate the systematic error to be ± 0.2.

The Apertif all-sky rate is comparable to that of other FRB surveys at the same frequencies at their given fluence sensitivity thresholds; the ASKAP rate in fly's-eye mode at 1300 MHz (Shannon et al. 2018), Parkes HTRU rate at 1300 MHz (Champion et al. 2016), and SUPERB rate at 1400 MHz (Bhandari et al. 2018) fall within our all-sky rate within errors. Although the UTMOST rate at 843 MHz (Farah et al. 2019) and the CHIME/FRB rate at 600 MHz (CHIME/FRB Collaboration et al. 2021a) appear to fall respectively below and above the Apertif all-sky rate, they are consistent within 3σ errors. With the current number of FRB detections, we cannot determine whether there is an evolution of the FRB rate with frequency.

In a non-evolving, constant density Euclidean Universe, the expected power law index of the fluence distribution is $\alpha = -1.5$. Although our observed power law index appears to be flatter, we cannot rule out that it is consistent with the Euclidean prediction within systematic errors. We can compare the Apertif $\alpha = 1.23 \pm 0.26$ to what has been reported by other FRB surveys. Bhandari et al. (2018) reported $\alpha = -2.2^{+0.6}_{-1.2}$ for the Parkes burst sample, while Shannon et al. (2018) determined $\alpha = -2.1^{+0.6}_{-0.5}$ for the ASKAP sample. James et al. (2019) later reanalysed these two FRB samples and determined the Parkes index to be $\alpha = -1.18 \pm 0.24$ and ASKAP to be $\alpha = -2.2 \pm 0.47$. While the combined power law index of both surveys is $\alpha = -1.55 \pm 0.23$, consistent with the Euclidean Universe, they are inconsistent with each other at 2.6σ. This discrepancy was interpreted as a difference in the cosmological population observed by each of these surveys, with ASKAP seeing nearby sources and Parkes more distant ones, following the average DM of each burst sample (See Fig. 6.15 and Table 6.2). Meanwhile, the index determined from the First CHIME/FRB Catalog is $\alpha = -1.40 \pm 0.11^{+0.060}_{-0.085}$, in agreement with the Euclidean prediction and in between the Parkes and ASKAP values (CHIME/FRB Collaboration et al. 2021a). This appears to concur with the average DM of the CHIME/FRB sample compared to the other two surveys. The measured Apertif index follows the apparent median-DM/power-law-index trend observed in the other surveys; the fluence cumulative distribution appears to be flatter for a sample of FRBs with larger DMs and thus redshifts. If this trend is confirmed with future FRB detections, it will provide with important information about how the FRB population evolves with redshift. However, when subdividing the CHIME/FRB catalog into high and low DM FRBs (above and below 500 pc cm^{-3}), these sub-samples follow an opposite trend; the high DM sample has $\alpha = -1.75 \pm 0.15$ and the low DM sample $\alpha = -0.95 \pm 0.15$. On average, the FRB samples mentioned in this section seem to be in agreement with the Euclidean Universe prediction. A comparison between the measured fluence cumulative distribution as a function of the median FRB DM of the aforementioned samples is shown in Fig. 6.22.

6.5.4 Motivation for future observations

Although repeating FRBs have been observed to shine at frequencies as high as 8 GHz (Gajjar et al. 2018), no one-off FRBs have been seen above the L-band (Petroff et al. 2022). Since the observed FRB radio frequency $\nu_{\rm obs}$ gets redshifted with distance, we can estimate the intrinsic, rest frame frequencies at which these FRBs emitted, $\nu_{0,\rm max}$, from their redshift upper limits: $\nu_{0,\rm max} = \nu_{\rm obs}(1 + z_{\rm max})$. For localised FRBs, we use the host galaxy redshift instead. We plot the

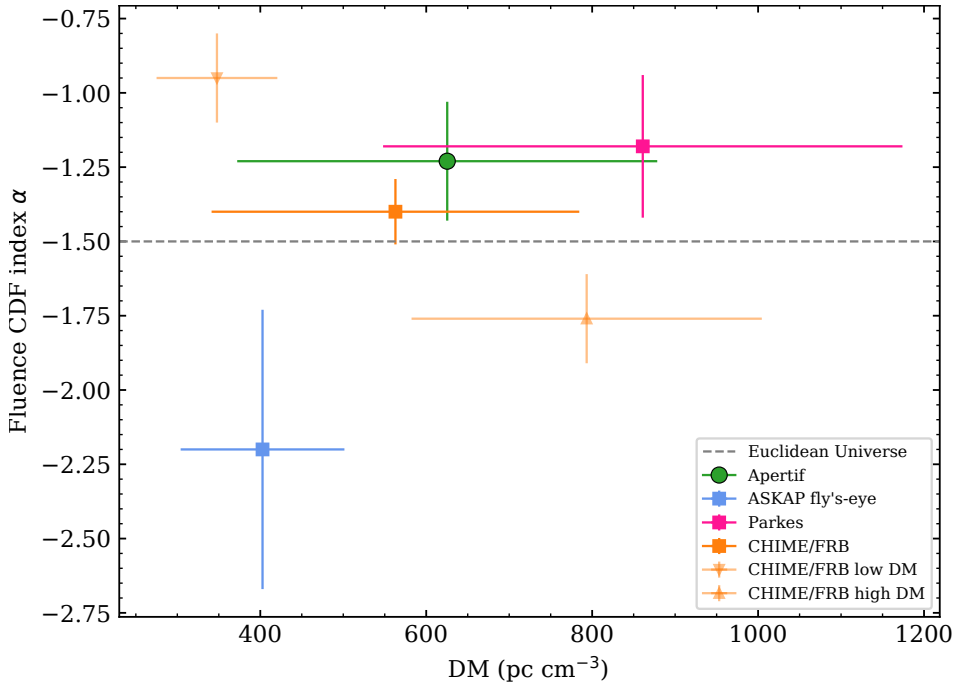

Figure 6.22: Fluence cumulative distribution power law indices (α) as a function of the DMs for each survey. Each data point gives the measured α as a function of the median DM with median absolute deviation errors. Parkes is shown as a pink square, ASKAP Fly's-Eye survey is shown as a blue square (James et al. 2019, α values from), CHIME/FRB as an orange square, the CHIME/FRB < 500 pc cm^{-3} sub-sample as a downwards orange triangle, CHIME/FRB > 500 pc cm^{-3} as an upwards triangle (CHIME/FRB Collaboration et al. 2021a), and Apertif is represented by a green circle. The predicted $\alpha = -1.5$ for an Euclidean Universe is shown by a dashed grey line.

rest frame frequencies as a function of the estimated FRB isotropic energy (Eq. 9 from Zhang 2018a) for all FRBs in the TNS database in Fig. 6.23, and we find 13 FRBs, for which the estimated intrinsic emission frequency is > 3 GHz; four from Apertif, eight from Parkes, and three from FAST (Zhu et al. 2020; Niu et al. 2021). For FRB 20200719A presented in this work, and for the Parkes FRB 20160102A (Bhandari et al. 2018), the estimated emission frequency is > 5 GHz. The detection of high-DM one-off FRBs in the L-band thus indicates that bursts are commonly emitted at higher frequencies. As local FRBs can be expected to do this too, FRB searches in S-band (2−4 GHz) and up are interesting. Although the generally smaller FoV reduces the raw detection rates, the individual beams shrink equally with increasing frequency, allowing for better localisation. When enough beams can be formed and searched, interferometric S-band searches such as those with the MeerKAT 1.75−3.5 GHz system (Kramer et al. 2018) could be fruitful.

Apertif operations have ceased and the ALERT survey finished. The science case for continued GHz FRB searching remains strong. From a larger sample of real-time detections, with immediate alerting and repointing of lower-frequency observatories, we can determine the emission bandwidth of one-off FRBs, and understand their emission mechanism. Based on the work pre-

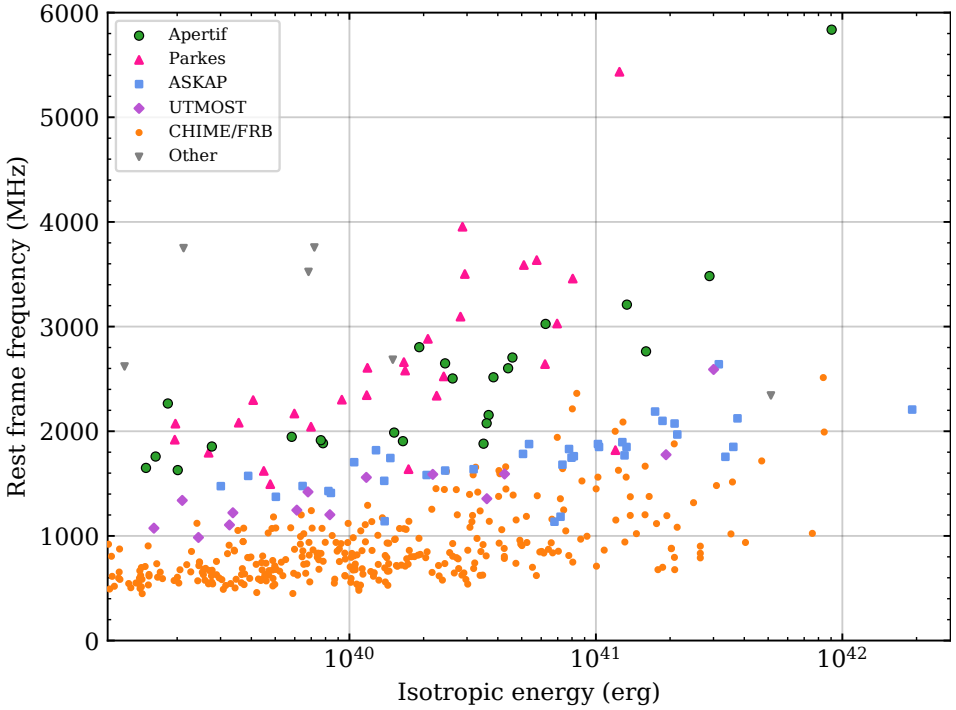

Figure 6.23: Rest frame frequency as a function of the isotropic energy of all FRBs in the TNS and Apertif. Apertif FRBs are shown as green circles, Parkes FRBs as pink upwards triangles, ASKAP FRBs as blue squares, UTMOST as purple diamonds, CHIME/FRB as orange circles, and all other FRBs as grey downwards triangles. Both the rest frame frequency and isotropic energy are upper limits with the exception of localised FRBs.

sented here, a larger sample of 1.4 GHz bursts could be investigated specifically for scattering and multi-component bursts. Such a system could be implemented as a coarse, total-intensity real-time search that preserves baseband data for detections. While the 1-dimensional nature of the WSRT allowed for full-field beamforming, it did limit the overall localisation precision. Up to now, 2-D interferometers equipped with PAFs (i.e., ASKAP) have not been able to tile out the complete primary beam with TABs, reducing the sensitivity (either through incoherent beamforming, or through the longer integration times in imaging mode). The ∼ms integration upgrade to ASKAP for coherent FRB detection over the entire FoV will increase detection rates while also providing good localisation.

As each WSRT dish has a large collecting area for a "large number−small diameter" array, improvements to the front ends can be a cost-effective way to increase the system sensitivity. Cryogenically cooled PAFs combine the strengths of the current system with reduced SEFD (Navarrini et al. 2018; Pingel et al. 2021). Such a successor to Apertif would increase the detection rate by a factor ∼4, and provide better localisation through the higher detection S/N.

6.6 Conclusions

In this work, we have reported the discovery of 18 new, so-far one-off, FRBs, and analysed the properties of the total of 24 bursts that were detected during the ALERT Apertif FRB survey between July 2019 and February 2022. For each FRB, we determine the localisation region and redshift upper limit and perform a flux calibration. We evaluate their morphology, determining the number of components and the spectral properties, and we study the propagation effects by verifying the presence of a resolved scattering tail in time and a scintillation pattern in frequency.

We localise each FRB to a narrow ellipse whose area depends on the detection S/N and the number of CBs where it was detected. The average localisation area is $\sim 7\,\mathrm{arcmin}^2$. For three new FRBs with a high S/N and a low DM, namely FRB 20200518A, FRB 20210317A, and FRB 20200419A, the expected number of galaxies contained within their comoving volume is 5 or less. Optical observations of their localisation regions will likely prove useful in identifying potential host galaxies. In the case of FRB 20211024B, where the expected number of galaxies within the comoving volume is between three and nine, we found four galaxies with a photometric redshift below the upper limit. Through a PATH analysis, we found the brightest and lowest redshift galaxy to be the most likely host, with $> 90\%$ probability. For all other FRBs, we did not find any potential galaxy candidates in the NED and GLADE galaxy databases.

The dispersion measure of our FRB sample resembles that of the Parkes (Champion et al. 2016; Bhandari et al. 2018) and UTMOST (Farah et al. 2019) FRBs. The median DM is $\sim 100\ \mathrm{pc\,cm^{-3}}$ and $\sim 200\ \mathrm{pc\,cm^{-3}}$ higher than the CHIME/FRB (CHIME/FRB Collaboration et al. 2021a) and the ASKAP (Shannon et al. 2018; Macquart et al. 2020) samples respectively. For the ASKAP sample, we cannot reject that the DMs have been drawn from a different intrinsic distribution than the Apertif FRBs. The larger Apertif DMs allow Apertif to observe a more distant population of FRBs than ASKAP. Furthermore, one of the Apertif bursts, FRB 20200719A, has the second largest DM of any FRB published to date, with DM$\sim 2778\ \mathrm{pc\,cm^{-3}}$. Its derived redshift upper limit $z \sim 3$ implies that one-off FRBs exist above 5 GHz and could be detected in the S-band. In the future, a large sample of highly dispersed FRBs like this one will help us determine the FRB rate as the Universe evolved.

One of the bursts, FRB 20200210A, shows both strong scattering and scintillation. From a joint DM-scattering redshift estimation (Cordes et al. 2022), we infer its redshift to be $z \sim 0.11$. This allows us to determine an upper limit of 2 kpc on the distance between the FRB and the scattering screen, which is fully consistent with being located in the host galaxy.

We find the observed scintillation bandwidth of most FRBs to be compatible with the expected Milky Way contribution from the NE2001 model within errors, although in many cases the measured values tend to be larger. Since most FRBs are detected at high galactic latitudes, this might be evidence that the MW ISM at high galactic latitudes is more uniform than what models predict, hence proving FRBs to be valuable tools for improving our knowledge on the Galactic electron density distribution.

A large fraction of the FRBs display a scattering tail > 0.2 ms at 1370 MHz. Most of these τ_{sc} are thus above the CHIME/FRB scattering sensitivity limit of 10 ms at 600 MHz, accounting for the difference in frequency. They thus reveal a population of highly scattered bursts unlikely

to be detected at lower frequencies. Such large scattering timescales are likely to be produced either in the burst environment or an intervening galaxy within the LoS (Chawla et al. 2022). For low redshift FRBs ($z \lesssim 1$), the low chances of intersecting a galaxy with a small impact parameter make a dense circumburst environment the most likely explanation. In the case of FRB 20200210A, the large scattering tail allows us to estimate its redshift to be $z \sim 0.11$ from a joint scattering-DM analysis (Cordes et al. 2022). From the simultaneous presence of scattering and scintillation, we can put an upper limit constraint of 2 kpc between the FRB and a first scattering screen. This confirms the observed scattering was produced within the host galaxy. Fast Radio Burst surveys at high frequencies offer the opportunity of studying FRBs produced in dense environments that would not be detectable at lower frequencies due to the increased scattering timescales and thus lower S/N.

Roughly $\sim 30\%$ of the bursts are composed of multiple components. Worth mentioning are the structures of FRB 20200216A, FRB 20200518A and FRB 20210530A, which display more than two subcomponents each. None show an evidence for (quasi-)periodic behaviour, as it was the case for FRB 20201020A (Pastor-Marazuela et al. 2022). By contrast, only $\sim 5\%$ of the bursts in the First CHIME/FRB Catalogue (Pleunis et al. 2021a) are found to have multiple components. We find this difference cannot be explained by the scattering timescales becoming larger at lower frequencies as $\tau_{sc} \propto \nu^{-4}$ alone; the difference might thus be due to the intrinsic FRB properties; either a smaller spacing that cannot be resolved at the CHIME/FRB resolution, or an inherent scarcity of multi-component bursts at lower frequencies.

Acknowledgements

We thank Jim Cordes and Stella Ocker for their useful input. This research was supported by the European Research Council under the European Union's Seventh Framework Programme (FP/2007-2013)/ERC Grant Agreement No. 617199 ('ALERT'), and by Vici research programme 'ARGO' with project number 639.043.815, financed by the Dutch Research Council (NWO). Instrumentation development was supported by NWO (grant 614.061.613 'ARTS') and the Netherlands Research School for Astronomy ('NOVA4-ARTS', 'NOVA-NW3', and 'NOVA5-NW3-10.3.5.14'). PI of aforementioned grants is JvL. EP further acknowledges funding from an NWO Veni Fellowship. SMS acknowledges support from the National Aeronautics and Space Administration (NASA) under grant number NNX17AL74G issued through the NNH16ZDA001N Astrophysics Data Analysis Program (ADAP). DV acknowledges support from the Netherlands eScience Center (NLeSC) under grant ASDI.15.406 This work makes use of data from the Apertif system installed at the Westerbork Synthesis Radio Telescope owned by ASTRON. ASTRON, the Netherlands Institute for Radio Astronomy, is an institute of NWO.

6.A Fast Radio Burst properties

This appendix contains the Tables 6.3 and 6.4 where the properties of the 24 FRBs detected during the Apertif survey are summarised.

Table 6.3: Apertif Fast Radio Burst properties.
[a] Central frequency $\nu_{\rm peak}$ for broadband bursts assumed to be the central frequency, 1370 MHz. For bursts with power law spectrum, 1520 MHz and 1220 MHz if they peak at the top or the bottom of the band respectively. Other values for narrowband bursts fitted to a gaussian spectrum.
[b] BW is the FWTM of the bursts with a gaussian spectrum or > 300 MHz for broadband bursts.

TNS Name	MJD barycentric	DM (pc cm^{-3})	N	Flux (Jy)	Fluence (Jy ms)	Width (ms)	$\tau_{\rm sc}$ (ms)	$\Delta\nu_{\rm sc}$ (MHz)	$\nu_{\rm peak}$ [a] (MHz)	BW [b] (MHz)
FRB 20190709A	58 673.218 777 99	662.83(8)	2	0.09(2)	0.52(10)	2.15(20)		6.14(606)	1370	>300
FRB 20190926B	58 752.031 731 03	957.15(80)	1	0.11(2)	5.83(117)	4.97(100)	0.78(39)		1370	>300
FRB 20191020B	58 776.781 603 36	464.82(22)	1	0.10(2)	2.78(56)	1.36(9)		14.72(1069)	1370	>300
FRB 20191108A	58 795.831 621 98	587.79(6)	1	0.94(19)	1[8]3)	0.63(1)			1370	>300
FRB 20191109A	58 796.549 633 59	531.17(20)	2	0.15(3)	4.08(82)	2.28(13)		9.02(269)	1370	>300
FRB 20200210A	58 889.309 294 16	439.67(52)	1	0.16(3)	5[7]11)	29.63(55)	12.65(26)	1.60(14)	1449(1)	169(6)
FRB 20200213A	58 892.022 475 46	1017.67(25)	1	0.26(5)	4.39(88)	1.02(3)		7.06(66)	1361(2)	145(7)
FRB 20200216A	58 895.443 484 62	478.67(16)	3	0.21(4)	9.23(185)	7.22(8)			1520	>300
FRB 20200224B	58 903.659 557 87	1449.54(123)	1	0.12(2)	1[5]3)	10.11(110)	3.73(42)		1520	>300
FRB 20200321A	58 929.829 020 69	914.71(4)	2	0.05(1)	4.48(90)	1.79(19)			1436(7)	226(27)
FRB 20200322A	58 930.286 708 55	1290.33(98)	1	0.07(1)	9.90(198)	13(1)	4.16(44)	9.44(460)	1406(7)	277(33)
FRB 20200323C	58 931.383 711 75	833.39(20)	1	0.10(2)	6.61(132)	3.89(25)	1.33(9)	11.56(236)	1520	>300
FRB 20200419A	58 958.079 145 29	248.53(27)	1	0.59(12)	7.37(147)	0.58(2)		15.00(159)	1370	>300
FRB 20200514A	58 983.360 700 20	1406.16(17)	1	0.14(3)	5.23(105)	2.18(12)			1370	>300
FRB 20200516A	58 985.973 360 36	361.15(43)	1	0.05(1)	2.59(52)	2.24(19)			1520	>300
FRB 20200518A	58 987.731 459 01	246.50(14)	4	0.13(3)	4.67(93)	3.95(17)		10.35(398)	1370	>300
FRB 20200523A	58 992.145 198 81	444(9)	1	0.04(1)	6.89(138)	50(9)	12(3)		1370	>300
FRB 20200719A	59 049.574 229 15	2778(6)	1	0.05(1)	1[5]3)	52(6)	21(3)		1459(11)	259(49)
FRB 20201020A	59 142.506 451 21	398.59(8)	5	0.36(7)	1[8]3)	2.13(2)		8.28(89)	1370	>300
FRB 20210124A	59 238.426 897 90	868.25(7)	1	0.11(2)	4.61(92)	2.87(24)	0.65(9)	3.41(58)	1370	>300
FRB 20210127A	59 241.360 472 89	891.22(11)	1	0.43(9)	6.56(131)	0.83(2)			1370	>300
FRB 20210317A	59 290.295 710 36	466.55(12)	1	0.27(5)	6.03(121)	1.14(5)	0.22(3)	4.76(59)	1370	>300
FRB 20210530A	59 364.167 613 89	1000.27(9)	4	0.29(6)	1[9]4)	4.15(14)			1370	>300
FRB 20211024B	59 511.388 218 06	509.39(11)	1	0.45(9)	16[5]9(332)	1.45(1)			1370	>300

Table 6.4: Apertif Fast Radio Burst properties.
[a] Milky Way DM from NE2001 model (Cordes & Lazio 2003) and halo DM from (Yamasaki & Totani 2020).
[b] $z_{\rm max}$ computed from (Zhang 2018a). [c] Spectral index si of bursts with power law spectrum.
[d] Scattering index α of bursts with scattering tail.
[e] Rest frame frequency upper limit $\nu_{0,\rm max}$.
[f] Isotropic energy upper limit.

TNS Name	RA	DEC	Loc. area (arcmin^2)	DM$_{\rm MW+halo}$ [a] (pc cm^{-3})	$z_{\rm max}$ [b]	CB	SB	si [c]	α [d]	$\nu_{0,\rm max}$ [e] (MHz)	$E_{\rm iso}$ [f] (erg)
FRB 20190709A	01h36m06.7s	+31d51m22.8s	1.22	52 + 32	0.65	10	36			2265	$4.06\,10^{39}$
FRB 20190926B	01h41m49.0s	+30d59m24.4s	16.67	51 + 32	0.97	7	39		$3.62^{+4.88}_{-3.3}$	2704	$3.31\,10^{40}$
FRB 20191020B	20h30m52.0s	+61d58m47.0s	15.43	102 + 44	0.35	5	14			1854	$2.08\,10^{39}$
FRB 20191108A	01h33m57.4s	+31d45m38.0s	16.78	51 + 32	0.57	21	37			2154	$8.68\,10^{39}$
FRB 20191109A	20h33m51.0s	+61d46m30.2s	0.72	105 + 44	0.42	18	44			1947	$2.38\,10^{39}$
FRB 20200210A	18h53m59.4s	+46d18m57.6s	1.91	70 + 47	0.37	9	37		$-10.44^{+1.9}_{-1.75}$	1881	$1.15\,10^{40}$
FRB 20200213A	09h22m23.0s	+77d01m59.6s	0.90	45 + 31	1.05	9	48			2802	$2.06\,10^{40}$
FRB 20200216A	22h08m24.1s	+16d34m22.5s	2.11	48 + 41	0.45	5	30	11.62 ± 2.51		1987	$8.56\,10^{39}$
FRB 20200224B	02h20m27.0s	+19d27m06.0s	6.06	44 + 31	1.54	14	33	5.4 ± 1.32		3479	$1.16\,10^{41}$
FRB 20200321A	09h28m11.6s	+76d00m56.3s	14.17	45 + 31	0.93	5	37			2647	$4.04\,10^{39}$
FRB 20200322A	22h13m02.2s	+15d16m38.0s	3.90	46 + 40	1.34	6	29		$-5.68^{+3.52}_{-3.83}$	3209	$8.08\,10^{40}$
FRB 20200323C	22h10m53.9s	+15d45m39.0s	8.31	47 + 40	0.84	12	18	6.25 ± 1.07	$-5.12^{+5.35}_{-3.14}$	2515	$1.75\,10^{40}$
FRB 20200419A	19h00m24.2s	+81d42m59.1s	5.25	55 + 35	0.19	32	56			1629	$1.19\,10^{39}$
FRB 20200514A	01h48m30.0s	+64d40m48.9s	24.83	181 + 44	1.21	2	40			3026	$3.79\,10^{40}$
FRB 20200516A	18h56m48.4s	+46d51m46.3s	28.86	73 + 47	0.28	18	22	7.87 ± 2.58		1758	$1.61\,10^{39}$
FRB 20200518A	09h36m45.0s	+77d22m33.8s	2.96	45 + 31	0.20	25	68			1648	$1.03\,10^{39}$
FRB 20200523A	18h55m41.3s	+47d10m09.2s	nan	72 + 46	0.38	24	19		$-4.69^{+6.82}_{-6.78}$	1886	$6.20\,10^{39}$
FRB 20200719A	09h18m40.6s	+77d22m55.9s	3.93	46 + 31	3.26	22	20		$-7.56^{+6.79}_{-6.95}$	5835	$6.18\,10^{41}$
FRB 20201020A	13h51m24.7s	+49d02m05.8s	0.76	29 + 32	0.39	29	17			1759	$2.89\,10^{39}$
FRB 20210124A	19h41m24.6s	+58d54m30.5s	0.84	80 + 44	0.83	11	48		$-2.1^{+3.17}_{-4.07}$	2504	$1.95\,10^{40}$
FRB 20210127A	16h49m56.3s	+26d37m29.3s	0.72	41 + 44	0.90	21	34			2599	$2.56\,10^{40}$
FRB 20210317A	19h36m27.3s	+59d52m03.0s	0.48	76 + 43	0.40	23	35		$-5.35^{+4.53}_{-8.16}$	1914	$3.62\,10^{39}$
FRB 20210530A	22h08m55.6s	+16d32m18.1s	2.93	47 + 40	1.02	6	36			2762	$1.57\,10^{41}$
FRB 20211024B	13h20m34.7s	+42d29m29.0s	0.69	25 + 31	0.52	18	40			1741	$5.22\,10^{39}$

Bibliography

Abbott, B. P., Abbott, R., Abbott, T. D., et al. 2017, *Gravitational Waves and Gamma-Rays from a Binary Neutron Star Merger: GW170817 and GRB 170817A*, The Astrophysical Journal, 848, L13

Abdo, A. A., Ackermann, M., Ajello, M., et al. 2009, *Detection of 16 Gamma-Ray Pulsars Through Blind Frequency Searches Using the Fermi LAT*, Science, 325, 840

Abdo, A. A., Ackermann, M., Ajello, M., et al. 2010, *The First Fermi Large Area Telescope catalog of Gamma-ray pulsars*, The Astrophysical Journal Supplement Series, 187, 460

Abdo, A. A., Ajello, M., Allafort, A., et al. 2013, *The Second Fermi Large Area Telescope Catalog of Gamma-Ray Pulsars*, ApJS, 208, 17

Abolfathi, B. 2018, *The Fourteenth Data Release of the Sloan Digital Sky Survey: First Spectroscopic Data from the Extended Baryon Oscillation Spectroscopic Survey and from the Second Phase of the Apache Point Observatory Galactic Evolution Experiment*, The Astrophysical Journal Supplement Series, 19

Adams, E. A. K. & van Leeuwen, J. 2019, *Radio surveys now both deep and wide*, Nature Astronomy, 3, 188

Aggarwal, K., Budavári, T., Deller, A. T., et al. 2021, *Probabilistic Association of Transients to their Hosts* (*PATH*), The Astrophysical Journal, 911, 95

Aggarwal, K., Law, C. J., Burke-Spolaor, S., et al. 2020, *VLA/realfast detection of burst from FRB180916.J0158+65 and Tests for Periodic Activity*, Research Notes of the AAS, 4, 94

Alexov, A., Hessels, J., Mol, J. D., Stappers, B., & van Leeuwen, J. 2010, *The LOFAR Pulsar Data Pipeline*, Astronomical DataAnalysisSoftware and Systems XIX, 434

Alp, D. & Larsson, J. 2020, *Blasts from the Past: Supernova Shock Breakouts among X-Ray Transients in the XMM-Newton Archive*, The Astrophysical Journal, 896, 39

Anna-Thomas, R., Connor, L., Burke-Spolaor, S., et al. 2022, *A Highly Variable Magnetized Environment in a Fast Radio Burst Source*, arXiv:2202.11112 [astro-ph], arXiv: 2202.11112

Anumarlapudi, A., Bhalerao, V., Tendulkar, S. P., & Balasubramanian, A. 2020, *Prompt X-Ray Emission from Fast Radio Bursts—Upper Limits with AstroSat*, The Astrophysical Journal, 888, 40, aDS Bibcode: 2020ApJ...888...40A

Baade, W. & Zwicky, F. 1934, *Cosmic Rays from Super-novae*, Proceedings of the National Academy of Science, 20, 259, aDS Bibcode: 1934PNAS...20..259B

Bailer-Jones, C. A. L., Rybizki, J., Fouesneau, M., Mantelet, G., & Andrae, R. 2018, *Estimating Distance from Parallaxes. IV. Distances to 1.33 Billion Stars in Gaia Data Release 2*, The Astronomical Journal, 156, 58

Baldry, I. K., Driver, S. P., Loveday, J., et al. 2012, *Galaxy And Mass Assembly* (*GAMA*)*: the galaxy stellar mass function at z < 0.06: GAMA: the galaxy stellar mass function*, Monthly Notices of the Royal Astronomical Society, no

Bannister, K. W., Deller, A. T., Phillips, C., et al. 2019, *A single fast radio burst localized to a massive galaxy at cosmological distance*, Science, 365, 565

Bannister, K. W., Shannon, R. M., Macquart, J.-P., et al. 2017, *The Detection of an Extremely Bright Fast Radio Burst in a Phased Array Feed Survey*, The Astrophysical Journal, 841, L12

Baring, M. G. & Harding, A. K. 2001, *Photon Splitting and Pair Creation in Highly Magnetized Pulsars*, ApJ, 547, 929

Barrau, A., Rovelli, C., & Vidotto, F. 2014, *Fast radio bursts and white hole signals*, Physical Review D, 90, 127503, publisher: American Physical Society

Bartel, N., Morris, D., Sieber, W., & Hankins, T. H. 1982, *The mode-switching phenomenon in pulsars*, The Astrophysical Journal, 258, 776

Basu, R., Mitra, D., Melikidze, G. I., & Skrzypczak, A. 2019, *Classification of subpulse drifting in pulsars*, Monthly Notices of the Royal Astronomical Society, 482, 3757

Bates, S. D., Lorimer, D. R., & Verbiest, J. P. W. 2013, *The pulsar spectral index distribution*, Monthly Notices of the Royal Astronomical Society, 431, 1352

Batten, A. 2019, *Fruitbat: A Python Package for Estimating Redshifts of Fast Radio Bursts*, Journal of Open Source Software, 4, 1399

Batten, A. J., Duffy, A. R., Wijers, N. A., et al. 2021, *The cosmic dispersion measure in the EAGLE simulations*, Monthly Notices of the Royal Astronomical Society, 505, 5356

Bañados, E., Venemans, B. P., Mazzucchelli, C., et al. 2018, *An 800-million-solar-mass black hole in a significantly neutral Universe at a redshift of 7.5*, Nature, 553, 473

Bejger, M., Gondek-Rosińska, D., Gourgoulhon, E., et al. 2005, *Impact of the nuclear equation of state on the last orbits of binary neutron stars*, Astronomy & Astrophysics, 431, 297

Belloni, T. M. & Motta, S. E. 2016, in Astrophysics of Black Holes: From Fundamental Aspects to Latest Developments, ed. C. Bambi, Astrophysics and Space Science Library (Berlin, Heidelberg: Springer), 61–97

Beloborodov, A. M. 2017, *A Flaring Magnetar in FRB 121102?*, The Astrophysical Journal, 843, L26

Beloborodov, A. M. 2020, *Blast Waves from Magnetar Flares and Fast Radio Bursts*, The Astrophysical Journal, 896, 142, publisher: American Astronomical Society

Beniamini, P., Wadiasingh, Z., & Metzger, B. D. 2020, *Periodicity in recurrent fast radio bursts and the origin of ultra long period magnetars*, Monthly Notices of the Royal Astronomical Society, 496, 3390

Bhandari, S., Bannister, K. W., Lenc, E., et al. 2020a, *Limits on precursor and afterglow radio emission from a fast radio burst in a star-forming galaxy*, The Astrophysical Journal, 901, L20

Bhandari, S., Heintz, K. E., Aggarwal, K., et al. 2022, *Characterizing the Fast Radio Burst Host Galaxy Population and its Connection to Transients in the Local and Extragalactic Universe*, The Astronomical Journal, 163, 69

Bhandari, S., Keane, E. F., Barr, E. D., et al. 2018, *The SUrvey for Pulsars and Extragalactic Radio Bursts – II. New FRB discoveries and their follow-up*, Monthly Notices of the Royal Astronomical Society, 475, 1427

Bhandari, S., Sadler, E. M., Prochaska, J. X., et al. 2020b, *The Host Galaxies and Progenitors of Fast Radio Bursts Localized with the Australian Square Kilometre Array Pathfinder*, The Astrophysical Journal, 895, L37

Bhardwaj, M., Gaensler, B. M., Kaspi, V. M., et al. 2021, *A Nearby Repeating Fast Radio Burst in the Direction of M81*, The Astrophysical Journal Letters, 910, L18

Bhat, N. D. R., Cordes, J. M., Camilo, F., Nice, D. J., & Lorimer, D. R. 2004, *Multifrequency Observations of Radio Pulse Broadening and Constraints on Interstellar Electron Density Microstructure*, The Astrophysical Journal, 605, 759

Bhat, N. D. R., Gupta, Y., & Rao, A. P. 1998, *Pulsar Scintillation and the Local Bubble*, The Astrophysical Journal, 500, 262

Bilous, A. V., Kondratiev, V. I., Kramer, M., et al. 2016, *A LOFAR census of non-recycled pulsars: average profiles, dispersion measures, flux densities, and spectra*, Astronomy & Astrophysics, 591, A134

Blackburn, J. K. 1995, *FTOOLS: A FITS Data Processing and Analysis Software Package*, in FTOOLS, Vol. 77, 367

Blanton, M. R. 2017, *Sloan Digital Sky Survey IV: Mapping the Milky Way, Nearby Galaxies, and the Distant Universe*, The Astronomical Journal, 35

Blaskiewicz, M., Cordes, J. M., & Wasserman, I. 1991, *A relativistic model of pulsar polarization*, The Astrophysical Journal, 370, 643

Bochenek, C. D., Ravi, V., Belov, K. V., et al. 2020, *A fast radio burst associated with a Galactic magnetar*, Nature, 587, 59

Bogdanov, S., Ho, W. C. G., Enoto, T., et al. 2019, *Neutron Star Interior Composition Explorer X-Ray Timing of the Radio and γ-Ray Quiet Pulsars PSR J1412+7922 and PSR J1849-0001*, The Astrophysical Journal, 877, 69

Brentjens, M. A. & Bruyn, A. G. d. 2005, *Faraday rotation measure synthesis*, Astronomy & Astrophysics, 441, 1217, number: 3 Publisher: EDP Sciences

Bruch, A. 2017, *Orbital variations and outbursts of the unusual variable star V1129 Centauri*, New Astronomy, 57, 51

Burke-Spolaor, S. & Bannister, K. W. 2014, *The Galactic position dependence of Fast Radio Bursts and the discovery of FRB011025*, The Astrophysical Journal, 792, 19

Burn, B. J. 1966, *On the Depolarization of Discrete Radio Sources by Faraday Dispersion*, Monthly Notices of the Royal Astronomical Society, 133, 67

Burrows, A. & Vartanyan, D. 2021, *Core-collapse supernova explosion theory*, Nature, 589, 29, number: 7840 Publisher: Nature Publishing Group

Cai, Y.-F., Sabancilar, E., & Vachaspati, T. 2012, *Radio bursts from superconducting strings*, Physical Review D, 85, 023530

Calderwood, T., Dobrzycki, A., Jessop, H., & Harris, D. 2001, *The Sliding-Cell Detection Program for Chandra X-ray Data*, Astronomical Society of the Pacific Conference Series, 238, 443

Caleb, M., Flynn, C., Bailes, M., et al. 2017, *The first interferometric detections of fast radio bursts*, Monthly Notices of the Royal Astronomical Society, 468, 3746

Caleb, M., Heywood, I., Rajwade, K., et al. 2022, *Discovery of a radio-emitting neutron star with an ultra-long spin period of 76 s*, Nature Astronomy, 1

Caleb, M. & Keane, E. 2021, *A Decade and a Half of Fast Radio Burst Observations*, Universe, 7, 453

Caleb, M., Keane, E. F., van Straten, W., et al. 2018, *The SUrvey for Pulsars and Extragalactic Radio Bursts - III. Polarization properties of FRBs 160102 and 151230*, Monthly Notices of the Royal Astronomical Society, 478, 2046

Caleb, M., Rajwade, K., Desvignes, G., et al. 2021, *Radio and X-ray observations of giant pulses from XTE J1810-197*, Monthly Notices of the Royal Astronomical Society, 510, 1996

Caleb, M., Stappers, B. W., Abbott, T. D., et al. 2020, *Simultaneous multi-telescope observations of FRB 121102*, Monthly Notices of the Royal Astronomical Society, 496, 4565

Callister, T., Kanner, J., & Weinstein, A. 2016, *Gravitational-Wave constraints on the progenitors of Fast Radio Bursts*, The Astrophysical Journal, 825, L12

Camilo, F., Ransom, S. M., Halpern, J. P., et al. 2006, *Transient pulsed radio emission from a magnetar*, Nature, 442, 892

Casentini, C., Verrecchia, F., Tavani, M., et al. 2020, *AGILE Observations of Two Repeating Fast Radio Bursts with Low Intrinsic Dispersion Measures*, The Astrophysical Journal, 890, L32

Cash, W. 1979, *Parameter estimation in astronomy through application of the likelihood ratio*, 228, 939

Chambers, K. C., Magnier, E. A., Metcalfe, N., et al. 2019, *The Pan-STARRS1 Surveys*

Chamma, M. A., Rajabi, F., Wyenberg, C. M., Mathews, A., & Houde, M. 2021, *Evidence of a shared spectro-temporal law between sources of repeating fast radio bursts*, Monthly Notices of the Royal Astronomical Society, 507, 246

Champion, D. J., Petroff, E., Kramer, M., et al. 2016, *Five new fast radio bursts from the HTRU high-latitude survey at Parkes: first evidence for two-component bursts*, Monthly Notices of the Royal Astronomical Society: Letters, 460, L30

Chandrasekhar, S. 1983, *On stars, their evolution and their stability*, in Nobel Lecture, Chicago, Illinois, USA

Chatterjee, S., Law, C. J., Wharton, R. S., et al. 2017, *The direct localization of a fast radio burst and its host*, Nature, 541, 58

Chaty, S. 2011, *Nature, Formation, and Evolution of High Mass X-Ray Binaries*, in ESO Workshop, Vol. 447 (San Martín, Viña del Mar, Chile: Astronomical Society of the Pacific), 29

Chawla, P., Andersen, B. C., Bhardwaj, M., et al. 2020, *Detection of Repeating FRB 180916.J0158+65 Down to Frequencies of 300 MHz*, The Astrophysical Journal Letters, 896

Chawla, P., Kaspi, V. M., Ransom, S. M., et al. 2022, *Modeling Fast Radio Burst Dispersion and Scattering Properties in the First CHIME/FRB Catalog*, The Astrophysical Journal, 927, 35

Chen, J. L. & Wang, H. G. 2014, *Frequency dependence of pulse width for 150 radio normal pulsars*, The Astrophysical Journal Supplement Series, 215, 11

Chen, K. & Ruderman, M. 1993, *Pulsar Death Lines and Death Valley*, ApJ, 402, 264
Cheng, K. S., Ruderman, M., & Zhang, L. 2000, *A Three-dimensional Outer Magnetospheric Gap Model for Gamma-Ray Pulsars: Geometry, Pair Production, Emission Morphologies, and Phase-resolved Spectra*, The Astrophysical Journal, 537, 964
CHIME/FRB Collaboration. 2020, *A bright millisecond-duration radio burst from a Galactic magnetar*, Nature, 587, 54
CHIME/FRB Collaboration, Amiri, M., Andersen, B., et al. 2020, *Periodic activity from a fast radio burst source*, Nature, 582, 351
CHIME/FRB Collaboration, Amiri, M., Andersen, B. C., et al. 2021a, *The First CHIME/FRB Fast Radio Burst Catalog*, The Astrophysical Journal, 257, 41
CHIME/FRB Collaboration, Amiri, M., Bandura, K., et al. 2019a, *A Second Source of Repeating Fast Radio Bursts*, Nature, 566, 8
CHIME/FRB Collaboration, Amiri, M., Bandura, K., et al. 2019b, *Observations of Fast Radio Bursts at Frequencies down to 400 Megahertz*, Nature, 566, 230
CHIME/FRB Collaboration, Andersen, B. C., Bandura, K., et al. 2021b, *Sub-second periodicity in a fast radio burst*, arXiv:2107.08463 [astro-ph]
CHIME/FRB Collaboration, Andersen, B. C., Bandura, K., et al. 2019c, *CHIME/FRB Detection of Eight New Repeating Fast Radio Burst Sources*, The Astrophysical Journal Letters, 885
CHIME/FRB Collabortion. 2021, *Recent high activity from a repeating Fast Radio Burst discovered by CHIME/FRB*, The Astronomer's Telegram, 14497, 1, aDS Bibcode: 2021ATel14497....1C
Chittidi, J. S., Simha, S., Mannings, A., et al. 2021, *Dissecting the Local Environment of FRB 190608 in the Spiral Arm of its Host Galaxy*, The Astrophysical Journal, 922, 173
Cho, H., Macquart, J.-P., Shannon, R. M., et al. 2020, *Spectropolarimetric Analysis of FRB 181112 at Microsecond Resolution: Implications for Fast Radio Burst Emission Mechanism*, The Astrophysical Journal, 891, L38
Coenen, T. 2013, *Searching for pulsars with LOFAR*, PhD thesis, University of Amsterdam, http://dare.uva.nl/cn/record/459730
Coenen, T., van Leeuwen, J., Hessels, J. W. T., et al. 2014, *The LOFAR pilot surveys for pulsars and fast radio transients*, Astronomy & Astrophysics, 570, A60
Connor, L. 2019, *Interpreting the distributions of FRB observables*, Monthly Notices of the Royal Astronomical Society, 487, 5753
Connor, L. & Ravi, V. 2021, *A detection of circumgalactic gas with fast radio bursts*, arXiv:2107.13692 [astro-ph], arXiv: 2107.13692
Connor, L., Sievers, J., & Pen, U.-L. 2016, *Non-cosmological FRBs from young supernova remnant pulsars*, Monthly Notices of the Royal Astronomical Society: Letters
Connor, L. & van Leeuwen, J. 2018, *Applying Deep Learning to Fast Radio Burst Classification*, The Astronomical Journal, 156, 256
Connor, L., van Leeuwen, J., Oostrum, L. C., et al. 2020, *A bright, high rotation-measure FRB that skewers the M33 halo*, Monthly Notices of the Royal Astronomical Society, 499, 4716
Cooke, J., Sullivan, M., Barton, E. J., et al. 2009, *Type IIn supernovae at redshift z 2 from archival data*, Nature, 460, 237
Cordes, J. M. 1978, *Observational limits on the location of pulsar emission regions*, The Astrophysical Journal, 222, 1006
Cordes, J. M. 1979, *Pulsar microstructure: periodicities, polarization and probes of pulsar magnetospheres.*, Australian Journal of Physics, 32, 9
Cordes, J. M. 1986, *Space velocities of radio pulsars from interstellar scintillations*, The Astrophysical Journal, 311, 183
Cordes, J. M. & Chatterjee, S. 2019, *Fast Radio Bursts: An Extragalactic Enigma*, Annual Review of Astronomy and Astrophysics, 57, 417
Cordes, J. M. & Lazio, T. J. W. 2003, *NE2001.I. A New Model for the Galactic Distribution of Free Electrons and its Fluctuations*, arXiv:astro-ph/0207156

Cordes, J. M. & McLaughlin, M. A. 2003, *Searches for Fast Radio Transients*, The Astrophysical Journal, 596, 1142

Cordes, J. M., Ocker, S. K., & Chatterjee, S. 2022, *Redshift Estimation and Constraints on Intergalactic and Interstellar Media from Dispersion and Scattering of Fast Radio Bursts*, The Astrophysical Journal, 931, 88

Cordes, J. M. & Rickett, B. J. 1998, *Diffractive Interstellar Scintillation Timescales and Velocities*, The Astrophysical Journal, 507, 846

Cordes, J. M. & Wasserman, I. 2016, *Supergiant pulses from extragalactic neutron stars*, Monthly Notices of the Royal Astronomical Society, 457, 232

Cordes, J. M., Weisberg, J. M., & Hankins, T. H. 1990, *Quasiperiodic microstructure in radio pulsar emissions*, The Astronomical Journal, 100, 1882

Cordes, J. M., Wharton, R. S., Spitler, L. G., Chatterjee, S., & Wasserman, I. 2016, *Radio Wave Propagation and the Provenance of Fast Radio Bursts*, arXiv:1605.05890 [astro-ph]

Cromartie, H. T., Fonseca, E., Ransom, S. M., et al. 2020, *Relativistic Shapiro delay measurements of an extremely massive millisecond pulsar*, Nature Astronomy, 4, 72

Cruces, M., Spitler, L. G., Scholz, P., et al. 2020, *Repeating behaviour of FRB 121102: periodicity, waiting times, and energy distribution*, Monthly Notices of the Royal Astronomical Society, 500, 448

Cucchiara, A., Levan, A. J., Fox, D. B., et al. 2011, *A Photometric Redshift of z ~ 9.4 for GRB 090429B*, The Astrophysical Journal, 736, 7

Cunningham, V., Cenko, S. B., Burns, E., et al. 2019, *A Search for High-energy Counterparts to Fast Radio Bursts*, The Astrophysical Journal, 879, 40

Cutler, C. & Flanagan, E. 1994, *Gravitational Waves from Mergin Compact Binaries: How Accurately Can One Extract the Binary's Parameters from the Inspiral Waveform?*, Physical Review D, 49, 2658

Dai, Z. G. & Zhong, S. Q. 2020, *Periodic Fast Radio Bursts as a Probe of Extragalactic Asteroid Belts*, The Astrophysical Journal, 895, L1

Daniel, S. A., Latham, D. W., Mathieu, R. D., & Twarog, B. A. 1994, *A photometric and radial-velocity analysis of the intermediate-age open cluster NGC 752*, Publications of the Astronomical Society of the Pacific, 106, 281

Day, C. K., Deller, A. T., Shannon, R. M., et al. 2020, *High time resolution and polarization properties of ASKAP-localized fast radio bursts*, Monthly Notices of the Royal Astronomical Society, 497, 3335

De, K., Gupta, Y., & Sharma, P. 2016, *Detection of polarized quasi-periodic microstructure emission in millisecond pulsars*, The Astrophysical Journal, 833, L10

De Luca, A., Salvaterra, R., Tiengo, A., et al. 2015, *An overview of the EXTraS project: Exploring the X-ray Transient and Variable Sky*, Proceedings of Swift: 10 Years of Discovery — PoS(SWIFT 10), 135

DeLaunay, J. J., Fox, D. B., Murase, K., et al. 2016, *Discovery of a transient gamma-ray counterpart to FRB 131104*, The Astrophysical Journal, 832, L1

Demorest, P. B., Pennucci, T., Ransom, S. M., Roberts, M. S. E., & Hessels, J. W. T. 2010, *A two-solar-mass neutron star measured using Shapiro delay*, Nature, 467, 3

Deng, W. & Zhang, B. 2014, *Cosmological implications of Fast Radio Burst / Gamma-Ray Burst Associations*, The Astrophysical Journal, 783, L35

Desvignes, G., Kramer, M., Lee, K., et al. 2019, *Radio emission from a pulsar's magnetic pole revealed by general relativity*, Science, 365, 1013

Dewey, R. J., Taylor, J. H., Weisberg, J. M., & Stokes, G. H. 1985, *A search for low-luminosity pulsars.*, ApJ, 294, L25

Dietrich, T., Hinderer, T., & Samajdar, A. 2021, *Interpreting binary neutron star mergers: describing the binary neutron star dynamics, modelling gravitational waveforms, and analyzing detections*, General Relativity and Gravitation, 53, 27

Dokuchaev, V. I. & Eroshenko, Y. N. 2017, *Recurrent fast radio bursts from collisions of neutron stars in the evolved stellar clusters*

D'Orazio, D. J., Levin, J., Murray, N. W., & Price, L. 2016, *Bright transients from strongly-magnetized neutron star-black hole mergers*, Physical Review D, 94, 023001

Dálya, G., Galgóczi, G., Dobos, L., et al. 2018, *GLADE: A Galaxy Catalogue for Multi-Messenger Searches in the Advanced Gravitational-Wave Detector Era*, Monthly Notices of the Royal Astronomical Society, 479, 2374

Edwards, R. T. & Stappers, B. W. 2002, *Drifting sub-pulse analysis using the two-dimensional Fourier transform*, Astronomy & Astrophysics, 393, 733

Eftekhari, T. & Berger, E. 2017, *Associating Fast Radio Bursts with Their Host Galaxies*, The Astrophysical Journal, 849, 162

Egorov, A. E. & Postnov, K. A. 2009, *On the possible observational manifestation of supernova shock impact on the neutron star magnetosphere*, Astronomy Letters, 35, 241

EHT Collaboration. 2019, *First M87 Event Horizon Telescope Results. I. The Shadow of the Supermassive Black Hole*, The Astrophysical Journal Letters, 17

EHT Collaboration. 2022, *First Sagittarius A* Event Horizon Telescope Results. I. The Shadow of the Supermassive Black Hole in the Center of the Milky Way*, The Astrophysical Journal Letters, 21

Esposito, P., Israel, G. L., Belfiore, A., et al. 2016, *EXTraS discovery of an 1.2-s X-ray pulsar in M 31*, Monthly Notices of the Royal Astronomical Society: Letters, 457, L5

Faber, S. M., Willmer, C. N. A., Wolf, C., et al. 2007, *Galaxy Luminosity Functions to z 1 from DEEP2 and COMBO-17: Implications for Red Galaxy Formation*, The Astrophysical Journal, 665, 265

Falcke, H. & Rezzolla, L. 2014, *Fast radio bursts: the last sign of supramassive neutron stars*, Astronomy & Astrophysics, 562, A137

Farah, W., Flynn, C., Bailes, M., et al. 2018, *FRB microstructure revealed by the real-time detection of FRB170827*, Monthly Notices of the Royal Astronomical Society, 478, 1209

Farah, W., Flynn, C., Bailes, M., et al. 2019, *Five new real-time detections of fast radio bursts with UTMOST*, Monthly Notices of the Royal Astronomical Society, 488, 2989

Farrell, S. A., Murphy, T., & Lo, K. K. 2015, *Autoclassification of the Variable 3XMM Sources Using the Random Forest Machine Learning Algorithm*, The Astrophysical Journal, 813, 28

Favata, F., Flaccomio, E., Reale, F., et al. 2005, *Bright X-Ray Flares in Orion Young Stars from COUP: Evidence for Star-Disk Magnetic Fields?*, The Astrophysical Journal Supplement Series, 160, 469

Feigelson, E. D. & Babu, G. J. 2012, Modern Statistical Methods for Astronomy : With R Applications (New York: Cambridge University Press)

Feng, Y., Li, D., Yang, Y.-P., et al. 2022, *Frequency Dependent Polarization of Repeating Fast Radio Bursts - Implications for Their Origin*, 62

Fisher, R. A. 1922, *On the interpretation of X2 from contingency tables, and the calculation of P.*, 9

Fisher, R. A. 1934, Statistical Methods for Research Workers, 5th edn., Biological Monographs and Manuals (Edinburgh: Oliver and Boyd)

Fonseca, E., Andersen, B. C., Bhardwaj, M., et al. 2020, *Nine New Repeating Fast Radio Burst Sources from CHIME/FRB*, The Astrophysical Journal, 891, L6

Fonseca, E., Cromartie, H. T., Pennucci, T. T., et al. 2021, *Refined Mass and Geometric Measurements of the High-Mass PSR J0740+6620*, The Astrophysical Journal Letters, 915, L12

Fox, D. W., Kaplan, D. L., Kulkarni, S. R., & Frail, D. A. 2001, *High-Resolution X-ray and Radio Observations of SGR 1900+14 in the Immediate Aftermath of a Giant Flare*, arXiv:astro-ph/0107520, arXiv: astro-ph/0107520

Frail, D. A., Jagannathan, P., Mooley, K. P., & Intema, H. T. 2016, *Known Pulsars Identified in the GMRT 150 MHz All-Sky Survey*, The Astrophysical Journal, 829, 119

Frail, D. A., Kulkarni, S. R., & Bloom, J. S. 1999, *A Relativistic Particle Outburst From The Soft Gamma-Ray Repeater SGR1900+14*, Nature, 398, 127

Fuchs, J. T., Dunlap, B. H., Dennihy, E., et al. 2016, *The Magnetic Cataclysmic Variable LSQ1725-64*, Monthly Notices of the Royal Astronomical Society, 462, 2382

Fuller, J. & Ott, C. D. 2015, *Dark matter-induced collapse of neutron stars: a possible link between fast radio bursts and the missing pulsar problem*, Monthly Notices of the Royal Astronomical Society: Letters, 450, L71

Gaia Collaboration. 2016, *The Gaia mission*, Astronomy & Astrophysics, 595, A1

Gaia Collaboration, Brown, A. G. A., Vallenari, A., et al. 2018, *Gaia Data Release 2. Summary of the contents and survey properties*, Astronomy & Astrophysics, 616, A1

Gajjar, V., Siemion, A. P. V., Price, D. C., et al. 2018, *Highest-frequency detection of FRB 121102 at 4-8 GHz using the Breakthrough Listen Digital Backend at the Green Bank Telescope*, The Astrophysical Journal, 863, 2

Gardenier, D. W. & van Leeuwen, J. 2021, *Multi-dimensional population modelling using frbpoppy: Magnetars can produce the observed fast radio burst sky*, Astronomy & Astrophysics, 651, A63

Gardenier, D. W., van Leeuwen, J., Connor, L., & Petroff, E. 2019, *Synthesising the intrinsic FRB population using frbpoppy*, Astronomy & Astrophysics, 632, A125, publisher: EDP Sciences

Gehrels, N. 1986, *Confidence limits for small numbers of events in astrophysical data*, The Astrophysical Journal, 303, 336

Geng, J. J. & Huang, Y. F. 2015, *Fast Radio Bursts: Collisions between Neutron Stars and Asteroids/Comets*, The Astrophysical Journal, 809, 24

Geyer, M. & Karastergiou, A. 2016, *The frequency dependence of scattering imprints on pulsar observations*, Monthly Notices of the Royal Astronomical Society, 462, 2587

Ghez, A. M., Morris, M., Becklin, E. E., Tanner, A., & Kremenek, T. 2000, *The accelerations of stars orbiting the Milky Way's central black hole*, Nature, 407, 349, number: 6802 Publisher: Nature Publishing Group

Ghisellini, G. 2017, *Synchrotron masers and fast radio bursts*, Monthly Notices of the Royal Astronomical Society, 465, L30

Giardino, G., Pillitteri, I., Favata, F., & Micela, G. 2008, *The X-ray luminosity of solar-mass stars in the intermediate age open cluster NGC 752*, Astronomy & Astrophysics, 490, 113

Gioia, I. M., Maccacaro, T., Schild, R. E., et al. 1990, *The Einstein Observatory Extended Medium-Sensitivity Survey. I - X-ray data and analysis*, The Astrophysical Journal Supplement Series, 72, 567

Giustini, M., Miniutti, G., & Saxton, R. D. 2020, *X-ray quasi-periodic eruptions from the galactic nucleus of RX J1301.9+2747*, Astronomy & Astrophysics, 636, L2

Gourdji, K., Michilli, D., Spitler, L. G., et al. 2019, *A sample of low energy bursts from FRB 121102*, The Astrophysical Journal, 877, L19

Graham, M. T., Cappellari, M., Li, H., et al. 2018, *SDSS-IV MaNGA: stellar angular momentum of about 2300 galaxies: unveiling the bimodality of massive galaxy properties*, Monthly Notices of the Royal Astronomical Society, 477, 4711

Grießmeier, J. M., Smith, D. A., Theureau, G., et al. 2021, *Follow-up of 27 radio-quiet gamma-ray pulsars at 110-190 MHz using the international LOFAR station FR606*, A&A, 654, A43

Gu, W.-M., Dong, Y.-Z., Liu, T., Ma, R., & Wang, J. 2016, *A Neutron Star-White Dwarf Binary Model for Repeating Fast Radio Burst 121102*, The Astrophysical Journal, 823, L28, publisher: American Astronomical Society

Guetta, D. & Piran, T. 2005, *The luminosity and redshift distributions of short-duration GRBs*, Astronomy & Astrophysics, 435, 421

Guidorzi, C., Orlandini, M., Frontera, F., et al. 2020, *Constraining the transient high-energy activity of FRB 180916.J0158+65 with Insight–HXMT follow-up observations*, Astronomy & Astrophysics, 642, A160

Gúrpide, A., Godet, O., Koliopanos, F., Webb, N., & Olive, J.-F. 2021, *Long-term X-ray spectral evolution of ultraluminous X-ray sources: implications on the accretion flow geometry and the nature of the accretor*, Astronomy & Astrophysics, 649, A104

Haberl, F. 2007, *The magnificent seven: magnetic fields and surface temperature distributions*, Ap&SS, 308, 181

Haensel, P., Zdunik, J. L., Bejger, M., & Lattimer, J. M. 2009, *Keplerian frequency of uniformly rotating neutron stars and strange stars*, Astronomy & Astrophysics, 502, 605

Halpern, J. P., Bogdanov, S., & Gotthelf, E. V. 2013, *X-ray Measurement of the Spin-Down of Calvera: a Radio- and Gamma-ray-Quiet Pulsar*, The Astrophysical Journal, 778, 120

Hambly, N., Steele, I., Hawkins, M., & Jameson, R. 1995, *Very low mass stars in the galactic cluster Praesepe*, Astronomy and Astrophysics Supplement Series, 109, 29

Hankins, T. H., Eilek, J. A., & Jones, G. 2016, *The Crab Pulsar at Centimeter Wavelengths. II. Single Pulses*, The Astrophysical Journal, 833, 47

Hanna, C., Megevand, M., Ochsner, E., & Palenzuela, C. 2009, *Method to estimate ISCO and ring-down frequencies in binary systems and consequences for gravitational wave data analysis*, Classical and Quantum Gravity, 26, 015009

Hansen, B. M. & Liebert, J. 2003, *Cool White Dwarfs*, Annual Review of Astronomy and Astrophysics, 41, 465

Hansen, B. M. S. & Lyutikov, M. 2001, *Radio and X-ray signatures of merging neutron stars*, Monthly Notices of the Royal Astronomical Society, 322, 695

Harding, A. K. 2017, *Pulsar Emission Physics: The First Fifty Years*, Proceedings of the International Astronomical Union, 13, 52

Hardy, L. K., Dhillon, V. S., Spitler, L. G., et al. 2017, *A search for optical bursts from the repeating fast radio burst FRB 121102*, Monthly Notices of the Royal Astronomical Society, 472, 2800

Haynes, M. P., Giovanelli, R., Martin, A. M., et al. 2011, *The Arecibo Legacy FAST ALFA Survey: The α.40 H I source catalog, its chracteristics and their impact on the derivation of the H I mass function*, The Astronomical Journal, 142, 170

Heintz, K. E., Prochaska, J. X., Simha, S., et al. 2020, *Host Galaxy Properties and Offset Distributions of Fast Radio Bursts: Implications for Their Progenitors*, The Astrophysical Journal, 903, 152

Helsel, D. R. 2004, Nondetects and Data Analysis: Statistics for Censored Environmental Data, 1st edn. (Hoboken, N.J: Wiley-Interscience)

Hernandez-Garcia, L., Masegosa, J., Gonzalez-Martin, O., et al. 2017, *The X-ray variability of Seyfert 1.8/1.9 galaxies*, Astronomy & Astrophysics, 602, A65

Hessels, J. W. T., Ransom, S. M., Stairs, I. H., et al. 2006, *A Radio Pulsar Spinning at 716 Hz*, Science, 311, 1901

Hessels, J. W. T., Spitler, L. G., Seymour, A. D., et al. 2019, *FRB 121102 Bursts Show Complex Time-Frequency Structure*, The Astrophysical Journal Letters, 876

Hessels, J. W. T., Stappers, B. W., Rutledge, R. E., Fox, D. B., & Shevchuk, A. H. 2007, *A Strong Upper Limit on the Pulsed Radio Luminosity of the Compact Object 1RXS J141256.0+792204*, Astronomy & Astrophysics, 476, 331

Hewish, A., Bell, S. J., Pilkington, J. D. H., Scott, P. F., & Collins, R. A. 1968, *Observation of a Rapidly Pulsating Radio Source*, Nature, 217, 709

Hewitt, D. M., Snelders, M. P., Hessels, J. W. T., et al. 2021, *Arecibo observations of a burst storm from FRB 20121102A in 2016*, arXiv:2111.11282 [astro-ph], arXiv: 2111.11282

Hilmarsson, G. H., Michilli, D., Spitler, L. G., et al. 2021, *Rotation Measure Evolution of the Repeating Fast Radio Burst Source FRB 121102*, The Astrophysical Journal, 908, L10

Hirata, K., Kajita, T., Koshiba, M., et al. 1987, *Observation of a neutrino burst from the supernova SN1987A*, Physical Review Letters, 58, 1490

Hotan, A. W., van Straten, W., & Manchester, R. N. 2004, *Psrchive and Psrfits : An Open Approach to Radio Pulsar Data Storage and Analysis*, Publications of the Astronomical Society of Australia, 21, 302

Houben, L. J. M., Spitler, L. G., ter Veen, S., et al. 2019, *Constraints on the low frequency spectrum of FRB 121102*, Astronomy & Astrophysics, 623, A42

Huijse, P., Estévez, P. A., Förster, F., et al. 2018, *Robust Period Estimation Using Mutual Information for Multiband Light Curves in the Synoptic Survey Era*, The Astrophysical Journal Supplement Series, 236, 12

Hurley, K., Li, P., Kouveliotou, C., et al. 1999, *ASCA discovery of an x-ray pulsar in the error box of SGR 1900+14*, The Astrophysical Journal, 510, 111

Hurley-Walker, N., Zhang, X., Bahramian, A., et al. 2022, *A radio transient with unusually slow periodic emission*, Nature, 601, 526

Imanishi, K., Nakajima, H., Tsujimoto, M., Koyama, K., & Tsuboi, Y. 2003, *A Systematic Study of X-Ray Flares from Low-Mass Young Stellar Objects in the ρ Ophiuchi Star-Forming Region with Chandra*, Publications of the Astronomical Society of Japan, 55, 653

in 't Zand, J. J. M., Kries, M. J. W., Palmer, D. M., & Degenaar, N. 2019, *Searching for the most powerful thermonuclear X-ray bursts with the Neil Gehrels Swift Observatory*, Astronomy & Astrophysics, 621, A53

Inoue, S. 2004, *Probing the cosmic reionization history and local environment of gamma-ray bursts through radio dispersion*, Monthly Notices of the Royal Astronomical Society, 348, 999

Ioka, K. 2003, *The Cosmic Dispersion Measure from Gamma-Ray Burst Afterglows: Probing the Reionization History and the Burst Environment*, The Astrophysical Journal, 598, L79

Ioka, K. & Zhang, B. 2020, *A Binary Comb Model for Periodic Fast Radio Bursts*, The Astrophysical Journal, 893, L26

James, C. W., Ekers, R. D., Macquart, J.-P., Bannister, K. W., & Shannon, R. M. 2019, *The slope of the source-count distribution for fast radio bursts*, Monthly Notices of the Royal Astronomical Society, 483, 1342

Janagal, P., Chakraborty, M., Bhat, N. D. R., Bhattacharya, B., & McSweeney, S. J. 2021, *Revisiting the subpulse drifting phenomenon in PSR J1822-2256: Drift Modes, Sparks, and Emission Heights*, Monthly Notices of the Royal Astronomical Society, 509, 4573

Jansen, F., Lumb, D., Altieri, B., et al. 2001, *XMM-Newton observatory. I. The spacecraft and operations*, Astronomy and Astrophysics, 365, L1

Johnston, S. & Romani, R. W. 2004, *Giant Pulses - A Brief Review*, Young Neutron Stars and Their Environments, IAU Symposium, 218, 315

Johnston, S., van Straten, W., Kramer, M., & Bailes, M. 2001, *High Time Resolution Observations of the Vela Pulsar*, The Astrophysical Journal, 549, L101

Jones, D. O., Rodney, S. A., Riess, A. G., et al. 2013, *The Discovery of the Most Distant Known Type Ia Supernova at Redshift 1.914*, The Astrophysical Journal, 768, 166

Josephy, A., Chawla, P., Fonseca, E., et al. 2019, *CHIME/FRB Detection of the Original Repeating Fast Radio Burst Source FRB 121102*, The Astrophysical Journal, 882, L18

Karastergiou, A., Chennamangalam, J., Armour, W., et al. 2015, *Limits on Fast Radio Bursts at 145 MHz with ARTEMIS, a real-time software backend*, Monthly Notices of the Royal Astronomical Society, 452, 1254

Karpova, A., Shternin, P., Zyuzin, D., Danilenko, A., & Shibanov, Y. 2017, *Observations of the Gamma-ray pulsar J1932+1916 in X-rays*, Monthly Notices of the Royal Astronomical Society, 466, 1757

Kasen, D. & Bildsten, L. 2010, *Supernova Light Curves Powered by Young Magnetars*, The Astrophysical Journal, 717, 245

Kashiyama, K., Ioka, K., & Mészáros, P. 2013, *Cosmological Fast Radio Bursts from Binary White Dwarf Mergers*, The Astrophysical Journal, 776, L39

Kashiyama, K. & Murase, K. 2017, *Testing the Young Neutron Star Scenario with Persistent Radio Emission Associated with FRB 121102*, The Astrophysical Journal, 839, L3

Kaspi, V. M. & Beloborodov, A. M. 2017, *Magnetars*, Annual Review of Astronomy and Astrophysics, 55, 261

Kaspi, V. M. & Kramer, M. 2016, *Radio Pulsars: The Neutron Star Population & Fundamental Physics*, number: arXiv:1602.07738 arXiv:1602.07738 [astro-ph]

Katz, J. 2014, *Coherent emission in fast radio bursts*, Physical Review D, 89, 103009, publisher: American Physical Society

Katz, J. I. 2016, *How soft gamma repeaters might make fast radio bursts*, The Astrophysical Journal, 826, 226, publisher: American Astronomical Society

Keane, E. F., Johnston, S., Bhandari, S., et al. 2016, *A Fast Radio Burst Host Galaxy*, Nature, 530, 453

Keane, E. F., Kramer, M., Lyne, A. G., Stappers, B. W., & McLaughlin, M. A. 2011, *Rotating Radio Transients: new discoveries, timing solutions and musings*, MNRAS, 415, 3065

Keane, E. F. & McLaughlin, M. A. 2011, *Rotating radio transients*, Bulletin of the Astronomical Society of India, 39, 333, aDS Bibcode: 2011BASI...39..333K

Keane, E. F. & Petroff, E. 2015, *Fast radio bursts: search sensitivities and completeness*, Monthly Notices of the Royal Astronomical Society, 447, 2852

Keane, E. F., Stappers, B. W., Kramer, M., & Lyne, A. G. 2012, *On the origin of a highly dispersed coherent radio burst: A highly dispersed coherent radio burst*, Monthly Notices of the Royal Astronomical Society: Letters, 425, L71

Kijak, J. & Gil, J. 1997, *Radio emission altitudes in pulsar magnetospheres*, Monthly Notices of the Royal Astronomical Society, 288, 631

Kilic, M., Allende Prieto, C., Brown, W. R., & Koester, D. 2007, *The Lowest Mass White Dwarf*, The Astrophysical Journal, 660, 1451

Kirkpatrick, J. D., Kellogg, K., Schneider, A. C., et al. 2016, *The AllWISE Motion Survey, Part 2*, The Astrophysical Journal Supplement Series, 224, 36

Kirsten, F., Marcote, B., Nimmo, K., et al. 2022, *A repeating fast radio burst source in a globular cluster*, Nature, 602, 585

Knight, H. S. 2006, *Observational Characteristics of Giant Pulses and Related Phenomena*, Chinese Journal of Astronomy and Astrophysics, 6, 41, publisher: IOP Publishing

Kocz, J., Ravi, V., Catha, M., et al. 2019, *DSA-10: a prototype array for localizing fast radio bursts*, Monthly Notices of the Royal Astronomical Society, 489, 919

Komesaroff, M. M. 1970, *Possible Mechanism for the Pulsar Radio Emission*, Nature, 225, 612

Kondratiev, V. I., McLaughlin, M. A., Lorimer, D. R., et al. 2009, *New Limits on Radio Emission from X-ray Dim Isolated Neutron Stars*, The Astrophysical Journal, 702, 692

Kondratiev, V. I., Verbiest, J. P. W., Hessels, J. W. T., et al. 2016, *A LOFAR census of millisecond pulsars*, Astronomy & Astrophysics, 585, A128

Kouveliotou, C., Fishman, G. J., Meegan, C. A., et al. 1993, *Recurrent burst activity from the soft γ-ray repeater SGR 1900+14*, Nature, 362, 728

Kouveliotou, C., Strohmayer, T., Hurley, K., et al. 1999, *Discovery of a Magnetar Associated with the Soft Gamma Repeater SGR 1900+14*, The Astrophysical Journal, 510, 115

Kramer, M., Johnston, S., & Van Straten, W. 2002, *High-resolution single-pulse studies of the Vela pulsar*, Monthly Notices of the Royal Astronomical Society, 334, 523

Kramer, M., Menten, K., Barr, E. D., et al. 2018, *The MeerKAT Max-Planck S-band System*, in Proceedings of MeerKAT Science: On the Pathway to the SKA — PoS(MeerKAT2016), Vol. 277 (SISSA Medialab), 003

Kravtsov, A. V. 2013, *The Size-Virial Radius Relation of Galaxies*, The Astrophysical Journal, 764, L31

Krishnakumar, M. A., Joshi, B. C., & Manoharan, P. K. 2017, *Multi-frequency Scatter Broadening Evolution of Pulsars. I*, The Astrophysical Journal, 846, 104

Kumar, P. & Bosnjak, Z. 2020, *FRB Coherent Emission from Decay of Alfven Waves*, Monthly Notices of the Royal Astronomical Society, 494, 2385

Kumar, P., Lu, W., & Bhattacharya, M. 2017, *Fast radio burst source properties and curvature radiation model*, Monthly Notices of the Royal Astronomical Society, 468, 2726

Kumar, P., Shannon, R. M., Flynn, C., et al. 2020, *Extremely band-limited repetition from a fast radio burst source*, Monthly Notices of the Royal Astronomical Society, 500, 2525

Kumar, P., Shannon, R. M., Lower, M. E., et al. 2022, *Circularly polarized radio emission from the repeating fast radio burst source FRB 20201124A*, Monthly Notices of the Royal Astronomical Society, 512, 3400

Kumar, P., Shannon, R. M., Osłowski, S., et al. 2019, *Faint Repetitions from a Bright Fast Radio Burst Source*, The Astrophysical Journal, 887, L30

Kuulkers, E., Norton, A., Schwope, A., & Warner, B. 2006, X-rays from cataclysmic variables, Vol. 39, pages: 421-460. Publication Title: Compact stellar X-ray sources

Laha, S., Younes, G., Wadiasingh, Z., et al. 2022, *Simultaneous View of FRB 180301 with FAST and NICER during a Bursting Phase*, The Astrophysical Journal, 930, 172

Lan, G.-X., Wei, J.-J., Zeng, H.-D., Li, Y., & Wu, X.-F. 2021, *Revisiting the luminosity and redshift distributions of long gamma-ray bursts*, Monthly Notices of the Royal Astronomical Society, 508, 52

Lanman, A. E., Andersen, B. C., Chawla, P., et al. 2022, *A Sudden Period of High Activity from Repeating Fast Radio Burst 20201124A*, The Astrophysical Journal, 927, 59

Lasker, B. M., Lattanzi, M. G., McLean, B. J., et al. 2008, *The Second-Generation Guide Star Catalog: Description and Properties*, The Astronomical Journal, 136, 735

Lattimer, J. M. 2012, *The Nuclear Equation of State and Neutron Star Masses*, Annual Review of Nuclear and Particle Science, 62, 485

Law, C. J., Abruzzo, M. W., Bassa, C. G., et al. 2017, *A Multi-telescope Campaign on FRB 121102: Implications for the FRB Population*, The Astrophysical Journal, 850, 76

Lawrence, E., Wiel, S. V., Law, C. J., Spolaor, S. B., & Bower, G. C. 2017, *The Non-homogeneous Poisson Process for Fast Radio Burst Rates*, The Astronomical Journal, 154, 117

Lazarus, P., Kaspi, V. M., Champion, D. J., Hessels, J. W. T., & Dib, R. 2012, *CONSTRAINING RADIO EMISSION FROM MAGNETARS*, The Astrophysical Journal, 744, 97

Leahy, D. A., Darbro, W., Elsner, R. F., et al. 1983, *On searches for pulsed emission with application to four globular cluster X-ray sources - NGC 1851, 6441, 6624, and 6712*, The Astrophysical Journal, 266, 160

Levin, L., Lyne, A. G., Desvignes, G., et al. 2019, *Spin frequency evolution and pulse profile variations of the recently re-activated radio magnetar XTE J1810-197*, Monthly Notices of the Royal Astronomical Society, 488, 5251

Levin, Y., Beloborodov, A. M., & Bransgrove, A. 2020, *Precessing flaring magnetar as a source of repeating FRB 180916.J0158+65*, The Astrophysical Journal Letters, 895, L30

Lewandowski, W., Kowalińska, M., & Kijak, J. 2015, *The analysis of the largest sample of multifrequency pulsar scatter time estimates*, Monthly Notices of the Royal Astronomical Society, 449, 1570

Li, D., Wang, P., Zhu, W. W., et al. 2021, *A bimodal burst energy distribution of a repeating fast radio burst source*, Nature, 598, 267, number: 7880 Publisher: Nature Publishing Group

Li, L., Li, Q.-C., Zhong, S.-Q., et al. 2022, *AT2020hur: A Possible Optical Counterpart of FRB 180916B*, The Astrophysical Journal, 929, 139

Li, L.-B., Huang, Y.-F., Geng, J.-J., & Li, B. 2018, *A model of fast radio bursts: collisions between episodic magnetic blobs*, Research in Astronomy and Astrophysics, 18, 061

LIGO Scientific Collaboration and Virgo Collaboration, Abbott, B., Abbott, R., et al. 2016, *Observation of Gravitational Waves from a Binary Black Hole Merger*, Physical Review Letters, 116, 061102

Lin, D., Webb, N. A., & Barret, D. 2012, *Classification of X-ray Sources in the XMM-Newton Serendipitous Source Catalog*, The Astrophysical Journal, 756, 27

Lingam, M. & Loeb, A. 2017, *Fast Radio Bursts from Extragalactic Light Sails*, The Astrophysical Journal, 837, L23

Liu, X. 2018, *A model of neutron-star–white-dwarf collision for fast radio bursts*, Astrophysics and Space Science, 363, 242

Lo, K. K., Farrell, S., Murphy, T., & Gaensler, B. M. 2014, *Automatic classification of time-variable X-ray sources*, The Astrophysical Journal, 786, 20

Long, K. & Pe'er, A. 2018, *Synchrotron Maser from Weakly Magnetized Neutron Stars as the Emission Mechanism of Fast Radio Bursts*, The Astrophysical Journal, 864, L12

Lorimer, D. & Kramer, M. 2004, Handbook of Pulsar Astronomy.pdf, Cambridge Observing Handbooks for Research Astronomers No. 4

Lorimer, D. R. 2008, *Binary and Millisecond Pulsars*, Living Reviews in Relativity, 11, 8

Lorimer, D. R., Bailes, M., McLaughlin, M. A., Narkevic, D. J., & Crawford, F. 2007, *A bright millisecond radio burst of extragalactic origin*, Science, 318, 777

Lorimer, D. R. & Xilouris, K. M. 2000, *PSR J1907+0918: A Young Radio Pulsar near SGR 1900+14 and G42.8+0.6*, The Astrophysical Journal, 545, 385

Lu, W. & Kumar, P. 2018, *On the radiation mechanism of repeating fast radio bursts*, Monthly Notices of the Royal Astronomical Society, 477, 2470

Luo, R., Wang, B. J., Men, Y. P., et al. 2020, *Diverse polarization angle swings from a repeating fast radio burst source*, Nature, 586, 693

Lyne, A. & Graham-Smith, F. 2012, Pulsar Astronomy, publication Title: Pulsar Astronomy ADS Bibcode: 2012puas.book.....L

Lyubarsky, Y. 2014, *A model for fast extragalactic radio bursts*, Monthly Notices of the Royal Astronomical Society: Letters, 442, L9
Lyubarsky, Y. 2020, *Fast Radio Bursts from Reconnection in a Magnetar Magnetosphere*, The Astrophysical Journal, 897, 1
Lyutikov, M. 2002, *Radio Emission from Magnetars*, The Astrophysical Journal, 580, L65
Lyutikov, M. 2013, *The electromagnetic model of short GRBs, the nature of prompt tails, supernova-less long GRBs and highly efficient episodic accretion*, The Astrophysical Journal, 768, 63
Lyutikov, M. 2020, *Radius-to-frequency Mapping and FRB Frequency Drifts*, The Astrophysical Journal, 889, 135
Lyutikov, M., Barkov, M., & Giannios, D. 2020, *FRB-periodicity: mild pulsar in tight O/B-star binary*, The Astrophysical Journal Letters, 893, L39
Lyutikov, M., Burzawa, L., & Popov, S. B. 2016, *Fast radio bursts as giant pulses from young rapidly rotating pulsars*, Monthly Notices of the Royal Astronomical Society, 462, 941
Löhmer, O., Kramer, M., Mitra, D., Lorimer, D. R., & Lyne, A. G. 2002, *Anomalous Scattering of Highly Dispersed Pulsars*, The Astrophysical Journal, 562, L157
Maan, Y. 2015, *Discovery of Low DM Fast Radio Transients: Geminga Pulsar Caught in the Act*, ApJ, 815, 126
Maan, Y. 2019, *Expected Imprints of the Carousel in Multi-frequency Pulsar Observations and New Evidence for Multi-altitude Emission*, The Astrophysical Journal, 870, 110
Maan, Y. & Aswathappa, H. A. 2014, *Deep searches for decametre-wavelength pulsed emission from radio-quiet gamma-ray pulsars*, Monthly Notices of the Royal Astronomical Society, 445, 3221
Maan, Y., Joshi, B. C., Surnis, M. P., Bagchi, M., & Manoharan, P. K. 2019, *Distinct Properties of the Radio Burst Emission from the Magnetar XTE J1810–197*, The Astrophysical Journal, 882, L9
Maan, Y., Surnis, M. P., Chandra Joshi, B., & Bagchi, M. 2022, *Magnetar XTE J1810-197: Spectro-temporal Evolution of Average Radio Emission*, ApJ, 931, 67
Maan, Y. & van Leeuwen, J. 2017, *Real-time searches for fast transients with Apertif and LOFAR*, arXiv:1709.06104 [astro-ph], arXiv: 1709.06104
Maan, Y., van Leeuwen, J., & Vohl, D. 2020, *Fourier domain excision of periodic radio frequency interference*, arXiv e-prints, arXiv:2012.11630
Macquart, J.-P., Prochaska, J. X., McQuinn, M., et al. 2020, *A census of baryons in the Universe from localized fast radio bursts*, Nature, 581, 391
Madau, P. & Dickinson, M. 2014, *Cosmic Star-Formation History*, Annual Review of Astronomy and Astrophysics, 52, 415
MAGIC Collaboration, Acciari, V. A., Ansoldi, S., et al. 2018, *Constraining very-high-energy and optical emission from FRB 121102 with the MAGIC telescopes*, Monthly Notices of the Royal Astronomical Society, 481, 2479
Majid, W. A., Pearlman, A. B., Prince, T. A., et al. 2021, *A Bright Fast Radio Burst from FRB 20200120E with Sub-100 Nanosecond Structure*, The Astrophysical Journal Letters, 919, L6
Malofeev, V. M. & Malov, O. I. 1997, *Detection of Geminga as a radio pulsar*, Nature, 389, 697
Malov, O. I., Malofeev, V. M., Teplykh, D. A., & Logvinenko, S. V. 2015, *The Geminga radio pulsar. New low-frequency results*, Astronomy Reports, 59, 183
Manchester, R. N., Hobbs, G. B., Teoh, A., & Hobbs, M. 2005, *The ATNF Pulsar Catalogue*, The Astronomical Journal, 129, 1993, arXiv: astro-ph/0412641
Mannings, A. G., Fong, W.-f., Simha, S., et al. 2021, *A High-resolution View of Fast Radio Burst Host Environments*, The Astrophysical Journal, 917, 75
Marcote, B., Nimmo, K., Hessels, J. W. T., et al. 2020, *A repeating fast radio burst source localised to a nearby spiral galaxy*, Nature, 577, 190
Marcote, B., Paragi, Z., Hessels, J. W. T., et al. 2017, *The Repeating Fast Radio Burst FRB 121102 as Seen on Milliarcsecond Angular Scales*, The Astrophysical Journal, 834, L8
Margalit, B., Metzger, B. D., Berger, E., et al. 2018, *Unveiling the engines of fast radio bursts, superluminous supernovae, and gamma-ray bursts*, Monthly Notices of the Royal Astronomical Society, 481, 2407

Marthi, V. R., Gautam, T., Li, D., et al. 2020, *Detection of 15 bursts from FRB 180916.J0158+65 with the uGMRT*, Monthly Notices of the Royal Astronomical Society: Letters, 499, L16

Martone, R., Guidorzi, C., Margutti, R., et al. 2019, *A cumulative search for hard X/γ-ray emission associated with fast radio bursts in Fermi/GBM data*, Astronomy & Astrophysics, 631, A62, publisher: EDP Sciences

Mason, K. 1985, *X-ray emission from cataclysmic variables*, Space Science Reviews, 40, 99

Masui, K., Lin, H.-H., Sievers, J., et al. 2015, *Dense magnetized plasma associated with a fast radio burst*, Nature, 528, 523

Mazets, E. P., Golenetskii, S. V., & Guryan, Y. A. 1979, *Soft gamma-ray bursts from the source B1900+14*, Soviet Astronomy Letters, 5, 343

Mazur, P. O. 2000, *Black Hole Uniqueness Theorems*

Mazzali, P. A., Röpke, F. K., Benetti, S., & Hillebrandt, W. 2007, *A Common Explosion Mechanism for Type Ia Supernovae*, Science, 315, 825

McClintock, T., Rozo, E., Becker, M. R., et al. 2019, *The Aemulus Project. II. Emulating the Halo Mass Function*, The Astrophysical Journal, 872, 53, publisher: American Astronomical Society

Mckinven, R., Gaensler, B. M., Michilli, D., et al. 2022, *A Large Scale Magneto-ionic Fluctuation in the Local Environment of Periodic Fast Radio Burst Source, FRB 20180916B*

Mckinven, R., Michilli, D., Masui, K., et al. 2021, *Polarization Pipeline for Fast Radio Bursts Detected by CHIME/FRB*, The Astrophysical Journal, 920, 138

McLaughlin, M. A., Lyne, A. G., Lorimer, D. R., et al. 2006, *Transient radio bursts from rotating neutron stars*, Nature, 439, 817

McQuinn, M. 2013, *Locating the "missing" baryons with extragalactic dispersion measure estimates*, The Astrophysical Journal, 780, L33

McWilliams, S. T. & Levin, J. 2011, *Electromagnetic extraction of energy from black hole-neutron star binaries*, The Astrophysical Journal, 742, 90

Melikidze, G. I., Gil, J. A., & Pataraya, A. D. 2000, *The Spark-associated Soliton Model for Pulsar Radio Emission*, The Astrophysical Journal, 544, 1081

Melrose, D. B. 1978, *Amplified linear acceleration emission applied to pulsars*, The Astrophysical Journal, 225, 557

Melrose, D. B. 2017, *Coherent emission mechanisms in astrophysical plasmas*, Reviews of Modern Plasma Physics, 1, 5

Mereghetti, S. 2011, *X-ray emission from isolated neutron stars*, Conference High-Energy Emission from Pulsars and their Systems, 21, 345

Mereghetti, S., Esposito, P., Tiengo, A., et al. 2006, *The First XMM-Newton Observations of the Soft Gamma-Ray Repeater SGR 1900+14*, The Astrophysical Journal, 653, 1423

Mereghetti, S., Rigoselli, M., Taverna, R., et al. 2021, *NICER Study of Pulsed Thermal X-Rays from Calvera: A Neutron Star Born in the Galactic Halo?*, ApJ, 922, 253

Mereghetti, S., Savchenko, V., Ferrigno, C., et al. 2020a, *INTEGRAL discovery of a burst with associated radio emission from the magnetar SGR 1935+2154*, The Astrophysical Journal, 898, L29

Mereghetti, S., Savchenko, V., Gotz, D., et al. 2020b, *ATel #13685: INTEGRAL IBIS and SPI-ACS detection of a hard X-ray counterpart of the radio burst from SGR 1935+2154*, The Astronomer's Telegram, 13685, 1

Merryfield, M., Tendulkar, S. P., Shin, K., et al. 2022, *An Injection System for the CHIME/FRB Experiment*

Metzger, B. D., Berger, E., & Margalit, B. 2017, *Millisecond Magnetar Birth Connects FRB 121102 to Superluminous Supernovae and Long-duration Gamma-Ray Bursts*, The Astrophysical Journal, 841, 14

Metzger, B. D., Margalit, B., & Sironi, L. 2019, *Fast radio bursts as synchrotron maser emission from decelerating relativistic blast waves*, Monthly Notices of the Royal Astronomical Society, 485, 4091

Michilli, D., Bassa, C., Cooper, S., et al. 2020, *The LOFAR tied-array all-sky survey (LOTAAS): Characterization of 20 pulsar discoveries and their single-pulse behaviour*, Monthly Notices of the Royal Astronomical Society, 491, 725

Michilli, D., Masui, K. W., Mckinven, R., et al. 2021, *An Analysis Pipeline for CHIME/FRB Full-array Baseband Data*, The Astrophysical Journal, 910, 147, publisher: American Astronomical Society

Michilli, D., Seymour, A., Hessels, J. W. T., et al. 2018, *An extreme magneto-ionic environment associated with the fast radio burst source FRB 121102*, Nature, 553, 182
Mikhailov, K. V. 2018, *The radio lighthouse from afar: In search of distant pulsars*, PhD thesis, University of Amsterdam, https://dare.uva.nl/search?identifier=d3a5406f-eb36-4bb8-a280-54a3edd0a52
Mingarelli, C. M. F., Levin, J., & Lazio, T. J. W. 2015, *Fast Radio Bursts and Radio Transients from Black Hole Batteries*, The Astrophysical Journal, 814, L20
Miniutti, G., Saxton, R. D., Giustini, M., et al. 2019, *Nine-hour X-ray quasi-periodic eruptions from a low-mass black hole galactic nucleus*, Nature
Mitra, D., Arjunwadkar, M., & Rankin, J. M. 2015, *Polarized quasiperiodic structures in pulsar radio emission reflect temporal modultaions of non-stationary plasma flow*, The Astrophysical Journal, 806, 236
Mitra, D. & Rankin, J. M. 2008, *On the subpulse modulation, polarization and sub-beam carousel configuration of pulsar B185726*, Monthly Notices of the Royal Astronomical Society, 385, 606
Mitra, D., Rankin, J. M., & Gupta, Y. 2007, *Absolute broad-band polarization behaviour of PSR B0329+54: a glimpse of the core emission process*, Monthly Notices of the Royal Astronomical Society, 379, 932
Morello, V., Keane, E. F., Enoto, T., et al. 2020, *The SUrvey for Pulsars and Extragalactic Radio Bursts - IV. Discovery and polarimetry of a 12.1-s radio pulsar*, MNRAS, 493, 1165
Mortlock, D. J., Warren, S. J., Venemans, B. P., et al. 2011, *A luminous quasar at a redshift of z = 7.085*, Nature, 474, 616
Mottez, F., Zarka, P., & Voisin, G. 2020, *Repeating fast radio bursts caused by small bodies orbiting a pulsar or a magnetar*, Astronomy & Astrophysics, 644, A145
Narayan, R. 1992, *The Physics of Pulsar Scintillation*, Philosophical Transactions: Physical Sciences and Engineering, 341, 151
Navarrini, A., Monari, J., Scalambra, A., et al. 2018, *Design of PHAROS2 Phased Array Feed*, in 2018 2nd URSI Atlantic Radio Science Meeting (AT-RASC), 1–4
Niino, Y., Doi, M., Sako, S., et al. 2022, *Deep Simultaneous Limits on Optical Emission from FRB 20190520B by 24.4 fps Observations with Tomo-e Gozen*, The Astrophysical Journal, 931, 109
Nimmo, K., Hessels, J. W. T., Keimpema, A., et al. 2021, *Highly polarized microstructure from the repeating FRB 20180916B*, Nature Astronomy, 5, 594
Nimmo, K., Hessels, J. W. T., Kirsten, F., et al. 2022a, *Burst timescales and luminosities as links between young pulsars and fast radio bursts*, Nature Astronomy, 6, 393, number: 3 Publisher: Nature Publishing Group
Nimmo, K., Hewitt, D. M., Hessels, J. W. T., et al. 2022b, *Milliarcsecond Localization of the Repeating FRB 20201124A*, The Astrophysical Journal Letters, 927, L3
Niu, C.-H., Aggarwal, K., Li, D., et al. 2022, *A repeating fast radio burst associated with a persistent radio source*, Nature, 606, 873, number: 7916 Publisher: Nature Publishing Group
Niu, C.-H., Li, D., Luo, R., et al. 2021, *CRAFTS for Fast Radio Bursts: Extending the Dispersion–Fluence Relation with New FRBs Detected by FAST*, The Astrophysical Journal Letters, 909, L8
Novara, G., Esposito, P., Tiengo, A., et al. 2020, *A Supernova Candidate at z = 0.092 in XMM–Newton Archival Data*, The Astrophysical Journal, 898, 37
Oakes, D. 1982, *A Concordance Test for Independence in the Presence of Censoring*, Biometrics, 38, 451
Ocker, S. K., Cordes, J. M., & Chatterjee, S. 2021, *Constraining Galaxy Halos from the Dispersion and Scattering of Fast Radio Bursts and Pulsars*, The Astrophysical Journal, 911, 102
Ocker, S. K., Cordes, J. M., Chatterjee, S., & Gorsuch, M. R. 2022a, *Radio Scattering Horizons for Galactic and Extragalactic Transients*, arXiv:2203.16716 [astro-ph]
Ocker, S. K., Cordes, J. M., Chatterjee, S., et al. 2022b, *The Large Dispersion and Scattering of FRB 20190520B Are Dominated by the Host Galaxy*, The Astrophysical Journal, 931, 87
Oosterloo, T., Verheijen, M., & van Cappellen, W. 2010, *The latest on Apertif*, Proceedings of Science, ISKAF2010 Science Meeting
Oostrum, L. C. 2020, *DARC: Data Analysis of Real-time Candidates*, https://doi.org/10.5281/zenodo.3784870

Oostrum, L. C. 2020, *Fast Radio Bursts with Apertif*, PhD thesis, University of Amsterdam, https://dare.uva.nl/search?identifier=abe5c8fa-1fdf-490b-ac0d-61e946f5791f

Oostrum, L. C., Maan, Y., van Leeuwen, J., et al. 2020, *Repeating fast radio bursts with WSRT/Apertif*, Astronomy & Astrophysics, 635, A61

Oostrum, L. C., van Leeuwen, J., Maan, Y., Coenen, T., & Ishwara-Chandra, C. H. 2020, *A search for pulsars in subdwarf B binary systems and discovery of giant-pulse emitting PSR J0533-4524*, MNRAS, 492, 4825

Oppenheimer, J. R. & Volkoff, G. M. 1939, *On Massive Neutron Cores*, Physical Review, 55, 374, publisher: American Physical Society

Oppermann, N., Yu, H.-R., & Pen, U.-L. 2018, *On the non-Poissonian repetition pattern of FRB121102*, Monthly Notices of the Royal Astronomical Society, 475, 5109

Ordog, A., Booth, R. A., Van Eck, C. L., Brown, J.-A. C., & Landecker, T. L. 2019, *Faraday Rotation of Extended Emission as a Probe of the Large-Scale Galactic Magnetic Field*, Galaxies, 7, 43, arXiv: 1903.11227

Osłowski, S., Shannon, R. M., Ravi, V., et al. 2019, *Commensal discovery of four fast radio bursts during Parkes Pulsar Timing Array observations*, Monthly Notices of the Royal Astronomical Society, 488, 868

Panessa, F., Savchenko, V., Ferrigno, C., Bazzano, A., & Ubertini, P. 2020, *INTEGRAL gamma-ray upper limits on the periodic FRB180916*

Parikh, A., José, J., Sala, G., & Iliadis, C. 2013, *Nucleosynthesis in Type I X-ray Bursts*, Progress in Particle and Nuclear Physics, 69, 225

Pastor-Marazuela, I. 2018, *Searching for fast transients in XMM-Newton data*, Master's thesis, Université de Toulouse, France, https://www.uva.nl/binaries/content/documents/personalpages/p/a/i.pastormarazuela/en/downloads/downloads/assets/asset

Pastor-Marazuela, I., Connor, L., van Leeuwen, J., et al. 2021, *Chromatic periodic activity down to 120 megahertz in a fast radio burst*, Nature, 596, 505

Pastor-Marazuela, I., van Leeuwen, J., Bilous, A., et al. 2022, *A fast radio burst with sub-millisecond quasi-periodic structure*, arXiv:2202.08002 [astro-ph]

Pearlman, A. B., Majid, W. A., Prince, T. A., et al. 2020, *Multiwavelength Radio Observations of Two Repeating Fast Radio Burst Sources: FRB 121102 and FRB 180916.J0158+65*, The Astrophysical Journal Letters, 905, L27

Perley, R. A. & Butler, B. J. 2017, *An Accurate Flux Density Scale from 50 MHz to 50 GHz*, The Astrophysical Journal Supplement Series, 230, 7

Petroff, E., Bailes, M., Barr, E. D., et al. 2015a, *A real-time fast radio burst: polarization detection and multiwavelength follow-up*, Monthly Notices of the Royal Astronomical Society, 447, 246

Petroff, E., Burke-Spolaor, S., Keane, E. F., et al. 2017, *A polarized fast radio burst at low Galactic latitude*, Monthly Notices of the Royal Astronomical Society

Petroff, E., Hessels, J. W. T., & Lorimer, D. R. 2019, *Fast radio bursts*, The Astronomy and Astrophysics Review, 27, 4

Petroff, E., Hessels, J. W. T., & Lorimer, D. R. 2022, *Fast radio bursts at the dawn of the 2020s*, The Astronomy and Astrophysics Review, 30, 2

Petroff, E., Keane, E. F., Barr, E. D., et al. 2015b, *Identifying the source of perytons at the Parkes radio telescope*, Monthly Notices of the Royal Astronomical Society, 451, 3933

Petroff, E., Oostrum, L. C., Stappers, B. W., et al. 2018, *A fast radio burst with a low dispersion measure*, Monthly Notices of the Royal Astronomical Society

Pierbattista, M., Harding, A. K., Grenier, I. A., et al. 2015, *Light-curve modelling constraints on the obliquities and aspect angles of the young Fermi pulsars*, Astronomy & Astrophysics, 575, A3

Pietsch, W. & Haberl, F. 2005, *XMM-Newton detection of type I X-ray bursts in M 31*, Astronomy & Astrophysics, 430, L45

Pilia, M., Burgay, M., Possenti, A., et al. 2020, *The lowest frequency Fast Radio Bursts: Sardinia Radio Telescope detection of the periodic FRB 180916 at 328 MHz*, The Astrophysical Journal Letters, 896, L40

Pineau, F.-X., Motch, C., Carrera, F., et al. 2011, *Cross-correlation of the 2XMMi catalogue with Data Release 7 of the Sloan Digital Sky Survey*, Astronomy & Astrophysics, 527, A126

Pingel, N. M., Pisano, D. J., Ruzindana, M., et al. 2021, *Commissioning the H i Observing Mode of the Beam Former for the Cryogenically Cooled Focal L-band Array for the GBT* (*FLAG*), The Astronomical Journal, 161, 163, publisher: American Astronomical Society

Pires, A. M., Haberl, F., Zavlin, V. E., et al. 2014, *XMM-Newton reveals a candidate period for the spin of the "Magnificent Seven" neutron star RX J1605.3+3249*, Astronomy & Astrophysics, 563, A50

Pires, A. M., Motch, C., & Janot-Pacheco, E. 2009, *A search for thermally emitting isolated neutron stars in the 2XMMp catalogue*, Astronomy & Astrophysics, 504, 185

Piro, A. L. 2012, *Magnetic Interactions in Coalescing Neutron Star Binaries*, The Astrophysical Journal, 755, 80

Piro, A. L. 2016, *The Impact of a Supernova Remnant on Fast Radio Bursts*, The Astrophysical Journal, 824, L32

Piro, L., Bruni, G., Troja, E., et al. 2021, *The fast radio burst FRB 20201124A in a star-forming region: Constraints to the progenitor and multiwavelength counterparts*, Astronomy & Astrophysics, 656, L15

Pitkin, M. 2018, *psrqpy: a python interface for querying the ATNF pulsar catalogue*, The Journal of Open Source Software, 3, 538

Planck Collaboration, Aghanim, N., Akrami, Y., et al. 2020, *Planck 2018 results: VI. Cosmological parameters*, Astronomy & Astrophysics, 641, A6

Platts, E., Caleb, M., Stappers, B. W., et al. 2021, *An analysis of the time-frequency structure of several bursts from FRB 121102 detected with MeerKAT*, Monthly Notices of the Royal Astronomical Society, 505, 3041

Platts, E., Weltman, A., Walters, A., et al. 2019, *A living theory catalogue for fast radio bursts*, Physics Reports, 821, 1

Pletsch, H. J., Guillemot, L., Allen, B., et al. 2013, *Einstein@Home discovery of four young gamma-ray pulsars in Fermi LAT data*, The Astrophysical Journal, 779, L11, arXiv: 1311.6427

Pleunis, Z., Good, D. C., Kaspi, V. M., et al. 2021a, *Fast Radio Burst Morphology in the First CHIME/FRB Catalog*, The Astrophysical Journal, 923, 1

Pleunis, Z., Michilli, D., Bassa, C. G., et al. 2021b, *LOFAR Detection of 110–188 MHz Emission and Frequency-dependent Activity from FRB 20180916B*, The Astrophysical Journal Letters, 911, L3

Plotnikov, I. & Sironi, L. 2019, *The synchrotron maser emission from relativistic shocks in Fast Radio Bursts: 1D PIC simulations of cold pair plasmas*, Monthly Notices of the Royal Astronomical Society, 485, 3816

Popov, S. B. & Postnov, K. A. 2010, *Hyperflares of SGRs as an engine for millisecond extragalactic radio bursts*, in Evolution of Cosmic Objects through their Physical Activity, Proceedings of the Conference dedicated to Viktor Ambartsumian's 100th anniversary (Publishing House of NAS RA), 129–132

Popov, S. B. & Postnov, K. A. 2013, *Millisecond extragalactic radio bursts as magnetar flares*

Price, D. C., Flynn, C., & Deller, A. 2021, *A comparison of Galactic electron density models using PyGEDM*, Publications of the Astronomical Society of Australia, 38, e038

Price, D. C., Foster, G., Geyer, M., et al. 2019, *A fast radio burst with frequency-dependent polarization detected during Breakthrough Listen observations*, Monthly Notices of the Royal Astronomical Society, 486, 3636

Prochaska, J. X., Macquart, J.-P., McQuinn, M., et al. 2019, *The low density and magnetization of a massive galaxy halo exposed by a fast radio burst*, Science, 366, 231

Prochaska, J. X. & Zheng, Y. 2019, *Probing Galactic haloes with fast radio bursts*, Monthly Notices of the Royal Astronomical Society, 485, 648, aDS Bibcode: 2019MNRAS.485..648P

Purcell, C. R., Van Eck, C. L., West, J., Sun, X. H., & Gaensler, B. M. 2020, *RM-Tools: Rotation measure* (*RM*) *synthesis and Stokes QU-fitting*, Astrophysics Source Code Library, ascl:2005.003

Pye, J. P., Rosen, S., Fyfe, D., & Schroeder, A. C. 2015, *A survey of stellar X-ray flares from the XMM-Newton serendipitous source catalogue: Hipparcos-Tycho cool stars*, Astronomy & Astrophysics, 581, A28

Qiang, D.-C., Li, S.-L., & Wei, H. 2022, *Fast radio burst distributions consistent with the first CHIME/FRB catalog*, Journal of Cosmology and Astroparticle Physics, 2022, 040

Qiu, H., Shannon, R. M., Farah, W., et al. 2020, *A population analysis of pulse broadening in ASKAP Fast Radio Bursts*, Monthly Notices of the Royal Astronomical Society, 497, 1382

Radhakrishnan, V. & Cooke, D. J. 1969, *Magnetic poles and the polarization structure of pulsar radiation*, Astrophysical Letters, 3, 225

Radhakrishnan, V. & Rankin, J. M. 1990, *Toward an empirical theory of pulsar emission. V. On the circular polarization in pulsar radiation*, The Astrophysical Journal, 352, 258

Radice, D., Bernuzzi, S., & Perego, A. 2020, *The Dynamics of Binary Neutron Star Mergers and of GW170817*, Annual Review of Nuclear and Particle Science, 70, 95

Rajabi, F., Chamma, M. A., Wyenberg, C. M., Mathews, A., & Houde, M. 2020, *A simple relationship for the spectro-temporal structure of bursts from FRB 121102*, Monthly Notices of the Royal Astronomical Society, 498, 4936

Rajwade, K. M., Bezuidenhout, M. C., Caleb, M., et al. 2022, *First discoveries and localizations of Fast Radio Bursts with MeerTRAP: real-time, commensal MeerKAT survey*, Monthly Notices of the Royal Astronomical Society, 514, 1961

Rajwade, K. M., Mickaliger, M. B., Stappers, B. W., et al. 2020, *Possible periodic activity in the repeating FRB 121102*, Monthly Notices of the Royal Astronomical Society, 495, 3551

Rane, A., Lorimer, D. R., Bates, S. D., et al. 2016, *A search for rotating radio transients and fast radio bursts in the Parkes high-latitude pulsar survey*, Monthly Notices of the Royal Astronomical Society, 455, 2207

Rankin, J. M. & Suleymanova, S. A. 2006, *The topology and polarisation of subbeams associated with the "drifting" subpulse emission of pulsar B0943+10: IV. Q-to-B-mode recovery dynamics*, Astronomy & Astrophysics, 453, 679

Ransom, S. M. 2001, *New Search Techniques For Binary Pulsars*, PhD thesis, Harvard University

Ravi, V. 2019, *The observed properties of fast radio bursts*, Monthly Notices of the Royal Astronomical Society, 482, 1966

Ravi, V., Catha, M., D'Addario, L., et al. 2019, *A fast radio burst localized to a massive galaxy*, Nature, 572, 352

Ravi, V., Shannon, R. M., Bailes, M., et al. 2016, *The magnetic field and turbulence of the cosmic web measured using a brilliant fast radio burst*, Science, 354, 41

Ravi, V., Shannon, R. M., & Jameson, A. 2015, *A Fast Radio Burst in the direction of the Carina dwarf spheroidal galaxy*, The Astrophysical Journal, 799, L5

Ray, P. S., Kerr, M., Parent, D., et al. 2011, *Precise Gamma-Ray Timing and Radio Observations of 17 Fermi Gamma-Ray Pulsars*, The Astrophysical Journal Supplement Series, 194, 17

Rayleigh, F. 1879, *XXXI. Investigations in optics, with special reference to the spectroscope*

Read, A. M., Rosen, S. R., Saxton, R. D., & Ramirez, J. 2011, *A new comprehensive 2D model of the point spread functions of the XMM-Newton EPIC telescopes: spurious source suppression and improved positional accuracy*, Astronomy and Astrophysics, 534, A34

Rees, M. J. 1977, *A better way of searching for black-hole explosions?*, Nature, 266, 333

Ridnaia, A., Golenetskii, S., Aptekar, R., et al. 2020, *ATel #13688: Konus-Wind observation of hard X-ray counterpart of the radio burst from SGR 1935+2154*, The Astronomer's Telegram, 13688, 1

Riess, A. G., Filippenko, A. V., Challis, P., et al. 1998, *Observational Evidence from Supernovae for an Accelerating Universe and a Cosmological Constant*, The Astronomical Journal, 116, 1009

Rigoselli, M., Mereghetti, S., Suleimanov, V., et al. 2019, *XMM-Newton observations of PSR J0726-2612, a radio-loud XDINS*, A&A, 627, A69

Rodríguez Castillo, G. A., Israel, G. L., Esposito, P., et al. 2018, *Discovery of a 3 s Spinning Neutron Star in a 4.15 hr Orbit in the Brightest Hard X-Ray Source in M31*, The Astrophysical Journal, 861, L26

Romani, R. W. & Watters, K. P. 2010, *Constraining Pulsar Magnetosphere Geometry with Gamma-Ray Light Curves*, The Astrophysical Journal, 714, 810

Rookyard, S. C., Weltevrede, P., & Johnston, S. 2015, *Constraints on viewing geometries from radio observations of γ-ray-loud pulsars using a novel method*, MNRAS, 446, 3367

Rosen, S. R., Webb, N. A., Watson, M. G., et al. 2016, *The XMM-Newton serendipitous survey. VII. The third XMM-Newton serendipitous source catalogue*, Astronomy and Astrophysics, 590, A1

Rowlinson, A., Bell, M. E., Murphy, T., et al. 2016, *Limits on Fast Radio Bursts and other transient sources at 182 MHz using the Murchison Widefield Array*, Monthly Notices of the Royal Astronomical Society, 458, 3506

Rubio-Herrera, E., Stappers, B. W., Hessels, J. W. T., & Braun, R. 2013, *A search for radio pulsars and fast transients in M31 using the WSRT*, Monthly Notices of the Royal Astronomical Society, 428, 2857

Ruderman, M. A. & Sutherland, P. G. 1975, *Theory of pulsars: polar gaps, sparks, and coherent microwave radiation.*, The Astrophysical Journal, 196, 51

Safarzadeh, M., Prochaska, J. X., Heintz, K. E., & Fong, W.-f. 2020, *Confronting the Magnetar Interpretation of Fast Radio Bursts through Their Host Galaxy Demographics*, The Astrophysical Journal Letters, 905, L30

Sagiv, A. & Waxman, E. 2002, *Collective Processes in Relativistic Plasma and Their Implications for Gamma-Ray Burst Afterglows*, The Astrophysical Journal, 574, 861, publisher: IOP Publishing

Salvaterra, R. 2015, *High redshift Gamma-Ray Bursts*, Journal of High Energy Astrophysics, 7, 35

Sand, K. R., Faber, J., Gajjar, V., et al. 2021, *Multiband Detection of Repeating FRB 20180916B*, arXiv:2111.02382 [astro-ph], arXiv: 2111.02382

Sand, K. R., Gajjar, V., Pilia, M., et al. 2020, *Low-frequency detection of FRB180916 with the uGMRT*, ATel

Sanidas, S., Cooper, S., Bassa, C. G., et al. 2019, *The LOFAR Tied-Array All-Sky Survey (LOTAAS): Survey overview and initial pulsar discoveries*, Astronomy & Astrophysics, 626, A104

Scargle, J. D. 1998, *Studies in Astronomical Time Series Analysis. V. Bayesian Blocks, a New Method to Analyze Structure in Photon Counting Data*, The Astrophysical Journal, 504, 405

Scargle, J. D., Norris, J. P., Jackson, B., & Chiang, J. 2013, *Studies in Astronomical Time Series Analysis. VI. Bayesian Block Representations*, The Astrophysical Journal, 764, 167

Scholz, P., Bogdanov, S., Hessels, J. W. T., et al. 2017, *Simultaneous X-Ray, Gamma-Ray, and Radio Observations of the Repeating Fast Radio Burst FRB 121102*, The Astrophysical Journal, 846, 80

Scholz, P., Cook, A., Cruces, M., et al. 2020, *Simultaneous X-Ray and Radio Observations of the Repeating Fast Radio Burst FRB 180916.J0158+65*, The Astrophysical Journal, 901, 165, publisher: American Astronomical Society

Scholz, P., Spitler, L. G., Hessels, J. W. T., et al. 2016, *The Repeating Fast Radio Burst FRB 121102: Multi-wavelength Observations and Additional Bursts*, The Astrophysical Journal, 833, 177

Sclocco, A., Heldens, S., & van Werkhoven, B. 2020, *AMBER: A real-time pipeline for the detection of single pulse astronomical transients*, SoftwareX, 12, 100549

Sclocco, A., van Leeuwen, J., Bal, H. E., & van Nieuwpoort, R. V. 2016, *Real-Time Dedispersion for Fast Radio Transient Surveys, using Auto Tuning on Many-Core Accelerators*, Astronomy and Computing, 14, 1

Sclocco, A., Van Nieuwpoort, R., & Bal, H. E. 2014, *Real-Time Pulsars Pipeline Using Many-Cores*, 3

Sclocco, A., Vohl, D., & van Nieuwpoort, R. V. 2019, *Real-Time RFI Mitigation for the Apertif Radio Transient System*, in 2019 RFI Workshop - Coexisting with Radio Frequency Interference (RFI), 1–8

Scott, D. W. 2015, Multivariate Density Estimation: Theory, Practice, and Visualization (John Wiley & Sons), google-Books-ID: pIAZBwAAQBAJ

Selsing, J., Krühler, T., Malesani, D., et al. 2018, *The host galaxy of the short GRB 111117A at z = 2.211: Impact on the short GRB redshift distribution and progenitor channels*, Astronomy & Astrophysics, 616, A48

Shand, Z., Ouyed, A., Koning, N., & Ouyed, R. 2016, *Quark nova model for fast radio bursts*, Research in Astronomy and Astrophysics, 16, 011

Shannon, R. M., Macquart, J.-P., Bannister, K. W., et al. 2018, *The dispersion–brightness relation for fast radio bursts from a wide-field survey*, Nature, 562, 386

Shannon, R. M. & Ravi, V. 2017, *Radio-interferometric Monitoring of FRB 131104: A Coincident AGN Flare, but No Evidence for a Cosmic Fireball*, The Astrophysical Journal, 837, L22

Shapiro, S. L., Teukolsky, S. A., & Wasserman, I. 1983, *Implications of the millisecond pulsar for neutron star models*, The Astrophysical Journal, 272, 702

Shitov, Y. P., Pugachev, V. D., & Kutuzov, S. M. 2000, *Low Frequency Radio Emission of Pulsar PSR J1907+0919 Associated with the Magnetar SGR 1900+14*, Pulsar Astronomy - 2000 and Beyond, 202

Sidoli, L. 2013, *Supergiant Fast X-ray Transients: a review*, arXiv:1301.7574 [astro-ph], arXiv: 1301.7574

Sidoli, L., Mereghetti, S., Sguera, V., & Pizzolato, F. 2012, *The XMM-Newton view of Supergiant Fast X-ray Transients: the case of IGRJ16418-4532*, Monthly Notices of the Royal Astronomical Society, 420, 554

Simha, S., Burchett, J. N., Prochaska, J. X., et al. 2020, *Disentangling the Cosmic Web toward FRB 190608*, The Astrophysical Journal, 901, 134

Sokolowski, M., Bhat, N. D. R., Macquart, J.-P., et al. 2018, *No Low-frequency Emission from Extremely Bright Fast Radio Bursts*, The Astrophysical Journal, 867, L12

Southworth, J., Gänsicke, B. T., & Breedt, E. 2011, *The Orbital Period Distribution of Cataclysmic Variables Found by the SDSS*, Proceedings of the International Astronomical Union, 7, 123

Spitler, L. G., Cordes, J. M., Hessels, J. W. T., et al. 2014, *Fast Radio Burst Discovered in the Arecibo Pulsar Alfa Survey*, The Astrophysical Journal, 790, 101

Spitler, L. G., Scholz, P., Hessels, J. W. T., et al. 2016, *A repeating fast radio burst*, Nature, 531, 202

Sridhar, N. & Metzger, B. D. 2022, *Radio Nebulae from Hyper-Accreting X-ray Binaries as Common Envelope Precursors and Persistent Counterparts of Fast Radio Bursts*, number: arXiv:2206.10486 arXiv:2206.10486 [astro-ph, physics:physics]

Sridhar, N., Metzger, B. D., Beniamini, P., et al. 2021, *Periodic Fast Radio Bursts from Luminous X-ray Binaries*, The Astrophysical Journal, 917, 13

Srostlik, Z. & Rankin, J. M. 2005, *Core and conal component analysis of pulsar B1237+25: Component analysis of pulsar B1237+25*, Monthly Notices of the Royal Astronomical Society, 362, 1121

Stappers, B. W., Hessels, J. W. T., Alexov, A., et al. 2011, *Observing pulsars and fast transients with LOFAR*, Astronomy & Astrophysics, 530, A80

Steeghs, D., Marsh, T. R., Barros, S. C. C., et al. 2006, *GEMINI spectroscopy of the ultra-compact binary candidate V407 Vul*, The Astrophysical Journal, 649, 382

Strüder, L., Aschenbach, B., Bräuninger, H., et al. 2001a, *Evidence for micrometeoroid damage in the pn-CCD camera system aboard XMM-Newton*, Astronomy & Astrophysics, 375, L5

Strüder, L., Briel, U., Dennerl, K., et al. 2001b, *The European Photon Imaging Camera on XMM-Newton: The pn-CCD camera*, Astronomy and Astrophysics, 365, L18

Szary, A. & van Leeuwen, J. 2017, *On the Origin of the Bi-drifting Subpulse Phenomenon in Pulsars*, ApJ, 845, 95

Szary, A., van Leeuwen, J., Weltevrede, P., & Maan, Y. 2020, *Single-pulse Modeling and the Bi-drifting Subpulses of Radio Pulsar B1839-04*, The Astrophysical Journal, 896, 168

Tan, C. M., Bassa, C. G., Cooper, S., et al. 2018, *LOFAR Discovery of a 23.5 s Radio Pulsar*, ApJ, 866, 54

Tavani, M., Ursi, A., Verrecchia, F., et al. 2020a, *ATel #13686: AGILE detection of a hard X-ray burst in temporal coincidence with a radio burst from SGR 1935+2154*, ATel, 13686, 1

Tavani, M., Verrecchia, F., Casentini, C., et al. 2020b, *Gamma-Ray and X-Ray Observations of the Periodic-repeater FRB 180916 during Active Phases*, The Astrophysical Journal, 893, L42, publisher: American Astronomical Society

Taylor, M. B. 2005, *TOPCAT & STIL: Starlink Table/VOTable Processing Software*, in TOPCAT & STIL, Vol. 347, 29

Tendulkar, S. P., Bassa, C., Cordes, J. M., et al. 2017, *The Host Galaxy and Redshift of the Repeating Fast Radio Burst FRB 121102*, The Astrophysical Journal, 834, L7

Tendulkar, S. P., Gil de Paz, A., Kirichenko, A. Y., et al. 2021, *The 60 pc Environment of FRB 20180916B*, The Astrophysical Journal, 908, L12

ter Veen, S., Enriquez, J. E., Falcke, H., et al. 2019, *The FRATS project: real-time searches for fast radio bursts and other fast transients with LOFAR at 135 MHz*, Astronomy & Astrophysics, 621, A57

Thompson, C. 2017, *Giant Primeval Magnetic Dipoles*, The Astrophysical Journal, 844, 65

Thornton, D., Stappers, B., Bailes, M., et al. 2013, *A Population of Fast Radio Bursts at Cosmological Distances*, Science, 341, 53

Tingay, S. J., Trott, C. M., Wayth, R. B., et al. 2015, *A search for Fast Radio Bursts at low frequencies with Murchison Widefield Array high time resolution imaging*, The Astronomical Journal, 150, 199

Tingay, S. J. & Yang, Y.-P. 2019, *A Search of TESS Full-frame Images for a Simultaneous Optical Counterpart to FRB 181228*, The Astrophysical Journal, 881, 30, publisher: American Astronomical Society
Tolman, R. C. 1939, *Static Solutions of Einstein's Field Equations for Spheres of Fluid*, Physical Review, 55, 364, publisher: American Physical Society
Tong, H., Liu, J., Wang, H. G., & Yan, Z. 2021, *Three aspects of the radius-to-frequency mapping in fast radio bursts*, Monthly Notices of the Royal Astronomical Society, 509, 5679
Tong, H., Wang, W., & Wang, H. G. 2020, *Periodicity in fast radio bursts due to forced precession by a fallback disk*, Research in Astronomy and Astrophysics, 20, 142
Totani, T. 2013, *Cosmological Fast Radio Bursts from Binary Neutron Star Mergers*, Publications of the Astronomical Society of Japan, 65, L12
Turner, M. J. L., Abbey, A., Arnaud, M., et al. 2001, *The European Photon Imaging Camera on XMM-Newton: The MOS cameras*, Astronomy & Astrophysics, 365, L27
Unwin, S. C., Redhead, A. C. S., Wilkinson, P. N., & Ewing, M. S. 1978, *Phase stability in the drifting subpulse pattern of PSR 0809+74*, Monthly Notices of the Royal Astronomical Society, 182, 711
Usov, V. V. & Katz, J. I. 2000, *Low frequency radio pulses from gamma-ray bursts?*, Astronomy and Astrophysics, 364, 655
Vachaspati, T. 2008, *Cosmic Sparks from Superconducting Strings*, Physical Review Letters, 101, 141301
Valtchanov, I., Pierre, M., & Gastaud, R. 2001, *Comparison of source detection procedures for XMM-Newton images*, Astronomy & Astrophysics, 370, 689
van Cappellen, W. A., Oosterloo, T. A., Verheijen, M. A. W., et al. 2022, *Apertif: Phased array feeds for the Westerbork Synthesis Radio Telescope: System overview and performance characteristics*, Astronomy & Astrophysics, 658, A146
van Haarlem, M. P., Wise, M. W., Gunst, A. W., et al. 2013, *LOFAR: The LOw-Frequency ARray*, Astronomy & Astrophysics, 556, A2
van Kerkwijk, M. H. & Kaplan, D. L. 2007, *Isolated neutron stars: magnetic fields, distances,and spectra*, Astrophysics and Space Science, 308, 191
van Leeuwen, A. G. J., Kouwenhoven, M. L. A., Ramachandran, R., Rankin, J. M., & Stappers, B. W. 2002, *Null-induced mode changes in PSR B0809+74*, Astronomy & Astrophysics, 387, 169
van Leeuwen, A. G. J., Stappers, B. W., Ramachandran, R., & Rankin, J. M. 2003, *Probing drifting and nulling mechanisms through theirinteraction in PSR B0809+74*, Astronomy & Astrophysics, 399, 223
van Leeuwen, J. 2014, *ARTS – the Apertif Radio Transient System*, in The Third Hot-wiring the Transient Universe Workshop (HTU-III), Santa Fe, NM, 79–79
van Leeuwen, J., Kasian, L., Stairs, I. H., et al. 2015, *The Binary Companion of Young, Relativistic Pulsar J1906+0746*, ApJ, 798, 118
van Leeuwen, J., Kooistra, E., Oostrum, L., et al. 2022, *The Apertif Radio Transient System (ARTS): Design, Commissioning, Data Release, and Detection of the first 5 Fast Radio Bursts*, arXiv e-prints, arXiv:2205.12362
van Leeuwen, J., Mikhailov, K., Keane, E., et al. 2020, *LOFAR radio search for single and periodic pulses from M 31*, A&A, 634, A3
van Leeuwen, J. & Stappers, B. W. 2010, *Finding pulsars with LOFAR*, A&A, 509, 7
van Leeuwen, J. & Timokhin, A. N. 2012, *On Plasma Rotation and Drifting Subpulses in Pulsars: Using Aligned Pulsar B0826-34 as a Voltmeter*, The Astrophysical Journal, 752, 155
Vedantham, H. K., Ravi, V., Hallinan, G., & Shannon, R. 2016, *The Fluence and Distance Distributions of Fast Radio Bursts*, The Astrophysical Journal, 830, 75
Verrecchia, F., Casentini, C., Tavani, M., et al. 2021, *AGILE Observations of Fast Radio Bursts*, The Astrophysical Journal, 915, 102, publisher: American Astronomical Society
Vieyro, F. L., Romero, G. E., Bosch-Ramon, V., Marcote, B., & del Valle, M. V. 2017, *A model for the repeating FRB 121102 in the AGN scenario*, Astronomy & Astrophysics, 602, A64
Voges, W., Aschenbach, B., Boller, T., et al. 1999, *The ROSAT all-sky survey bright source catalogue*, Astronomy and Astrophysics, 349, 389
Wadiasingh, Z., Beniamini, P., Timokhin, A., et al. 2020, *The Fast Radio Burst Luminosity Function and Death Line in the Low-twist Magnetar Model*, The Astrophysical Journal, 891, 82

Wang, J.-S., Yang, Y.-P., Wu, X.-F., Dai, Z.-G., & Wang, F.-Y. 2016, *Fast Radio Bursts from the Inspiral of Double Neutron Stars*, The Astrophysical Journal, 822, L7

Wang, W., Zhang, B., Chen, X., & Xu, R. 2019, *On the Time-Frequency Downward Drifting of Repeating Fast Radio Bursts*, The Astrophysical Journal, 876, L15

Watson, M. G., Schröder, A. C., Fyfe, D., et al. 2009, *The XMM-Newton serendipitous survey. V. The Second XMM-Newton serendipitous source catalogue*, Astronomy and Astrophysics, 493, 339

Watters, K. P., Romani, R. W., Weltevrede, P., & Johnston, S. 2009, *An Atlas For Interpreting Gamma-Ray Pulsar Light Curves*, The Astrophysical Journal, 695, 1289

Waxman, E. 2017, *On the Origin of Fast Radio Bursts* (*FRBs*), The Astrophysical Journal, 842, 34, publisher: American Astronomical Society

Weltevrede, P., Stappers, B. W., & Edwards, R. T. 2007, *The subpulse modulation properties of pulsars at 92cm and the frequency dependence of subpulse modulation*, Astronomy & Astrophysics, 469, 607

Wenger, M., Ochsenbein, F., Egret, D., et al. 2000, *The SIMBAD astronomical database. The CDS reference database for astronomical objects*, Astronomy and Astrophysics Supplement Series, 143, 9

Woosley, S. E. 2010, *Bright Supernovae from Magnetar Birth*, The Astrophysical Journal, 719, L204

Xi, S.-Q., Tam, P.-H. T., Peng, F.-K., & Wang, X.-Y. 2017, *Search for GeV Counterparts to Fast Radio Bursts with Fermi*, The Astrophysical Journal, 842, L8

Xin, L. P., Li, H. L., Wang, J., et al. 2021, *Constraints on Optical Emission of FAST-detected FRB 20181130B with GWAC Synchronized Observations*, The Astrophysical Journal, 922, 78

Xu, H., Niu, J. R., Chen, P., et al. 2021, *A fast radio burst source at a complex magnetised site in a barred galaxy*, arXiv:2111.11764 [astro-ph], arXiv: 2111.11764

Xu, S. & Zhang, B. 2016, *On the origin of the scatter broadening of fast radio burst pulses and astrophysical implications*, The Astrophysical Journal, 832, 199

Yamasaki, S. & Totani, T. 2020, *The Galactic Halo Contribution to the Dispersion Measure of Extragalactic Fast Radio Bursts*, The Astrophysical Journal, 888, 105

Yamasaki, S., Totani, T., & Kiuchi, K. 2018, *Repeating and non-repeating fast radio bursts from binary neutron star mergers*, Publications of the Astronomical Society of Japan, 70

Yang, Y.-P. & Zhang, B. 2018, *Bunching Coherent Curvature Radiation in Three-dimensional Magnetic Field Geometry: Application to Pulsars and Fast Radio Bursts*, The Astrophysical Journal, 868, 31, publisher: American Astronomical Society

Yao, J. M., Manchester, R. N., & Wang, N. 2017, *A New Electron Density Model for Estimation of Pulsar and FRB Distances*, The Astrophysical Journal, 835, 29

Yi, S.-X., Cheng, K. S., & Luo, R. 2019, *Clumpy jets from black hole–massive star binaries as engines of fast radio bursts*, Monthly Notices of the Royal Astronomical Society, 483, 4197

Zanazzi, J. J. & Lai, D. 2020, *Periodic Fast Radio Bursts with Neutron Star Free/Radiative Precession*, The Astrophysical Journal, 892, L15

Zane, S., Haberl, F., Israel, G. L., et al. 2011, *Discovery of 59 ms Pulsations from 1RXS J141256.0+792204* (*Calvera*), Monthly Notices of the Royal Astronomical Society, 410, 2428

Zhang, B. 2013, *A Possible Connection between Fast Radio Bursts and Gamma-Ray Bursts*, The Astrophysical Journal, 780, L21

Zhang, B. 2018a, *Fast Radio Burst Energetics and Detectability from High Redshifts*, The Astrophysical Journal, 867, L21

Zhang, B. 2018b, *FRB 121102: A Repeatedly Combed Neutron Star by a Nearby Low-luminosity Accreting Supermassive Black Hole*, The Astrophysical Journal, 854, L21

Zhang, B. 2020a, *Fast Radio Bursts from Interacting Binary Neutron Star Systems*, The Astrophysical Journal, 890, L24, aDS Bibcode: 2020ApJ...890L..24Z

Zhang, B. 2020b, *The physical mechanisms of fast radio bursts*, Nature, 587, 45

Zhang, B.-B. & Zhang, B. 2017, *Repeating FRB 121102: Eight-year Fermi-LAT Upper Limits and Implications*, The Astrophysical Journal, 843, L13, publisher: American Astronomical Society

Zhang, F. 2017, *Pulsar magnetospheric convulsions induced by an external magnetic field*, Astronomy & Astrophysics, 598, A88

Zhang, G. Q., Yi, S. X., & Wang, F. Y. 2020a, *The Rarity of Repeating Fast Radio Bursts from Binary Neutron Star Mergers*, The Astrophysical Journal, 893, 44

Zhang, R. C. & Zhang, B. 2022, *The CHIME Fast Radio Burst Population Does Not Track the Star Formation History of the Universe*, The Astrophysical Journal Letters, 924, L14

Zhang, S.-N., Tuo, Y.-L., Xiong, S.-L., & Li, C.-K. 2020b, *ATel #13687: Insight-HXMT detection of a bright short x-ray counterpart of the Fast Radio Burst from SGR 1935+2154*, The Astronomer's Telegram, 13687, 1

Zhang, Y., Geng, J.-J., & Huang, Y.-F. 2018, *Fast Radio Bursts from the Collapse of Strange Star Crusts*, The Astrophysical Journal, 858, 88

Zhang, Z., Gilfanov, M., Voss, R., et al. 2011, *Luminosity functions of LMXBs in different stellar environments*, Astronomy & Astrophysics, 533, A33, arXiv: 1103.4486

Zhu, W. & Feng, L.-L. 2021, *The dispersion measure and scattering of FRBs: Contributions from the intergalactic medium, foreground halos, and hosts*, The Astrophysical Journal, 906, 95

Zhu, W., Li, D., Luo, R., et al. 2020, *A Fast Radio Burst Discovered in FAST Drift Scan Survey*, The Astrophysical Journal, 895, L6

Zolotukhin, I. Y., Bachetti, M., Sartore, N., Chilingarian, I. V., & Webb, N. A. 2017, *The Slowest Spinning X-Ray Pulsar in an Extragalactic Globular Cluster*, The Astrophysical Journal, 839, 125

Contribution from co-authors

Here listed is the bibliographic information of the papers included in this thesis. The relative contribution of every coauthor is represented by their order in the author list. All chapters of this thesis were written under the supervision or co-supervision of Joeri van Leeuwen.

Chapter 2: *New upper limits on low-frequency radio emission from isolated neutron stars with LOFAR*
I. Pastor-Marazuela S. M. Straal, J. van Leeuwen, V. I. Kondratiev.
To be submitted to *Astronomy & Astrophysics*

Chapter 3: *The EXOD search for faint transients in XMM-Newton observations: Method and discovery of four extragalactic Type I X-ray bursters*
I. Pastor-Marazuela, N. A. Webb, D. T. Wojtowicz, and J. van Leeuwen.
Astronomy & Astrophysics, Volume 640, A124, August 2020

Chapter 4: *Chromatic periodic activity down to 120 MHz in a Fast Radio Burst*
I. Pastor-Marazuela, L. Connor, J. van Leeuwen, Y. Maan, S. ter Veen, A. Bilous, L. Oostrum, E. Petroff, S. Straal, D. Vohl, J. Attema, O. M. Boersma, E. Kooistra, D. van der Schuur, A. Sclocco, R. Smits, E. A. K. Adams, B. Adebahr, W. J. G. de Blok, A. H. W. M. Coolen, S. Damstra, H. Dénes, K. M. Hess, T. van der Hulst, B. Hut, V. M. Ivashina, A. Kutkin, G. M. Loose, D. M. Lucero, Á. Mika, V. A. Moss, H. Mulder, M. J. Norden, T. Oosterloo, E. Orrú, M. Ruiter, S. J. Wijnholds.
Nature, Volume 596, Issue 7873, p.505-508, August 2021

Chapter 5: *A Fast Radio Burst with sub-millisecond quasi-periodic structure*
I. Pastor-Marazuela, J. van Leeuwen, A. Bilous, L. Connor, Y. Maan, L. Oostrum, E. Petroff, S. Straal, D. Vohl, E. A. K. Adams, B. Adebahr, J. Attema, O. M. Boersma, R. van den Brink, W. A. van Cappellen, A. H. W. M. Coolen, S. Damstra, H. Dénes, K. M. Hess, J. M. van der Hulst, B. Hut, A. Kutkin, G. Marcel Loose, D. M. Lucero, Á. Mika, V. A. Moss, H. Mulder, M.J. Norden, T. A. Oosterloo, K. Rajwade, D. van der Schuur, A. Sclocco, R. Smits, J. Ziemke.
Submitted to *Astronomy & Astrophysics*. arXiv e-prints, arXiv:2202.08002

Chapter 6: *Morphological evolution with frequency in Fast Radio Bursts as exposed by the Apertif survey*
I. Pastor-Marazuela, J. van Leeuwen, L. Oostrum, E. Petroff, A. Bilous, L. Connor, Y. Maan, S. Straal, D. Vohl, P. Atri, O. M. Boersma, K. Rajwade, ARTS Builders, Apertif Builders.
To be submitted to *Astronomy & Astrophysics*

Other publications

Co-authored articles

1. *The Apertif Radio Transient System* (*ARTS*)*: Design, Commissioning, Data Release, and Detection of the first 5 Fast Radio Bursts.*
   J. van Leeuwen, E. Kooistra, L. Oostrum, L. Connor, J. E. Hargreaves, Y. Maan, **I. Pastor-Marazuela**, E. Petroff, D. van der Schuur, A. Sclocco, S. M. Straal, D. Vohl, S. J. Wijnholds, E. A. K. Adams, B. Adebahr, J. Attema, C. G. Bassa, J. E. Bast, A. Bilous, W. J. G. de Blok, O. M. Boersma, A. H. W. M. Coolen, H. Dénes, S. Damstra, J. P. R. de Reijer, D. W. Gardenier, Y. G. Grange, A. W. Gunst, K. M. Hess, H. A. Holties, B. Hut, A. Kutkin, G. M. Loose, D. M. Lucero, Á. Mika, K. Mikhailov, R. Morganti, V. A. Moss, H. Mulder, M. J. Norden, T. A. Oosterloo, E. Orrú, Z. Paragi, A. P. Schoenmakers, K. J. C. Stuurwold, S. ter Veen, W. A. van Cappellen, J. M. van der Hulst, G. N. J. van Diepen, Y. Y. Wang, A. W. Zanting, and J. Ziemke.
   Submitted to *Astronomy & Astrophysics*. arXiv e-prints, arXiv:2205.12362

2. *The intermediate polar cataclysmic variable GK Persei 120 years after the nova explosion: a first dynamical mass study.*
   A. Álvarez-Hernández, M. A. P. Torres, P. Rodríguez-Gil, T. Shahbaz, G. C. Anupama, K. D. Gazeas, M. Pavana, A. Raj, P. Hakala, G. Stone, S. Gomez, P. G. Jonker, J.-J. Ren, G. Cannizzaro, **I. Pastor-Marazuela**, W. Goff, J. M. Corral-Santana, and R. Sabo.
   MNRAS, Volume 507, Issue 4, pp.5805-5819, November 2021.

3. *A bright, high rotation-measure FRB that skewers the M33 halo.*
   L. Connor, J. van Leeuwen, L. C. Oostrum, E. Petroff, Y. Maan, E. A. K. Adams, J. J. Attema, J. E. Bast, O. M. Boersma, H. Dénes, D. W. Gardenier, J. E. Hargreaves, E. Kooistra, **I. Pastor-Marazuela**, R. Schulz, A. Sclocco, R. Smits, S. M. Straal, D. van der Schuur, D. Vohl, B. Adebahr, W. J. G. de Blok, W. A. van Cappellen, A. H. W. M. Coolen, S. Damstra, G. N. J. van Diepen, B. S. Frank, K. M. Hess, B. Hut, G. M. Loose, D. M. Lucero, Á. Mika, V. A. Moss, H. Mulder, T. A. Oosterloo, M. Ruiter, H. Vedantham, N. J. Vermaas, S. J. Wijnholds, and J. Ziemke.
   MNRAS, Volume 499, Issue 4, pp.4716-4724, December 2020.

4. *Initial characterization of interstellar comet 2I/Borisov*
   P. Guzik, M. Drahus, K. Ruse, W. Waniak, G. Cannizzaro, and **I. Pastor-Marazuela**.
   Nature Astronomy, Volume 4, p. 53-57, January 2020.

Telegrams and circulars

1. ATel #15197: *Detection of two bright bursts from FRB20201124A with Apertif at the Westerbork Synthesis Radio Telescope.*
   P. Atri, A. Bilous, J. van Leeuwen, Y. Maan, **I. Pastor-Marazuela**, E. Petroff, S. Straal.
2. ATel #15168: *GBT observations of SGR J1935+2154 during its recent high-energy bursting activity phase.*
   Y. Maan, S. Straal, J. van Leeuwen, **I. Pastor-Marazuela**.
3. ATel #13100: *Interstellar Comet gb00234.*
   P. Guzik, M. Drahus, K. Rusek, W. Waniak, G. Cannizzaro, **I. Pastor-Marazuela**.
4. GCN #25744: *LIGO/Virgo S190910h: WHT spectroscopy of Gaia19ebl, Gaia19eba, Gaia19eaz.*
   I. Pastor-Marazuela, G. Cannizzaro, P. Jonker, K. Maguire, M. Fraser, M. Perez Torres.
5. GCN #25733: *LIGO/Virgo S190910h: WHT spectroscopy of AT2019pyz/PS19fbi.*
   K. Maguire, S. Smartt, P. Jonker, G. Cannizzaro, **I. Pastor-Marazuela**, M. Fraser, A. Levan, M. Perez-Torres, S. Srivastav.
6. GCN #25730: *LIGO/Virgo S190910h: WHT spectroscopy of ZTF19abygvmp/AT2019pzg.*
   G. Cannizzaro, **I. Pastor-Marazuela**, P. Jonker, K. Maguire, M. Fraser.
7. GCN #25732: *LIGO/Virgo S190910h and S190910d: WHT photometry of ZTF candidates.*
   G. Cannizzaro, **I. Pastor-Marazuela**, P. Jonker, K. Maguire, M. Fraser, S. Brennan, M Perez Torres.
8. GCN #25725: *LIGO/Virgo S190910d: WHT spectroscopy of ZTF19abyfhov, ZTF19abyfhaq, ZTF19abyfbii* G. Cannizzaro, **I. Pastor-Marazuela**, P. Jonker, K. Maguire, M. Fraser.
9. GCN #25724: *LIGO/Virgo S190901ap: WHT spectroscopy of Gaia19dzi.* G. Cannizzaro, **I. Pastor-Marazuela**, P. Jonker.

Resumen español

Aunque el cielo nocturno parece eterno e inmutable, cada cierto tiempo surgen nuevas fuentes de luz transitorias, que aparecen y se desvanecen repentinamente. Estas señales astrofísicas transitorias son el resultado de algunos de los procesos más energéticos del Universo, y suelen involucrar ‘‘objetos compactos”. Los objetos compactos son cadáveres estelares, los restos de estrellas que ya no pueden seguir fusionando elementos en su núcleo. Las estrellas más ligeras, como nuestro Sol, se convierten en enanas blancas. Las que inicialmente tienen una masa superior a 8 veces la del Sol se convierten en estrellas de neutrones. Las más masivas de todas, con más de 25 masas solares, acaban siendo agujeros negros. Estos objetos compactos generan unas condiciones físicas extremas de densidad, composición, rotación, campos magnéticos, o también gravedad. Estas condiciones son prácticamente imposibles de reproducir en la Tierra, lo que convierte a los objetos compactos en laboratorios ideales para comprobar las leyes de la física.

En 2007 descubrieron un nuevo tipo de fuente transitoria con propiedades asombrosas. Se detectó en frecuencias de radio, y no duró más que un milisegundo, menos de lo que se tarda en parpadear. En esta señal, las frecuencias bajas llegaban con mucho más retraso que las altas. Este retraso, que es proporcional a la cantidad de materia que la señal de radio ha atravesado en su recorrido, implicaba que se había producido extremadamente lejos, mucho más allá de la Vía Láctea. Bautizaron a este tipo de fuentes transitorias como ‘‘Ráfagas Rápidas de Radio”, o FRBs del inglés ‘‘Fast Radio Bursts”. Hasta la fecha no se había predicho que estas ráfagas pudieran existir, lo que marcó el inicio de un nuevo campo de investigación con el objetivo de descifrar su origen.

Durante los primeros años tras este hallazgo, el ritmo de detecciones apenas creció. La cantidad de teorías que se habían propuesto intentando explicar la procedencia de las FRBs era incluso superior al número total de FRBs encontradas. Pero según se iban descubriendo más FRBs, varios radiotelescopios por todo el mundo empezaron a buscar estas misteriosas señales. Hoy en día, se han encontrado más de 600 FRBs. La gran mayoría se han visto solo una vez, cada una en una dirección y a una distancia diferente; estas son las que llamamos ‘‘singulares”. Originalmente se propuso que las FRBs singulares eran el producto de eventos ‘‘cataclísmicos”, en los que la fuente que origina la ráfaga es destruida durante el proceso. Sin embargo, hay otras FRBs que se repiten, aunque lo hacen a tiempos irregulares entre una ráfaga y la siguiente. Para que esto sea posible, la fuente de estas repetidoras tiene que sobrevivir al proceso de emisión. Actualmente, una de las mayores preguntas sin resolver en el campo de investigación de las FRBs es si las FRBs singulares y las repetidoras tienen el mismo origen, pero las singulares tienen un nivel de actividad menor, o si en cambio tienen orígenes completamente diferentes.

En abril de 2020, un mágnetar galáctico ya conocido previamente emitió una señal de radio con una luminosidad extraordinaria, muy parecida a las ráfagas rápidas de radio. Esta es la mejor

evidencia que tenemos del tipo de fuente que podría dar lugar a las FRBs. Pero vamos a definir primero lo que es un mágnetar. Una estrella que tiene entre 8 y 25 veces la masa del Sol acaba su vida en una explosión de supernova, cuando ya se han fusionado todos los elementos en su núcleo. Durante la supernova, las capas externas de la estrella son expulsadas violentamente hacia fuera, mientras que el núcleo se contrae abruptamente, convirtiéndose en una estrella de neutrones. El núcleo entero, con una vez y media la masa del Sol, se comprime en un una esfera de tan solo 10 kilómetros de radio. Por conservación del momento angular, esta compresión hace que la estrella de neutrones gire sumamente rápido, entre una y mil veces por segundo. Además, el campo magnético también aumenta hasta aproximadamente 10^{12} veces el de la Tierra, lo que las convierte en los imanes más fuertes del Universo. Las estrellas de neutrones pueden emitir ondas radio por sus polos magnéticos, y si estos están orientados en la dirección correcta, desde la Tierra se puede ver una emisión periódica según giran. A este tipo de estrellas de neutrones se les llama ‘‘púlsares”. Los magnetares son estrellas de neutrones con campos magnéticos aún más fuertes. Sus magnetosferas suelen ser caóticas y retorcidas, y a veces experimentan épocas de actividad cuando la magnetosfera cambia su configuración. Esto provoca emisiones electromagnéticas que pueden verse en rayos X, rayos gamma, y ocasionalmente en radio.

Empecé mi doctorado cuando tan solo se conocían unas 30 FRBs, la misma semana en que se inauguró Apertif. Apertif es un nuevo instrumento instalado en el Westerbork Synthesis Radio Telescope (WSRT), un conjunto de 14 antenas de radio que observan al mismo tiempo como un solo radiotelescopio, instalado en los Países Bajos. Este potente instrumento puede observar una amplia superficie celeste con alta resolución de tiempo y frecuencia. Estas características hacen que Apertif esté perfectamente adaptado para encontrar nuevas FRBs en el cielo, y este ha sido uno de sus principales objetivos. La búsqueda de FRBs con Apertif empezó en julio de 2019, y duró hasta febrero de 2022, tan solo unos meses antes de escribir estas líneas.

El objetivo de mi tesis, titulada *“Explorando la conexión entre las estrellas de neutrones y las ráfagas rápidas de radio”*, ha sido determinar qué tipo de fuentes astrofísicas podrían ser responsables de generar FRBs. Para cumplir este objetivo, una gran parte de mi trabajo se ha centrado en recopilar y analizar FRBs con Apertif. He estudiado las propiedades observacionales de las FRBs y las he comparado con las características de otras fuentes galácticas que entendemos un poco mejor, principalmente con estrellas de neutrones. También he desarrollado una herramienta que podría ayudar a detectar emisión a altas energías procedente de FRBs extragalácticas, lo que nos permitiría concretar mejor su origen.

En el Capítulo 2, hicimos unas observaciones a muy bajas frecuencias de cuatro púlsares que solo se han visto brillar a altas energías, pero nunca en radio. En los púlsares, la emisión en radio a bajas frecuencias es a menudo más fácil de detectar que a altas frecuencias. Los púlsares que observamos comparten varias características con los magnetares, que se cree que originan FRBs. Por lo tanto, estudiarlos es importante para entender cómo se producen ráfagas de radio tan brillantes, y cómo evolucionan sus progenitores. No detectamos emisión en radio en estas fuentes, así que determinamos que su flujo es muy bajo.

En el Capítulo 3, presentamos el algoritmo EXOD. Creamos este algoritmo para buscar fuentes de rayos X transitorias débiles en observaciones tomadas con XMM-Newton, un telescopio de rayos X que orbita alrededor de la Tierra. La emisión similar a una FRB que emitió el mágnetar

galáctico iba acompañada de una ráfaga de rayos X, por lo que las FRBs extragalácticas podrían estar también asociadas a emisiones a altas energías. Por lo tanto, buscar este tipo de emisiones simultáneas es importante para entender el origen de las FRBs. En este capítulo describimos las propiedades de 35 nuevas fuentes que identificamos a través de estas búsquedas de variabilidad. Descubrimos que cuatro de las fuentes eran estrellas de neutrones extragalácticas orbitando alrededor de otra estrella convencional, en un sistema binario. Estas estrellas de neutrones van absorbiendo materia de su estrella acompañante, lo que hace que brillen a temperaturas muy altas, emitiendo rayos X. Se conocen muchos sistemas binarios como este en la Vía Láctea, pero muy pocos en nuestra galaxia vecina, Andrómeda. Con estos cuatro nuevos descubrimientos, duplicamos la población de estrellas de neutrones conocidas en Andrómeda.

En el Capítulo 4, llevamos a cabo una larga campaña de observación de una FRB repetidora muy especial. Esta FRB se descubrió en 2018, y después de detectar decenas de repeticiones, los descubridores se dieron cuenta de que la fuente se activaba periódicamente, cada 16 días. Durante unos 5 días por ciclo, se podían ver varias ráfagas a tiempos irregulares, pero después la fuente se apagaba por completo antes de volver a activarse en el siguiente ciclo. Esta fue la primera fuente en la que se encontró tal comportamiento periódico. Para intentar entender mejor qué es lo que podía provocar esa actividad periódica, observamos la fuente con Apertif, y también con LOFAR, otro radiotelescopio en los Países Bajos que observa a muy bajas frecuencias. Mediante estas observaciones, descubrimos algo inesperado. Encontramos más de 50 ráfagas con Apertif, pero también la detectamos 9 veces con LOFAR. Esta es la detección de FRBs a frecuencias más bajas hasta la fecha. La existencia de emisión a tales frecuencias significa que la FRB tiene un entorno despejado a su alrededor, sin una densa nube de material que absorbería las bajas frecuencias de radio, haciéndolas indetectables. Podría esperarse la presencia de esa nube de material, por ejemplo, si la FRB estuviera rodeada por los restos de una supernova. Determinamos también que la FRB se activaba antes, pero durante menos tiempo, a altas frecuencias (Apertif) que a bajas frecuencias (LOFAR), como se representa en la Imagen A. Esto es justo lo contrario de lo que la interpretación principal sobre la periodicidad predecía. Esta teoría proponía que la FRB era un mágnetar que se encontraba en un sistema binario con otra estrella que emitía fuertes vientos. Estos vientos ocultarían la emisión radio del mágnetar, y solo cuando este último estuviera en dirección de la Tierra podrían verse las ráfagas escapando del viento. Pero en esta situación, las frecuencias más altas deberían escapar con mayor facilidad y por lo tanto se verían durante más tiempo, a diferencia de lo que observamos. Otra hipótesis parecía cuadrar con nuestras observaciones mucho mejor : la periodicidad podría provocarla un mágnetar girando extremadamente despacio, con un periodo de 16 días. Nunca se ha visto un mágnetar que pueda girar tan despacio, así que es cuestionable que tal fuente exista. Sin embargo, esto podría explicar que la emisión a bajas frecuencias se vea durante más tiempo, porque este es un efecto que se ve también en púlsares galácticos. Nuestros descubrimientos son una prueba adicional del vínculo que existe entre las FRBs repetidoras y los magnetares.

En el Capítulo 5 presentamos una nueva FRB singular con unas características únicas que detectamos con Apertif. Esta FRB está formada por cinco componentes separadas regularmente por tan solo 0.4 milisegundos. La separación es tan pequeña que el periodo de rotación de una estrella de neutrones no podría explicarla; a tal velocidad, la estrella se destruiría. La fusión de dos objetos

compactos es aún menos probable, porque dos objetos no pueden orbitar alrededor del otro más rápido de lo que pueden rotar alrededor de sí mismos. En cambio, se ha visto que la emisión en radio de muchos púlsares y magnetares galácticos puede presentar morfologías complejas. Por lo tanto concluimos que un mágnetar con una configuración magnética compleja podría explicar la estructura que observamos en esta FRB. Nuestro estudio aporta pruebas de que también hay una conexión entre las FRBs singulares y los magnetares.

En el Capítulo 6, el último, presentamos todas las nuevas FRBs singulares que encontramos con Apertif. Hallamos en total 24 nuevas ráfagas, una de las mayores recopilaciones de FRBs hasta la fecha. Entre estas FRBs, encontramos varias con morfologías complejas, muchas más de las que esperábamos a partir de detecciones previas de otras FRBs. Además identificamos varias FRBs que, por sus propiedades observacionales, deben de situarse en entornos con densas nubes de materia. En comparación con la FRB periódica del Capítulo 4, que se situaba en un entorno despejado, esto implica que las FRBs pueden ubicarse en medios muy diferentes, o tener edades diversas. Si Apertif fuera capaz de mirar a todo el cielo a la vez, detectaría casi 500 FRBs al día, casi tantos como se conocen actualmente.

En conclusión, durante mi doctorado he estudiado las características de FRBs singulares y repetidoras, he desarrollado herramientas para buscar su emisión en rayos X equivalente, y he estudiado púlsares, uno de los análogos galácticos más cercanos a las FRBs. También he conseguido establecer equivalencias entre las propiedades observacionales de FRBs repetidoras y singulares con las estrellas de neutrones hipermagnéticas, y he caracterizado las propiedades del conjunto de FRBs singulares usando Apertif. Este estudio y otros similares abren la puerta a que, con el tiempo, podamos confirmar si todas las FRBs provienen de estrellas de neutrones.

Figure A: Interpretación artística de la FRB periódica (Capítulo 4) vista por Apertif y LOFAR. A la izquierda se ven algunas de las antenas de Apertif, que detecta frecuencias altas (azul) antes y durante menos tiempo. Las antenas de la derecha son de LOFAR, que detecta las emisiones a baja frecuencia (rojo) más tarde y durante más tiempo. Joeri van Leeuwen.

English summary

Although the night sky seems to be eternal and unchanging, every once in a while new ‘‘transient” sources suddenly appear and vanish. These transient astrophysical signals are the product of some of the most energetic processes in the Universe, and they often involve ‘‘compact objects”. Compact objects are stellar corpses, the remains of stars that can no longer fuse elements in their cores. The lightest stars, like our Sun, become white dwarfs at the end of their lives. Those that initially have more than 8 times the mass of the Sun become neutron stars, while the most massive stars, with more than 25 solar masses, become black holes. These compact objects have extreme physical conditions of density, composition, rotation, magnetic fields, and/or gravity. These conditions are often impossible to reproduce on Earth, making compact objects ideal laboratories to test the laws of physics.

In 2007, a perplexing new type of transient source was discovered. It was detected at radio wavelengths, and its duration was of just a millisecond, shorter than the blink of an eye. The lowest frequencies of the radio signal arrived much later than the highest frequencies. This large delay, which is proportional to the amount of matter the signal has traveled through, and hence the distance, implied that the radio waves had originated very far away, beyond the Milky Way! This type of radio transient was baptised Fast Radio Burst (FRB). Nobody had predicted such signals to exist, and thus the quest to decipher their origin started.

During the following years after the discovery of the first FRB, the number of new detections increased very slowly. For several years, the amount of theories of what these FRBs could be was larger than the actual number of known sources. But as the number of FRBs kept growing, many radio telescopes all over the world started searching for these puzzling sources. Today, more than 600 FRBs have been found. The large majority of those have only been seen once; they are called the ‘‘one-offs” or ‘‘non-repeaters”. These bursts were originally proposed to originate from ‘‘cataclysmic” events, where the source that produces the burst is destroyed in the process. However, others repeat, but they do so at irregular times between consecutive bursts. The source of these repeaters must be long-lived. Currently, one of the main unanswered questions in the FRB field is whether repeaters and one-offs have the same origin, but one-offs are less active sources, or if instead they are produced by completely different processes altogether.

In April 2020, a previously known galactic magnetar was seen to emit an extremely bright FRB-like burst. This is the best evidence we have of what the FRB progenitors can be. But let’s first define what a ‘‘magnetar” is. When a star of initially between 8 and 25 times the mass of the Sun, it ends its life in a supernova explosion, once it has fused all the elements in the core. During the supernova, the outer layers of the star are violently ejected while its core abruptly contracts, becoming a neutron star. The whole nucleus, roughly one and a half times as massive as the Sun, is compressed into a sphere of just 10 km in radius! By conservation of the angular momentum,

this compression will make the neutron star rotate extremely fast, between one and a thousand times per second. Additionally, it will increase the magnetic field to roughly 10^{12} times that of the Earth, making them the strongest magnets of the Universe. Neutron stars can emit radio waves through their magnetic poles, and if these are oriented in the right direction, a periodic radio emission can be seen from Earth as they rotate. This type of neutron stars with periodic emission are known as ‘‘pulsars”. Magnetars are neutron stars with even more extreme magnetic fields. Their magnetosphere is often chaotic and twisted, and they sometimes undergo periods of activity when the magnetosphere changes its configuration. This produces emission that can be seen in X-rays, γ-rays, and occasionally in radio.

I started this thesis the same week Apertif was inaugurated. Apertif was a new instrument installed at the Westerbork Synthesis Radio Telescope (WSRT), an array of radio telescopes in the Netherlands. This powerful instrument was capable of looking at a large region of the sky with a high time and frequency resolution. These observing properties made Apertif perfectly suited to find new FRBs in the sky, and this was one of its main goals. The FRB survey started in July 2019 and lasted until February 2022, just a few months before the time of writing. The goal of my thesis has been to determine what types of sources could be in charge of producing the FRB emission. To achieve this goal, a great part of the work has focused on the data collection and analysis of the Apertif FRBs. I have studied the observable FRB features and compared them to the properties of other galactic sources whose origin we are able to grasp, mainly neutron stars. I have also developed a tool that might help us detect high-energy emission from FRBs, which would further constrain their provenance.

In Chapter 2, we carried out low frequency radio observations of four pulsars that have only been seen at high energies, but not in radio. In pulsars, low frequency radio emission is often easier to detect than high frequency emission. The pulsars we observed share various properties with magnetars, which are though to produce FRBs. Their study is thus important to understand how such bright radio bursts are produced, and how their progenitors evolve. We did not find any emission from these sources, but we highly constrained their flux.

In Chapter 3 we present the EXOD algorithm. We developed EXOD to look for faint X-ray transients in observations taken with XMM-Newton, an X-ray space telescope that orbits around Earth. The FRB-like emission from the galactic magnetar was simultaneously seen as a bright X-ray burst. Hence, extragalactic FRBs might be associated to X-ray transients, which makes looking for such signatures important to understand the FRB origin. In this Chapter, we describe the properties of 35 new sources that we identified through these variability searches. Four of them turned out to be extragalactic neutron stars orbiting around another star. The neutron stars swallow mass from their stellar companion, which makes them shine at very high temperatures (in the X-rays). Many such binary systems are known in the Milky Way, but very few were known in our neighbouring galaxy Andromeda. With these four new discoveries, we doubled the population of known neutron stars in Andromeda.

For Chapter 4, we carried out a long follow up observation campaign of a very special repeating FRB. This FRB was discovered in 2018, and after seeing tens of repetitions, the discoverers found that the source became active periodically, every 16 days. During $\sim$5 days per period, several bursts could be seen at irregular times, but then the source turned off until the beginning

of the next period. This is the first source where such a periodic behaviour was observed. To better understand what the origin of such periodicity could be, we observed the FRB with Apertif, and with LOFAR, another radio telescope in the Netherlands that observed at extremely low frequencies. What we found was very surprising. We detected the FRB more than 50 times with Apertif. But we also detected it 9 times with LOFAR, which were the lowest frequency detections of an FRB ever! The existence of such low frequency emission means the FRB lives in a clean environment, without a dense cloud of material that would restrict the radio emission from escaping. Such cloud of material would be expected, for instance, from a young supernova remnant. We found that the FRB became active earlier and for a shorter time at high frequencies (Apertif) than at low frequencies (LOFAR), as illustrated in Fig. A. This is the exact opposite of what the leading theory for the periodicity interpretation predicted. The theory suggested that the FRB was a magnetar in a binary system with another star emitting strong stellar winds. These winds would shield the radio emission from the magnetar, and only when the latter was in the direction of Earth would the FRBs escape the strong wind. But in such scenario, high frequency emission would escape more easily, and it should be seen for longer, as opposed to what we observed. Another scenario appeared to match our observations much better: the periodicity could be produced by a magnetar rotating extremely slowly, with a period of 16 days. A magnetar with such a long period has never been found before, and it could be challenging for such a source to exist. However, this would explain why the low frequency emission was seen for longer. Our discoveries are an additional indication of the link between repeating FRBs and magnetars.

In Chapter 5, we present a new one-off FRB with unique properties that we discovered with Apertif. This new FRB is composed of five components with a regular spacing of just 0.4 milliseconds. The spacing is so small, that it cannot be explained by the rotation period of a neutron star; at such speeds, the star would be destroyed. The merger of two compact objects is even less likely, since two objects cannot orbit each other faster than they can themselves rotate. However, many galactic pulsars, as well as magnetars, have been seen to show complex morphologies in their radio emission. We thus conclude that a magnetar with a complex magnetospheric configuration could explain the structure we observe in this FRB. Our study supplies proof of a link between one-off FRBs and magnetars.

The final Chapter 6 presents all the new one-off FRBs that we discovered during the Apertif survey. We found a total of 24 new sources, which is one of the largest FRB collections so far. In these FRBs, we found many with complex morphologies, way more than what we expected from the previously existing FRB detections. Additionally, we identify several FRBs that must live in dense clouds of material to explain their radio properties. This means that FRBs can exist in different environments or have different ages. If Apertif was able to look at the whole sky at the same time, it would find almost 500 FRBs per day.

To conclude, during my PhD I have studied the characteristics of one-off and repeating FRBs, developed tools to look for their X-ray counterparts, and studied pulsars, some of the closest FRB analogues in our galaxy. I have established links between the observable features of repeating and one-off FRBs with hypermagnetic neutron stars, and I have characterised the properties of the FRB population with Apertif. This will ultimately help us determine the nature of FRBs.

Figure A: Artistic interpretation of the periodic FRB (Chapter 4) as seen with Apertif and LOFAR. The antennas on the left are some of the WSRT dishes, which sees the high frequency (blue) bursts earlier and for a shorter time. The antennas on the right are from LOFAR, which sees the bursts at lower frequencies (red) later and for longer. Credit: Joeri van Leeuwen.

Nederlandse samenvatting

De nachtelijke hemel lijkt misschien eeuwig en onveranderlijk, maar af en toe verschijnen tijdelijk nieuwe bronnen aan het firmament. Deze voorbijgaande astronomische signalen worden gecreëerd door sommige van de meest energetische processen in ons heelal, en ze zijn vaak het product van ‘‘compacte objecten”. Die compacte objecten zijn de overblijfselen van sterren, gevormd wanneer een ster in haar binnenste geen nieuwe elementen meer over heeft voor kernfusie. De lichtste sterren, zoals onze Zon, eindigen hun leven als witte dwerg ster. Sterren die geboren zijn met meer dan 8 keer de massa van de Zon worden neutronensterren, maar de zwaarste sterren, die meer dan 25 zo zwaar zijn als de Zon, worden een zwart gat. Deze verschillende compacte objecten herbergen extreme dichtheden, materialen, omwentelingssnelheden, magneetvelden, en/of zwaarteveldsterkte. Die condities zijn vaak onmogelijk op aarde te bereiken. Daardoor zijn compacte objecten ideale laboratoria om de wetten der natuur te testen.

In 2007 werd, tot algemene verbazing, een nieuw type kortdurende hemelbron ontdekt. De flits werd gezien op radiogolflengten, en duurde maar een milliseconde: korter dan het knipperen van je oog. Op de laagste radio frequenties kwam het signaal veel later aan dan op de hoogste. Deze vertraging, die evenredig is met de hoeveelheid materie waar het signaal doorheen gereisd is, en dus met de afstand, maakte duidelijk dat de radiogolven heel ver weg waren ontstaan, ver voorbij de uiterste rand van onze Melkweg! De snelle radioflitsen werden ”Fast Radio Burst” (FRB) gedoopt. Ze waren onverwacht, niet voorspeld. De zoektocht naar het ontcijferen van hun oorsprong begon.

In de paar jaar volgend op de ontdekking van de eerste FRB nam het aantal nieuwe detecties maar zeer langzaam toe. Jarenlang was het aantal theorieën over deze FRB’s groter dan het aantal FRB’s zelf. Naarmate het aantal FRB’s echter groeide, gingen meer en meer radiotelescopen over de wereld op zoek naar deze raadselachtige bronnen. Heden ten dage zijn er meer dan 600 FRB’s gevonden. De grote meerderheid daarvan is slechts één enkele maal waargenomen; deze noemen we de ”eenmalige” of ”niet-herhalende” flitsen. Oorspronkelijk werd gedacht dat de uitbarstingen het gevolg waren van ‘‘cataclysmische’’ gebeurtenissen, waarbij de bron de uitbarsting niet overleeft. Maar sommige FRB’s blijken opnieuw te flitsen, te herhalen. Dat doen ze met onregelmatige tussenpozen. De bron van die herhalende flitsen moet dus een langere levensduur hebben, en niet vernietigd worden in de uitbarsting. Eén van de belangrijkste openstaande vragen in het FRB vakgebied is of herhalende en eenmalige flitsen dezelfde oorsprong hebben. Misschien zijn de eenmalige uitbarstingen minder actieve bronnen. Of worden ze door totaal andere processen geproduceerd?

In april 2020 werd op een al bekende magnetar in onze Melkweg opeens ook een extreem heldere FRB-achtige uitbarsting gezien. Daarmee is die flits plotseling de beste aanwijzing die we hebben over de oorsprong van FRB’s. Wat een ‘magnetar’ is? Een ster met een geboortegewicht van 8

tot 25 maal dat van de Zon eindigt haar leven in een supernova-explosie, nadat ze alle mogelijke elementen in haar binnenste heeft gekernfuseerd. Tijdens de supernova worden de buitenste lagen van de ster met geweld weggeslingerd, terwijl de kern abrupt samentrekt en een neutronenster wordt. Die hele kern, ruwweg anderhalf keer zo zwaar als de Zon, wordt dan samengeperst tot een bol met een straal van slechts 10 km! Door het behoud van het impulsmoment draait deze verse neutronenster ook nog eens extreem snel rond, tussen de één en duizend keer per seconde. Bovendien wordt het magnetisch veld bij de ineenstorting een biljoen (duizend miljard) keer zo groot als dat van de aarde. Daarmee zijn neutronensterren de sterkste magneten van het heelal. Neutronensterren kunnen radiogolven uitzenden vanaf hun magnetische polen, en als deze polen bij het ronddraaien ook richting de aarde wijzen, zien we vanaf hier periodieke radiostraling. Dit soort neutronensterren met periodieke emissie heet 'pulsars'. Wel nu, magnetars zijn neutronensterren met nog extremere magnetische velden. Hun magnetosfeer is vaak chaotisch en verwrongen, en soms zijn ze een tijdje elektromagnetisch actief wanneer de magnetosfeer van configuratie verandert. Dan zendt de magnetar röntgenstraling, gammastraling of soms radiostraling uit.

Ik begon aan dit proefschrift in de week dat Apertif ook startte. Apertif was een nieuw ontvangersysteem voor de Westerbork telescoop. Dit krachtige instrument was in staat een groot deel van de hemel te beslaan, met een hoge tijds- en frequentieresolutie. Daarmee was Apertif perfect geschikt om nieuwe FRB's te vinden, en daarmee één van de hoofddoelen van het systeem. Dit FRB onderzoek begon in juli 2019 en duurde tot februari 2022, slechts een paar maanden geleden, nu ik dit schrijf. Het doel van mijn proefschrift was om te bepalen welke bronnen er achter het FRB fenomeen kunnen zitten. Om dat te bereiken, bestond mijn werk hoofdzakelijk uit het verzamelen en analyseren van de Apertif FRB's. Ik heb hun karakteristieke eigenschappen bestudeerd en die vergeleken met andere soorten galactische bronnen die we beter kennen, voornamelijk neutronensterren. Ik heb daarnaast ook een methode ontwikkeld en gebruikt om eventuele röntgenstraling van FRB's te detecteren, waardoor we onze kennis over deze bronnen nog verder kunnen verdiepen.

In Hoofdstuk 2 onderzoeken we vier pulsars, die alleen bij hoge energie (röntgen- of gammastraling) waren gezien, maar nooit in radio. We hebben geprobeerd die lichtzwakke bronnen toch waar te nemen, door een zeer lange sluitertijd te gebruiken op lage radio frequenties, met een zeer gevoelige Nederlandse radiotelescoop, LOFAR. Bij pulsars is die laagfrequente radioemissie namelijk soms duidelijker dan de hoogfrequente emissie. De pulsars die we onderzochten hebben verschillende overeenkomsten met de magnetars, waarvan we denken dat ze FRB's produceren. Het is dus belangrijk magnetars te bestuderen, als we willen begrijpen hoe zulke heldere radio-uitbarstingen worden geproduceerd. We hebben echter geen radiostraling van de bronnen gedetecteerd. We weten nu wel beter hoe lichtzwak ze zijn.

In Hoofdstuk 3 presenteren we het EXOD algoritme. We hebben de EXOD methode ontwikkeld om zwakke kortstondige röntgenbronnen te vinden in waarnemingen door XMM-Newton, de röntgenruimtetelescoop die om de aarde cirkelt. De FRB-achtige emissie van de eerdergenoemde magnetar in onze Melkweg werd tegelijk uitgezonden met een heldere röntgenuitbarsting. Extragalactische FRB's kunnen dus ook samenvallen met kortstondige röntgenbronnen. Het vinden van die overeenkomst is dus belangrijk om de oorsprong van FRB's te begrijpen. In dit hoofdstuk

beschrijven we de 35 nieuwe bronnen die we met onze nieuwe variabiliteitsmethode hebben geïdentificeerd. Vier van deze bronnen blijken extragalactische neutronensterren te zijn. Ze draaien allen in dubbelsterren rond een andere ster. De neutronensterren slokken massa op van hun begeleider, waardoor ze zeer heet worden en fel schijnen, in röntgenstraling. In de Melkweg zijn veel van dergelijke dubbelsterren bekend, maar in ons buurstelsel Andromeda nog niet. Met deze ontdekkingen hebben we de populatie van bekende neutronensterren in Andromeda verdubbeld.

Hoofdstuk 4 beschrijft onze intensieve waarneemcampagne op een zeer bijzondere herhalende FRB. Recent was in het herhalende flitspatroon van deze FRB ontdekt dat de bron periodiek, elke 16 dagen, actief werd. Alleen gedurende 5 piekdagen per cyclus waren op onregelmatige tijdstippen meerdere uitbarstingen te zien. Daarna betrachtte de bron radiostilte, tot het begin van de volgende periode. Dit is de eerste bron waarbij zulk periodiek gedrag is waargenomen. Om te begrijpen wat de oorzaak van die regelmatigheid kan zijn, hebben we de FRB waargenomen met Apertif en met LOFAR, tegelijkertijd. Wat we vonden was zeer verrassend. We zagen de FRB meer dan 50 keer met Apertif. Maar we hebben de bron ook 9 keer gedetecteerd met LOFAR, en dat waren de laagst-frequente detecties van een FRB, ooit! Het bestaan van deze laag-frequente emissie betekent dat de FRB zich in een lege, heldere omgeving bevindt, en niet, zoals eerder wel gedacht, omgeven wordt door een dichte wolk van materiaal die de radio-emissie absorbeert. Een dergelijke elektronen- of gaswolk zou je bijvoorbeeld wel verwachten bij een jonge supernovarest. We konden aantonen dat de FRB bij hoge frequenties (Apertif) eerder en korter actief was dan bij lage frequenties (LOFAR), zoals te zien in Fig. A. Dit is tegenovergesteld aan de voorspellingen van de tot dan toe vooraanstaande theorie voor de periodiciteit. Die stelde dat de FRB afkomt van een magnetar die een dubbelstersysteem vormt met een begeleider die sterke sterwinden uitblaast. Deze sterwinden zouden dan de radio-emissie van de magnetar in de meeste richtingen afschermen. Slechts bij bepaalde standen van de dubbelsterbaan kunnen FRB's aan de sterke wind ontsnappen in de richting van de aarde. Maar in dit scenario zou de hoogfrequente emissie gemakkelijker ontsnappen, en langer te zien zijn – het tegenovergestelde van onze waarnemingen. We concluderen dat een ander scenario veel beter overkomt met onze bevindingen: de periodiciteit zou kunnen worden veroorzaakt door een magnetar die zeer langzaam ronddraait, één maal per 16 dagen. Een magnetar met een dergelijke lange periode is nog niet eerder gevonden, en is misschien moeilijk te vormen. Het verklaart echter wel waarom de laagfrequente emissie langer te zien was. Onze ontdekkingen zijn een extra aanwijzing voor het verband tussen de herhalende FRB's en magnetars.

In Hoofdstuk 5 presenteren we een nieuwe eenmalige FRB die we met Apertif hebben ontdekt. Deze nieuwe FRB heeft unieke eigenschappen: zo bestaat de flits uit vijf componenten, met een regelmatige, tussenliggende periode van slechts 0,4 milliseconde. Die onderlinge tijdsduur is zo klein, dat deze niet kan worden verklaard door de rotatieperiode van een neutronenster; zulke rotatiesnelheden kan zelfs een neutronenster niet overleven. Een spiraliserende fusie van twee compacte objecten is nog onwaarschijnlijker. Wel is bij veel pulsars, en ook bij magnetars, een vergelijkbare complexe vorm van de radiolichtkromme waargenomen. We concluderen dan ook dat een magnetar met een dergelijke magnetosfeer de FRB structuur kan verklaren. Daarmee levert onze studie bewijs voor een verband tussen eenmalige FRB's en magnetars.

Het laatste Hoofdstuk, 6, beschrijft het volledige ensemble FRB's dat we met Apertif hebben ontdekt. We hebben in totaal 24 nieuwe flitsen gevonden, één van de grootste sets FRB's ooit. In deze FRB's vinden we veel bronnen met een complexe lichtkromme, veel meer verwacht uit eerder onderzoek. Bovendien blijken verschillende FRB's in dichte wolken van materiaal te moeten leven, om hun radio-eigenschappen te kunnen verklaren. Dat betekent dat FRB's zich in zeer verschillende omgevingen ophouden, of verschillende leeftijden kunnen hebben. Apertif ziet maar een deel van de hemel, dus maar een deel van de FRBs; over de gehele hemel blijken rond de 500 FRB's per dag af te gaan, die in principe fel genoeg zijn voor een Apertif detectie.

Zo heb ik tijdens mijn promotie de eigenschappen van zowel eenmalige als herhalende FRB's bestudeerd, methodes ontwikkeld om naar hun röntgentegenhangers te zoeken, en onderzoek gedaan naar pulsars, de meest nabije verwanten van FRB's in onze Melkweg. Ik heb aangetoond dat herhalende en eenmalige FRB's zich vaak gedragen zoals hypermagnetische neutronensterren, en ik heb de eigenschappen van de hele FRB populatie gekarakteriseerd met Apertif. Mede daarmee zullen we uiteindelijk de aard van FRB's bepalen.

Figure A: Illustratie van de periodiek herhalende FRB (Hoofstuk 4), waargenomen met Apertif en LOFAR. Links, enkele van de Westerbork schotels, die de hoogfrequente (blauwe) flitsen eerder en voor kortere tijd zien. De antennes rechts zijn LOFAR, die de uitbarstingen op lagere frequenties (rood) later en langer ziet. Beeld: Joeri van Leeuwen.

Acknowledgements

Here it comes, the end of another chapter. It has been an exciting, exhausting, chaotic, dramatic, rewarding, and successful one. There has been a whole pandemic in between, and rivalries that little have to do with science. But I have also experienced a lot of support and solidarity from my team, colleagues, friends, and family. It has been a challenge, and completing it is a personal achievement that I want to share with those who have contributed to the happy ending.

Joeri, I would like to thank you for giving me the opportunity of working in the incredible field of fast radio bursts as your PhD student. All the discoveries we have made with Apertif have made for an exciting journey. I am really grateful for all your support and encouragement, especially during the last two years. It has been tough, but you have always made sure I was okay. Thank you for giving me freedom with my research while guiding me, for giving importance to the mental health and work-life balance, and for helping me continue with my career in astronomy. Especially, thank you and for trusting me more than I trust myself – I am slowly learning to do it as well. Ralph, thank you for your excitement about my research on all our discussions, for your insightful thoughts about science and life in general, and for caring so much about my progress and well-being.

During my PhD, I have had the chance of being a part of a wonderful research group that has allowed me to learn and improve so much as a scientist. Emily and Liam, I owe a lot of the things I know about FRBs to working with you. All our conversations and collaborations have been truly stimulating all along my PhD. Samayra, Leon and David, you have been my older academic siblings, and I am really grateful for all your patience and uninterested help. Oli, even if our research topics differ, I have really enjoyed working with you. You are a very fun and kind person, and I am sure you are going to have an excellent end of your thesis. Yuyang, you have been a great addition to our group, and I wish you a good continuation during your PhD. Anya, I appreciate how smart and knowledgeable you are, even if you always try to deny it. Working with you has always been a pleasure. Sander and Yogesh, I have great memories of the data acquisition with LOFAR and the excitement when we found the R3 bursts. Dany, thank you for being so helpful and caring. Kaustubh and Pikky, you have both added so much to our meetings and discussions since you joined the group, and I am really happy about it. I hope we can continue collaborating in the future.

I want to thank Natalie Webb for being my master supervisor and allowing me to have a great first research experience. I also want to thank Nathalie Degenaar for being my mentor at API during the past two years, and for every time you have been there to listen. Further, I want to thank Sera Markoff and Lex Kaper for our yearly PhD progress monitoring interviews, which still sounded scary but were valuable to me. I am also grateful for being the teaching assistant to

Rudy Wijnands and Henny Lamers, and for all I learned about optical observations at API and about stellar physics with them.

I'm really grateful to Milena, Susan, and Renee, and for all you have done to hold API together since I got here. I could not have imagined any other staff members as loving and caring as you are. Martin, thank you for being a consistent presence in all events, and for sharing your wisdom about all API matters. I also want to thank Christianne Vink for keeping my mental health in check, and for your empathy and understanding.

My fellow PhD students are some of the best people I know, and I am really grateful for having shared many experiences with them in the last four years. Starting with my paranymphs, Geert and Ben. Geert, it has been so fun sharing an office with you. I will miss your knocks on my desk and our gossip during coffee breaks. Ben, you are such an adventurous and good natured person! I will miss having you as a human replacement for wikipedia. I hope we can keep meeting in Edinburgh or Manchester. Kenzie, you were the best flatmate I could wish for, even if understanding your Scottish was a bit tough at first! Maxwell and I miss having you and Elliot at home. Before you go to Boston, we should take a photo with nobody in it. Frank, you're such a fun person to be with! You have been my main source of random facts and news about the Netherlands, and the spirit of most borrels I have attended. Vlad, you are so fun and thoughtful, and you have contributed so much to my integration at API. I am grateful you were around when I got to the Netherlands. Eva, my favourite French API, I was so lucky to be your office mate and to be TAing with you for two years! I really miss all of our conversations in French and Spanish, believing nobody else understood. David, thank you so much for taking such a good care of Maxwell during the pandemic, and for always seeming so jovial! I am sorry I never went to the football and volleyball sessions you organised in return. Eleanor, thank you for being such a good listener, I always feel understood when I talk to you. Alex, thank you for your support of my foodstagram account while it lasted. Annelotte, thank you for always having a smile on your face! Talking to you always manages to cheer me up. Kelly, I miss sitting next to you in the office, and now you are on the other side of the world! Claire, Lieke, Arkadip, Vatsal, Deniz and Dimitris, the Avengers would not be complete without you. You have all together made API such an amazing place to work, but also to celebrate. I will miss you all deeply.

There are also many people who already left, but who helped me feel welcome at API since day one. Alicia, muchísimas gracias por ser mi buddy y por el cariño que has mostrado siempre, desde las entrevistas del doctorado. Thank you Alice, Macla, Nina, Amruta, Mark, Aastha, Matthieu, Guglielmo, Lorenzo, Kaustubh, and Frank. I wish there had been more overlap in the time we spent at API. And I also thank many of the current and past APIs. Pragya, I really appreciate you and admire your research. I hope we can keep in touch, at least in future FRB meetings. I also want to thank Difeng, Sara, Jure, Lorenzo, Sam, Emanuele, and Amaël for all the nice conversations we have had throughout the years.

During my PhD I had my first experiences as a teaching assistant, and many of the master students I had are now PhD students themselves! Floris, Mitchel, Mark, Omar, Stephanie, Devarshi, Dion, Hinna, I could not have wished for better students. And to the younger generations, especially Iris, Danté, Akshata, Anwesh, Wanga, Kate, Fabienne, Kevin, Pushpita, Yves, I wish you all the best during the rest of your PhD. You now have the responsability to keep the API spirit up.

Y aquí acaba un capítulo que ha sido emocionante, agotador, caótico, dramático, gratificante y exitoso. El doctorado es un camino de rosas con espinas. No hay nada regalado, ni fácil, y aparte de una pandemia he encontrado rivalidades ajenas a la investigación. Ha sido un reto, y completarlo es un logro personal que quiero compartir con todos los que han contribuido al final feliz.

He tenido la suerte de contar con muchas personas que me apoyaban desde el extranjero. Berta, Esther y Paulina, mis chicas, después de tantos años conociéndonos seguís siendo mis mejores amigas, y sé que estáis ahí siempre que lo necesito. Os agradezco todo lo que hemos vivido juntas y espero impaciente a lo que nos queda por delante. Elvira, mi primita, e Irene, la prima favorita, gracias por ejercer también de amigas. Sandrine, merci beoucoup pour ton amitié depuis la fac, et pour tous les moments qu'on a passé ensemble même quand j'étais déjà partie aux Pays Bas. Alex et Ombeline, vous étiez la colloc de la joie, et j'ai adoré vous acueillir à Amsterdam. Il faut que vous veniez aussi à Manchester! Gracias a todos mis primos guays, siempre listos para cotillear y reíros de cualquier cosa. Gracias a mis tías y primos Marazuela y a mis tíos Pastor por estar siempre pendientes de mis andanzas.

Quiero agradecerles principalmente a papá, mamá, Gabriel y Jimena, a quienes dedico esta tesis, por todo el apoyo, cariño y confianza que me han dado desde que me fui de Segovia con diecisiete años con el sueño de ser astrofísica. No podría haberlo cumplido sin vosotros. Papá, no me perdonarías si no recordara aquí las noches en que de pequeña me sacabas a la terraza a mirar las estrellas cuando no podía dormir. Mamá, gracias por todo tu amor y cariño. Ya sé que te costó mucho cuando me fui, pero sé que ahora estás muy orgullosa de mí. Gabriel y Jimena, mis hermanitos, gracias por ser mis compañeros de juegos y desdichas, y por el diseño de la portada de esta tesis.

Andrés, a ti te dedico las últimas frases porque no soy capaz de imaginarme cómo habría podido acabar esta tesis sin ti. Durante estos años has sido mi mayor apoyo científico y moral. Me has dado amor y ánimos, y has sido mi mejor colaborador no oficial. Eres el que más entiende todo lo que he vivido, porque has pasado por ello a la vez. Gracias por aguantarme y acompañarme durante esta última etapa, ya estoy deseando empezar contigo la próxima.

Y ahora... ¡A por el siguiente capítulo!

Inés Pastor-Marazuela,
6 September 2022